STUDY OF SURFACE PLASMON RESONANCE IN TRANSITION METAL NITRIDE THIN FILMS

Thesis submitted to
University of Calicut, Kerala
in partial fulfilment of the requirements for
the award of the degree of

DOCTOR OF PHILOSOPHY IN PHYSICS
under the Faculty of Science

By

LIYA TONY

Under the supervision of

Dr. S. Sankara Narayanan Potty

CENTRE FOR MATERIALS FOR ELECTRONICS TECHNOLOGY [C-MET]
(Scientific Society, Ministry of Electronics and Information Technology, Government of India)

Athani P.O, M.G. Kavu, Thrissur 680581, Kerala, India
www.cmet.gov.in

APRIL 2025

सेन्टर फॉर मेटिरियल्स फॉर इलेक्ट्रॉनिक्स टेक्नोलॉजी (सी-मेट)
(वैज्ञानिक संस्था, इलेक्ट्रॉनिक्स और सूचना प्रौद्योगिकी मंत्रालय, भारत सरकार)
षोरनूर रोड, मुलँगुन्नतुकावु पोस्ट, अत्तानि, त्रिशूर - 680 581, केरला, भारत

CENTRE FOR MATERIALS FOR ELECTRONICS TECHNOLOGY
(Scientific Society, Ministry of Electronics and Information Technology, Government of India)
Shoranur Road, P.O. Mulangunnathukavu, Athani, Thrissur - 680 581, Kerala, India
Tel : EPABX : 91-487-2201156-59 (4 LINES). Fax : 91-487-2201347
E-mail : cmett@cmet.gov.in URL : www.cmet.gov.in

Date..................

CERTIFICATE

This is to certify that the thesis titled **"STUDY OF SURFACE PLASMON RESONANCE IN TRANSITION METAL NITRIDE THIN FILMS "** submitted to University of Calicut in partial fulfilment of the requirements for the award of the degree of **Doctor of Philosophy in Physics** under the Faculty of Science, University of Calicut, is a record of the authentic work carried out by **Mrs. LIYA TONY**, at Centre for Materials for Electronics Technology (C-MET), Thrissur, under my guidance. The work presented in this thesis has not been submitted for any other degree or diploma of this or any other University and has been found to have no plagiarism using the software approved by the UGC/University.

Thrissur

Dr. S. Sankara Narayanan Potty
Supervising Guide

Head Quarters : Panchwati, Off Dr Homi Bhabha Road, NCL (PO), Pune - 411008, Tel : 91-020 25898141, 25898390, 25899273

सेन्टर फॉर मेटिरियल्स फॉर इलेक्ट्रॉनिक्स टेक्नोलॉजी (सी-मेट)
(वैज्ञानिक संस्था, इलेक्ट्रॉनिक्स और सूचना प्रौद्योगिकी मंत्रालय, भारत सरकार)
षोरनूर रोड, मुलेंगुन्नतुकावु पोस्ट, अत्तानि, त्रिशूर - 680 581, केरला, भारत

CENTRE FOR MATERIALS FOR ELECTRONICS TECHNOLOGY
(Scientific Society, Ministry of Electronics and Information Technology, Government of India)
Shoranur Road, P.O. Mulangunnathukavu, Athani, Thrissur - 680 581, Kerala, India
Tel : EPABX : 91-487-2201156-59 (4 LINES), Fax : 91-487-2201347
E-mail : cmet@cmet.gov.in URL : www.cmet.gov.in

Dr. S N Potty
Scientist
snpotty@cmet.gov.in

25.08.2025

CERTIFICATE

This is to certify that all the suggestions recommended by the adjudicators of PhD thesis of Ms. Liya Tony have been incorporated and implemented in the thesis titled, “Study of surface plasmon resonance in transition metal nitride thin films”.

Dr. S Sankara Narayanan Potty
Research Supervisor

DECLARATION

I hereby declare that the work presented in the thesis entitled "**STUDY OF SURFACE PLASMON RESONANCE IN TRANSITION METAL NITRIDE THIN FILMS"** is based on the original work done by me under the guidance of **Dr. S Sankara Narayanan Potty, Scientist, C-MET Thrissur** and has not been included in any other thesis submitted previously for the award of any degree. The contents of the thesis are undergone plagiarism check using **Ithenticate** software at C.H.M.K. Library, University of Calicut, and the similarity index found within the permissible limit. I also declare that the thesis is free from AI generated contents.

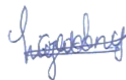

Thrissur **LIYA TONY**

ACKNOWLEDGEMENT

I am deeply grateful to all those who have contributed to the successful completion of this thesis. This journey would not have been possible without the support, encouragement, and expertise of numerous individuals and institutions. Each one of you has played a vital role in shaping this work, and it is with sincere appreciation that I take this opportunity to acknowledge your contributions. From academic guidance to personal support, your presence has been invaluable, and I am truly thankful for all the help I received throughout this endeavour.

First and foremost, I would like to express my deepest gratitude to my thesis supervisor, ***Dr. S.N. Potty****, for his unwavering guidance, mentorship, and support throughout my research. His insightful feedback, valuable suggestions, and constant encouragement played a pivotal role in the successful completion of this thesis. The efforts he had taken during paper and thesis correction is remarkable.*

. I am deeply grateful ***to Dr R. Ratheesh, (Center Head)*** *for his co-ordination and support. I also acknowledge* ***Director (Dr. B. Rajesh)****, the head of my institution, providing permission to carry out this work and permitting to use the research facilities in the C-MET. The former director,* ***Dr N. Raghu****, for their leadership, which provided the academic environment that fostered my research. Their vision and support made this work possible. I would also like to express my appreciation to* ***Dr.Muraleedharan kuttanelloor****,* ***Dr. C.P. Vinod*** *and* ***Dr. Sandhip Dhara, Dr.Kumar V*** *for their guidance and encouragement during this research.*

I would like to express my sincere gratitude to ***Mr. I. Packia Selvam*** *for his invaluable assistance and guidance in helping me navigate the challenges encountered during my research. His constructive feedback during my work presentations was also immensely helpful. extend my sincere thanks to* ***Mr. Praveen Kadhane*** *for his assistance, and prompt help with all the technical aspects of my work. I extend my sincere gratitude to* ***Dr. RSC Bose*** *for providing the information on recent scientific scenario.*

I would like to acknowledge ***Mr.Dharmaraj, Mr.Shakeer*** *for their excellent service and technical expertise in maintaining and repairing the instruments used in my*

research. Their prompt responses and efficiency were crucial in ensuring that my research proceeded without major setbacks.

I am also deeply grateful to my seniors, especially ***Dr. A. K. Sivadasan Dr. Prabeesh P, Dr. Soumya K*** *along with colleagues* ***Sreedevi Janardhanan, Sumesh K, Sajeesh K and Vishnu K N*** *for their collaborative spirit, intellectual discussions, and for providing a productive and supportive work environment. Their camaraderie made this journey much more enjoyable and fulfilling.*

To my friends, especially ***Merin Pullikottil, Anagha Baby, Jumana P.J, and Gadha Menon K,*** *I extend my heartfelt thanks for their moral support, encouragement, and understanding during the challenging times of my research. Their belief in me and their ability to offer a listening ear when needed were a great source of comfort.*

I gratefully acknowledge the financial support provided by DST INSPIRE and travel grant support from ANRF-ITS for this research. Their funding enabled me to acquire the necessary resources and conduct my work with the required tools and materials.

My sincere thanks also go to my collaborators at IISc CENSE and UGC-DAE Indore, for their valuable insights and for sharing their experimental facility. Our collaboration significantly enriched the quality of my research. I acknowledge the support of Mr.Majo for FESEM and Raman measurements

I acknowledge my gratitude to administrative officer, Ainance officer and all my colleagues at C-MET especially Mrs. Priyadarshini for UV-Visible analysis, Mr. Arun for SEM analysis. Extend my sincere gratitude to project students Aparna, Indrajith, Kesline, Sanvid and Answara.

I am deeply grateful to my parents (Appa, Amma, Mummy, Daddy), for constant presence, encouragement, and understanding during the most difficult times, this been a source of strength and inspiration. Special gratitude to Mr.Naveen, for being true pillar of support, always lifting me up when I needed it most. I express my gratitude to my siblings, I owe my deepest gratitude for their endless love, encouragement, and belief in me.

*I thank my daughter **Izza Naveen** whose joy, love, and understanding have been the light of my life. And for motivating me with her smiling face. And special thanks to Kunju and Lilly for their prayers.*

*Last but not the least, I praise and indebted to **ALMIGHTY** for being the unfailing source of support, comfort and strength throughout the completion of my research work.*

LIYA TONY

Dedicate to
All my Well wishers

Abstract of PhD thesis (Physics) – Liya Tony, C-MET Thrissur

STUDY OF SURFACE PLASMON RESONANCE IN TRANSITION METAL NITRIDE THIN FILMS

Converting light into plasmons contributes to the extension of photonics into nano size region. Plasmonic phenomena arise from the collective oscillations of free electrons in a material when an electromagnetic ray is incident on it. Metals have abundance of free electrons, and hence metallic elements are required in plasmonic structures. Gold and silver have traditionally been used for such applications because they exhibit surface plasmon properties in the visible wavelength region. However, these metals are expensive and have some limitations that make them unsuitable for potential device applications. In current scenario of plasmonics discipline, alternatives to traditional metals are being sought primarily.

Transition metal nitrides are a better alternative plasmonic material in the visible region. This thesis focuses on the development of two technologically important transition metal nitrides, titanium and zirconium nitrides, with plasmonic characteristics in visible region. One of the essential properties for plasmonic behaviour is high carrier density (of the order of $10^{22}/cm^3$), which is crucial to achieve the required negative permittivity in the wavelength region of interest. Being non-stoichiometric, the opto-electronic properties of these nitrides depend mainly on their preparation routes. They can have high carrier concentrations in the above order, thereby achieving metallic behaviour in the visible region. Another important property required for efficient plasmonics is reduced dielectric loss, which necessitates correlated opto-electrical property analysis and structural confirmation in the developed films.

Although transition metal nitride film properties depend on stoichiometry and deposition method, this work also aims to examine process dependence in titanium nitride films, which further tunes the material structure and plasmonic properties. Rather than using a vacuum deposition for thin film fabrication, the focus was to develop a cost-effective novel approach for the fabrication of titanium nitride plasmonic film by opting nitridation of ammonia. Initial understanding on material properties was achieved through comprehensive study on TN films developed by sputtering technique. Then, opted nitridation routes for converting titanium metal and titanium dioxide films into plasmonic TiN, of which the latter proved to be a cost-effective approach. In each case, the plasmonic properties were investigated and excited surface plasmon polariton in the optimized films using a prism base Kretschmann configuration in a wavelength interrogation method.

Zirconium nitride is projected in the literature to be a better plasmonic material than titanium nitride in the visible region. In this work, the properties of DC sputtered zirconium nitride films were investigated, and the structural, optical, and electrical properties were studied in the context of plasmonics. Finally, surface plasmon polariton was successfully excited in the Kretschmann configuration, proving zirconium nitride to be an excellent alternative plasmonic material. The research findings were published in three international journals and at several conferences.

Liya Tony 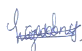
Research scholar
Centre for Materials for Electronics Technology (C-MET), Thrissur

Dr. S Sankara Narayanan Potty
Scientist E (Research Guide)
Centre for Materials for Electronics Technology (C-MET), Thrissur

പിഎച്ച്ഡി പ്രബന്ധത്തിന്റെ സംഗ്രഹം – ലിയ ടോണി, ഭൗതികശാസ്ത്ര ഗവേഷണ വിദ്യാർത്ഥി, സി-മെറ്റ് തൃശൂർ

ട്രാൻസിഷൻ മെറ്റൽ നൈട്രൈഡ് തിൻ ഫിലിമുകളിലെ സർഫസ് പ്ലാസ്മോൺ അനുരണനത്തെക്കുറിച്ചുള്ള പഠനം.

പ്രകാശത്തിന്റെ ദീർഘതരംഗദൈർഘ്യം ഫോട്ടോണിക്സിനെ ഉപ-തരംഗദൈർഘ്യ വ്യവസ്ഥയിലേക്ക് കൊണ്ടുപോകുന്നതിന് ഒരു തടസ്സമാണ്. പ്രകാശത്തെ പ്ലാസ്മോണുകളാക്കി മാറ്റുന്നതിലൂടെ ഈ പ്രശ്നം പരിഹരിക്കാൻ കഴിയും. ഒരു വസ്തുവിൽ ഒരു വൈദ്യുതകാന്തിക കിരണം പതിക്കുമ്പോൾ അതിലുള്ള സ്വതന്ത്ര ഇലക്ട്രോണുകളുടെ കൂട്ടായ ആന്ദോളനങ്ങളിൽ നിന്നാണ് പ്ലാസ്മോണിക് പ്രതിഭാസങ്ങൾ ഉണ്ടാകുന്നത്. ലോഹങ്ങൾക്ക് ധാരാളം സ്വതന്ത്ര ഇലക്ട്രോണുകൾ ഉണ്ട്, അതിനാൽ പ്ലാസ്മോണിക് ഘടനകളിൽ ലോഹ മൂലകങ്ങൾ ആവശ്യമാണ്. ദൃശ്യതരംഗദൈർഘ്യ മേഖലയിൽ സർഫസ് പ്ലാസ്മോൺ ഗുണങ്ങൾ പ്രകടിപ്പിക്കുന്നതിനാൽ സ്വർണ്ണവും വെള്ളിയും പരമ്പരാഗതമായി അത്തരം പ്രയോഗങ്ങൾക്ക് ഉപയോഗിക്കുന്നു. എന്നിരുന്നാലും, ഈ ലോഹങ്ങൾ വിലയേറിയതും ഉപയോഗസാധ്യതയുള്ള ഉപകരണ നിർമ്മാണങ്ങൾക്ക് അനുയോജ്യമല്ലാത്ത ചില പരിമിതികളുള്ളതുമാണ്. പ്ലാസ്മോണിക്സ് വിഭാഗത്തിന്റെ നിലവിലെ സാഹചര്യത്തിൽ, പരമ്പരാഗത ലോഹങ്ങൾക്ക് പകരമുള്ള ബദലുകൾ ഗവേഷകർ പ്രധാനമായും തേടിക്കൊണ്ടിരിക്കുന്നു.

ദൃശ്യപ്രകാശശ്രേണിയിൽ ട്രാൻസിഷൻ ലോഹ നൈട്രൈഡുകൾ മികച്ച ഒരു ബദൽ പ്ലാസ്മോണിക് വസ്തുവാണ്. ഈ പ്രബന്ധം ശ്രദ്ധ കേന്ദ്രീകരിക്കുന്നത് ദൃശ്യമേഖലയിൽ പ്ലാസ്മോണിക് സ്വഭാവസവിശേഷതകളുള്ള രണ്ട് പ്രധാനപ്പെട്ട ട്രാൻസിഷൻ ലോഹ നൈട്രൈഡുകളായ ടൈറ്റാനിയം നൈട്രൈഡ്, സിർക്കോണിയം നൈട്രൈഡ് എന്നിവയുടെ വികസനത്തിലാണ്. പ്ലാസ്മോണിക് സ്വഭാവത്തിന് അത്യാവശ്യമായ ഗുണങ്ങളിലൊന്ന് ഉയർന്ന ഇലക്ട്രോൺ സാന്ദ്രതയാണ് ($10^{22}/cm^3$ എന്ന കണക്കിൽ), ഇത് ഉദ്ദേശിക്കുന്ന തരംഗദൈർഘ്യ മേഖലയിൽ അവശ്യം വേണ്ടുന്ന നെഗറ്റീവ് പെർമിറ്റിവിറ്റി കൈവരിക്കുന്നതിന് നിർണായകമാണ്. സുവ്യക്തമായൊരു രാസസമീകരണം (സ്റ്റോയിക്കിയോമെട്രി) ഇല്ലാത്തതിനാൽ , ഈ നൈട്രൈഡുകളുടെ ഒപ്റ്റോ-ഇലക്ട്രോണിക് ഗുണങ്ങൾ പ്രധാനമായും അവയെ നിർമിക്കുന്ന വിവിധ രീതികളെ ആശ്രയിച്ചിരിക്കുന്നു. മുകളിൽ പറഞ്ഞ ഉയർന്ന ഇലക്ട്രോൺ സാന്ദ്രത ഇത്തരം പദാർത്ഥങ്ങളിൽ ഉണ്ടാക്കാൻ സാധിക്കും, അതുവഴി ദൃശ്യപ്രകാശമേഖലയിൽ ലോഹ സ്വഭാവം കൈവരിക്കാനുമാകും. കാര്യക്ഷമമായ പ്ലാസ്മോണിക്സിന് ആവശ്യമായ മറ്റൊരു പ്രധാന സ്വഭാവം കുറഞ്ഞ ഡൈഇലക്ട്രിക് നഷ്ടമാണ്, ഇതിന് വികസിപ്പിച്ചെടുക്കുന്ന നേർത്ത ഫിലിമുകളിൽ പരസ്പരബന്ധിതമായ ഒപ്റ്റോ-ഇലക്ട്രിക്കൽ സ്വഭാവവിശകലനവും ഘടനാപരമായ സ്ഥിരീകരണവും ആവശ്യമാണ്.

ട്രാൻസിഷൻ ലോഹ നൈട്രൈഡ് ഫിലിമിന്റെ ഗുണങ്ങൾ സ്റ്റോയ്ക്കിയോമെട്രിയെയും ഫിലിം ഉണ്ടാക്കുന്ന രീതിയെയും ആശ്രയിച്ചിരിക്കുന്നുവെങ്കിലും, ടൈറ്റാനിയം നൈട്രൈഡ് ഫിലിമുകളിലെ നിർമാണ ആശ്രിതത്വം പരിശോധിക്കാനും ഈ പ്രബന്ധം ലക്ഷ്യമിടുന്നുണ്ട്, ഇത് പദാർത്ഥ ഘടനയെയും പ്ലാസ്മോണിക് ഗുണങ്ങളെയും കൂടുതൽ ട്യൂൺ ചെയ്യുന്നു. തിൻ ഫിലിം നിർമ്മാണത്തിനായി ശൂന്യത അടിസ്ഥനത്തിലുള്ള ഒരു നിർമാണരീതിക്ക് പകരം, അമോണിയയെ വിഘടിപ്പിച്ചുള്ള നൈട്രിഡേഷൻ രീതി തിരഞ്ഞെടുത്ത് ടൈറ്റാനിയം നൈട്രൈഡ് പ്ലാസ്മോണിക് ഫിലിം നിർമിക്കാനായി ചെലവ് കുറഞ്ഞ ഒരു പുതിയ സമീപനം വികസിപ്പിക്കുക എന്നതിലായിരുന്നു കൂടുതൽ ശ്രദ്ധ കൊടുത്തത്. ഇതിനായി, ശൂന്യത അടിസ്ഥാനമാക്കിയുള്ള സ്പട്ടറിംഗ് രീതിയിലൂടെ വികസിപ്പിച്ചെടുത്ത ടൈറ്റാനിയം നൈട്രൈഡ് ഫിലിമുകളുടെ പദാർത്ഥഗുണങ്ങളെക്കുറിച്ചുള്ള സമഗ്രമായ പ്രാരംഭപഠനത്തിനുശേഷമാണ് ടൈറ്റാനിയം ലോഹഫിലിമിൽ നിന്നും ടൈറ്റാനിയം ഡൈ ഓക്സൈഡ് ഫിലിമിൽ നിന്നും പ്ലാസ്മോണിക് ടൈറ്റാനിയം നൈട്രൈഡ് ഉണ്ടാക്കുന്നതിനുള്ള നൈട്രിഡേഷൻ റൂട്ടുകൾ പഠനത്തിന് വിധേയമാക്കിയത്; അതിൽ രണ്ടാമത്തേത് ചെലവ് കുറഞ്ഞ സമീപനമാണെന്ന് തെളിഞ്ഞു. ഓരോ രീതിയിലും, തരംഗദൈർഘ്യം അടിസ്ഥാനമാക്കിയുള്ള പ്രിസം ഉപയോഗിക്കുന്ന ക്രെറ്റ്ഷ്മാൻ രീതി ഉപയോഗിച്ചാണ് വികസിപ്പിച്ചെടുത്ത ഫിലിമുകളിൽ പ്ലാസ്മോണിക് ഗുണങ്ങൾ അന്വേഷിച്ചതും സർഫസ് പ്ലാസ്മോണുകളെ ഉത്തേജിപ്പിച്ചതും.

ദൃശ്യപ്രകാശമേഖലയിൽ ടൈറ്റാനിയം നൈട്രൈഡിനേക്കാൾ മികച്ച പ്ലാസ്മോണിക് വസ്തുവായി സിർക്കോണിയം നൈട്രൈഡ് പ്രവചിക്കപ്പെട്ടിട്ടുണ്ട്. ഈ പ്രബന്ധത്തിൽ ഡയറക്ട് കറന്റിലൂടെ സ്പട്ടർ ചെയ്തെടുത്ത സിർക്കോണിയം നൈട്രൈഡ് ഫിലിമുകളുടെ ഗുണങ്ങൾ പഠിക്കുകയും പ്ലാസ്മോണിക്സിന്റെ വെളിച്ചത്തിൽ ഘടനാപരവും കൂടാതെ ഓപ്റ്റിക്കൽ, വൈദ്യുത ഗുണങ്ങളും പഠനവിധേയമാക്കുകയും ചെയ്തു. അവസാനം, ക്രെറ്റ്ഷ്മാൻ രീതിയിൽ സർഫസ് പ്ലാസ്മോൺ പോളാരിറ്റൺ വിജയകരമായി ഉത്തേജിപ്പിച്ച് എടുക്കുകയും, സിർക്കോണിയം നൈട്രൈഡ് ഒരു മികച്ച ബദൽ പ്ലാസ്മോണിക് വസ്തുവാണെന്ന് തെളിയിക്കുകയും ചെയ്തു. ഗവേഷണ കണ്ടെത്തലുകൾ മൂന്ന് അന്താരാഷ്ട്ര ജേണലുകളിൽ പ്രസിദ്ധീകരിക്കുകയും നിരവധി കോൺഫറൻസുകളിലും അവതരിപ്പിക്കുകയും ചെയ്തിട്ടുണ്ട്.

CONTENTS

	Preface	xiv
	List of Figures	xxi
	List of Tables	xxviii
	List of Abbreviations	xxx
Chapter No	**Title**	**Page No**
1	**Introduction to Plasmonics**	
	Introduction	1
	1.1 Basics of Plasmonics	3
	1.1.1 Plasma Frequency	4
	1.1.2 Surface and Volume Plasmons	4
	1.1.3 Localized Surface Plasmon Resonance and Surface Plasmon Resonance	6
	1.2 Dispersion Relation	7
	1.3 Dielectric Function	8
	1.4 Excitation Configurations	10
	1.4.1 Evanescent Waves	10
	1.4.2 Prism Coupling	11
	1.4.3 Waveguide Geometry	13
	1.4.4 Grating Configuration	14
	1.5 Areas of Application In Plasmonics	15
	1.6 Limitation of Conventional Plasmonic Materials	18
	1.7 Alternative Plasmonic Materials	22
	1.8 Plasmonic Properties of Transition Metal Nitrides	24
	1.9 Titanium Nitride	25
	1.10 Zirconium Nitride	28
	1.11 Motivation of the Work	30
	1.12 Objective of the Thesis	31
	1.13 References	32-46
2	**Experimental techniques**	
	Introduction	47
	2.1 Substrate cleaning	47
	2.2 Coating techniques	48
	2.2.1 Magnetron reactive sputtering	49
	2.2.2 Spin coating	51
	2.2.3 Gas nitridation	54
	2.3 Structural analysis	56

	2.3.1 Glancing angle XRD	56
	2.3.2 X-ray photoelectron spectroscopy	58
	2.3.3 Raman spectroscopic analysis	61
	2.4 Microstructure analysis	63
	2.4.1 Field enhanced scanning electron microscopy (FE-SEM)	63
	2.4.2 Atomic force microscopy	65
	2.5 Electrical properties via Hall measurements	66
	2.6 Optical properties	69
	2.6.1 Reflectance Spectra and Dispersion relation	69
	2.6.2 Bandgap estimation using Tauc plot from transmittance spectra	73
	2.7 Excitation of surface plasmon polaritons via Kretchsmann type prism configuration	74
	2.8 Summary	77
	2.9 References	78-82
3	**Investigation of plasmonic properties in RF sputtered titanium nitride thin films**	
	Introduction	83
	3.1 Development of titanium nitride films	84
	3.2 Structural properties of RF sputtered Titanium nitride films	85
	3.2.1 X-ray diffraction analysis	85
	3.2.2 X-ray photoelectron spectroscopy	88
	3.2.3 Raman Spectroscopic Analysis	92
	3.3 Surface and microstructure analysis	95
	3.3.1 Morphology analysis: FESEM	95
	3.3.2 Atomic force microscopy Analysis	97
	3.4 Electrical properties in TiN films	100
	3.5 Optical properties	102
	3.6 Excitation of Surface plasmons in the titanium nitride films	108
	3.7 Conclusion	111
	3.8 References	112-116
4	**Investigation of plasmonic properties in TiN_X thin films derived from nitridation of Titanium metal films**	
	Introduction	117
	4.1 Development of TiN films	119

	4.1.1 Film Preparation	119
	4.1.2 Nitridation Conditions	120
	4.2 Structural Analysis	121
	4.2.1 G1-XRD Studies	121
	4.2.2 XPS Studies	123
	4.3 Microstructural Analysis	127
	4.3.1 FE-SEM Studies	127
	4.3.2 Atomic Force Microscopic Analysis	129
	4.4 Electrical Property Analysis	131
	4.5 Optical Property Analysis	134
	4.6 Plasmonic Property Analysis	139
	4.7 Conclusion	145
	4.8 References	146-149
5	**Investigation of surface plasmon resonance properties in TiN_X thin films fabricated from spin coated TiO_2 thin films**	
	Introduction	151
	5.1 Development of TiN thin film	152
	5.1.1 Mechanism of conversion to titanium nitride	153
	5.1.2 Spin coating of titanium dioxide thin film	154
	5.1.3 Nitridation of the spin-coated TiO_2 film	154
	5.2 Investigation of the structural properties of the films	156
	5.2.1 Grazing incident X-ray diffraction studies	156
	5.2.2 X-ray photoelectron spectroscopy	158
	5.2.3 Analysis of Raman spectra	162
	5.3 Morphology analysis	165
	5.3.1 Surface morphology	165
	5.3.2. Atomic force microscopic analysis	166
	5.4 Investigation of the electrical properties of the films	168
	5.5 Optical properties of the films	171
	5.5.1 Estimation of energy band gap	171
	5.5.2 Plasmonic properties	172
	5.6 Excitation of surface plasmon resonance	175
	5.7 Conclusion	178

	5.8 References	179-185
6	**Investigation of plasmonic properties in RF sputtered Zirconium nitride thin films**	
	Introduction	187
	6.1 Development of zirconium nitride films for plasmonic applications	188
	6.2 Structural properties sputtered Zirconium nitride films	189
	6.2.1 X-ray diffraction Studies	189
	6.2.2 X-ray Photoelectron Spectroscopic analysis	191
	6.3 Morphological analysis	196
	6.4 Electrical properties	198
	6.5 Optical properties	200
	6.6 Investigation of plasmonic properties	205
	6.7 Conclusion	208
	6.8 References	209-212
7	**Summary of thesis**	**213**
8	**Recommendations**	**217**

PREFACE

The wavelength of light restricts the extension of photonics into nanosize regime. Plasmonics offers a solution to this problem by converting light into plasmons. Plasmonic phenomena arise from the collective oscillations of free electrons in a material when an electromagnetic field is incident on it. Therefore, plasmonic structures require metallic elements, which have a large number of free electrons. When an electromagnetic field interacts with a cloud of free electrons at a metal-electric interface, they can support a wave of fluctuations in charge density, creating a mode known as a surface plasmon. Since the surface plasmon resonance frequency is in the visible wavelength region, metals such as gold and silver have traditionally been used for plasmonic applications. These metals exhibit high chemical stability and higher shift in resonance, which are necessary for various plasmonic applications. However, these metals are expensive and have other limitations such as island formation in very thin layers during deposition, band-to-band transitions, and surface roughness due to thermal evaporation. Therefore, the need of the hour is to develop new or alternative plasmonic materials to develop cost-effective plasmonic devices. In this context, to develop metal substitutes in the visible range, materials with free carrier densities in the order of 10^{22} cm^{-3} are needed. Transition metal nitrides can have such high carrier concentrations and are explored as plasmonic materials functioning in the visible frequencies.

The objective of the present work was to develop transition metal nitride (TMN) thin films (TiN and ZrN) with required carrier concentration to exhibit plasmonic property in visible region. TMN materials are non-stoichiometric and hence the properties are composition dependent. Here, composition tunablity has been attempted in the films by adopting various preparation routes. Sputtering is one of the most widely used physical vapour deposition techniques for coating thin films of transition metal nitrides, and hence this technique was adopted initially. As a novel technique, then opted ammonia nitridation route for the fabrication of plasmonic TiN thin films.

Free electrons in a material provide the required negative real permittivity in the frequency of interest, which is an essential property for any plasmonic material. A

major disadvantage that needs to be avoided for optimum performance of plasmonic materials is the loss associated with them, arising from interband electronic transitions, caused by the light-matter interaction. For exciting surface plasmons, the evanescent electrical field generated at the metal-dielectric interface, generated through a prism geometry, is conventionally adopted for wavevector matching. This process is very much dependent on the thickness of the films. Hence, plasmonic behavior in transition metal nitrides have been achieved by optimizing the material properties such as carrier concentration and mobility by varying coating parameters, and also by fine-tuning the film thickness.

The overall thesis comprises of 8 chapters, explanation for each thesis chapter is given as follows

Chapter 1 provides introductory topics on basic plasmonics and various methodologies required for plasmonic excitation. The challenges and limitations faced when using traditional materials such as gold and silver in plasmonic applications are described in detail. The requirements and properties of alternative plasmonic materials are explained in this chapter. The chapter ends up combining the advantages of titanium nitride and zirconium nitride in the context of plasmonics, which are chosen as an alternative platform.

Chapter 2 discusses the overall experimental methodology used for the development and characterization of the plasmonic transition metal nitride films. The approach was to study a correlated structural, morphological, electrical and optical characterization of the developed films. Such correlated methodology helps to tune material properties suitable for plasmonic excitation in films. The elemental compositions were confirmed with X-ray photoelectron spectroscopy and the vacancy analysis by Raman spectroscopy, with initial phase formation by gracing incidence x-ray diffraction. Dielectric functions were extracted by employing Drude-Lorentz model from the optical reflectance spectra, and linked with the results of the electrical property analysis. The experimental setup for surface plasmon polariton excitation in prism geometry configuration is also described in this chapter.

Chapter 3 discusses the detailed investigation of the structure and correlation of the opto-electrical properties in radio frequency sputtered titanium nitride films. The study focused on how various parameters such as, gas composition and RF power, affect the electrical and optical properties of the coated film in the context of surface plasmon resonance applications. Films with required carrier density and negative permittivity were fabricated by this technique through the modification of the stoichiometry, the N/Ti ratio, of the coated films. The structural analysis revealed changes in the preferred orientation and the XPS analysis showed a variation of the nitrogen content in the deposited films.

In **Chapter 4**, the novel approach of nitridation for developing titanium nitride thin films is discussed. In the previous chapter, nitrogen gas served as source of nitrogen during sputtering, and the Ti metal was used as the target for sputtering. Here, the nitrogen evolved from disassociation of ammonia gas was used as nitrogen source, such process is termed as nitridation. The nitridation process offers a better platform for tuning the titanium and nitrogen compositions to achieve plasmonic behaviour in the visible region of the electromagnetic spectrum. The radio frequency sputtered titanium metal film served as the titanium source. The Ti films were subjected to ammonia gas nitridation with variable temperature to change the nitrogen content incorporated in the sample. By varying both thickness and nitridation temperature, the stoichiometry in the nitridated thin films were tuned. Further investigations were carried out to evaluate the plasmonic performance in the films. Tuning of the material properties helped achieve the required carrier density, negative permittivity, and low dielectric loss in the films. Surface plasmons were successfully excited in the optimised films in prism configuration in wavelength interrogation mode.

Chapter 5, the focus was on a cost-effective route for developing titanium nitride plasmonic films. The previous chapters described the plasmonic properties in RF-sputtered titanium nitride films with respect to stoichiometry, and also described the transformation of Ti metal film into TiNx films through nitridation. In this working chapter, The methodology consisted of preparing titanium dioxide films via spin coating, followed by nitridation reaction using ammonia gas. The difficulty in obtaining porous-free TiN thin films via the nitridation route was

overcome, and this approach provided excellent material properties for plasmonic applications in the visible region. The resistivity showed remarkable difference from Ωcm to mΩcm upon conversion from TiO_2 to TiN_x. The conversion to highly conducting behaviour with required carrier density led to possess plasmonic behaviour in the films. The correlated opto-electrical properties confirmed the necessary conditions for the surface plasmon polariton. In this Chapter, for the first time, the development of plasmonic titanium nitride thin films through the conversion of titanium dioxide, having the required carrier concentration of 10^{22}/cc for plasmonic application in visible region is discussed.

In **Chapter 6**, the plasmonic performance of another important transition metal nitride, zirconium nitride (ZrN) is discussed. Stoichiometric zirconium nitride films possessing enhanced plasmonic properties due to high quality factor were fabricated by the sputtering. The dielectric loss in ZrN were much lower in comparison to TiN and the plasma wavelength showed a blue shift. The structural confirmation and opto-electrical property analysis have been carried out to investigate the plasmonic performance in the films. The surface plasmons were successfully excited in the films using prism geometry in wavelength interrogation. The zirconium nitride film exhibited much better plasmonic performance than the titanium nitride film.

Chapter 7 concludes the major findings of the thesis work. The process dependency of titanium nitride films in the context of plasmonic performance has been discussed. The current investigations demonstrated the fabrication of films with metallic conductivity and low loss required for plasmonic behavior in the visible region. The **Chapter 8** proposes the future direction of the research work

List of Papers Published in International Journals

1. **Liya Tony**, I Packia Selvam, S.N. Potty (2024), Composition tunablity and correlated property analysis of titanium nitride films for plasmonic applications, Ceramics International, 50, 8, 2024, 13185-13195, https://doi.org/10.1016/j.ceramint.2024.01.230

2. **Liya Tony**, I. Packia Selvam., C.P.Vinod, S.N. Potty. (2025), Enhanced light–matter interaction in gas nitridation-derived TiNx thin films for potential plasmonic applications. Journal of Materials Science, 60, 178-194. https://doi.org/10.1007/s10853-024-10520-y

3. **Liya Tony**, I. Packia Selvam, Sandip Dhara, S.N. Potty (2025), Enhanced plasmonic performance of TiO_2 derived TiN films via gas nitridation, Materials Science and Engineering: B, 311, 2025, 117807, https://doi.org/10.1016/j.mseb.2024.117807.

List of Conference Proceedings

1. **Liya Tony**, Packia Selvam, S. N. Potty; Tunable plasmonic refractive sensor based on titanium metal film. AIP Conf. Proc. 31 August 2023; 2783 (1): 020017. https://doi.org/10.1063/5.0158678

List of Paper Presented in Seminar / Conferences

1. Presented a poster on "Fabrication and Plasmonic Characterization of Zirconium Nitride Thin Films for Refractive Index Sensing Applications", **Liya Tony**, I Packia Selvam, S N Potty in **4th International conferemce on optoelectronic and nanomaterials for advanced technology** (**icONMAT 2025**) held at Cochin University of Science & Technology (CUSAT) during 12-14 Feb 2025 (*This paper bagged the Best Poster Award)*

2. Presented a poster on "Titanium nitride as alternative metamaterial via gas nitridation", **Liya Tony**, I Packia Selvam, S N Potty in the **14th International Conference series META 2024 on Metamaterials**, Photonic Crystals and Plasmonics, (Scopus-indexed), held at **Toyama, Japan** during 16-19th July 2024.

3. reented a paper on "Novel method for the fabrication of titanium nitride thin films from sputtered metal films", **Liya Tony**, I Packia Selvam, S N Potty in the **International Conference on Optics, Photonics and Quantum Information (OPTIQ -2023),** XLVI in the series of Annual Symposia of the Optical Society of India held at Cochin University of Science & Technology (CUSAT) during December 11- 13, 2023.

4. Presented a paper on "Tunable electrical and optical properties in titanium nitride thin films deposited by RF sputtering", **Liya Tony**, I Packia Selvam, S N Potty in the **International Conference on Emergent Phenomena and Quantum Technologies (ICEPQT-2023)**, Central University of Kerala, Kasaragod.

5. Presented a poster on "The effect of post annealing atmosphere conditions on RF sputtered Titanium nitride thin films", **Liya Tony**, I Packia Selvam, S N Potty in the **International materials conclave** organized by C-MET Pune in March 2023.

6. Presented a poster "Plasmonic Sensing Property of Titanium Nitride Films in Kretschmann Configuration" **Liya Tony**, I Packia Selvam, S N Potty. in the **World Sensor Congress** organized by Centre for Materials for Electronics Technology (C-MET) Thrissur, in March 2022.

7. Presented Paper "Tunable Plasmonic Refractive Index Sensor Based On Titanium Metal Film", **Liya Tony,** I Packia Selvam, S N Potty in the I**nternational conference NANOICON-2022** organized by IUCND, Cochin University of Science & Technology (CUSAT) in January 2022.

LIST OF FIGURES

Fig No:	Figure caption	Page No:
1.1	Relation between the operating speeds and critical dimensions of different chip-scale device technologies	2
1.2	Schematic representations of (a) surface and (b) volume plasmons	5
1.3	Dispersion relation of a) light line (yellow) b) through material (red) c) surface plasmon polariton (blue)	7
1.4	Schematic diagram of the prism geometry configuration for SPP excitation (a) Otto configuration and (b) Kretschmann configuration	11
1.5	Schematic representation of waveguide configuration for SPP excitation	13
1.6	Schematic diagram indicating the grating configuration for SPP excitation	14
1.7	Lycurgus Cup (a) in reflected light and (b) in transmitted light, (c) Chartres Cathedral Window	15
1.8	Various applications in plasmonic realm	16
1.9	Contribution of different factors in the dielectric loss (ε_2) in gold metal film	19
1.10	Comparison of the dielectric functions in different materials	24
1.11	Crystal structures of titanium nitride	26
1.12	Crystal structure of zirconium nitride	28

1.13	The spectra of the real (a) and imaginary (b) parts of the permittivity of Au, TiN and ZrN versus wavelength	30
2.1	Process flow for the substrate cleaning	48
2.2	Schematic process indicting sputtering method	50
2.3	Schematic of sputtering system	51
2.4	Steps involved in spin coating technique	52
2.5	Images of (a) spin coater unit and (b) hot plate	54
2.6	Schematic of the nitridation process	54
2.7	Schematic diagram of a) X-ray diffraction b) grazing incidence XRD	56
2.8	(a) Schematic diagram of XPS instrument and (b) the band structure diagram	59
2.9	Representation of optical and acoustic modes	62
2.10	Schematic diagram of Raman spectrometer	63
2.11	a) Process occur when electron beam and material interacts b) Schematic of experimental setup of FESEM	64
2.12	Schematic diagram describing the Principle of AFM	65
2.13	Schematic diagram describing the Principle of a)Vander Pauw measurement b) apparatus	69
2.14	The experimental setup used for the reflectance measurement	72
2.15	Schematic diagram indicating the total internal reflection	74
2.16	Evanescent wave in the metal dielectric interface	75

2.17	Experimental setup for Kretschmann configuration; the component names are given in the figure	75
3.1	X-ray diffraction patterns of the as-deposited titanium nitride films a) TIN1, b) TIN2, c) TIN3 and TiN4	85
3.2	Variation of average crystallite size with Ar : N_2 ratio	87
3.3	Variations in Ti 2p (a, b, c) and N1s peak (e, f, g) for the films TIN1, TIN2, TIN3 deposited with different nitrogen concentrations (d,h), and TIN4, with low power (140W)	89
3.4	Variation of N/Ti ratio in the coated films with Ar:N_2 ratio	89
3.5	Raman spectra for the films a) TIN1 b) TIN2 c) TIN3 and d) TIN4	92
3.6	Variation of surface morphology of TiN films with N/Ti ratio, a) TIN1 b) TIN2 c) TIN3 and d) TIN4	95
3.7	Cross-sectional FESEM images of TiN films, a) TIN1 b) TIN2 c) TIN3 and d) TIN4	96
3.8	2D and 3D images of titanium nitride films, a) TIN1 b) TIN2 c) TIN3 and d) TIN4	98
3.9	Variation of roughness with the N/Ti ratio	99
3.10	Variation of carrier concentration and mobility in RF sputtered titanium nitride films with respect to nitrogen concentration.	102
3.11	Reflectance spectra of the films with various N/Ti ratios	102

3.12	Reflectance spectra with fitted curves a) for TIN1, TIN2 and TIN4, respectively	105
3.13	Extracted real and the imaginary parts of the dielectric function of (a) TIN1, (b) TIN2 and (c) TIN4	105
3.14	Simulated SPR curves for the samples a) TIN1 and b) TIN2 and c) TIN4, and (left) improved SPR curve with reduced loss in TIN1 (right)	109
4.1	Schematic representation of the whole process a) RF sputtered titanium metal film b) process of nitridation, c) titanium nitride film after nitridation, and d) SPR excitation in Kretschmann configuration	118
4.2	Deposition conditions of titanium metal films	119
4.3	GI-XRD pattern obtained for titanium metal films after nitridation a) TIN145, b) TIN150, c) TIN155 and d) TIN160	122
4.4	Detailed scans of Ti2p (a, c, e, g) and N1s spectra (b, d, f, h) of samples with respect to the nitridation temperatures TIN145, TIN150, TIN155 and TIN160, respectively	125
4.5	FE-SEM images of the samples nitridated a) TIN145, b) TIN150, c) TIN155 and d) TIN160; e) composition analysis in depth profiling; f) composition analysis on the film surface; g) typical elemental distribution curve	127
4.6	3D AFM images of TiN films nitridated at temperatures a) TIN145, b) TIN150, c) TIN155 and d) TIN160	129
4.7	2D AFM images of TiN films nitridated at temperatures a) TIN145, b) TIN150, c) TIN155 and d) TIN160	130

4.8	Variation of average surface roughness with nitridation temperature	131
4.9	Electrical properties of nitridated titanium nitride films (a) with different nitridation temperature (b) with variable thickness	132
4.10	Reflectance spectra of titanium nitride films having carrier concentration of $10^{22}/cm^3$	135
4.11	Fitted reflectance curves (left) and the real and imaginary parts of the permittivity values extracted from fitted curves for the films a) TIN045, b) TIN150 and c) TIN255 (right)	137
4.12	Surface plasmon resonance excitation in titanium nitride films with different thickness (a) TIN045 and (b) TiN150	140
4.13	Surface plasmon resonance excitation in titanium nitride films with variable angle of incidence for the film TIN045	143
5.1	Different structures of TiO_2 a) Anatase b) Rutile c) Brookite	152
5.2	As-deposited TiO_2 b) after nitridation at 800 °C c) after nitridation at 950 °C	155
5.3	The GI-XRD patterns obtained for a) as-deposited TiO_2 b) after nitridation at 800 °C c) after nitridation at 950 °	156
5.4	Survey scan XPS spectra of the films a) titanium dioxide b) titanium dioxide after nitridation at 800ºC c) titanium dioxide after nitridation at 950ºC	158
5.5	High resolution scan spectra of (a, b) Ti 2p and O 1s of air annealed TiO_2 film, (b,c) Ti 2p and N 1s of 800°C nitridated film, and (e, f) Ti 2p and N 1s of 950°C nitridated film, respectively.	159

5.6	Raman spectra of the films a) titanium dioxide b) after nitridation at 800°C c) after nitridation at 950 °C	163
5.7	Surface morphology of a) TiO_2 film, and the films niridated at temperatures b) 800 °C and c) 950 °C	166
5.8	Cross-section images of the films nitridated at temperatures a) 800 °C and b) 950 °C	166
5.9	2D and 3D AFM images of a) TiO_2 film and the films nitridated at temperatures b) 800 °C and c) 950 °C	168
5.10	Low energy XPS spectrum of a) titanium dioxide, b) after nitridation at 800ºC, c) after nitridation at 950ºC	170
5.11	Energy bandgap estimated for the films a) titanium dioxide b) nitridated at 800°C, and c) nitridated at 950°C	172
5.12	(a) Reflectance spectra of TIO_2, TIN80, TIN95, (b) extracted dielectric permittivity values for TIN95, (c) quality factor of TIN950	173
5.13	SPR theoretical curve obtained in angular interrogation mode	175
6.1	GI-XRD patterns of the zirconium nitride films deposited with two sputtering power, 60W (left) and 80W (right), and with different Ar/N_2 gas compositions (ZRN1 to ZRN 6). The ICDD file 00-035-0753 of cubic zirconium nitride is shown at the bottom	190
6.2	Survey scan spectrum, high resolution scan spectra of Zirconium and nitrogen of DC sputtered zirconium nitride thin film samples (ZRN1, ZRN2 and ZRN3) deposited with different Ar/N_2 gas compositions at constant DC power of 60W	191

6.3	Survey scan spectrum, high resolution scan spectra of Zirconium and nitrogen of DC sputtered zirconium nitride thin film samples (ZRN4, ZRN5 and ZRN6) deposited with different Ar/N_2 gas compositions at constant DC power of 80W	192
6.4	Variation in elemental composition with respect to amount of nitrogen gas during deposition with power (a) 60W and (b) 80W	194
6.5	Surface morphology of zirconium nitride thin films coated at sputtering power of 60 W (ZRN1, ZRN2 and ZRN3) and 80W (ZRN4, ZRN5 and ZRN6) with variable nitrogen gas concentration	196
6.6	Cross-section images of zirconium nitride thin films deposited at sputtering power of 60W (ZRN1, ZRN2, ZRN3) and 80W (ZRN4, ZRN5, ZRN6) with different nitrogen gas concentrations	197
6.7	Variations in the thickness of the films deposited with different nitrogen gas concentrations at constant power	198
6.8	Reflectance spectra of DC sputtered ZrN_x films.	200
6.9	Reflected spectra of the ZRN samples a) ZRN4 b) ZRN5 along with fitted patterns	200
6.10	Extracted real (a) and imaginary (b) parts of the complex permittivity, and the quality factor of DC sputtered ZrN_x films (c) of films having high carrier concentration	201
6.11	Surface plasmon resonance excitation curve obtained in ZRN4 and ZRN5 in Kretchsmann configuration at an incidence angle of 45°.	205
6.12	Surface plasmon resonance curves obtained in the films (a) ZRN4 and (b) ZRN5 with different angles of incidence, 45°, 51° and 58°	205

LIST OF TABLES

Table No:	Table caption	Page No:
3.1	Experimental conditions used for RF sputtering	85
3.2	Estimated Average Crystallite Size	87
3.3	List of Raman modes in titanium nitride	93
3.4	Variation of RMS roughness with the N/Ti ratio	98
3.5	Summary of Hall measurement results of TiNx films with varying N/Ti ratio	101
3.6	Summary of fitting parameters used for extracting permittivity values from the reflectance spectra	106
3.7	Summary of the results obtained from the reflectance spectra	107
4.1	Assigned bonds to binding energy values	126
4.2	Results of the composition measurements	128
4.3	Electrical properties of titanium nitride films after nitridation	132
4.4	Parameters used for fitting the reflectance spectra for the samples a) TIN045 b) TIN150 and c) TIN255	138
4.5	Quality factor estimated for the samples a) TIN045 b) TIN150 and c) TIN255	139
5.1	Analysis of GI-XRD peak values	156
5.2	Peak assignments for TiO_2, TiN, TiON	161
5.3	Raman modes of titanium dioxide and titanium nitride	164
5.4	Average surface roughness in TiO_2 and nitridated films	168
5.5	Electrical properties of titanium nitride films with different nitridation temperature	169
6.1	Experimental conditions used for sputtering	189

6.2	Peak assignments for ZrN	193
6.3	Variation in elemental composition with respect to amount of nitrogen gas during deposition	195
6.4	Electrical properties of ZrN films	199
6.5	Fitting parameters used for Drude Lorentz fitting	201
6.6	Estimated crossover wavelength of the ZrN film sample	203

LIST OF ABBREVIATIONS

AFM	Atomic Force Microscopy
D-L model	Drude Lorentz model
FESEM	Field Emission Scanning Electron Microscopy
LA mode	Longitudinal Acoustic mode
LO mode	Longitudinal Optic mode
SPP	Surface Plasmon Polariton
TA mode	Transverse Acoustic mode
TCO	Transparent Conducting Oxide
TMN	Transition Metal Nitride
TO mode	Transverse Optic mode
XPS	X-ray Photo electron Spectroscopy

CHAPTER 1

INTRODUCTION TO PLASMONICS

Recent years demanded faster technologies in every field with cost-effective approaches, such as, in telecommunication, sensing, optical devices and imaging etc. Each and every era requires faster, efficient and easier technology for human benefit. The invention of new technologies in this direction were focussed on two main points; one is the cost- effectiveness and the other is the miniaturisation of the devices. From the past centuries, the developments in the semiconductor technology created a positive feed back loop with optical communication developments. The semiconductor technology advanced the optical communication by the invention of optical fibres and lasers. These two areas have revolutionized our capability to process information, and the speed at which we can process it. Because of the scaling of semiconductor electronic components predicted from the empirical observation by Moore's law [1], the transistor has been scaled down from about 200 nm to 35 nm within the last decade, to achieve drastically higher operating speeds. Further significant scaling, however, poses many substantial difficulties such as short-channel effects, gate leakage and drastically increasing power density [2,3]. As a result of these challenges, alternative technologies have gained significant attention in the quest to increase information processing speeds. As one such alternative technology, the field of plasmonics has the potential to support our ever-increasing needs for information processing [4-5].

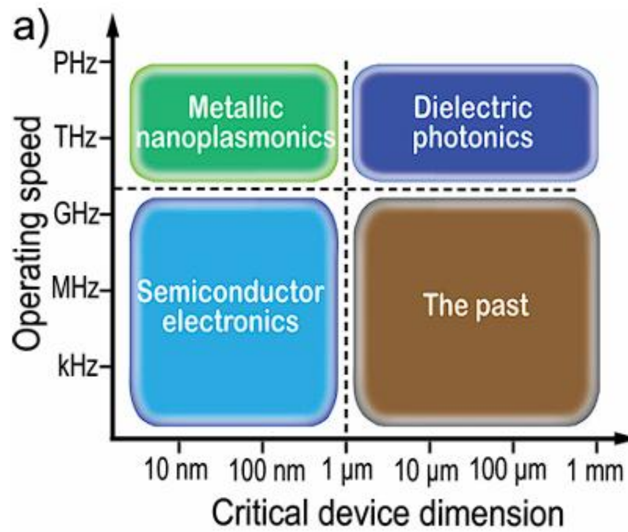

Fig 1.1 Relation between the operating speeds and critical dimensions of different chip-scale device technologies [4].

Fig. 1.1 represents the various domains in terms of operating speed and device sizes [4,5]. These are believed to be highly dependent on the special material characteristics of metals (plasmonics), insulators (photonics), and semiconductors (electronics). The dashed lines show the physical constraints of various technologies; for example, connection delay time difficulties limit the speed of semiconductor circuits to roughly 10GHz. The basic physics of diffraction place a limit on the scope of dielectric photonics. In this scenario, the plasmonics can serve as a bridge between similar-speed dielectric photonics and similar-size nano-electronics, which is expected to exhibit superior performance in comparison with others.

Plasmonics is a significant aspect of the captivating realm of nanophononics, delving into the confinement of electromagnetic fields within dimensions comparable to or smaller than the wavelength [6]. This discipline involves the interaction of electromagnetic radiation with conduction electrons at metallic interfaces or in metallic nanostructures [7], resulting in an amplified optical near field of sub-wavelength size. This field

deals with the coupling of light to free carrier electrons in metals, and allows breaking the diffraction limit for the localization of light into subwavelength dimensions with strong field enhancements leading to novel device concepts for the aforementioned applications [8-9]. An exciting aspect of plasmonics is that, by coupling the energy and momentum of a photon with the collective oscillations of free electrons in metals, it merges the features of photonics and electronics [10,4]. The next section will discuss about plasmons classification, and their properties in detail. The enormous developments in the field of plasmonic is delayed by the dissipative loss in the materials used in certain wavelength region [11]. Surface plasmons decay as they move along the surface due to the conversion of optical energy to heat [12]. The propagation length is typically determined by the excitation configuration, frequency of operation, and field symmetry of the plasmon mode of the supporting medium in addition to the metal properties [13].

1.1 BASICS OF PLASMONICS

Photons are quanta of light and the phonons are quanta of lattice vibration. Similarly, plasmons are quanta of plasma oscillations [8]. They are collective and coherent electromagnetic oscillation coupled to electrons in metal. The first ever plasmons behaviour was proposed by David Pines and David Bohm as collective oscillation of free electron gas [14]. They developed a physical picture of behaviour of electron in dense electron gas. The free electrons of metal are influenced by a force opposite to that of changing incident magnetic field. The resulting motion of electron will be 180° out of phase with charge of electron [15]. This coupling of electron and light in metals breaks the diffraction limit of for localization of light

into subwavelength dimension called surface plasmon polariton, which is having better field enhancement and merges both photonics and electronics realm [16].

1.1.1 Plasma frequency

Plasmons are characterised by the frequency of oscillation called plasma frequency (ω_p). The frequency of oscillation is given by

$$\boldsymbol{\omega_p = \sqrt{\frac{Ne^2}{m\varepsilon_0}}} \quad \text{..................(1.1)}$$

where N is the density of electrons in metal, *m* and *e* is the effective mass and charge of electron, respectively. ε_0 is the permittivity of free space [17]. Plasma frequency marks the distinction between the optical properties in materials. When the incident light frequency is less than the plasma frequency ($\omega<\omega_p$), the light exhibit reflection property. When $\omega > \omega_p$, the material allows the light to pass through it, and the transmission takes place [18].

1.1.2 Surface and Volume plasmons

There exist two different types of plasmons in a material depending on its position called surface and volume plasmons. According to the position of existence of location of plasmon polaritons, they are of the following two types,

1. Surface plasmon polariton: Electromagnetic excitations propagating at the interface between a dielectric and a conductor, evanescently confined in the perpendicular direction [19]

2. Volume (bulk) plasmon polariton: bulk plasmons that are longitudinal excitations in the volume of a metal, not coupled with an external electromagnetic field [20]

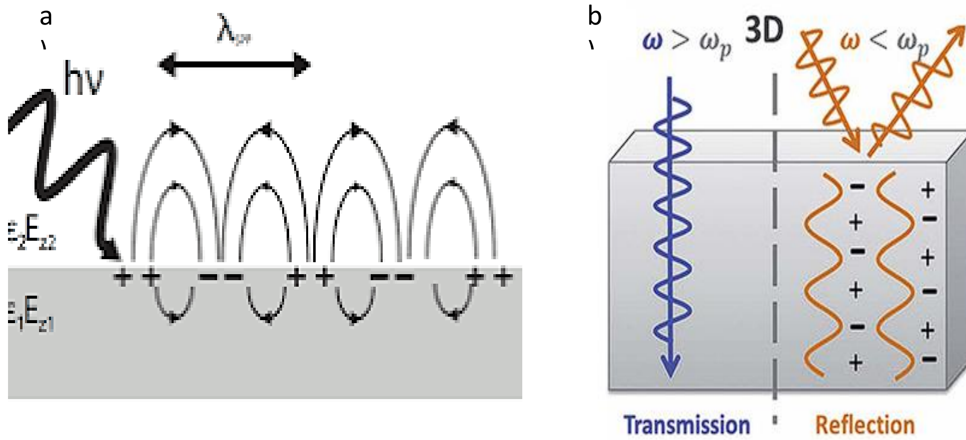

Fig 1.2 Schematic representations of (a) surface and (b) volume plasmons [15,21]

Surface plasmons are widely used in applications such as plasmonic sensing [22], surface-enhanced Raman spectroscopy (SERS) [23], photovoltaics [24], and photothermal therapies [25] because of their sensitivity to surface conditions. While others are important in high-energy applications and are studied using techniques like EELS [26]. They provide insights into the electronic structure of materials, but are not typically used in light-based applications. These differences are crucial for understanding how materials behave in optical and electronic devices, particularly in the fields of plasmonics and nanotechnology.

Surface plasmons offer efficient light-matter coupling due to the momentum matching mechanism that occurs when specific geometries are efficiently used [27], whereas the longitudinal character of volume plasmon hinders the coupling with light, and typically require energetic particles (like electrons)

for excitation [28]. This limits their use in many light-based technologies. Volume plasmons occur throughout the material's interior and are not as sensitive to surface conditions, making them less useful for applications requiring surface-level detection [29]. In the case of the surface plasmons, the resonance frequency can be tuned by varying the excitation mechanism, angle of incidence etc., as well as by altering the refractive index of the surrounding medium. The present study focus on the surface plasmon resonance investigations.

1.1.3 Localized surface plasmon resonance (LSPR) and surface plasmon resonance

In general, SPR occurs in two distinct forms localized surface plasmon resonance and surface plasmon resonance. The first deals with interaction of light with metallic nanostructure when the wavelength of light is comparable with dimension of nanostructure within the diffraction limit. They are non-propagative oscillations [30]. LSPR concentrates the electromagnetic (em) field around the nanostructure, which decays with a penetration depth of ~30nm [31]. The latter one deals with interaction of surface plasmon polariton in thin film with *p*-polarised light. These cannot be excited directly by hitting electromagnetic radiation; as discussed earlier, it demands a momentum matching mechanism. The enhanced electromagnetic field in SPR decays with penetration depth of ~100-200nm [31]. Comparison of LSPR and SPR sensing devices indicates improved sensing performance in the latter [32]. The present work focuses on the surface plasmon resonance excitation in thin films. In order to understand the principle behind the mechanism of momentum matching and surface plasmon excitation one should have thorough knowledge on the dispersion relation of light and surface plasmon polariton.

1.2 DISPERSION RELATION

Dispersion curve shows the relationship between variation in the wavevector with respect to frequency of a wave. The x axis represents the wavevector (k) and y axis represents frequency (ω) of the electromagnetic wave. In plasmonics, the dispersion relation describes the relationship between the frequency and wavevector (or momentum) of a plasmon, which dictates how plasmonic waves propagate and interact with light. This is crucial for understanding and designing plasmonic devices.

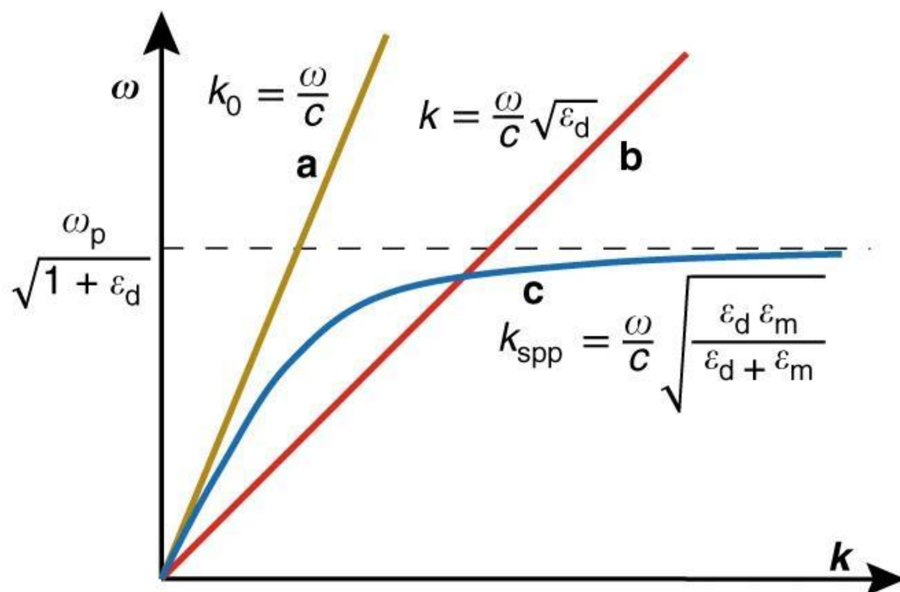

Fig. 1.3 Dispersion relation of a) light line (yellow) b) through material (red) c) surface plasmon polariton (blue) [33]

For the light line in air medium, dispersion relation is given by $k_0 = \frac{\omega}{c}$, where ω and c are the angular frequency of incident light and speed of light, respectively, which is represented by yellow colour in the Fig. 1.3. When the light passes through a medium of permittivity ε_d, the corresponding momentum will change by a factor $\sqrt{\varepsilon_d}$, as indicated by red line. The blue line indicates the momentum corresponding to surface plasmon polariton (SPP) exist in metal-dielectric interface. The SPP dispersion curve therefore lies to the right of the light line of the dielectric (given by $\omega = ck$), and excitation by three-dimensional light beams is possible by employing special techniques for phase-matching [8]. Higher momentum is required for the incident light in order to match with the SPP momentum. The additional momentum is obtained by adopting particular geometry configurations. This upcoming section reviews the most common techniques for SPP excitation, various optical techniques for phase-matching such as prism and grating coupling as well as excitation using highly focused beams will be presented.

1.3 DIELECTRIC FUNCTION

For plasmonic behaviour, it is unavoidable that the material must have negative permittivity in the frequency of interest [34]. To further understand negative permittivity, it is necessary to gain basic knowledge about dielectric permittivity. Dielectric function $\varepsilon(\omega)$ is termed as the response of a material to an applied external electric field. The response varies with the angular frequency (ω) of the electric field/electromagnetic wave.

The dielectric function is given by

$$\varepsilon(\omega)=\varepsilon_1(\omega)+\varepsilon_2(\omega) \qquad (1.2)$$

where ε_1, ε_2 are the real and imaginary parts of the complex permittivity. The real part comprises the strength of polarisation by external electric field and imaginary part describes the loss in the polarising material [35]. Loss mechanisms in the near-infrared (NIR), visible, and soft-UV frequency ranges may be broadly classified as arising from phenomena related to conduction electrons (intraband effects), core electrons (interband effects) and lattice vibrations (phonons) [36,37]. In thin metal films, there exist sea of free electrons and the Drude model attributes the contribution of the free electron gas to the dielectric function, whereas in semiconductors there are both free electrons and bound electrons. In this case, Lorentz model provides a picture of the bound electron contribution to the dielectric function [38]. The electric potentials of these bound electrons can be described by a spring-like system, so this model accepts a unique set of electrons with different binding energies, where each system is a Lorentz oscillator. The combined Drude-Lorentz model dielectric function, used for investigating the dielectric function of non-metal films is given in the equation 1.3 [38,39]. Detailed explanation is given experimental section 2.7.1.

$$\varepsilon = \varepsilon_\infty - \frac{\omega_{pu}^2}{\omega^2 - i\Gamma_D \omega} + \sum_{j=1}^{2} \frac{f_j \omega_{oj}^2}{\omega_{0j}^2 - \omega^2 + i\gamma_j \omega} \dots\dots\dots (1.3)$$

where ε_∞ is the high frequency dielectric constant, a constant or greater than unity; Γ_D is the drude damping factor; and ω_{0j} is the Lorentz oscillator with damping factor γ_j. $\Gamma = \frac{e}{\mu m^*}$ is the loss related Drude relaxation rate, or called momentum scattering rate [40].

1.4 EXCITATION CONFIGURATIONS

From the previous discussions, it is evident that the momentum of light line should be increased in order to match that of the surface plasmon polariton exist in the metal-dielectric interface. Phase-matching to SPPs can be achieved by various configurations, as described in this section.

1.4.1 Evanescent waves

The term evanescent means tending to vanish. Evanescent fields are non-propagating electromagnetic fields exponentially decaying waves with distance, generates when total internal reflection occurs at interface between two media. Evanescent fields are also formed during diffraction. The non-propagating nature is the main characteristics of evanescent wave. The energy of these field is confined in the vicinity of oscillating source [42]. Most of the field concentrated in a thin boundary layer very close to the interface; for that reason, it is referred to as a surface wave [43]. The evanescent fields have higher momentum when compared to the normal light. This evanescent field can be generated to overcome the momentum mismatch between light and surface plasmons, in order to excite surface plasmon resonance. This can be achieved through the following methods.

1.4.2 Prism coupling

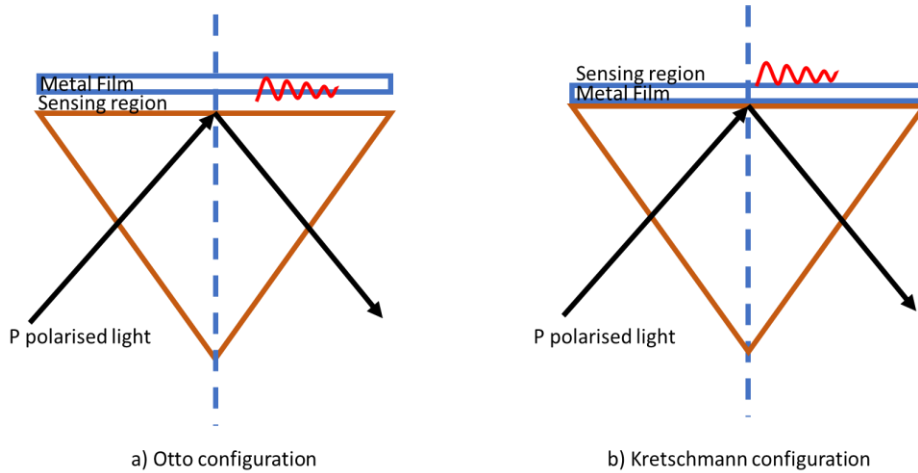

Fig. 1.4. Schematic diagram of the prism geometry configuration for SPP excitation (a) Otto configuration and (b) Kretschmann configuration

between two insulators of different dielectric constants. Consider one insulator as air for ease. A beam reflected at the interface between the insulator of higher dielectric constant ε, usually in the form of a prism, as shown in Fig.1.5. The in-plane momentum of metal is given by [8],

$$K_x = K\sqrt{\varepsilon}\, sin\theta \text{..............}(1.4)$$

which is sufficient to excite SPPs at the interface between the metal and the lower-index dielectric, i.e. in this case at the metal/air interface. This way, SPPs can be excited. The coupling scheme is based on the attenuated total internal reflection.

The coupling can be done in the following two configurations, as shown in Fig.1.4.

- Otto configuration: The *p* polarised light falls on the prism tunnel through the thin air gap and falls on the metal air interface at an angle greater than critical angle, and acquire sufficient momentum with the generation of evanescent waves, as seen in Fig. 1.4 (a). The change in the refractive index of sensing medium will change the SPP excitation wavelength [44].
- Kretschmann method: In this configuration, the metal film coated on glass substrate is attached to the prism by a suitable index matching fluid. The *p* polarised light falls on the one side of prism at an angle greater than the critical angle, and the evanescent field will be generated outwards at the metal-air interface, which will have sufficient momentum to excite the polariton in metal-dielectric interface. Proper thickness of the film is necessary for the SPP excitation. Corresponding excitations are sensitive to the refractive index and temperature changes in the surrounding/sensing medium [45].

The most commonly used configuration with ease of device fabrication is offered by Kretchsmann configuration methodology. The prime importance for this configuration is the improved and high sensitivity for detecting surface plasmon resonance compared to other techniques [46].

1.4.3 Waveguide geometry

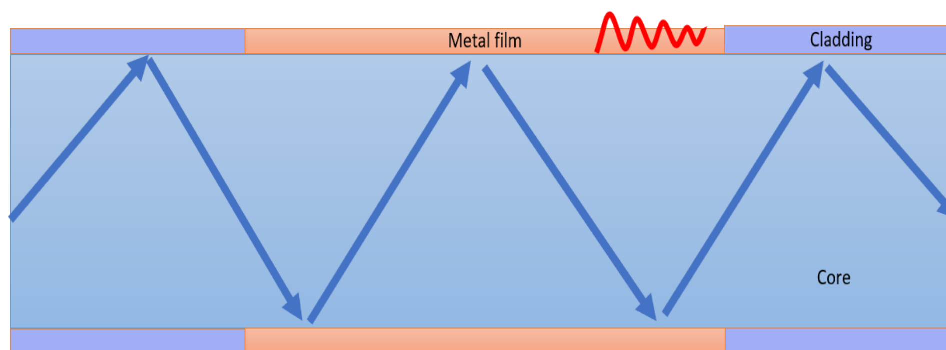

Waveguide geometry

Fig. 1.5 Schematic representation of waveguide configuration for SPP excitation

Optical waveguides are waveguides that transmit light through the principle of total internal reflection, using a core surrounded by a cladding with a lower refractive index. Light will propagate through a multimode optical fibre only if it enters the fibre at certain discrete angles and depends on the core and cladding. The removal of a small portion of cladding and coating it with metal film. When light enters at an angle greater than the critical angle of core-metal interface, the evanescent wave will be generated at the uncladded portion, as in the case of the prism geometry, which couples with the surface plasmon polariton exist in the metal surface. The extend of coupling depends on the mode of the fibre, geometry of the fibre, numerical aperture of the fibre etc. [47].

The optical waveguide geometry miniaturises the device size, however, one need to remove the cladding and coating the fibre carefully to coat the metal film. This configuration is largely used in the medical diagnostic industries, where the dimension of the device matters [48].

1.4.4 Grating configuration

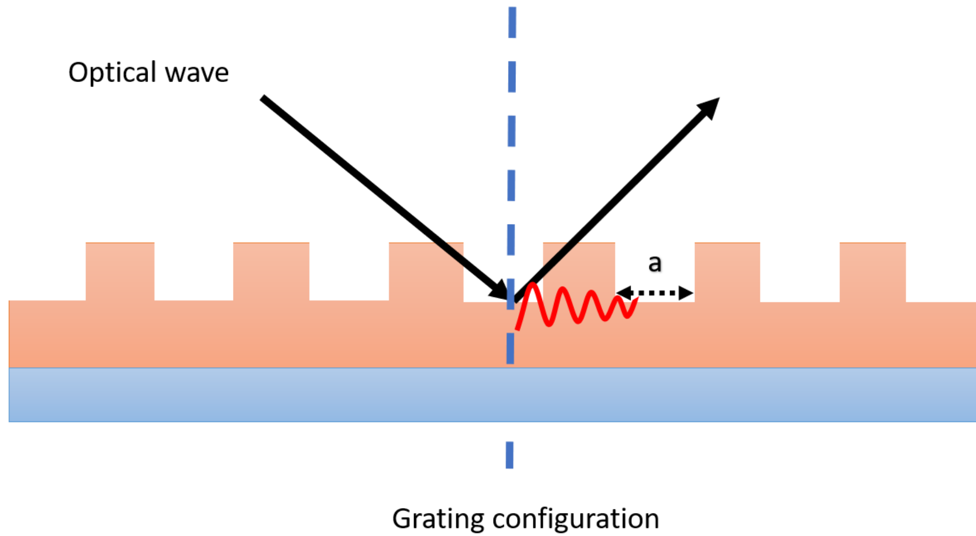

Fig. 1.6 Schematic diagram indicating the grating configuration for SPP excitation

and simplicity in designs [49,50]. The periodic patterns on the surface of metal film provides an additional momentum for the incident light. The grating pattern facilitates the coupling of incident light whenever the momentum matches as per the given equation,

$$K_{SPP} = k\ sin\theta\ \pm vg \ldots\ldots\ldots\ldots\ldots\ldots\ldots (1.5)$$

where v =1,2,3,.. and $g = \frac{2\pi}{a}$, a is lattice spacing of pattern [51]. Depth of grating, periodicity of grating pattern, choice of metal film all depends on the SPR excitation curve nature [52]. They are widely used in chemical

sensing and microfluidic analysis. Although it offers a miniaturisation of device, patterning of the metal surface requires sophisticated techniques such as lithography and that increase the cost of the device [53].

1.5 AREAS OF APPLICATION IN PLASMONICS

The first ever application of plasmonics is found in the ancient drawings. Mixing different sizes of gold and silver nanoparticles with glass produced different coloured glasses which were used for decorating buildings, some examples of early glassworks include, the Lycurgus Cup - a cup, which shows a green colour when shown under reflecting light conditions and red when shown in transmitting light conditions, as shown in Fig.1.6(a) [54]. The artwork found in the windows of Cathedrals like that of the north rose window of Chartres Cathedral in Chartres, France is shown in Fig.1.6(b) [55]; this is another example of early glasswork that was later discovered to be based on plasmonics. Current application realm of plasmonic is much wider and extends to the telecommunication [56], transformation optics [57], metamaterials [58], and optical tweezers [33], etc.

Fig 1.7 (a) Lycurgus Cup (a) in reflected light and (b) in transmitted light, (c) Chartres Cathedral Window

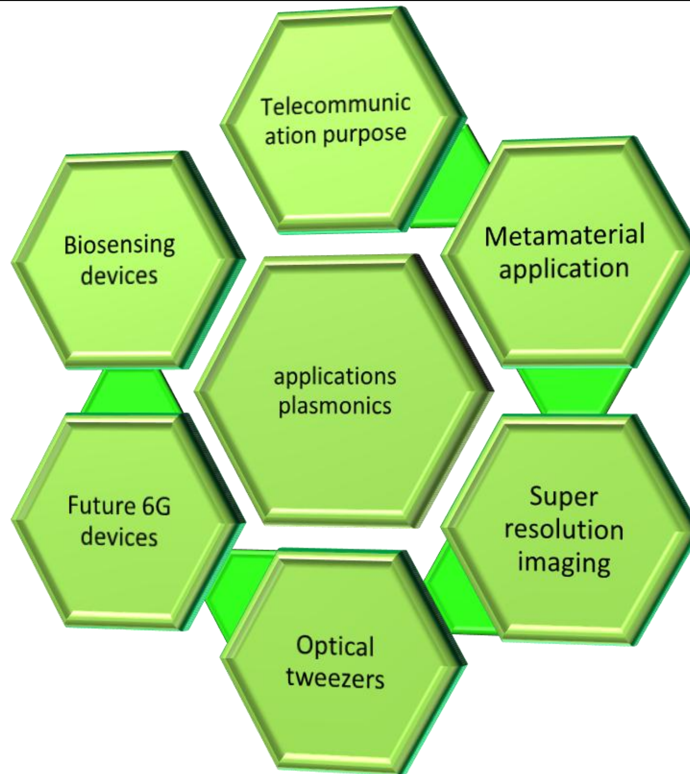

Fig 1.8 Various applications in plasmonic realm

integrability [59-62]. In this context, the unique ability of metallic structures to capture and concentrate light at subwavelength dimensions has emerged as a promising solution. In contrast to their photonic (limited in size by diffraction laws) and nanoelectronics (interconnection), where transmission are carried out by electrons and photons. By leveraging the properties of plasmonic modes, which involve the resonant coupling of electromagnetic waves to collective free-electron oscillations at metal surfaces, a new realm of possibilities has emerged. The potential for developing devices that combine the high data speed of optical signals with the compact size of

electronic circuits holds great promise as discussed in introduction section. This can be achieved through the synergistic integration of photonic, plasmonic, and electronic components on the same chip, enabling the realization of ultrafast board-to-board and chip-to-chip communications [63–65]. Furthermore, the utilization of surface plasmon resonances has opened doors for applications such as wireless optical links, optoelectronic conversion of optical-to-THz and THz-to-optical signals [66]. These advancements not only address the need for faster technologies but also pave the way for cost-effective approaches in telecommunication and sensing, ultimately benefiting humanity in various ways. The integration of metallic structures into telecommunications technology has revolutionized data transmission, power consumption, and on-chip integrability. Now, with the seamless integration of fibres-to-THz communication front-ends and the exploration of nanoscale analogies of radio frequency (RF) antennas in the optical frequency range, there is a vast potential for advancements in telecommunications technology [67–71].

In the year 2019, an unforeseen illness referred to as the coronavirus (SARS-CoV-2) was identified in Wuhan, China, triggering a worldwide pandemic. Moreover, the coronavirus has had a substantial impact on the global economy and has led to a discernible shift in the societal behaviour of individuals in order to prevent contracting the rapidly transmissible, infectious virus [72]. Conventional methodologies typically entail a culturing period ranging from 2 to 24 hours, as seen in RT-PCR. Consequently, there was a pressing need for immediate identification techniques of the virus that could provide precise, dependable, and instantaneous outcomes to contain the further spread of the virus. So Plasmonic technology presents an effective sensing approach in relation to the real-time process [73].

A high numerical aperture (NA) microscope objective serves as the foundation for optical tweezers, focusing a laser beam to create a gradient force at the focus. The optical potential well formed by this point has the ability to capture objects as small as microns. However, the precision of trapping is limited because the diffraction limit dictates that the size of the focal spot must be on the same order as the wavelength of the focused light, or several hundred nanometres [74-75]. Surface plasmon engineering has the most potential for manipulating objects at the nanoscale among the various subfields of near-field nano-optics. The strong light absorption and scattering characteristics of microscopic metallic objects make conventional trapping difficult [76–78]. However, plasmonic configurations can get around these challenges [79]. These challenges will be discussed next.

1.6 Limitation of conventional plasmonic materials

Irrespective of wider application field of plasmonics, the materials required for these application needs more consideration in recent scenario. The most widely used plasmonic materials are conventional metals such gold, silver, aluminium. The most and primary property of the plasmonic material is to have adequate carrier concentration in order to have plasma frequency in the respective wavelength region of interest [80]. Hence, metals are highly favoured in visible region since they have a carrier concentration of the order of $10^{23}/cm^3$ in turn shows a surface plasmon resonance excitation in UV-visible region.

In the plasmonic realm, silver and gold are known as conventional plasmonic material since centuries because their SPR is observed in visible region. SPR is observed in UV region for most of the other metals. In gold and silver, the d-electron bands have lower energy than the conduction bands [81].

In order to qualify a material for plasmonic applications, necessary criteria are to have negative permittivity and low loss nature within the desired wavelength range [33]. Hence, evaluation of dielectric function is next prime criteria for the occurrence of surface plasmon resonance. ~~With respect to~~ Depending on the sign of the real part of the dielectric constant (ε_1), a material may be classified as either metallic (plasmonic) or dielectric[82]. Plasmonic materials show a negative real part of the permittivity in the desired wavelength region, whereas dielectric materials show a positive real part of the permittivity in the wavelength range of interest. Value of the imaginary part of the dielectric constant (ε_2) indicates optical losses in these materials [83]. As the ε_2 value increases, the optical losses will also increase. To reduce optical losses, materials with a small imaginary component of the permittivity are generally favoured.

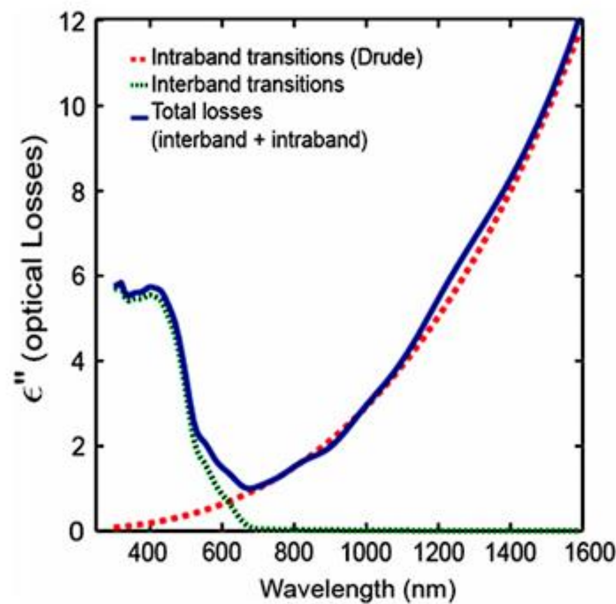

Fig 1.9 Contribution of different factors in the dielectric loss (ε_2) in gold metal film [89]

The loss mechanism in plasmonic material mainly arises from the interaction of conduction and bound electrons inside the material [84]. The imaginary part of permittivity depends on three important loss mechanisms: interband transitions, intraband transitions and additional scattering losses due to defects in solids [85]. Losses from the conduction electrons emerge from interactions of electron-electron and electron-phonons, which comes under the intraband effects. Losses due to intraband contributions primarily arise from conduction-band electrons. Since the conduction electrons have a near continuum of available states, their interaction with an electromagnetic field is well described by classical theory [86-87]. Along with that the grain boundary scattering and lattice defect scattering contributes to the loss. Fig. 1.9 shows the dielectric loss present in gold sample predicted by Johnson et al., which depicts the contribution of intraband and interband transition to the imaginary value of the permittivity [88]. The increased imaginary permittivity value of metal in optical frequency region deteriorates the plasmonic properties. Hence, it is ideal to have a material with lower imaginary permittivity values. Apart from this there are many other reasons that leads to the development of **alternative plasmonic material**, which are listed below.

- High value of real part of permittivity: For designing the transformation optic (TO) devices, the major consideration is given to ratio of real part of permittivity of metal and dielectric must be nearly comparable [89,90]. The primary criteria is to have balanced polarisation response from metal and dielectric [91,92]. The geometric fill fractions of the metal and dielectric is highly tunable to match the design requirements when it fulfils the above criteria. Thus, the value of real permittivity should be low, to have comparable nature to that of dielectric. However,

the metals are having high value of real permittivity, which hinders application in TO devices.

- Nanofabrication challenges: Due to the distinct morphology of metal films, when they are deposited by thermal means, they grow as discontinuous films, and island formation may also occur, which affects the optical properties of the metal film [93]. In addition, metals are having adhesive issue on some substrates and shows a percolation threshold when grown on glass and other common substrates [94,95].
- Grain boundary scattering: Thick films will always have large grains and thin films have small grain structure that will increase the grain boundary scattering in thin films [96]. This grain boundary scattering increase the dielectric loss [97]. To eliminate grain boundary scattering in metals, there are attempts to enable single crystal growth [98] that further reduces dielectric loss by reducing grain scattering contribution[99],
- Surface roughness: In metal films, there is an increased roughness property, which drastically affect the dielectric permittivity [100].
- Chemical stability: Metals such as silver are prone to surface oxidation when exposed to the atmosphere, which creates additional problems in device manufacturing and integration [101].
- Compatibility issues: Metals generally gold are not compatible with CMOS fabrication process, this further complicates nanoelectronics and plasmonic device integration. Since the metals diffuse into silicon forms defects [102].
- Tunablity issues: Carrier concentration in metals are not tunable, and hence the optical properties.

- Expensive: Conventional plasmonic materials, such as gold and silver, are highly expensive. The versatility of the plasmonic devices is effected by the cost of the device.

In the overall situation, metals are not a convenient choice in the application of point of view. For real applications, the drawbacks in employing conventional noble metals must be rectified. They have to be replaced by more STABLE, TUNABLE, COST-EFFECTIVE materials. This introduces the novel realm of research "**ALTERNATIVE PLASMONIC MATERIAL".**

1.7 ALTERNATIVE PLASMONIC MATERIALS

The hunt for efficient plasmonic materials necessitates the development of alternative materials capable of overcoming the aforementioned issues**.** As described above, the main idea is to have a material with reduced value of real permittivity and imaginary permittivity (loss) than metals to make it suitable for TO devices and metamaterial application [103-106]. Metal losses can be minimized using a variety of methods. However, methods that are easily implementable and incorporated into devices are the most technologically significant.

1. Turning a semiconductor to metallic behaviour: By heavily doping, semiconductors can be converted to possess enough free carriers, and the material's optical properties become metallic in the desired wavelength range [104,105].
   Example: Transparent conducting oxides (TCO) [106] III-V semiconductors [107]
2. Metals to less metallic: Reduce free carriers from metals by converting to other compounds, so as to reduce the carrier

concentration to the desired value to have lower real part of permittivity in desired wavelength range [108,89].

Example: Silicides and Germanides, Transition metal nitrides etc

Both these approaches resulted in the successful development of alternative plasmonic material with better plasmonic characteristics than the traditional plasmonic metals. In the first category, transparent conducting oxides are the better alternative, where metal oxides are subjected to efficient doping. Indium tin oxide (ITO) [109], Gallium doped zinc oxide (GZO) [108], Aluminium doped zinc oxide (AZO) [110, 111] are of prime importance with achievable carrier concentration ~$10^{21}/cm^3$ with plasma frequency in NIR region [107]. These materials pose solid solubility issues while trying to increase the carrier concentration by doping, and hence that they are not suitable as alternative plasmonic materials in the visible region [112]. Transition metal nitrides (TMN) plays a replacement in this scenario, as they can have carrier concentration in the order of $10^{22}/cm^3$ with plasma frequency in the visible region [113]. The optical properties of TMN largely depend on the deposition conditions because of their non-stoichiometric nature [114]. The composition of metal nitrides varies from metal-rich to stoichiometric and then nitrogen-rich. Thus, by careful tuning of the compositions, the carrier concentration, plasma frequency and other properties can be altered.

This entire work focuses on alternative plasmonic materials that exist in the visible region of the electromagnetic spectrum. Hence, it is adequate to choose TMN such titanium nitride, zirconium nitride as metal alternatives in plasmonics realm. A more detailed structure-property overview of titanium nitride (TiNx) and zirconium nitride (ZrNx) is detailed below.

1.8 PLASMONIC PROPERTIES OF TRANSITION METAL NITRIDES

Fig 1.10 illustrates the comparison of dielectric function values of conventional metals, TCO and transition metal nitrides [89]. Analysis of real and imaginary permittivity values of different materials conveys which is the best alternative plasmonic material. Here, the motive is to develop a material with lower loss and negative permittivity in visible region of electromagnetic spectrum. Titanium nitride and zirconium nitride serve as better alternative in this scenario. Furthermore, when focusing on the visible region of the spectrum, it can be seen that gold has a higher value of imaginary permittivity than TiN and ZrN. Therefore, this proves that TCO is a better alternative in the NIR region, while TMN is in the visible region.

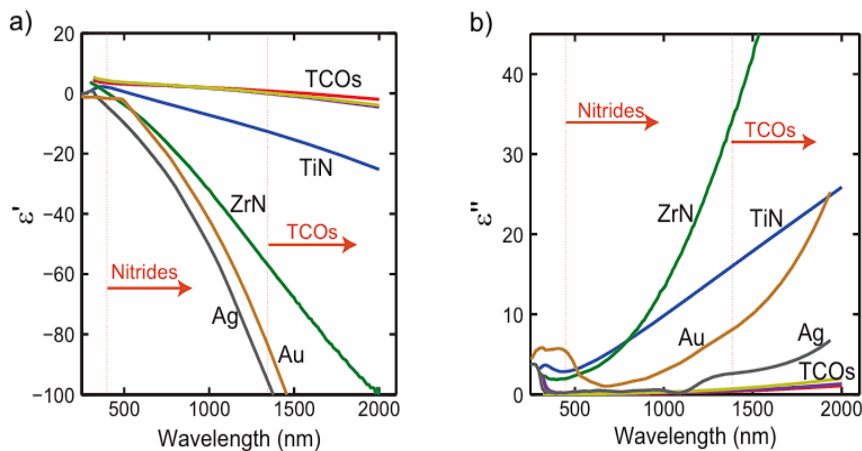

Fig 1.10 Comparison of the dielectric functions in different materials [89]

1.9 TITANIUM NITRIDE

Titanium nitride (TiN) is a hard ceramic material that has been widely used in industry to create protective coatings over cutting tools and air craft components [115-117]. As already pointed out, TiN's stoichiometry affects all of the material properties, including its appearance, conductivity, hardness, and other characteristics. In the world of materials, engineering of TiN's stoichiometry for specific application become crucial. To obtain variable non-stoichiometric compositions in the material, it is necessary to vary the deposition conditions. The colour of titanium nitride films can be varied from metallic grey to light yellow by varying the nitrogen partial pressure during vacuum deposition of the films. Such coatings are excellent for high-temperature ornamental automobile applications because of variable colour and temperature withstanding nature [118-119]. The covalent bond between titanium and nitrogen makes them tougher. The refractory metal nature of transition metal nitrides qualifies them for high temperature device application. TiN films are also attractive due to their lower electrical resistivity in the range of 50-200 μΩcm, depending on the stoichiometry of the compound [120]. They are extensively used in the field of microelectronics as barrier diffusion layer [121], adhesion layer [122], and are also compatible with CMOS technology [123]. In recent research scenario, theoretical predictions on titanium nitride as an alternative plasmonic material in the visible and near-IR region using a prism geometry configuration have been reported based on its tunable stoichiometry [124]. Plasmonic promises break-through in device application of electronic devices [125], bio-sensing [126], solar energy harvesting [127-129] and anti-reflection coatings[130]. The primary benefit is its tailorable material properties with deposition conditions, and the lower dielectric loss inherent with wide band gap and reduced intra-band transitions [131].

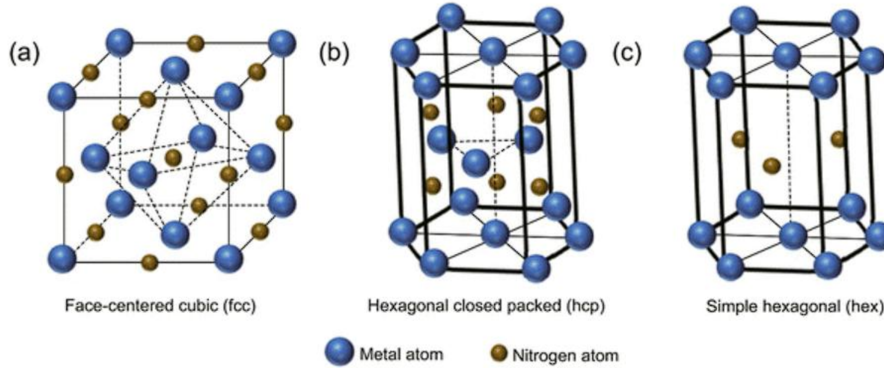

Fig 1.11 Crystal structures of titanium nitride [131]

Titanium nitride exist in three distinct crystal structures (i) face-centered cubic (fcc), (ii) hexagonally close-packed (hcp), and iii) simple hexagonal (hex) [132]. The structure varies with respect to the stoichiometry in the samples [133]. The stable composition of titanium nitride ranges from $TiN_{0.6}$ to $TiN_{1.16}$, which exist in cubic symmetry and lattice constant in that case is a = 0.4241 nm [134]. The vacancies in the film attributes to further optical and electrical properties in films.

TMN can be tuned to exhibit plasmonic properties in both visible and NIR region [135-137], due to the higher tunablity of their carrier densities. Carrier concentration largely depends on the composition of metal-nitrogen. Being metal, titanium is having higher carrier concentration, and the carrier concentration decreases with the addition of nitrogen. This transition metal compound is formed with a hybridized N 2p/Ti 3d covalent bond and a Ti 3d metal bond [138,139]. The outer 3 electrons in Ti metal forms covalent bond with nitrogen and one remains redundant. This metal bond further causes the stoichiometric TiN to have $10^{22}/cm^{-3}$ carrier concentration since $1cm^3$ of TiN comprises 10^{22} Ti atoms[140,141]. These redundant electrons cause modification in the band structure by forming a

shallow donor level below fermi level of TiN [142]. These electrons require lower activation energy and get promoted to the conduction band. All these factors necessitate the study of composition tunablity associated with the plasmonic properties in the films.

Mena et al investigated the comparative performance TiN and Au for near and far field nanoantenna applications with localised surface plasmon resonance phenomena, by fabricating nanostructures on TiN film [143]. Similarly, Guler et al reported the high absorption properties of TiN nanostructures with 50nm cubic nanoparticle [144]. These authors used lithography process to fabricate nanostructure for plasmonic excitation. However, thin films possessing enhanced electrical and optical properties can be explored for surface plasmonic resonance applications in prism geometry configuration, and can be used conveniently for various sensing applications. Qiu et al reported surface plasmon resonance excitation of TiN thin films via prism geometry configuration; however, it lacks the support of electrical and optical property analysis [145]. Further, there are reports on the developments of reusable TiN substrate for surface plasmon resonance based heterodyne phase interrogation sensor [146].

The fabrication route for transition metal nitride thin film has attracted significant interest due to their potential application and properties, as explained. Since material properties depend largely on composition/stoichiometry, adopting various fabrication routes will provide more opportunity to clearly tune the composition. In general, the fabrication routes of TiN for these applications consist of expensive techniques, such as physical vapour deposition (PVD) [123] and chemical vapour deposition (CVD) [147]. The high complexity of these routes and the associated high maintenance cost of the systems is one of the main reasons to necessitate the development of simple processing routes for the fabrication of TiN films.

The overall work aims to develop cost-effective fabrication routes through a step-by-step modification of the ammonia gas nitridation process for plasmonic titanium nitride thin films. For a better understanding, vacuum technique is also used in this work to identify material properties.

1.10 ZIRCONIUM NITRIDE

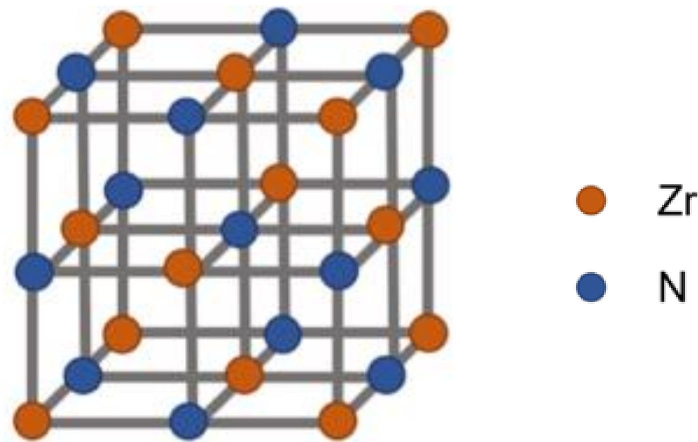

Fig 1.12 Crystal structure of zirconium nitride [148]

Zirconium nitride (ZrN) is another class of alternative plasmonic material belongs to the same category of transition metal nitrides. Zirconium metal, similar to the other metals (eg. Ti, Hf) of the group IVb of the periodic table of elements, has hexagonal structure and has four valence electrons. In particular its electronic configuration is $[Kr]4d^2 5s^2$, and it forms bonds with N atoms (valence electronic configuration $2s^2 2p^3$) [149]. Nitrogen is miscible in a wide range of stoichiometries into hcp Zr. The formation of the equi-atomic compound having cubic rock salt structure (B1-ZrN) is the most distinct feature of zirconium nitride [150]. B1-ZrN is a widely studied

material, due to diverse range of applications, such as solar selective coatings [151], infrared reflectors [152], protective and decorative coatings [153,154], superconductors [155-157], diffusion barrier layers [158-160], and photovoltaic back-contacts [161-164]. In comparison to titanium nitride, zirconium nitride exhibits 3 characteristic differences.

1. Higher oxidation resistance [165]
2. Lower dielectric loss: The carrier density remains the same for plasmonic behaviour to occur in the visible region, resulting in stronger and blue-shifted plasmonic response in comparison to TiN [166].
3. Lattice constant: Large lattice constant (0.4567nm) in comparison to titanium nitride [165].

Although ZrN possess similar behaviour to TiN, there is remarkable difference in its optical properties. In 1969, Knosp et al. first investigated the optical properties of zirconium nitride [167]. For the plasmonic activity, both the nanoparticle and thin film forms can be used. Researchers reported ZrN nanoparticle fabrication by laser ablation and wire explosion methods [168,169]. For the analysis of the dielectric function, ellipsometry or reflectance measurements have been used in the available literature. This thesis focusses on the plasmonic properties of materials in the visible region. Figure 1.13 represents a very focused comparison of the TiN and ZrN dielectric functions in the visible region of the electromagnetic spectrum, calculated from the data sets [170]. From Fig 1.13(a), the negative value of the real part of permittivity of ZrN is higher than that of titanium nitride, and lower than that of conventional metal gold. Of primary importance is the screened plasma energy or cross-over energy (E_{ps}), which is the spectral energy at which $\varepsilon_1 = 0$, which exhibits a blue shift in wavelength [171]. In addition to this, the dielectric loss, ε_2, is lower in

comparison to TiN. Overall, ZrN has been shown to be a better plasmonic material than TiN [149].

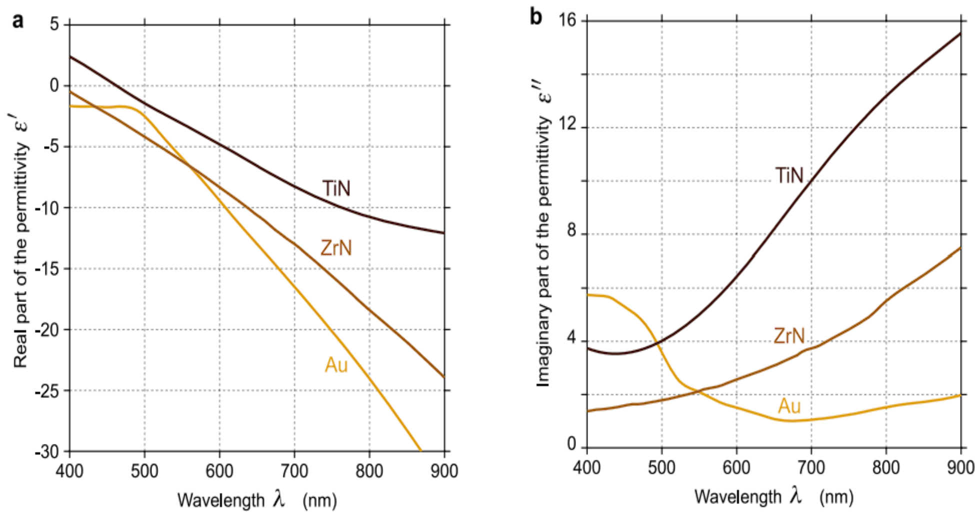

Fig. 1.13. The spectra of the real (a) and imaginary (b) parts of the permittivity of Au, TiN and ZrN versus wavelength [170]

1

In 2019, Chang et al. reported the deposition parameter dependence on the plasmonic behaviour of titanium nitride thin film during RF sputtering process [172]. As discussed in section 1.9, transition metal nitride films are composition dependent, and composition tunability further tunes the plasmonic nature. The problem lies with the sophisticated vacuum-based technique required for this film fabrication. In this thesis, the initial chapter focusses on analysing the deposition parameter dependency of titanium nitride compositions in RF sputtered films. In this thesis, the initial chapter focuses on analysing the deposition parameter dependence of titanium nitride compositions in RF sputtered films. In view of the initial vacuum-

based approach inferences, a newer fabrication route, nitridation with ammonia, is opted for plasmonic titanium nitride film fabrication. The advantage is on the cost-effectiveness associated with this fabrication route. In Chapter 6, the plasmonic properties of zirconium nitride, an improved alternative material, are discussed; the films for this study were fabricated using a vacuum deposition approach.

1.12 OBJECTIVES OF THE THESIS

The prime objectives of the thesis entitled “Study of surface plasmon resonance in transition metal nitride thin films” are as follows

1. Investigation of plasmonic properties in RF sputtered titanium nitride thin films
2. Investigation of plasmonic properties in TiN_X thin films derived from nitridation of titanium metal films.
3. Investigation of surface plasmon resonance properties in TiN_X thin films fabricated from spin coated TiO_2 thin films
4. Investigation of plasmonic properties in DC sputtered zirconium nitride thin films

1.13 REFERENCES

1. Moore, Gordon. (1965). Cramming more components onto integrated circuits, Electronics, 38, 114 doi: 10.1109/N-SSC.2006.4785860.

2. Schaller, R. (1997). Moore's law: past, present and future. IEEE Spectrum, 34(6), 52–59. https://doi.org/10.1109/6.591665.

3. Lundstrom, M. (2003). Moore's law forever? Science 299, 210–211. https://doi.org/10.1126/science.1079567

4. Brongersma, M. L., & Shalaev, V. M. (2010). The case for plasmonics. Science, 328, 440-441. https://doi.org/10.1126/science.1186905

5. Naik, G.V., Shalaev, V.M. and Boltasseva, A. (2013), Alternative Plasmonic Materials: Beyond Gold and Silver. Adv. Mater., 25, 3264-3294. https://doi.org/10.1002/adma.201205076.

6. Pitarke, J.M. & Silkin, V. & Chulkov, E.V. & Echenique, P.M.. (2006). Theory of surface plasmons and surface-plasmon polaritons. Reports on Progress in Physics. 70. 10.1088/0034-4885/70/1/R01.

7. Fang, Z. and Zhu, X. (2013), Plasmonics in Nanostructures. Adv. Mater., 25: 3840-3856. https://doi.org/10.1002/adma.201301203

8. Maier, Stefan. (2007). Plasmonics: Fundamentals and Applications. 10.1007/0-387-37825-1.

9. Lal, Surbhi & Link, Stephan & Halas, Naomi. (2007). Lal, S., Link, S. & Halas, N. J. Nano-optics from sensing to waveguiding. Nature Photon. 1, 641-648. Nat Photon. 1. 641-648. 10.1038/nphoton.2007.223.

10. Atwater, H. A (2007). The promise of plasmonics. Sci. Am. 296, 56–62.

11. Alexandra Boltasseva, Harry A. Atwater, Low-Loss Plasmonic Metamaterials. Science 331,290-291(2011). DOI:10.1126 /science. 1198258

12. Jacob B. Khurgin, Greg Sun;(2011) Scaling of losses with size and wavelength in nanoplasmonics and metamaterials. Appl. Phys. Lett; 99 (21): 211106.

13. Dastmalchi, B., Tassin, P., Koschny, T. and Soukoulis, C.M. (2016), A New Perspective on Plasmonics: Confinement and Propagation Length of Surface Plasmons for Different Materials and Geometries. Adv. Opt. Mater., 4, 177-184.

14. Pines, David; Bohm, David. (1952). A Collective Description of Electron Interactions: II. Collective vs Individual Particle Aspects of the Interactions, 85, 338–353. doi:10.1103/physrev.85.338

15. Ming Li, Scott K. Cushing and Nianqiang Wu, (2014) Plasmon-enhanced optical sensors:: Analyst, 2015,140, 386 DOI: 10.1039/c4an01079e

16. Naik, Gururaj & Kim, Jongbum & Kinsey, Nathaniel & Boltasseva, Alexandra. (2014). Alternative Plasmonic Materials. Handbook of Surface Science. 4. 189-221. 10.1016/B978-0-444-59526-3.00006-9.

17. Bertolotti, Mario; Sibilia, Concita; M. Guzman, Angela. (2017). [Springer Series in Optical Sciences] Evanescent Waves in Optics, 206, 127–168. doi:10.1007/978-3-319-61261-4_5

18. Horn, A. (2022). Optical Properties of an Electron Gas. In: The Physics of Laser Radiation–Matter Interaction. Springer, Cham. https://doi.org/10.1007/978-3-031-15862-9_10

19. Homola, Jiri. (2008). Surface Plasmon Resonance Sensors for Detection of Chemical and Biological Species. Chem. Rev. 108. 462-93. 10.1021/cr068107d.

20. N. W. Ashcroft and D. N. Mermin, Solid Stat. Physics, Cengage Learning, 1976.

21. Aftab, M., Mansha, M. S., Iqbal, T., & Farooq, M. (2024). Surface plasmon excitation: theory, configurations, and applications. Plasmonics, 19, 1701-1719.

22. M. Fukui, T. Okamoto, M. Haraguchi, (2006), Linear and nonlinear optical response of concentric metallic nanoshells, Handai Nanophotonics, 2, 31-54, DOI: 10.1016/S1574-0641(06)80009-4.

23. Peter Muys, (2012), Electromagnetic field equations of the volume plasmon, Opt. Lett. 37, 4928-4930

24. Xia, Chunlei & Yin, Chunrong & Kresin, Vitaly. (2009). Photoabsorption by Volume Plasmons in Metal Nanoclusters. 10.48550/arXiv.0904.2948.

25. Matthew E. Stewart, Christopher R. Anderton, Lucas B. Thompson, Joana Maria, Stephen K. Gray, John A. Rogers, and Ralph G. Nuzzo, (2008) Nano structured plasmonic sensors, Chem. Rev. 108, 494-521, DOI: 10.1021/cr068126n

26. Han, X., & Zhao, B. (2020). Surface-enhanced Raman scattering (SERS) and applications. In Elsevier eBooks (pp. 349–386). https://doi.org/10.1016/b978-0-12-818870-5.00010-1

27. Ai, B., Fan, Z., & Wong, Z. J. (2022). Plasmonic–perovskite solar cells, light emitters, and sensors. Microsystems & Nanoengineering, 8. https://doi.org/10.1038/s41378-021-00334-2

28. Höflich, K., Gösele, U., & Christiansen, S. (2009). Are volume plasmons excitable by classical light?. Physical review letters, 103(8), 087404.

29. Huang, X., Jain, P. K., El-Sayed, I. H., & El-Sayed, M. A. (2007). Plasmonic photothermal therapy (PPTT) using gold nanoparticles. Lasers in Medical Science, 23, 217-228. https://doi.org/10.1007/s10103-007-0470-x

30. Hutter, E., & Fendler, J. H. (2004). Exploitation of localized surface plasmon resonance. Advanced materials, 16(19), 1685-1706.

31. Takemura, K. (2021). Surface Plasmon Resonance (SPR)- and Localized SPR (LSPR)-Based Virus Sensing Systems: Optical Vibration of Nano- and Micro-Metallic Materials for the Development of Next-Generation Virus Detection Technology. Biosensors, 11, 250. https://doi.org/10.3390/bios11080250

32. Cao, J., Galbraith, E. K., Sun, T., & Grattan, K. T. V. (2011, August). Comparison of surface plasmon resonance and localized surface plasmon resonance-based optical fibre sensors. In *Journal of Physics: Conference series* (Vol. 307, No. 1, p. 012050). IOP Publishing.

33. Y. Zhang, C. Min, X. Dou, X. Wang, H. P. Urbach and X. Somekh M. G. and Yuan, Plasmonic tweezers: for nanoscale optical trapping and beyond Light Sci Appl, vol. 10, p. 59, 2021.

34. Li, Y., Liberal, I., & Engheta, N. (2019). Structural dispersion-based reduction of loss in epsilon-near-zero and surface plasmon polariton waves. Science advances, 5(10), eaav3764. https://doi.org/10.1126/sciadv.aav3764

35. Drachev, V. P., Chettiar, U. K., Kildishev, A. V., Yuan, H. K., Cai, W., and Shalaev, V. M. (2008). The Ag dielectric function in plasmonic metamaterials. Opt. Express 16, 1186–1195

36. Cai, W., and Shalaev, V. (2009). *Optical Metamaterials: Fundamentals and Applications.* Springer Verlag, New York.

37. Khurgin, J. B. (2020). Fundamental limits of hot carrier injection from metal in nanoplasmonics. Nanophotonics, 9, 453-471.

38. Lorentz, H. A. (1916). The theory of electrons and its applications to the phenomena of (Vol. 29). B G Teubner.

39. Eldlio, M., Che, F., & Cada, M. (2013, September). Drude-Lorentz model of semiconductor optical plasmons. In IAENG Transactions on Engineering Technologies: Special Issue of the World Congress on Engineering and Computer Science 2012 (pp. 41-49). Dordrecht: Springer Netherlands.

40. Patsalas, P.; Kalfagiannis, N.; Kassavetis, S. Optical Properties and Plasmonic Performance of Titanium Nitride, Materials, 8 (2015) 3128-3154. DOI:10.3390/ma8063128

41. Takayama, O.; Bogdanov, A.A.; Lavrinenko, A.V. (2017). Photonic surface waves on metamaterial interfaces, J. Condens. Matter Phys. 29, 463001. doi:10.1088/1361-648X/aa8bdd .

42. Bratash, Oleksii & Buhot, Arnaud & Leroy, Loïc & Engel, Elodie. (2024). Optical fiber biosensors toward in vivo detection. Biosensors and Bioelectronics. 251. 116088. 10.1016/j.bios.2024.116088.

43. Richard G. Hobbs, Vitor R. Manfrinato, Yujia Yang, Sarah A. Goodman, Lihua Zhang, Eric A. Stach, and Karl K. Berggren, (2016), High-Energy Surface and Volume Plasmons in Nanopatterned Sub-10 nm Aluminum Nanostructures, Nano Letters 16, 4149-4157, DOI: 10.1021/acs.nanolett.6b01012

44. Otto, A. (1968). Excitation of nonradiative surface plasma waves in silver by the method of frustrated total reflection. Z. Physik 216, 398-410. https://doi.org/10.1007/BF01391532

45. Kretschmann, E. & Raether, H. (1968). Notizen: Radiative Decay of Non Radiative Surface Plasmons Excited by Light. Zeitschrift für Naturforschung A, 23(12), 2135-2136. https://doi.org/10.1515/zna-1968-1247

46. Savović, S., & Djordjevich, A. (2004). Influence of numerical aperture on mode coupling in step-index plastic optical fibers. Appl. Opt., 43, 5542-5546. doi: 10.1364/ao.43.005542.

47. Odaci, Cem & Aydemir, Umut. (2021). The surface plasmon resonance-based fiber optic sensor: A theoretical comparative study with 2D TMDC materials. Results in Optics. 3. 100063. 10.1016/j.rio.2021.100063.

48. Zeni, L., Perri, C., Cennamo, N., Arcadio, F., D'Agostino, G., Salmona, M., & Gobbi, M. (2020). A portable optical-fibre-based surface plasmon resonance biosensor for the detection of therapeutic antibodies in human serum. Sci. Rep., 10, 11154. DOI: 10.1038/s41598-020-68050-x

49. Turker, B., Guner, H., Ayas, S., Ekiz, O. O., Acar, H., Guler, M. O., & Dâna, A. (2011). Grating coupler integrated photodiodes for plasmon resonance based sensing. Lab on a Chip, 11, 282-287.

50. Guner, H.; Ozgur, E.; Kokturk, G.; Celik, M.; Esen, E.; Topal, A.E.; Ayas, S.; Uludag, Y.; Elbuken, C.; Dana, A. (2017). A smartphone based surface plasmon resonance imaging (SPRi) platform for on-site biodetection. Sensor Actuat. B-Chem., 239, 571-577..

51. Homola, J., Koudela, I., & Yee, S. S. (1999). Surface plasmon resonance sensors based on diffraction gratings and prism couplers: sensitivity comparison. Sensor Actuat. B-Chem., 54, 16-24.

52. Murugan, D., Tintelott, M., Narayanan, M. S., Vu, X. T., Kurkina, T., Rodriguez-Emmenegger, C., & Pachauri, V. (2024). Recent advances in grating coupled surface plasmon resonance technology. Adv. Opt. Mater., 12, 2401862.

53. Sanju Rani,, Somnath C. Roy,(2022), Chapter 13 - Nanotube- and nanowire-based sensors for air quality monitoring, Hybrid and Combined Processes for Air Pollution Control, Elsevier, , 307-345, 10.1016/B978-0-323-88449-5.00014-0

54. Freestone, I., Meeks, N., Sax, M., & Higgitt, C. (2007). The Lycurgus cup-a roman nanotechnology. Gold bulletin, 40, 270-277.

55. Reynolds, Aislin. (2013). The Development of Stained Glass in Gothic Cathedrals.

56. Barbillon, G. (2019). Plasmonics and its applications. Materials, 12, 1502.

57. Huidobro, P. A., Nesterov, M. L., Martín-Moreno, L., & García-Vidal, F. J. (2010). Transformation optics for plasmonics. Nano letters, 10, 1985-1990.

58. Yao, K., & Liu, Y. (2014). Plasmonic metamaterials. Nanotechnology Reviews, 3, 177-210.

59. Araguillin, Ricardo & Mendez, Angel & Gonzales, José & Costa Vera, Cesar. (2024). Comparative evaluation of wavelength-scanning Otto and Kretschmann configurations of SPR biosensors for low analyte concentration measurement. Journal of Physics: Conference Series. 2796. 10.1088/1742-6596/2796/1/012009.

60. Wijayanto, Yusuf Nur & Murata, Hiroshi & Shiomi, Hidehisa & Okamura, Yasuyuki. (2011). Electro-Optic Microwave-Lightwave Converter Using Patch Antenna Embedded with a Narrow Gap for Optical Modulation. 10.1364/CLEO_AT.2011.JWA122.

61. Leuthold, J., Bonjour, R., Salamin, Y., Hoessbacher, C., Heni, W., Haffner, C., & Dalton, L. R. (2018,). Plasmonics for communications. In 2018 Optical Fiber Communications Conference and Exposition (OFC) (pp. 1-3). IEEE.

62. Thraskias, Christos & Lallas, E.N. & Neumann, Niels & Schares, Laurent & Offrein, Bert & Henker, Ronny & Plettemeier, Dirk & Ellinger, Frank & Leuthold, Juerg & Tomkos, Ioannis. (2018). Survey of Photonic and Plasmonic Interconnect Technologies for Intra-Datacenter and High-Performance Computing Communications. IEEE Communications Surveys & Tutorials. PP. 1-1. 10.1109/ COMST.2018.2839672.

63. Ummethala, S., Harter, T., Koehnle, K., Li, Z., Muehlbrandt, S., Kutuvantavida, Y., ... & Koos, C. (2019). THz-to-optical conversion in wireless communications using an ultra-broadband plasmonic modulator. Nature photonics, 13, 519-524.

64. Cuba-Zúñiga, D., Mafra, S., Mejía-Salazar, J., Montejo-Sánchez, S., Fernandez, E., & Céspedes, S. (2019). Visible Light V2V Cooperative Communication Under Environmental Interference. In *Proceedings of the XXXVII Brazilian Symposium on Telecommunications and Signal (SBrT 2019),* Petrópolis, Brazil (Vol. 29).

65. Savaliya, P. B., Gupta, N., & Dhawan, A. (2019). Steerable plasmonic nanoantennas: Active steering of radiation patterns using phase change materials. Opt. Express, 27, 31567-31586.

66. F. Carvalho, W. O., & Mejía-Salazar, J. R. (2020). Plasmonics for Telecommunications Applications. Sensors, 20, 2488. https://doi.org/10.3390/s20092488

67. Zia, Rashid & Schuller, Jon & Chandran, Anu & Brongersma, Mark. (2006). Plasmonics: the next chip-scale technology. Materials Today. 20-27. 10.1016/S1369-7021(06)71572-3.

68. Burla M, Salamin Y, Bonjour R, Abrecht F, Hoessbacher C, Haffner C, Heni W, Fedoryshyn Y, Werner D, Baeuerle B, Josten A. (2019),Integrated photonic and plasmonic technologies for microwave signal processing enabling mm-wave and sub-THz wireless communication systems. In Proceedings of the Broadband Access Communication Technologies XIII, San Francisco, CA, USA,; Volume 1094505.

69. Atabaki, Amir & Moazeni, Sajjad & Pavanello, Fabio & Gevorgyan, Hayk & Notaros, Jelena & Alloatti, Luca & Wade, Mark & Sun, Chen & Kruger, Seth & Meng, Huaiyu & Qubaisi, Kenaish & Wang, Imbert & Zhang, Bohan & Khilo, Anatol & Baiocco, Christopher & Popovic, Milos & Stojanovic, Vladimir & Ram, Rj. (2018). Integrating photonics with silicon nanoelectronics for the next generation of systems on a chip. Nature. 556. 10.1038/s41586-018-0028-z.

70. Alù, Andrea & Engheta, Nader. (2010). Wireless at the Nanoscale: Optical Interconnects using Matched Nanoantennas. Phys. Rev. Lett. 104. 213902. 10.1103/PhysRevLett.104.213902.

71. Yang Y, Zhao D, Gong H, Li Q, Qiu M. (2014) Plasmonic sectoral horn nanoantennas. Opt Lett., 39, 3204-7. doi: 10.1364/OL.39.003204.

72. Afridi, A.; Kocaba¸ S. E. (2016), Beam steering and impedance matching of plasmonic horn nanoantennas. Opt. Exp., 24, 25647–25652.

73. Cohen, M.; Abulafia, Y.; Lev, D.; Lewis, A.; Shavit, R.; Zalevsky, Z. (2017),Wireless Communication with Nanoplasmonic Data Carriers: Macroscale Propagation of Nanophotonic Plasmon Polaritons Probed by Near-Field Nanoimaging. Nano Lett., 17, 5181–5186.

74. Castro, Andreia & Melo, M & Siqueira, J & Zanella, Fernando & Mejía-Salazar, J. & Cerqueira S. Jr, Arismar. (2020). Plasmonic Nanoantennas for 6G Intra/Inter-Chip Optical-Wireless Communications. 10.1109/ 6GSUMMIT49458.2020.9083901.

75. Wei, Ivy & Pan, Deng & Zhang, Shunping & Li, Zhipeng & Li, Qiang & Liu, Ning & Wang, Wenhui & Xu, Hongxing. (2018). Plasmon Waveguiding in Nanowires. Chemical Reviews. 118. 10.1021/acs.chemrev.7b00441.

76. Hamza, Mohga & Othman, Muhammad & Swillam, Mohamed. (2022). Plasmonic Biosensors: Review. Biology. 11. 621. 10.3390/ biology 11050621.

77. Haque, Mohammad Ashraful & Rahad, Rummanur & Rakib, A K M & Sharar, Shadman Shahriar & Sagor, Rakibul. (2023). Plasmonic sensor for rapid detection of water adulteration in honey and quantitative measurement of lactose concentration in solution. Results in Physics. 51C. 106733. 10.1016/j.rinp.2023.106733.

78. Marago, Onofrio M. & Jones, Philip & Gucciardi, P. & Volpe, Giovanni & Ferrari, Andrea. (2013). Optical trapping and manipulation of nanostructures. Nature nanotechnology. 8. 807-19. 10.1038/nnano.2013.208.

79. Erickson, David & Serey, Xavier & Chen, Yih-Fan & Mandal, Sudeep. (2011). Nanomanipulation using near field photonics. Lab on a chip. 11. 995-1009. 10.1039/c0lc00482k.

80. Lee, S. Y. (2020). Carrier concentration dependency of plasma frequency in SiInZnO/Ag/SiInZnO transparent multilayer. Phys. B Condens. Matter, 592, 412242.

81. Rhodes, C., Franzen, S., Maria, J. P., Losego, M., Leonard, D. N., Laughlin, B., & Weibel, S. (2006). Surface plasmon resonance in conducting metal oxides. J. Appl. Phys., 100, 054905.

82. Yu, H., Peng, Y., Yang, Y., & Li, Z. Y. (2019). Plasmon-enhanced light–matter interactions and applications. npj Computational Materials, 5, 45.

83. Holliman, J. E., Schaef, H. T., McGrail, B. P., & Miller, Q. R. (2022). Review of foundational concepts and emerging directions in metamaterial research: design, phenomena, and applications. Materials Advances, 3, 8390-8406

84. Bosanac, L., Aabo, T., Bendix, P. M., & Oddershede, L. B. (2008). Efficient optical trapping and visualization of silver nanoparticles. Nano letters, 8, 1486-1491.

85. Hansen, P. M., Bhatia, V. K., Harrit, N., & Oddershede, L. (2005). Expanding the optical trapping range of gold nanoparticles. Nano letters, 5, 1937-1942.

86. Zhan, Q. (2004). Trapping metallic Rayleigh particles with radial polarization. Optics express, 12, 3377-3382.

87. West, P.R., Ishii, S., Naik, G.V., Emani, N.K., Shalaev, V.M. and Boltasseva, A. (2010), Searching for better plasmonic materials. Laser & Photon. Rev., 4, 795-808. https://doi.org/10.1002/lpor.200900055

88. Johnson, P. B., & Christy, R. W. (1972). Optical constants of the Noble Metals. Phys. Rev. B 6, 4370-4379. https://doi.org/10.1103/physrevb.6.4370

89. Naik, G. V., Kim, J., & Boltasseva, A. (2011). Oxides and nitrides as alternative plasmonic materials in the optical range. Optical materials express, 1, 1090-1099.

90. Hsieh, W. T., Wu, P. C., Khurgin, J. B., Tsai, D. P., Liu, N., & Sun, G. (2017). Comparative analysis of metals and alternative infrared plasmonic materials. ACS photonics, 5, 2541-2548.

91. Drude, P. (1900), Zur Elektronentheorie der Metalle. Ann. Phys., 306: 566-613. https://doi.org/10.1002/andp.19003060312

92. Alexander V. Kildishev and Vladimir M. Shalaev (2008), Engineering space for light via transformation optics, Opt. Lett. 33, 43-45

93. Cohen, R. W., Cody, G. D., Coutts, M. D., & Abeles, B. (1973). Optical properties of granular silver and gold films. Phys. Rev. B, 8, 3689.

94. Kazmerski, L. L., & Racine, D. M. (1975). Growth, environmental, and electrical properties of ultrathin metal films. J. Appl. Phys., 46, 791-795.

95. Pashley, D. W. (1959). The preparation of smooth single crystal surfaces of silver by an evaporation technique. Phil. Mag., 4, 316-323.

96. Fuchs, K. (1938,). The conductivity of thin metallic films according to the electron theory of metals. *In Mathematical Proceedings of the Cambridge Philosophical Society* (Vol. 34, No. 1, pp. 100-108). Cambridge University Press.

97. Kraus, W. A., & Schatz, G. C. (1983). Plasmon resonance broadening in small metal particles. J. Chem. Phys., 79, 6130-6139.

98. Park, J. H., Ambwani, P., Manno, M., Lindquist, N. C., Nagpal, P., Oh, S. H., & Norris, D. J. (2012). Single-crystalline silver films for plasmonics. Adv. Mater. (Deerfield Beach, Fla.), 24, 3988-3992.

99. Cheng, Fei, Chien-Ju Lee, Junho Choi, Chun-Yuan Wang, Qiang Zhang, Hui Zhang, Shangjr Gwo, Wen-Hao Chang, Xiaoqin Li, and Chih-Kang Shih. (2019). Epitaxial growth of optically thick, single crystalline silver films for plasmonics. ACS Appl. Mater. Interfaces., 3189-3195.

100. Kretschmann, E. (1972). Decay of non radiative surface plasmons into light on rough silver films. Comparison of experimental and theoretical results. Opt. Commun., 6, 185-187.

101. Campbell, W. E., & Thomas, U. B. (1938). Films on freshly abraded copper surfaces. Nature, 142 (3588), 253-254.

102. Rakib, A. K. M., Rahad, R., Faruque, M. O., & Sagor, R. H. (2023). ZrN-based plasmonic sensor: a promising alternative to traditional noble metal-based sensors for CMOS-compatible and tunable optical properties. Opt. Exp., 31, 25280-25297.

103. Krzysztofik, W. J., & Cao, T. N. (2019). Metamaterials in Application to Improve Antenna. Metamaterials and Metasurfaces, 63.

104. Hoffman, A. J., Alekseyev, L., Howard, S. S., Franz, K. J., Wasserman, D., Podolskiy, V. A.,& Gmachl, C. (2007). Negative refraction in semiconductor metamaterials. Nat. Mater. 6, 946-950.

105. Naik, G. V., & Boltasseva, A. (2010). Semiconductors for plasmonics and metamaterials. Phys. Status Solidi RRL, 4, 295-297.

106. Babicheva, V. E., Boltasseva, A., & Lavrinenko, A. V. (2015). Transparent conducting oxides for electro-optical plasmonic modulators. Nanophotonics, 4, 165-185.

107. Taliercio, T., & Biagioni, P. (2019). Semiconductor infrared plasmonics. Nanophotonics, 8, 949-990.

108. Blaber, M. G., Arnold, M. D., & Ford, M. J. (2010). A review of the optical properties of alloys and intermetallics for plasmonics. J. Condens. Matter Phys., 22, 143201.

109. Kim, D. H., Park, M. R., Lee, H. J., & Lee, G. H. (2006). Thickness dependence of electrical properties of ITO film deposited on a plastic substrate by RF magnetron sputtering. Appl. Surf. Sci., 253, 409-411.

110. Kim, K. H., Park, K. C., & Ma, D. Y. (1997). Structural, electrical and optical properties of aluminum doped zinc oxide films prepared by radio frequency magnetron sputtering. J. Appl. Phys., 81(12), 7764-7772.

111. Vadakkedath Gopi, S., Karuvanveettil, S., Packia Selvam, I., & Potty, S. N. (2025). Near-Infrared Plasmonic Planar Films: Advancements in Aluminum-Doped Zinc Oxide for Sensing and Telecommunications Applications. ACS Appl. Electron. Mater. 7, 2557–2563 DOI: https://doi.org/10.1021/acsaelm.5c00014

112. Yoon, M. H., Lee, S. H., Park, H. L., Kim, H. K., & Jang, M. S. (2002). Solid solubility limits of Ga and Al in ZnO. Journal of materials science letters, 21, 1703-1704.

113. Wittmer, M. (1985). Properties and microelectronic applications of thin films of refractory metal nitrides. J. Vac. Sci. Technol. A. 3, 1797–1803 (1985), https://doi.org/10.1116/1.573382

114. Steinmüller-Nethl, D., Kovacs, R., Gornik, E., & Rödhammer, P. (1994). Excitation of surface plasmons on titanium nitride films: determination of the dielectric function. Thin Solid Films, 237, 277-281.

115. Perry, A. J. (1990). A contribution to the study of poisson's ratios and elasticconstants of TiN, ZrN and HfN. Thin Solid Films, 193, 463-471. DOI:10.1016/S0040-6090(05)80056-2.

116. Kužel Jr, R., Černý, R., Valvoda, V., Blomberg, M., & Merisalo, M. (1994). Complex XRD microstructural studies of hard coatings applied to PVD-deposited TiN films Part I. Problems and methods. Thin Solid Films, 247, 64-78. DOI:10.1016/0040-6090(94)90477-4.

117. Roquiny, P., Bodart, F., & Terwagne, G. (1999). Colour control of titanium nitride coatings produced by reactive magnetron sputtering at temperature less than 100 C. Surface and Coatings Technology, 116, 278-283.DOI:10.1016/S0257-8972(99)00076-6.

118. Randhawa, H. (1988). Hard coatings for decorative applications. Surface and Coatings Technology, 36, 829-836., DOI:10.1016/0257-8972(88)90023-0

119. Chang, L. C., Liu, B. W., & Chen, Y. I. (2018). Mechanical properties and oxidation behavior of multilayered Hf–Si–N coatings. Coatings, 8, 354. DOI:10.3390/coatings8100354.

120. Ma, D., Deng, Q., Liu, H., & Leng, Y. (2021). Effect of ion energy on the microstructure and properties of titanium nitride thin films deposited by high power pulsed magnetron sputtering. Coatings, 11, 579. DOI:10.3390/coatings11050579

121. Yokoyama, N., Hinode, K., & Homma, Y. (1991). LPCVD titanium nitride for ULSIs. J. Electrochem. Soc., 138, 190. DOI:10.1149/1.2085535.

122. Dauskardt, R. H., Lane, M., Ma, Q., & Krishna, N. (1998). Adhesion and debonding of multi-layer thin film structures. Engineering Fracture Mechanics, 61, 141-162.DOI:10.1016/S0013-7944(98)00052-6.

123. Naik, G. V., Schroeder, J. L., Ni, X., Kildishev, A. V., Sands, T. D., & Boltasseva, A. (2012). Titanium nitride as a plasmonic material for visible and near-infrared wavelengths. Opt. Mater. Express., 2, 478-489. DOI:10.1364/OME.2.000478.

124. Sheldon, M. T., Van de Groep, J., Brown, A. M., Polman, A., & Atwater, H. A. (2014). Plasmoelectric potentials in metal nanostructures. Science, 346 (6211), 828-831.DOI: 10.1126/science.1258405.

125. Anker, J. N., Hall, W. P., Lyandres, O., Shah, N. C., Zhao, J., & Van Duyne, R. P. (2008). Biosensing with plasmonic nanosensors. Nat. Mater., 7, 442-453.DOI:10.1038/nmat2162

126. Atwater, H. A., & Polman, A. (2010). Plasmonics for improved photovoltaic devices. Nature materials, 9, 205-213.

127. Aubry, A., Lei, D. Y., Fernández-Domínguez, A. I., Sonnefraud, Y., Maier, S. A., & Pendry, J. B. (2010). Plasmonic light-harvesting devices over the whole visible spectrum. Nano letters, 10, 2574-2579. DOI:10.1021/nl101235d

128. Pelayo García De Arquer, F.; Mihi, A.; Konstantatos, G. Molecular interfaces for plasmonic hot electron photovoltaics. Nanoscale 7, (2015) 2281–2288. DOI: 10.1039/c4nr06356b.

129. Shidong Zhang, Fuyao Yan, Yang Yang, Mufu Yan, Yanxiang Zhang, Jinhao Guo, Hongtao Li, Effects of sputtering gas on microstructure and tribological properties of titanium nitride films, App Surf Sci, 488, (2019) 61-69, DOI: 10.1016/j.apsusc.2019.05.148.

130. Claesson, Y., Georgson, M., Roos, A., & Ribbing, C. G. (1990). Optical characterisation of titanium-nitride-based solar control coatings. Solar Energy Materials, 20, 455-465.

131. Khurgin, J. B., & Boltasseva, A. (2012). Reflecting upon the losses in plasmonics and metamaterials. MRS bulletin, 37, 768-779.

132. Zhong, Y., Xia, X., Shi, F., Zhan, J., Tu, J., & Fan, H. J. (2016). Transition metal carbides and nitrides in energy storage and conversion. Advanced science, 3, 1500286.

133. Holmberg, B. O., Yhland, M., & Dahlbom, R. (1962). Structural studies on the titanium-nitrogen system. Acta Chem. Scand, 16, 1255-61.

134. Zhang, L., Shao, M., Wang, Z., Zhang, Z., He, Y., Yan, J., ... & Li, Y. (2022). Comparison of tribological properties of nitrided Ti-N modified layer and deposited TiN coatings on TA2 pure titanium. Tribology International, 174, 107712.

135. Beyza Nur Günaydın, Mert Gülmez, Milad Torabfam, Zeki Semih Pehlivan, Atacan Tütüncüoğlu, Cemre Irmak Kayalan, Erhan Saatçioğlu, Mustafa Kemal Bayazıt, Meral Yüce, Hasan Kurt. (2023), Plasmonic Titanium Nitride Nanohole Arrays for Refractometric Sensing. ACS Applied Nano Materials, 6, 20612-20622, DOI: 10.1021/acsanm.3c03050

136. M. Noginov, L. Gu, J. Livenere, G. Zhu, A. Pradhan, R. Mundle, M. Bahoura, Y. Barnakov, and V. Podolskiy, (2011), Transparent conductive oxides: Plasmonic materials for telecom wavelengths, Appl. Phys. Lett. 99, 021101 DOI: 10.1063/1.3604792.

137. Frolich and M. Wegener, (2011), Spectroscopic characterization of highly doped ZnO films grown by atomic-layer deposition for three-dimensional infrared metamaterials," Opt. Mater. Express 1, 883–889 DOI : 10.1364/OME.1.000883.

138. Patsalas, P., & Logothetidis, S. (2003). Erratum: Interface Properties and Structural Evolution of TiN/Si and TiN/GaN Heterostructures, Journal of Applied Physics, 94(8), 5438-5438.

139. Walker, C. G. H., Matthew, J. A. D., Anderson, C. A., & Brown, N. M. D. (1998). An estimate of the electron effective mass in titanium nitride using UPS and EELS. Surface science, 412, 405-414.

140. Jeyachandran, Y. L., Narayandass, S. K., Mangalaraj, D., Areva, S., & Mielczarski, J. A. (2007). Properties of titanium nitride films prepared by direct current magnetron sputtering. Materials Science and Engineering: A, 445, 223-236.

141. Samsonov, G.V., (1969), Nitrides, Moscow: Naukova, Dumka.

142. Solovan, M. N., Brus, V. V., Maistruk, E. V., & Maryanchuk, P. D. (2014). Electrical and optical properties of TiN thin films. Inorganic materials, 50, 40-45.

143. Mena N. Gadalla, Andrew S. Greenspon, Michele Tamagnone, Federico Capasso and Evelyn L. Hu, (2019) Excitation of Strong Localized Surface Plasmon Resonances in Highly Metallic Titanium Nitride Nano-Antennas for Stable Performance at Elevated Temperatures, ACS Appl. Nano Mater. 6, 3444–3452, (2019), DOI: 10.1021/acsanm.9b00370

144. U. Guler, S. Suslov, A. V. Kildishev, A. Boltasseva and V. M. Shalaev, (2015), Colloidal Plasmonic Titanium Nitride Nano particles: Properties and Applications, Nanophotonics, 4, 269-276 DOI :10.1515/nanoph-2015-0017

145. Qiu, G., Ng, S. P., & Wu, C. M. L. (2018). Label-free surface plasmon resonance biosensing with titanium nitride thin film. Biosensors and Bioelectronics, 106, 129-135.

146. Sun, R. J., Huang, H. J., Hsiao, C. N., Lin, Y. W., Liao, B. H., Chou Chau, Y. F., & Chiang, H. P. (2020). Reusable TiN substrate for surface plasmon resonance heterodyne phase interrogation sensor. Nanomaterials, 10, 1325.

147. Su, J., Boichot, R., Blanquet, E., Mercier, F., & Pons, M. (2019). Chemical vapor deposition of titanium nitride thin films: Kinetics and experiments. CrystEngComm, 21, 3974-3981.

148. Liu, T., Ran, Y., Wang, T., Yu, X., Hu, G., Jiang, Z., & Wang, Z. (2023). Structural, plasmonic and electronic properties of zirconium carbonitride thin films prepared by dual ion beam deposition. Applied Physics A, 129, 453.

149. Patsalas, P. (2019). Zirconium nitride: A viable candidate for photonics and plasmonics?. Thin Solid Films, 688, 137438.

150. Ul-Hamid, A. (2020). Microstructure, properties and applications of Zr-carbide, Zr-nitride and Zr-carbonitride coatings: a review. Materials Advances, 1, 1012-1037.

151. Blickensderfer, R. L. L. R., Deardorff, D. K., & Lincoln, R. L. (1977). Spectral reflectance of TiNx and ZrNx films as selective solar absorbers. Solar energy, 19, 429-432. doi:10.1016/0038-092X(77)90019-6.

152. Perry, A. J. (1988). On the existence of point defects in physical vapor deposited films of TiN, ZrN, and HfN. J. Vac. Sci. Technol. A: Vac. Surf. Films., 6, 2140-2148. doi:10.1116/1.575205.

153. Tung, H. M., Huang, J. H., Tsai, D. G., Ai, C. F., & Yu, G. P. (2009). Hardness and residual stress in nanocrystalline ZrN films: Effect of bias voltage and heat treatment. Materials Science and Engineering: A, 500, 104-108. doi:10.1016/j.msea.2008.09.006.

154. Niyomsoan, S., Grant, W., Olson, D. L., & Mishra, A. B. (2002). Variation of color in titanium and zirconium nitride decorative thin films. Thin Solid Films, 415, 187-194.doi:10.1016/S0040 6090(02)00530-8.

155. Zhu, Y., Ikeda, M., Murakami, Y., Tsukazaki, A., Fukumura, T., & Kawasaki, M. (2007). Low-temperature growth of highly crystalline superconducting ZrN thin film on c-GaN layer by pulsed laser deposition. Jpn. J. Appl. Phys., 46, L1000. doi:10.1143/JJAP.46.L1000.

156. Geerk, J., Linker, G., & Smithey, R. (1986). Electron tunneling into superconducting ZrN. Physical review letters, 57, 3284.doi:10.1103/PhysRevLett.57.3284.

157. Tanabe, K., Asano, H., Katoh, Y., & Michikami, O. (1987). Properties of superconducting ZrN thin films deposited by dc reactive magnetron sputtering. Jpn. J. Appl. Phys., 26, L570.. doi:10.1143/JJAP.26.L570.

158. Sato, M., Takeyama, M. B., Hayasaka, Y., Aoyagi, E., & Noya, A. (2011). Barrier properties of thin ZrNx films prepared by radical-assisted surface reaction. Jpn. J. Appl. Phys., 50, 05EA07. doi:10.1143/JJAP.50.05EA07.

159. Takeyama, M. B., Sato, M., Aoyagi, E., & Noya, A. (2010). Reactively sputtered nanocrystalline ZrN Film as extremely thin diffusion barrier between Cu and SiO2. Jpn. J. Appl. Phys., 49, 05FA06. doi:10.1143/JJAP.49.05FA06.

160. Golshani, N., Mohammadi, V., Schellevis, H., Beenakker, C. I. M., & Ishihara, R. (2014). Research Update: Reactively sputtered nanometer-thin ZrN film as a diffusion barrier between Al and boron layers for radiation detector applications. APL Materials, 2. doi:10.1063/1.4897959.

161. Veszelei, M., Andersson, K. E., Roos, A., & Ribbing, C. G. (1993, October). Optical constants of sputtered ZrN films for heat mirror applications. In Optical Materials Technology for Energy Efficiency and Solar Energy Conversion XII (Vol. 2017, pp. 25-34). SPIE. doi:10.1117/12.161968.

162. Malmström, J., Schleussner, S., & Stolt, L. (2004). Enhanced back reflectance and quantum efficiency in Cu (In, Ga) Se2 thin film solar cells with a ZrN back reflector. Appl. Phys. Lett., 85, 2634-2636.. doi:10.1063/1.1794860.

163. Mahieu, S., Leroy, W. P., Van Aeken, K., Wolter, M., Colaux, J., Lucas, S., ... & Depla, D. (2011). Sputter deposited transition metal nitrides as back electrode for CIGS solar cells. Solar Energy, 85, 538-544. doi:10.1016/j.solener.2010.12.021.

164. Krc, J., Sever, M., Campa, A., Lokar, Z., Lipovsek, B., & Topic, M. (2017). Optical confinement in chalcopyrite based solar cells. Thin Solid Films, 633, 193-201. doi:10.1016/j.tsf.2016.08.056.

165. Abadias, G., Koutsokeras, L. E., Siozios, A., & Patsalas, P. (2013). Stress, phase stability and oxidation resistance of ternary Ti–Me–N (Me= Zr, Ta) hard coatings. Thin Solid Films, 538, 56-70.

166. Patsalas, P., Kalfagiannis, N., Kassavetis, S., Abadias, G., Bellas, D. V., Lekka, C., & Lidorikis, E. J. M. S. (2018). Conductive nitrides: Growth principles, optical and electronic properties, and their perspectives in photonics and plasmonics. Materials Science and Engineering: R: Reports, 123, 1-55.

167. Knosp, H., & Gerold, V. (1969). optical constants in the systems Titanium-TiN-TiC and Zirconium-ZrN-ZrC. Z Metallkunde, 60, 627-635.

168. Reinholdt, A., Detemple, R., Stepanov, A. L., Weirich, T. E., & Kreibig, U. (2003). Novel nanoparticle matter: ZrN-nanoparticles. Appl. Phys. B, 77, 681-686. doi:10.1007/s00340-003-1298-0. 107.

169. Reddy, R. S., Kamaraj, M., Mudali, U. K., Chakravarthy, S. R., & Sarathi, R. (2012). Generation and characterization of zirconium nitride nanoparticles by wire explosion process. Ceramics International, 38, 5507-5512. doi:10.1016/j.ceramint.2012.03.065.

170. Lalisse, A., Tessier, G., Plain, J., & Baffou, G. (2016). Plasmonic efficiencies of nanoparticles made of metal nitrides (TiN, ZrN) compared with gold. Scientific reports, 6, 38647.

171. Metaxa, C., Kassavetis, S., Pierson, J. F., Gall, D., & Patsalas, P. (2017). Infrared plasmonics with conductive ternary nitrides. ACS Applied Materials & Interfaces, 9, 10825-10834.

172. Chang, Chun-Chieh, John Nogan, Zu-Po Yang, Wilton JM Kort-Kamp, Willard Ross, Ting S. Luk, Diego AR Dalvit, Abul K. Azad, and Hou-Tong Chen. (2019). Highly plasmonic titanium nitride by room-temperature sputtering. Scientific reports, 9, 15287.

CHAPTER 2

EXPERIMENTAL TECHNIQUES

This chapter presents a brief report on the synthetic approach utilized to prepare plasmonic transition metal nitride thin films, as well as the methods for investigating their structural, morphological, electrical, and optical properties to pave the way for further research on plasmonic excitations. There are several processes for the deposition of thin layers of transition metal nitrides on substrates. Here, we report on the thin-film fabrication using both gas nitridation and sputtering techniques. We have chosen a general approach for characterising the coated nitride films, which consists of grazing incident x-ray diffraction and x-ray photoelectron spectroscopy for initial structural validation. The vacancy defect in the films were investigated by Raman spectroscopic analysis. Field emission scanning electron microscopy was used for the investigation of surface morphology of the films. Roughness analysis has been carried out with atomic force microscopic technique. High carrier concentration is necessary for exhibiting plasmonic behaviour in materials. In order to prove the required negative permittivity in the desired wavelength, the reflectance spectra of the films were recorded, and from which the real and imaginary values of the permittivity has been extracted using Drude-Lorentz approximation. After establishing the required carrier concentration, negative permittivity, and low loss behaviour in thin films, the surface plasmons were excited using prism geometry configuration. The experimental methods are explained in the following sections.

2.1 SUBSTRATE CLEANING

In general, the substrate used for the thin film deposition in this study is soda lime glass (SLG) because of the availability and low-cost. The contamination presents on the sample severely affect the physical adhesion and other targeted properties of the films. Hence, Substrate cleaning is

crucial to obtaining a uniform, defect-free film coating. In order to clean the substrate free of dust and other particles and also from organic residues, a unique substrate cleaning process is adopted for both SLG and quartz, as shown in Fig. 2.1

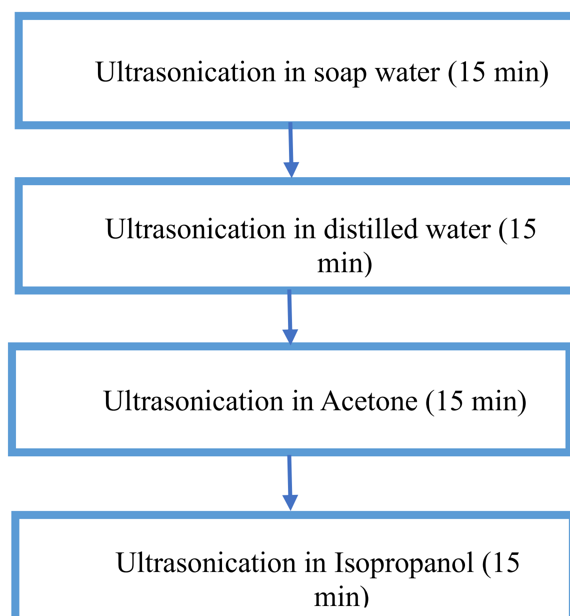

Fig 2.1 Process flow for the substrate cleaning

Finally, the cleaned substrates were dried in flow of nitrogen gas and kept in desiccators.

2.2 Coating techniques

In general, the transition metal nitride (TMN) films were fabricated via complex techniques such as atomic layer deposition [1], chemical vapour deposition (CVD) [2], pulsed laser deposition [3] and physical vapour deposition (PVD) [4]. Here, the objective was to fabricate nitride thin films through cost-effective approach. Solution-based methods and vacuum based

methods are available for the fabrication of thin films. The solution-based methods are simple and cheaper as compared to other methods. As discussed in chapter 1, the first focus on the fabrication of titanium nitride thin films was via RF reactive magnetron sputtering. The study then extended first to gas nitridation, where the base film was coated on substrates using vacuum-based method, and then to a complete solution-based fabrication approach.

2.2.1 Magnetron reactive sputtering

Sputtering is one of the vacuum-based thin film deposition techniques. The momentum transfer between plasma ions and target molecule give rise to erosion of target material, and these molecules/atoms are condensed onto substrates forming a thin film of the same. If the plasma ion is having positive charge, it is called cathodic arc sputtering [5-6]. Prior to deposition, if there is a chemical reaction between sputtered atom and gas present inside the chamber, then it is called reactive sputtering. The process is carried out at 10^{-3} to 10^{-6}mbar of pressure that enables contamination-free thin film with high purity.

In this study, a reactive sputtering technique has been used for the formation of transition metal nitride films. The metal particles were bombarded from the metal target using Ar^{+} ions in plasma and the ejected metal particles reacts with nitrogen and forms transition metal nitride, which is deposited on the rotating substrate kept above the target inside the vacuum chamber. Depending on the voltage applied between substrate and target, there exist radio frequency (RF) sputtering and direct current (DC) sputtering. In RF sputtering, an AC voltage with a frequency 13.56 MHz is used so that polarity between substrate and target is altered. In order to direct the sputtered atoms, a particular magnetic alignment is provided below the

target called magnetron. Magnetic field lines of magnetron will focus the plasma and controls sputtered materials to the substrate, which will enhance the deposition rates. DC sputtering uses only conducting metal targets whereas both conducting and non-conducting targets are used in RF sputtering [7].

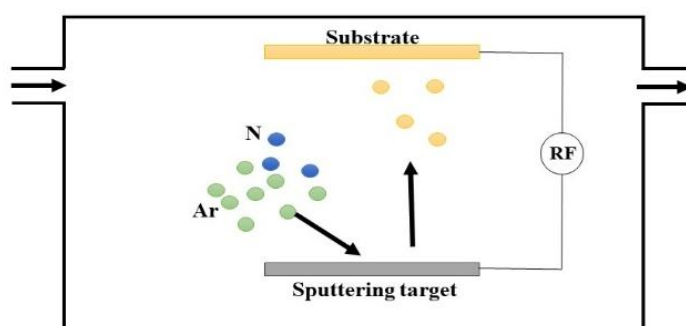

Fig 2.2 Schematic process indicting sputtering method

The schematic of a sputtering process is shown in Fig 2.3. The chamber is connected to a vacuum pumping system comprising of a rotary pump to evacuate the chamber to a base pressure of 10^{-3} mbar along with a high vacuum pump such as diffusion or turbomolecular pump that produces a vacuum up to 10^{-8} mbar. Low pressure increases the mean free path of the molecules and allows them to reach the substrate without losing energy via further collisions. Proper optimisation of sputtering power, working pressure, substrate to target distance and substrate temperature are required for obtaining good quality thin films. The substrate were loaded onto a rotation stage and rotation was optimised to 10rpm to ensure the uniformity in the coated films. Mass flow controllers are used in order to purge specific amount of sputtering and reactive gases. Two types gauges are used for

measuring pressure inside the chamber, a) penning gauge with pressure range from 10^{-3}mbar to 10^{-8}mbar and b) pirani gauge up to 10^{-3}mbar

In present work, a Hind High Vac make sputtering system equipped with diffusion and rotatory pump, having 2' magnetron was used for coating. The schematic diagram of the whole equipment is shown in Fig 2.3.

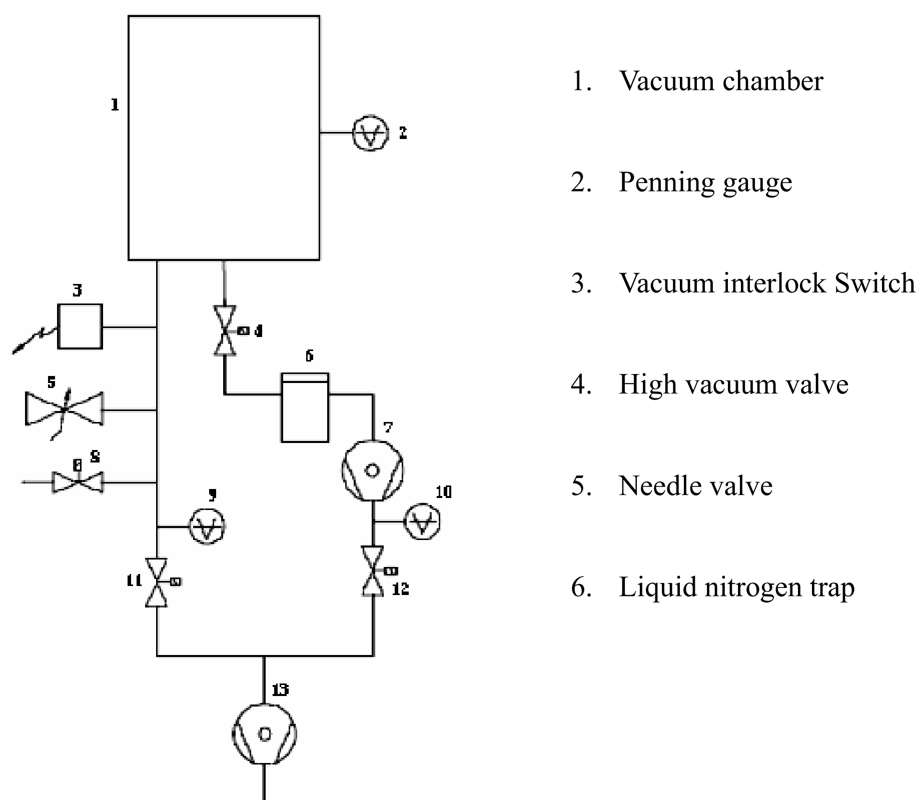

Fig 2.3 schematic of sputtering

2.2.2 Spin coating

Spin coating is an age-old, efficient, cost-effective technology belongs to solution based thin film deposition technique. In spin coating, the precursor solution is dispensed on a flat surface and the spinning of the substrate spread the solution uniformly throughout the area forming thin films. The

whole process consist of 3 steps solution dispense, spinning of the substrates and drying of the film [8]. The properties of the film and thickness depends on precursor solution, substrate, substrate rotation, adhesive nature of solution etc. The steps involved in the process is as shown in Fig 2.4.

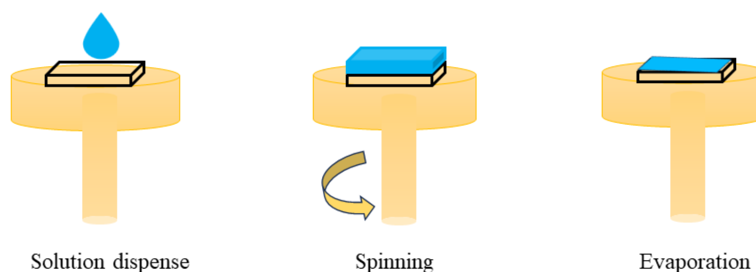

Fig 2.4 Steps involved in spin coating

Solution dispenses

There exist 2 different mechanisms to dispense solution on the substrate.

Static dispense : A particular amount of precursor solution is placed on centre of the substrate and then the chuck is rotated at a particular speed. The amount of solution dispensed depends on the viscosity of the solution and dimensions of the substrate. To ensure proper coverage over the entire substrate, more solution is required when the viscosity is higher and the substrate area is larger.

Dynamic dispense: the solution is dispensed while rotating the substrate on low speed. This will ensure uniform coating of the film and avoid wastage of the coating solution.

Spinning of substrate

The dispense step is followed by spinning of the substrate. The chuck is rotated with higher spinning speed for a particular time, which results in the proper spread of the dispense solution on top of the substrate. The spinning speed, spinning duration along with viscosity and concentration of the solution affects the thickness of the film [9]. The centripetal force allow thinning of the solution on the substrate. The thickness of the film (h_f) is inversely proportional to square root of the angular speed (ω) [5].

Solvent evaporation

Drying step depends on the precursor solution; this step carry out the evaporation of solvents and stabilizing agents in the solution. This step is optional if the solvents evaporates in the room temperature. For thick solutions higher drying time is necessary to achieve stability of the thin films.

In order to deposit TiO_2 thin films for the present work, a Chemat Technology make KW-4A spin coater was used. A hot plate is used for drying the coated film. The image of the spin coater used for the study is shown in Fig. 2.5.

Fig 2.5 Images of (a) spin coater unit and (b) hot plate

2.2.3 Gas nitridation

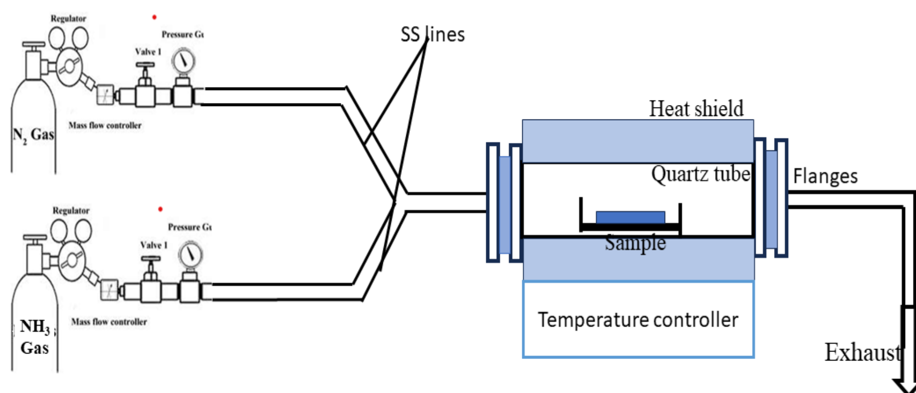

Fig 2.6 Schematic of the nitridation process

Nitridation is a surface reaction procedure widely used for metal container case hardening in industries, since metal-nitrogen covalent bond formation promotes hardness in the material. Introducing nitrogen as a component can be achieved using liquid, gas or plasma ion nitriding. Nitrogen can be introduced as an element using liquid, gaseous, or plasma ion nitriding. Gas nitriding is a thermal treatment process for diffusing nitrogen into steels by introducing ammonia (NH_3/N_2) gas in a furnace and heating to desired temperature. Ammonia gas has been used for the gas nitridation because of the easiness in producing nascent nitrogen. Tjokro et al reported faster internal nitridation rate while using ammonia atmosphere [10], which is attributed to the lower N–H bond energies in ammonia, compared with the N–N bond energies in N_2 [11-12]. It disassociates at lower temperature (~450°C), compared to the nitrogen gas (~3000°C), to nascent nitrogen, and constitutes the nitrogen source.

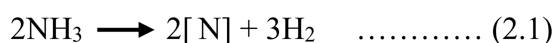

$$2NH_3 \longrightarrow 2[N] + 3H_2 \quad \ldots\ldots\ldots\ldots (2.1)$$

In order to successfully carry out repeatable nitriding process, the following process parameters should be controlled adequately. This can be incorporated with simple instrumentation and methods.

(i) Furnace temperature
(ii) Duration of nitriding process
(iii) Gas flow rate
(iv) Process chamber dimension

The schematic diagram indicating the nitridation setup is shown in Fig. 2.6. The purging gas lines were completely made of stainless-steel lines and fittings due to the corrosive nature of the ammonia gas. The advantage of

nitridation over other process is the easiness to carry out the process and in addition, the hydrogen produced will impart a reduced atmosphere in the chamber (quartz tube).

2.3 STRUCTURAL ANALYSIS

Both qualitative and quantitative analysis of transition metal nitride thin films were carried out using X-ray diffraction, x-ray photoelectron spectroscopy and Raman studies. Each technique is described in detail in the following sections.

2.3.1 Glancing angle XRD

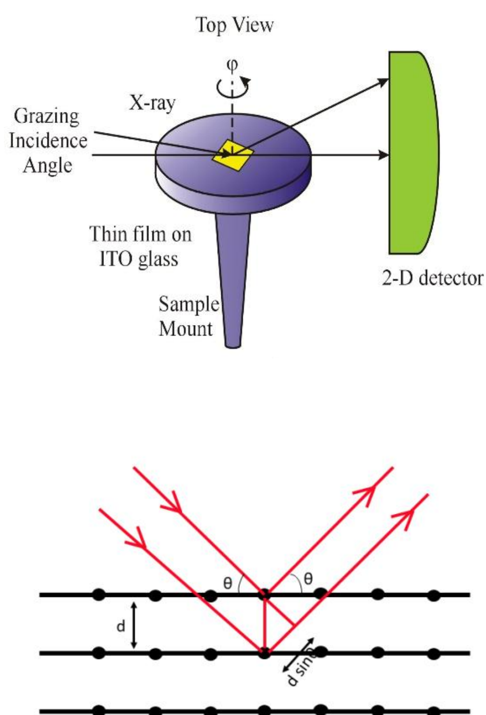

Fig. 2.7 Schematic diagram of a) X-ray diffraction b) grazing incidence XRD [13]

Xray diffraction is non-destructive first ever characterisation technique of any material study to confirm the structure and phase purity of any material. The interplanar distance of any material lies in the wavelength comparable to that of x-ray radiation, and hence diffraction occurs. When x-ray radiation (generally Cu K_α radiation) is incident on crystalline material with long range order, the diffraction occurs and the pattern obtained will be a fingerprint of the particular material composition. The schematic diagram describing the x-ray diffraction is shown in Fig. 2.7(a).

The Bragg's law, which gives the criteria for obtaining a diffraction pattern, is given by

$$n\lambda = 2d\sin\theta \text{ …….. (2.2)}$$

where n is the integer represents order of diffraction, θ is the angle of diffraction, d is the interplanar spacing and λ is the wavelength of the x-ray used. For each diffraction angle that satisfy the above condition, there occurs a diffraction peak, which gives information about the interplanar spacing, crystalline structure and phase purity. In the case of thin films coated on substrates, to nullify the contribution of the substrate, the diffraction pattern of thin films is analysed using Grazing Incidence X–ray diffraction (GI-XRD) technique. The penetration depth of the x-ray beam is controlled by adjusting the grazing angle in the GI-XRD setup. The schematic diagram of GI XRD set up is shown in Fig. 2.7(b). The penetration depth is given by

$$\text{Penetration depth} = \frac{Sin\alpha}{\mu} \text{ ……………(2.3)}$$

where α and μ are the grazing angle and linear mass absorption of the material of interest, respectively [14].

Comparison of the measured diffraction data with the standard Powder Diffraction File (PDF) provided by the International Centre for Diffraction Data (ICDD) will confirm the phase. In the present study, the as-prepared samples were analysed with GI-XRD mode using Rigaku make Ultima IV machine.

Rather than the lattice parameter, the GI-XRD pattern is also used to estimate the crystalline size, lattice strain, dislocation density, density of the sample and several other structural parameters. The well-known Scherrer formula is used to estimate the average crystalline size 'D' [15],

$$D = \frac{0.9\lambda}{\beta \cos\theta} \quad \ldots\ldots\ldots\ldots\ldots\ldots\ldots\ldots\ldots\ldots (2.4)$$

where λ and β are the x-ray wavelength and the full width at half maximum (FWHM) at the corresponding θ position of the peak, respectively. Lattice constants (a, b, c) can be estimated from the obtained d value from the XRD pattern; the structure corresponds to stoichiometric transition metal nitride is cubic and the lattice constant a=b=c and α=β=γ=90° is estimated using the equation,

$$d = \frac{a}{(h^2+k^2+l^2)^{1/2}} \quad \ldots\ldots\ldots\ldots\ldots\ldots\ldots\ldots\ldots (2.5)$$

where h, k, l are the miller indices corresponding to each plane.

2.3.2 X-ray photoelectron spectroscopy

X-Ray photoelectron spectroscopy is the highly sophisticated surface sensitive technique used to measure elemental composition in thin films [16,17]. In the process of the photoemission [18], an x-ray beam with energy hυ is incident on a specimen followed by the ejection of a core level electron. The emitted electrons are then analysed with their energies, and the

curve is plotted with energy of the emitted electron versus intensity (counts per second). The kinetic energy of the ejected photoelectron is given by

$$KE = h\upsilon - (BE + \phi) \quad \text{(2.6)}$$

where hυ is quanta of energy of incident photon and BE is binding energy of electron and ϕ is the work function of the material/sample [19]. The schematic representation is shown in Fig.2.8. If the incident photon is having energy hυ, BE +ϕ is used for the emission of the electron from the sample surface and the remaining energy is converted to kinetic energy of the electron. The binding energy corresponding to electrons in each core level is a constant irrespective of the energy of incident beam, which is inferred from the above equation, instead introduce a variation in the KE of the ejected electron. Corresponding to each valency state present in the sample, a peculiar binding energy peak is produced in the XPS spectra.[20]

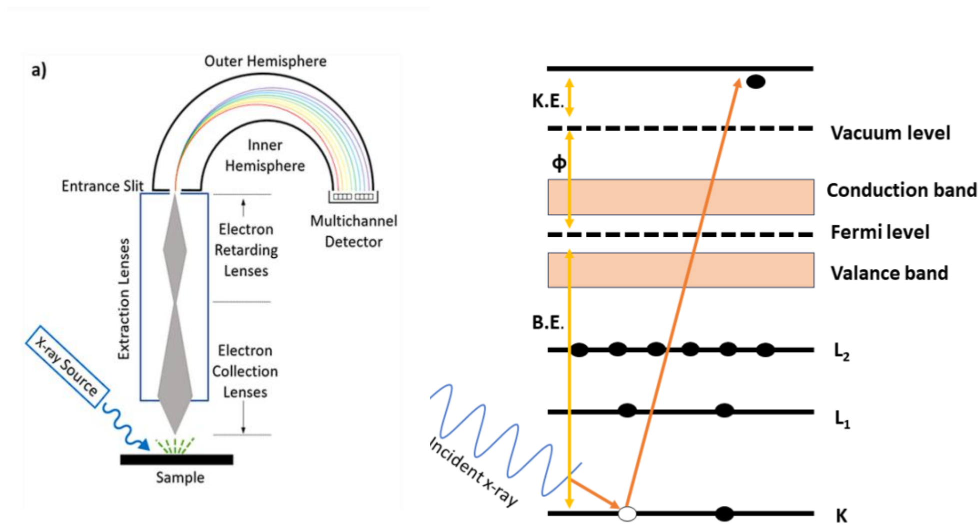

Fig 2.8 (a) Schematic diagram of XPS instrument and
(b) the band structure diagram

In this report, used Kratos AXIS ULTRA (AXIS 165) and Thermo-scientific K alpha+ spectrometer instruments for the XPS measurements, with a mono-chromated Al K alpha gun source (1486.6eV). The spectra were recorded for Zr 3d, Ti 2p and N 1s core level with a binding energy from176-186, 454-464 eV and 394-396 eV, respectively according to the elements. The XPS curves obtained from the films were referenced to the C1s line of the adventitious carbon set at 284.6 eV. The peaks of XPS curve were deconvoluted using XPSPEAK41 software with Gaussian–Lorentzian (GL) function and Shirley (non-linear) background correction. The peaks are fitted using the software XPSPEAK4.1 in order to calculate the stoichiometry in the coated films.

The background subtraction is of major concern for the stoichiometric calculation in transition metal nitride compounds [21]. Jaeger et al reported that Tougaard background subtraction is adequate for Ti $2p_{3/2}$ Ti $2p_{1/2}$, since it fulfils the quantum mechanical requirements and yields an area ratio of 0.515 of the same peaks [22], Tougaard background subtraction considers contribution of an induced electric-field, generated with interaction of moving electron in solid and that of emitted electron. The background intensity is present in materials those exhibit high carrier concentration like titanium nitride [23-24].

The surface composition analysis of the films was estimated from the integrated area ratio after proper normalisation with sensitivity factors (ASF) using following equation [25],

$$\text{Aomic \% of } A = \frac{\frac{A}{a}}{\frac{A}{a}+\frac{B}{b}} \ldots\ldots\ldots\ldots\ldots\ldots..(2.7)$$

where A and B represents area under elements, a and b represent atomic sensitivity factors for respective elements

2.3.3 Raman spectroscopic analysis

Stoichiometric transition metal nitrides exist in rock salt structure of NaCl. Due to the O_h symmetry of molecule, they are Raman inactive. According to Stoehr et al, even stoichiometric titanium nitride has defects that result in the first and second order Raman peaks [26]. Hence, Raman spectroscopy can be used to identify vacancy induced defects in transition metal nitrides.

Raman spectroscopy is a non-destructive material characterisation technique. The inelastic scattering during light-matter interaction, contributes changes in the vibrational-rotational states of a system [27-28]. When an electromagnetic wave interacts with a molecule, the initial polarisation present in the molecule undergoes a change with respect to vibration and rotational energies. The scattering in the material produces 3 frequency components,

A. Elastically scattered/Rayleigh scattering ($\upsilon=\upsilon_0$): The major component goes without any change in the wavelength of the incident beam
B. Stokes scattering ($\upsilon = \upsilon_0 - \upsilon_m$): The scattered light will have higher wavelength than incident laser, higher intensity since ground states are highly populated
C. Antistokes scattering ($\upsilon = \upsilon_0 + \upsilon_m$): The scattered light will have lower wavelength than incident laser , less intense

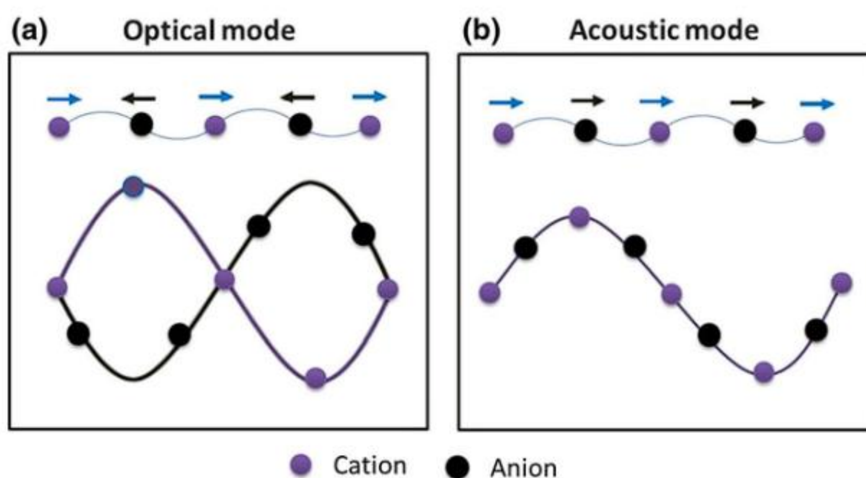

Fig 2.9 Representation of optical and acoustic modes [29]

The stokes lines are more intense compared to anti-stokes. Since they are arising from lower energy level where population of state is high. The crystal will have both acoustic and optical phonons (lattice vibrations) when the unit cell has more than one atom in it. Light readily excites optical phonons. Both positive and negative ions swing together in acoustic phonons. Positive and negative phonons oscillate against one another in optical phonons. The representation is as shown in Fig. 2.9. The Raman spectroscopy measurements for the present work were recorded with Horiba Labram HR system. A laser emitting at 532 nm was used to excite the samples. The acquisition time of 10s and grating of 1800 lines/cm is used.

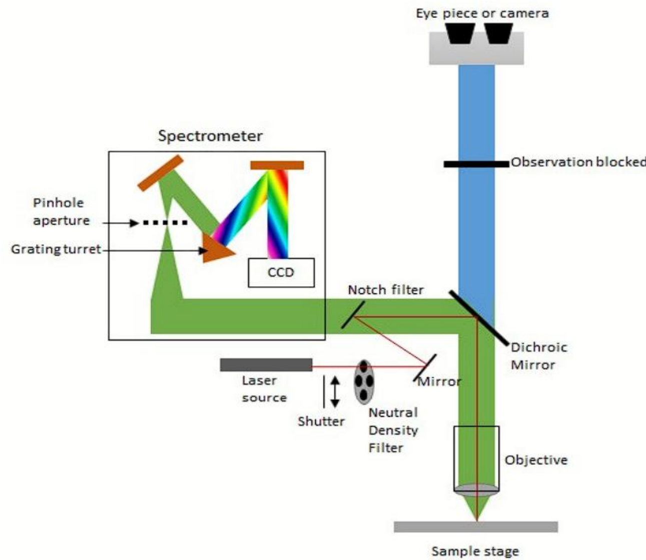

Fig 2.10 Schematic diagram of Raman spectrometer [30]

2.4 MICROSTRUCTURE ANALYSIS

2.4.1 Field enhanced scanning electron microscopy (FE-SEM)

Scanning electron microscopy is utilized for capturing the surface microstructural properties of a material. With SEM, a sample's image is created by projecting a stream of concentrated electrons onto its surface and examining the secondary and backscattered electrons that result. This process yields data about the sample's composition and topography. An optical microscope cannot match the magnification and resolution that a SEM can offer. The maximum magnification of an optical microscope is x1000, whereas the greatest magnification of a SEM is x300000, related to the wavelength of light. In order to enhance the resolution of the images, one has to reduce the wavelength of the beam. It is possible to tune the same

depending on the accelerating voltage of the electron beam used [31]. FESEM and SEM works on the same principle; instead of thermionic emission, FESEM uses a field emission gun as electron source, which in turn increases the resolution. In FESEM, a field emission cathode in the electron gun provides a narrow beam at low and high electron energies [32].

The produced electron beam is focussed by 3 magnetic lenses and allowed to fall on the specimen. These are periodically deflected by deflection coil in order to ensure spreading on the surface under examination [33]. The produced secondary electrons from the surface is directed to a collector, where the intensity of current is recorded. Depending on the collected data, an image of the surface is constructed. The schematic diagram of FESEM is shown in Fig. 2.11.

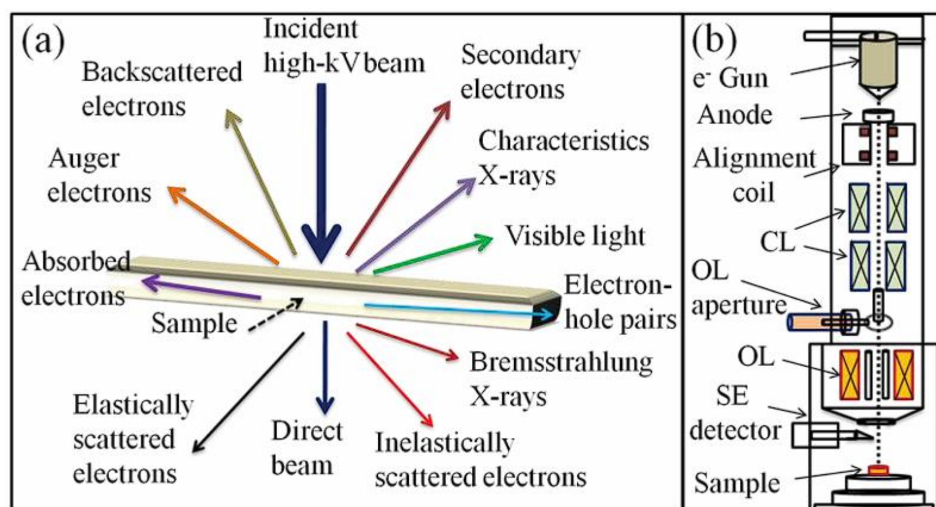

Fig. 2.11 a) Process occur when electron beam and material interacts

b) Schematic of experimental setup of FESEM

2.4.2 Atomic force microscopy

Atomic force microscopy delivers the 3D topography of the sample such as thin films, powder etc. The resolution varies from angstroms to micrometre scale. AFM is one of the scanning probe microscopy, where probe performs a raster scan all over the surface of film. The motion of the probe from each pass across the surface is recorded as a 2D line profile, shown on the left side in Fig. 2.12. These line profiles are combined to form a 3D image of the surface [34].

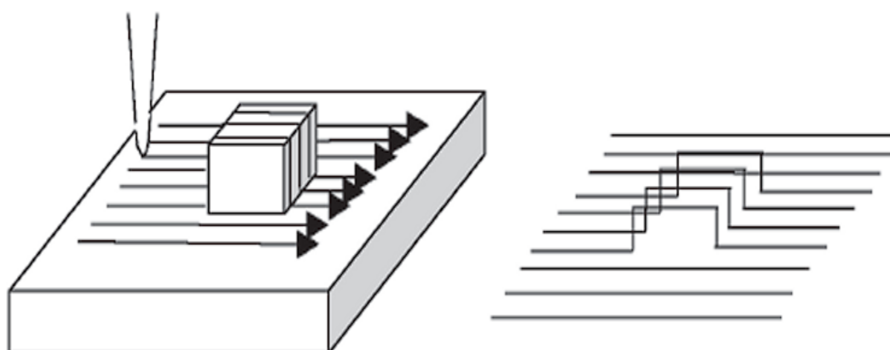

Fig 2.12 Schematic diagram describing the Principle of AFM

The probe tip is attached to a cantilever - laser beam mechanism and further variation in light reflection intensity is collected with the aid of photodetector. The fluctuation in the force on probe deflects the laser focussed on cantilever. By recording the photodetector current, the surface topography is recreated. There are three different modes for the operation of AFM, they are

1) contact mode, also called static mode
2) tapping mode, also called intermittent contact
3) non-contact mode

Tapping mode is a gentler way to measure surface topography and consequently surface roughness. The tip gently interacts with the surface at a constant oscillation amplitude in this dynamic mode, which oscillates at a resonance frequency. In order to select a larger amplitude for stiff, robust materials and a smaller amplitude for softer materials, the user defines the oscillation amplitude at which the tip images the surface. The instrument's z piezo feedback loop then maintains the oscillation's cantilever amplitude constant across the image. This *z* piezo motion provides the topography information; almost any surface topography [35].

There are two prevalent roughness parameters typically measured. The arithmetic mean deviation from the mean, written as

$$\text{Ra} = \frac{1}{n}\sum_{i=1}^{n}|y_i| \quad \ldots\ldots\ldots\ldots\ldots\ldots(2.8);$$

and the root mean square deviation from the mean, expressed as [36]

$$\text{Rq} = \sqrt{\frac{1}{n}\sum_{i=1}^{n}y_i^2} \quad \ldots\ldots\ldots\ldots\ldots(2.9)$$

In present work, Bruker dimension icon and Bruker Innova SPM instruments in tapping mode were used for measuring the surface roughness of the nitride thin film samples.

2.5 ELECTRICAL PROPERTIES VIA HALL MEASUREMENTS

For the investigation of surface plasmon resonance properties, carrier concentration measurement is important. The negative permittivity associated with high carrier concentration is a necessary criterion for the exhibiting surface plasmon resonance properties in thin films.

Hall measurement is used to obtain carrier charge density, resistivity and mobility of charge carriers. The underlying phenomenon behind this is Hall effect technique. When an electric current is passed through a thin film in a magnetic field-oriented perpendicular to the current, a Lorentz force proportional to the current and magnetic field is developed across the sample, which directs the charge carriers. In general, Hall voltage is the generation of transverse voltage in a current carrying semiconductor in external applied magnetic field [37]. The Lorentz force is given by

$$F = q\,(E+V\times B)\;\ldots\ldots\ldots\ldots\ldots\ldots\ldots(2.10)$$

where q is the elementary charge, v is the velocity of particle, E and B are the applied electric and magnetic fields of the sample, respectively. The underlying principle behind the Hall Effect is the Lorentz force [38].

This transverse potential difference is known as the Hall Voltage and its magnitude is given by

$$V_H = \frac{IB}{qnd}\ldots\ldots\ldots\ldots\ldots\ldots\ldots\ldots(2.11)$$

where I is the current, B is the magnitude of magnetic field, q is the elementary charge (q = $1.6\text{x}10^{-19}$ C), n is the volume charge density or carrier density and d is the thickness of the sample. From this, one will get the carrier charge density, after measuring the Hall voltage. Hall voltage will be a negative value for n-type semiconductors, that is, if the charge carriers are electrons or negative ions; positive for p-type semiconductors when the charge carriers are holes or positive ions.

By using van der Pauw method, one can determine the sheet resistance and consequently the Hall mobility and sheet density [39].

$$\mu = \frac{|V_H|}{R_S I B} \quad \text{...(2.12)}$$

where μ is the hall mobility and R_S is the sheet resistance obtained via van der Pauw method. This method utilises an arbitrarily shaped, thin-plate sample containing four ohmic contacts at the periphery of the plate. Two characteristic resistances for the two terminals are obtained by passing current two adjacent terminals and measuring the voltage across the other two adjacent terminals and then the values of the two characteristic resistances are plugged into the van der Pauw equation to get the sheet resistance. The van der Pauw equation is

$$e^{\frac{-pR_A}{R_S}} + e^{\frac{-pR_B}{R_S}} = 1 \quad \text{....................................(2.13)}$$

here $R_A = \frac{V_{43}}{I_{12}}$ and $R_B = \frac{V_{43}}{I_{23}}$............................(2.14)

Here, R_A and R_B are the characteristic resistances [40]. Experimental setup for Hall measurements using van der Pauw method is shown in the Fig.2.3. Ecopia make HMS-3000 Hall measurement system having a magnetic field of 1.05 T at room temperature was used for measuring the electrical properties, mobility, carrier density, and resistivity of the films coated in this work.

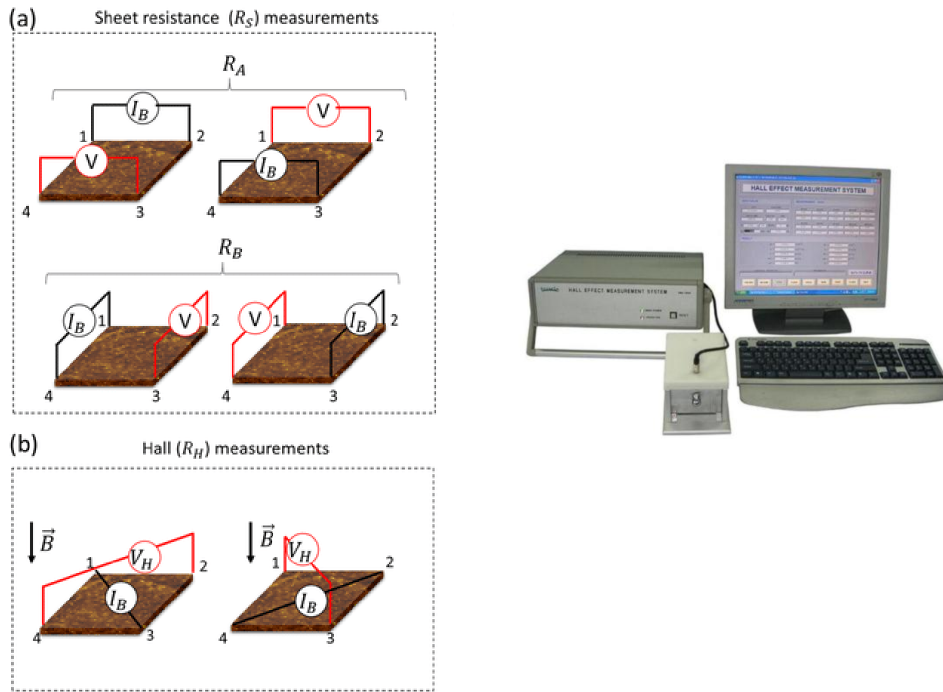

Fig 2.13 a) Hall measurement set up in van der Pauw configuration,
b) instrument used for the Hall measurements [41]

2.6 OPTICAL PROPERTIES

2.6.1 Reflectance Spectra and Dispersion relation

The previous discussions on the properties of transition metal nitride described the transition nature of the same from semiconductor to metal like nature. The interaction of the electromagnetic wave with thin films having increased free carrier concentration leads to a combined effect of higher reflectivity and wide bandgap nature with material composition [42-43]. Here, the main objective is to demonstrate the negative permittivity and low loss properties of the films for plasmonic application in the visible region.

In 19th century Paul Drude proposed a model to explain the dielectric function of the metals in response to the electric field with the assumption of existence of free electron carriers [44-45]. The dielectric function is given by

$$\varepsilon_r = \varepsilon_\infty - \frac{\omega_p^2}{\omega(\omega + j\gamma)} \qquad (2.15)$$

where ε_∞ is the high frequency permittivity value, γ is the damping term, and ω_p is the plasma frequency. The plasma frequency is given by

$$\omega_p = \sqrt{\frac{Ne^2}{\varepsilon_0 m^*}} \qquad (2.16)$$

where m^*, e and n are the electron effective mass, the electron charge, and the carrier density, respectively, and ε_0 is the permittivity of free space.

While considering bound electrons, one has to consider the Lorentz model, which accounts for the bound electrons. This model is most suited for the materials with bound electrons such as semiconductors, where the electrons are bound to the nucleus via a hypothetical spring and behave like a damped harmonic oscillator [46-48]. In semiconductors, both free electrons as well as bound electron exist, and hence, it is more acceptable to consider a combined model of Drude and Lorentz approaches. According to this combined model, the complex electrical permittivity is defined as [49],

$$\varepsilon = \varepsilon_\infty - \frac{\omega_{pu}^2}{\omega^2 - i\Gamma_D\omega} + \sum_{j=1}^{2} \frac{f_j\omega_{oj}^2}{\omega_{0j}^2 - \omega^2 + i\gamma_j\omega} \quad \ldots\ldots\ldots (2.17)$$

where ε_∞ is high frequency dielectric constant, greater than unity, Γ_D is the Drude damping factor and ω_{0j} is the Lorentz oscillator with damping factor γ_j. $\Gamma = \frac{e}{\mu m^*}$, is the loss related Drude relaxation rate, or called momentum

scattering rate. When the value of Lorentz oscillator frequency ω_{0j} is zero, the above equation reduces to the dispersion relation corresponding to Drude model alone. Hence, for adopting free electron contribution, one need to consider the value of ω_{0j}=0 and $\omega_{pu} = \omega_p$.

Reflection from a metal film depends on the light-matter interaction [50]. The metals having high carrier concentration give rise to higher reflectance. The Fresnel's law of reflection predicts the relationship between the permittivity and percentage of reflection, which depends on the angular frequency of incident light (equation 2.18). By measuring the frequency dependent optical reflectivity spectra, it is possible to extract the optical functions and dielectric function from the same [51]. The normal-incidence reflectivity R expressed via the dielectric function $\varepsilon(\omega)$ according to the Fresnel formula [52],

$$R = \left(\frac{1-\sqrt{\varepsilon}}{1+\sqrt{\varepsilon}}\right)^2 \quad \text{……………………..(2.18)}$$

The above expression can be solved for the dielectric function of the materials complex in nature with real and imaginary parts of the permittivity. Thus, by considering equations 2.17 and 2.18, the analysis of negative dielectric permittivity and low loss nature of the films can be carried out. A standard tool RefFit [53] has been used in this work. Fresnel formula is used in this tool, and as discussed, the Drude- Lorentz model is the foundation of this formula. The central assumption in the calculations is that all measurable optical quantities (such as reflectivity, penetration depth etc.) can be expressed in terms of the complex frequency-dependent dielectric function $\varepsilon(\omega) = \varepsilon_1(\omega) + i\,\varepsilon_2(\omega)$ of the material under study [54].

Fig 2.14 The experimental setup used for the reflectance measurement [55]

In this work, an Ocean Optics make Flame T-XR1 fibre-optic spectrophotometer has been used for measuring the reflectance spectra in the wavelength range 400–900 nm, at normal incidence, using a visible-NIR reflectance probe. Front surface-protected aluminum mirror on fused silica substrate(Ocean Optics) is used as standard reflector. The experimental setup used for the reflectance measurement is shown in Fig. 2.14. The dielectric functions of the films were extracted using the software RefFit, where the measured reflectance spectra were matched to theoretical spectra derived based on the Drude-Lorentz model.

2.6.2 Bandgap estimation using Tauc plot from transmittance spectra

Absorbance of the material can be expressed as

$$A = log_{10}\left(\frac{I}{I_0}\right) = -log_{10}T \text{ ....(2.19)}$$

where, A is the absorbance, I is the intensity of transmitted light, I_0 is the intensity of incident light and T is the transmittance [56]. Absorption coefficient (α) of the thin film can be calculated from transmittance data obtained from UV visible spectra,

$$\alpha = \frac{1}{\mathrm{d}}\left[-\ln\frac{\%\mathrm{T}}{100}\right] \text{............................(2.20)}$$

where, d is the thickness of the film. The optical band gap can be estimated using Tauc's relation [56]

$$\alpha h\upsilon = A\left(h\upsilon - E_g\right)^n \text{.........................(2.21)}$$

where, A is a constant, h is the Plank's constant, v is frequency and Eg is the energy band gap. The value of n characterize the transition process, which take up values 2, 2/3, ½ and 1/3 for the probability transitions of direct allowed, direct forbidden, indirect allowed and indirect forbidden transitions, respectively [57]. Transition metal nitrides, being a direct band gap material, n is taken as 2, and the band gap values of the films can be estimated by extrapolating the linear portion of the $(\alpha h v)^2$ versus $h v$ plot to the x intercepting point at $y = 0$ [58].

2.7 EXCITATION OF SURFACE PLASMON POLARITONS VIA KRETCHSMANN TYPE PRISM CONFIGURATION

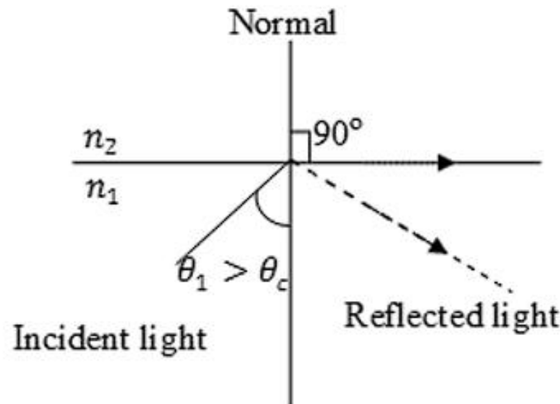

Fig. 2.15 Schematic diagram indicating the total internal reflection [59]

Ir 'e
p :e
p ,s
discussed in the first chapter, section 1.4 three configurations are used for this purpose, and here prism geometry configuration is used for the excitation using thin films. The critical angle (θ_c) in total internal reflection (TIR) at an interface with refractive index n_1 and n_2 is given by

$$\theta_c = \sin^{-1}(\frac{n_2}{n_1}) \qquad (2.22)$$

For air and glass (n_2=1.5) interface, the critical angle is 41.8°. The total internal reflection is schematically represented in the Fig. 2.15.

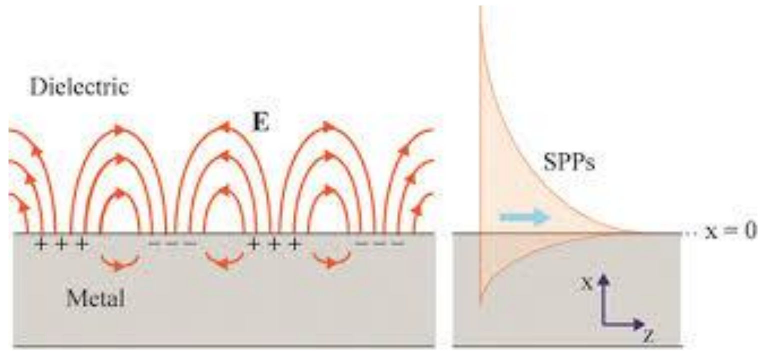

Fig 2.16. Evanescent wave in the metal dielectric interface [60]

TIR generates a form of the oscillating electric and/or magnetic field that does not propagate as an electromagnetic wave, but whose energy is spatially concentrated in the vicinity of the source, called evanescent wave [61]. Due to reflected light, the evanescent field is generated on the opposite site of the interface, and its amplitude decreases exponentially along the direction of the wave propagation [61-62], as shown in Fig. 2.16. The detailed explanation on this is given in the chapter 1 section 1.4.1

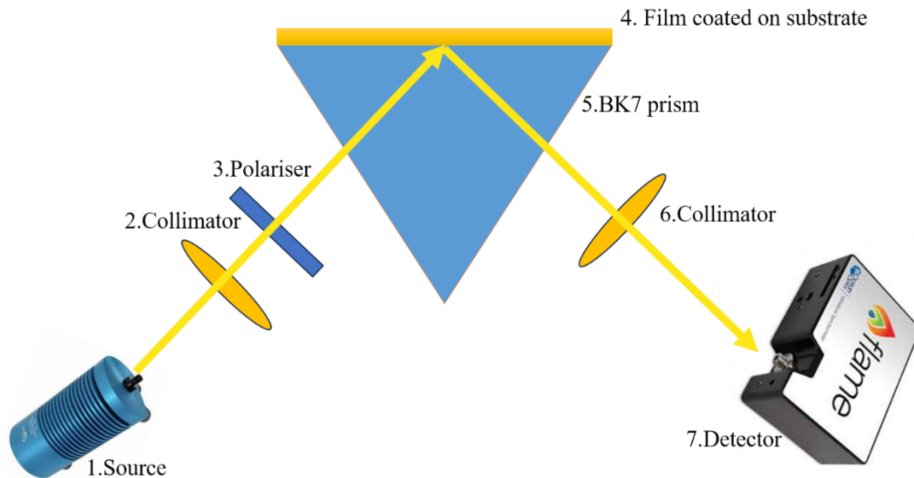

Fig 2.17. Experimental setup for Kretschmann configuration; the component names are given in the figure

In general, the mechanism used for SPR excitation throughout this work is Kretschmann configuration. The experimental setup used for the same is given in Fig. 2.17. The experimental setup for the SPR excitation in Kretschmann configuration consists of 3 parts. The first part comprise of source, a tungsten halogen lamp, which illuminate white light in the wavelength range 400-2100nm, with launching optics, collimating lens and an input optical fibre. The collimator is used for focussing the light beam to prism and a linear polariser is required for polarising the light.

The second part consist of a coated thin film with required properties attached to a BK7 prism via index matching fluid. The films under this investigation were coated on glass or quartz (refractive index n= 1.5) substrates. The whole setup is mounted on optic bench, where the angle of incidence can be adjusted from 45°-60°.

The last part includes collimating lens which collects reflected light from one side of the prism and directed to a spectrometer (Flame T-XR1, Ocean Optics spectrophotometer) via an outlet fibre. The spectra are recorded using an Oceanview software. The obtained SPR curve is plotted in wavelength interrogation mode, that is, in wavelength versus reflectivity plot.

Various experimental techniques used for the fabrication of transition metal nitride thin films along with major components, basic principles, and a schematic diagram were explained in this chapter. Furthermore, the main tools and methods for characterizing the structural, morphological, optical, and electrical characteristics of the transition metal nitride thin films made via different methods were explained in detail, as well as the specifics of the plasmonic property of the produced films.

2.8 SUMMARY

Various experimental techniques used for the fabrication of transition metal nitride thin films along with basic principles, major components and schematic diagram were described in this chapter. Furthermore, the main tools and methods used for investigating the structural, morphological, electrical, optical and plasmonic properties of the transition metal nitride thin films developed for this work were explained in detail.

2.9 REFERENCES

1. Dhruv Fomra, Ray Secondo, Kai Ding, Vitaliy Avrutin, Natalia Izyumskaya, Ümit Özgür, Nathaniel Kinsey (2020), Plasmonic titanium nitride via atomic layer deposition: A low-temperature route. J. Appl. Phys. 127, 103101. https://doi.org/10.1063/1.5130889

2. Ramanuja, N & Levy, R.A & Dharmadhikari, S.N & Ramos, E & Pearce, C.W & Menasian, S.C & Schamberger, P.C & Collins, C.C. (2002). Synthesis and Characterization of Low Pressure Chemically Vapor Deposited Titanium nitride Films Using $TiCl_4$ and NH_3. Mater. Lett. 57. 261-269. DoI: 10.1016/S0167-577X(02)00776-0.

3. Chowdhury R, Vispute RD, Jagannadham K, Narayan J. (1996), Characteristics of titanium nitride films grown by pulsed laser deposition. J Mater Res.; 11, 1458–69. 10.1557/jmr.1996.0182.

4. Jeyachandran, Y. L., Narayandass, Sa. K., Mangalaraj, D., Areva, S., & Mielczarski, J. A. (2007). Properties of titanium nitride films prepared by direct current magnetron sputtering. Mater. Sci. Eng. A, 445, 223–236. https://doi.org/10.1016/J.MSEA.2006.09.021

5. Chopra, K. L., & Klerrer, J. (1969). *Thin film phenomena*. McGraw-Hill, New York

6. *Ohring, Milton. Materials Science of Thin Films (2nd ed.).* Academic Press. *P. 215.*

7. Tripathi, S. K., & Ridhi, R. (2023). Semiconductor oxide nanomaterial. In *Carbon Nanomaterials and their Nanocomposite-Based Chemi-resistive Gas Sensors* (pp. 41-74). Elsevier.

8. Nandy, S., & Chae, K. H. (2023). Chemical synthesis of ferrite thin films. In Ferrite Nanostructured Magnetic Materials (pp. 309-334). Woodhead Publishing.

9. Scriven, L. E. (1988). *Physics and Applications of DIP Coating and Spin Coating*. MRS Proceedings. Cambridge University Press (CUP). 121: 717.

10. Tjokro, K., Young, D.J. (1995). Comparison of internal nitridation reactions in ammonia and in nitrogen. Oxid Met 44, 453-474 https://doi.org/10.1007/BF01058247

11. Taylor Lyman (1964), Metals Handbook, Vol. 2, Heat Treating, Cleaning and Finishing,ASM Handbook Committee, American Society for Metals,

12. Chang, An-jae & Rhee, Shi-Woo & Baik, Sunggi. (2005). Kinetics and Mechanisms for Nitridation of Floating Aluminum Powder. J. Am. Ceram. Soc. 78, 33 - 40. DOI: 10.1111/j.1151-2916.1995.tb08357.x.

13. Deng, Lulu & Wang, Kewei & Yan, Han & Britten, James & Xu, Gu. (2011). Phase and Texture of Solution-Processed Copper Phthalocyanine Thin Films Investigated by Two-Dimensional Grazing Incidence X-Ray Diffraction. Crystals. 1. 10.3390/cryst1030112.

14. Cullity B D, Stock S R, (2001) *Elements of X-ray diffraction*, Third Edn, Prentise Hall, New Jersey,

15. Ryland, A. L. (1958). X-ray diffraction. J. Chem. Educ., 35, 80.

16. Nascente, P. A. (2005). Materials characterization by X-ray photoelectron spectroscopy. J. Mol. Catal. A Chem., 228, 145-150.

17. Engelhard, M. H., Droubay, T. C., & Du, Y. (2017). *X-ray photoelectron spectroscopy applications* (No. PNNL-SA-111274). Pacific Northwest National Lab.(PNNL), Richland, WA (United States). Environmental Molecular Sciences Lab. (EMSL).

18. T. Yokoyama, in *Instrumental Analysis of Coordination Compounds*, Volume 2, Royal Society of Chemistry, 2024, ch. 10, pp. 301-332.

19. Stefan Hufner, (2003), Photoelectron Spectroscopy Principles and Applications. Springer-Verlag Berlin Heidelberg, New York 10,

20. Fred A. Stevie, Carrie L. Donley, (2020), Introduction to x-ray photoelectron spectroscopy, J. Vac. Sci. Technol. A 38, 063204.

21. J.H. Scofield, (1976) , Hartree-Slater subshell photoionization cross-sections at 1254 and 1487 eV, J. Electron Spectrosc. Relat. Phenomena., 8(2), 129-137,

22. Dominik Jaeger, Jörg Patscheider, (2012) A complete and self-consistent evaluation of XPS spectra of TiN, J. Electron Spectrosc. Relat. Phenomena., 185,523-534 ,

23. Tougaard S, (1997) Universality Classes of Inelastic Electron Scattering Cross-sections. Surf. Interface Anal. 25 137-154,

24. M. Repoux, (1992) A new asymmetric Pseudo-Voigt function for more efficient fitting of XPS lines, Surf. Interface Anal. 18 567–570.

25. C.D. Wagner, (1983) Sensitivity factors for XPS analysis of surface atoms, J. Electron Spectrosc. Relat. Phenom. 32, 99–102.

26. Stoehr, M. & Shin, C.-S & Petrov, Ivan & Greene, J. (2011). Raman scattering from TiNx ($0.67 \leq x \leq 1.00$) single crystals grown on MgO(001). Journal of App Phy. 110. 10.1063/1.3651381

27. Long, Derek Albert, Long D A, (1977) *Raman spectroscopy* McGraw-Hill, New York, 276.

28. Colthup N, (2012), *Introduction to infrared and Raman spectroscopy*, Elsevier.

29. Velu, Nirmal & Arivanandhan, Mukannan & Koyoma, T. & Udono, H. & Inatomi, Yuko & Hayakawa, Y. (2016). Effects of varying indium composition on the thermoelectric properties of $In_xGa_{1-x}Sb$ ternary alloys. Appl. Phys. A. 122. DOI: 10.1007/s00339-016-0409-9.

30. Smith R, Wright K L, Ashton L, (2016), Raman spectroscopy: an evolving technique for live cell studies, Analyst.141, 3590.

31. Reimer, L. (2000). Scanning Electron Microscopy: Physics of Image Formation and Microanalysis, Second Edition. Measurement Science and Technology. 11. 1826. 10.1088/0957-0233/11/12/703.

32. Giannuzzi, Lucille. (2018). *Scanning Electron Microscopy and X-Ray Microanalysis* 4th Edition, Springer, 2018, 550. 24. 1. DOI: 10.1017/S1431927618015271.

33. Eckertová, L. (1986). *Physics of Thin Films*. Springer.

34. West, Paul & Starostina, Nataliya. (2004). Atomic Force Microscopy. Adv. Mater. Proc. 162. 35-37.

35. Garth J. Simpson, Dana L. Sedin, and Kathy L. Rowlen, (**1999**), Surface Roughness by Contact versus Tapping Mode Atomic Force Microscopy, *Langmuir 15*, 1429-1434

36. Chin Y. Poon, Bharat Bhushan, (1995) Comparison of surface roughness measurements by stylus profiler, AFM and non-contact optical profiler, Wear, 190,1 ,76-88,

37. Ellmer K, Hall effect and conductivity measurements in semiconductor crystals and thin films, Charact. Mater. (2012) 1.

38. van der Pauw, L. J. (1958). A method of measuring the resistivity and Hall coefficient on lamellae of arbitrary shape. Philips technical review, 20, 220-224.

39. Edward Ramsden, (2006) Chapter 1 - Hall-Effect Physics, Hall-Effect Sensors (Second Edition), Newnes, 1-10,DOI:10.1016/B978-075067934-3/50002-8

40. van der Pauw. (1958). A method of measuring specific resistivity and Hall effect of discs of arbitrary shape. Philips Res. Rep, 13, 1-9.

41. Melios, Christos & Huang, Nathaniel & Callegaro, Luca & Centeno, Alba & Cultrera, Alessandro & Cordon, Alvaro & Panchal, Vishal & Arnedo, Israel & Redo-Sanchez, Albert & Etayo, D. & Fernandez, Montserrat & Lopez, Alex & Rozhko, Sergiy & Txoperena, Oihana & Zurutuza, Amaia & Kazakova, Olga. (2020). Towards standardisation of contact and contactless electrical measurements of CVD graphene at the macro-, micro- and nano-scale. Sci. Rep. 10. DOI: 10.1038/s41598-020-59851-1.

42. Ian R. Hooper and J. Roy Sambles, (2008), Some considerations on the transmissivity of thin metal films, Opt. Express 16, 17258-17267

43. I. V. Antonets, L. N. Kotov, S. V. Nekipelov & E. N. Karpushov (2004) Conducting and reflecting properties of thin metal films. Tech. Phys. 49, 1496-1500. https://doi.org/10.1134/1.1826197

44. Fox M (2010) *Optical properties of solids*, 2nd edn. Oxford University Press, Oxford, pp 33-44

45. Chuang S (2009) *Physics of photonic devices*, 2nd edn. Wiley, New York, pp 193–196

46. Rivas J G, Snchez-Gil J A, Kuttge M, Bolivar P H, Kurz H (2006) Optically switchable mirrors for surface plasmon polaritons propagating on semiconductor surfaces. Phys. Rev. B 74, 245–324

47. Huang Y, Ho ST (2006) Computational model of solid state, molecular, or atomic media for FDTD simulation based on a multilevel multi-electron system governed by Pauli exclusion and Fermi-Dirac thermalization with application to semiconductor photonics. Opt Express 14, 3569–3587

48. Hryciw A, Jun YC, Brongersma ML (2010) Plasmonic: electrifying plasmonics on silicon., Nat. Mater. 9, 3-4

49. F. Wooten, *Optical Properties of Solids*, Academic press, New York, *Academic Press, New York* 10003. United Kingdom Edition, (1972).

50. A. E. Kaplan (2018), Metallic nanolayers: a sub-visible wonderland of optical properties. J. Opt. Soc. Am. B 35, 1328-1340

51. Shun-Tung Yen and Pei-Kang Chung (2015), Extraction of optical constants from maxima of fringing reflectance spectra, Appl. Opt. 54, 663-668

52. Fresnel, A, (1831), interactions with the polarization of light, Ann. Phys., 98: 68-90. https://doi.org/10.1002/andp.18310980503.

53. A. B. Kuzmenko (2005) Kramers-Kronig constrained variational analysis of optical spectra. Rev. Sci. Instrum. 76, 083108. DOI: https://doi.org/10.1063/1.1979470

54. *Yamamoto, Kiyoshi & Masui, Akio & Ishida, Hatsuo. (1994). Kramers–Kronig analysis of infrared reflection spectra with perpendicular polarization. Applied Optics. 33. 6285-6293. 10.1364/AO.33.006285.*

55. The Ocean Optics manual. http://oceanoptics.com/wp-content/uploads/FlameIO.pdf.

56. *Tauc, J. (1968).Optical properties and electronic structure of amorphous Ge and Si". Mater. Res. Bull. 3,* 37-*46.* DOI*:*10.1016/0025-5408(68)90023-8.

57. Chopra K L, Paulson P D, Dutta V, Thin film solar cells: an overview. Prog. Photovoltaics Res. Appl. 12 (2004).

58. Patrycja Makuła, Michał Pacia, and Wojciech Macyk, (**2018**), How to Correctly Determine the Band Gap Energy of Modified Semiconductor Photocatalysts Based on UV–Vis Spectra J. Phys. Chem. Lett. *9*, 6814-6817, DOI: 10.1021/acs.jpclett.8b02892

59. Solovan, M.N., Brus, V.V., Maistruk, E.V. (2014), Electrical and optical properties of TiN thin films. Inorg. Mater. 50, 40-45.

60. Sanong Ekgasit, Chuchaat Thammacharoen, and Wolfgang Knoll (2004), Surface Plasmon Resonance Spectroscopy Based on Evanescent Field Treatment, Anal. Chem. 76, 3, 561–568,

61. Jahani, S., Kim, S., Atkinson, J.. Controlling evanescent waves using silicon photonic all-dielectric metamaterials for dense integration. Nat. Commun. 9, 1893 (2018).

62. Kumar, G., Sarswat, P.K. (2016). Interaction of Surface Plasmon Polaritons with Nanomaterials. In: Geddes, C. (Eds.) *Reviews in Plasmonics*, 2015. Springer, Cham.

CHAPTER 3

INVESTIGATION OF PLASMONIC PROPERTIES IN RF SPUTTERED TITANIUM NITRIDE THIN FILMS

Introduction

Sputtering is one of the most widely used physical vapour deposition techniques for coating thin films of transition metal nitrides [1]. The studies on TiN_x films were already carried out by reactive sputtering, which proved the ability of the coatings to exhibit plasmonic properties [2-3]. In general, these films were coated on Silica, MgO and sapphire substrates in order to achieve optimum electrical properties. However, it can be seen that these studies lack detailed correlation of opto-electrical properties leading to the plasmonic behaviour.

This chapter discusses the detailed investigation of the structure and the correlation of the opto-electrical properties of the radio frequency sputtered titanium nitride films on low-cost cover glass slides in the context of plasmonic properties. The stoichiometry, the N/Ti ratio, of the coated films largely determines the opto-electrical properties of the films. In sputtering, the composition varies in accordance with the $Ar:N_2$ ratio, sputtering power along with other deposition parameters. Hence, the study focused on how various parameters such as, gas composition and RF power, affect the electrical and optical properties of the coated film on glass substrates, in the context of surface plasmon resonance applications. Various characterization techniques have been used to validate the structural and the plasmonic properties of the films developed. Raman spectroscopy, XPS, and grazing incident X-ray diffraction have been used for the structural analysis and the defect chemistry studies related to the N/Ti ratio. Opto-electrical properties were carried out to confirm the important plasmonic properties, low loss and negative permittivity of the deposited films. For this, dispersion relations were estimated from reflectance spectra of the films by Drude-Lorentz approximation. Carrier concentration was

calculated by Hall effect measurements. As described in section 6 of the Chapter 2, the Fresnel's relation was used for the theoretical simulations for SPR excitation, using a 3-layer geometry. Finally, surface plasmons were experimentally excited in the titanium nitride films coated on glass substrates using the prism geometry configuration in wavelength interrogation mode.

3.1 DEVELOPMENT OF TiN FILMS

Titanium nitride films were reactively RF sputtered using a 2-inch diameter titanium metal target (99.99%) using argon (99.999%) as sputtering gas and nitrogen (99.999%) as reactive gas. The chamber was initially evacuated to a base pressure of 3×10^{-6} mbar and then 15sccm of Argon was purged into the chamber using a mass flow controller and pre-sputtered for 5 minutes. Specific amount of nitrogen gas was then admitted to the chamber, and maintained the working pressure at 3×10^{-3} mbar. Depositions were carried out at room temperature onto pre-cleaned microscopic cover glass slides. During the deposition, the substrate to target distance was kept constant at 55mm. The magnetron was facing the substrate at an angle of 30° and set substrate rotation of 10 rpm in order to assure the uniformity of coated films. Prior to coating, the substrates were cleaned ultrasonically in soap water, distilled water, acetone and isopropanol successively for 15 minutes each and then dried in nitrogen gas flow. In the present study, RF power of 160W was used for the depositions of the films. The Ar:N_2 ratio is varied in this power in order to change the composition in thin films. Recent report shows reduced loss behaviour in the coated films with decreased RF power [4]. Hence, the analysis was further extended with a reduced power (140W) also. The sample preparation details are summarised in Table 3.1.

Table 3.1. Experimental conditions used for RF sputtering

Sample name	Power (W)	Ar:N_2 ratio (sccm)
TIN1	160	15:3
TIN2	160	15:4
TIN3	160	15:5
TIN4	140	15:3

3.2 STRUCTURAL PROPERTIES OF RF SPUTTERED TITANIUM NITRIDE FILMS

3.2.1 X-ray diffraction analysis

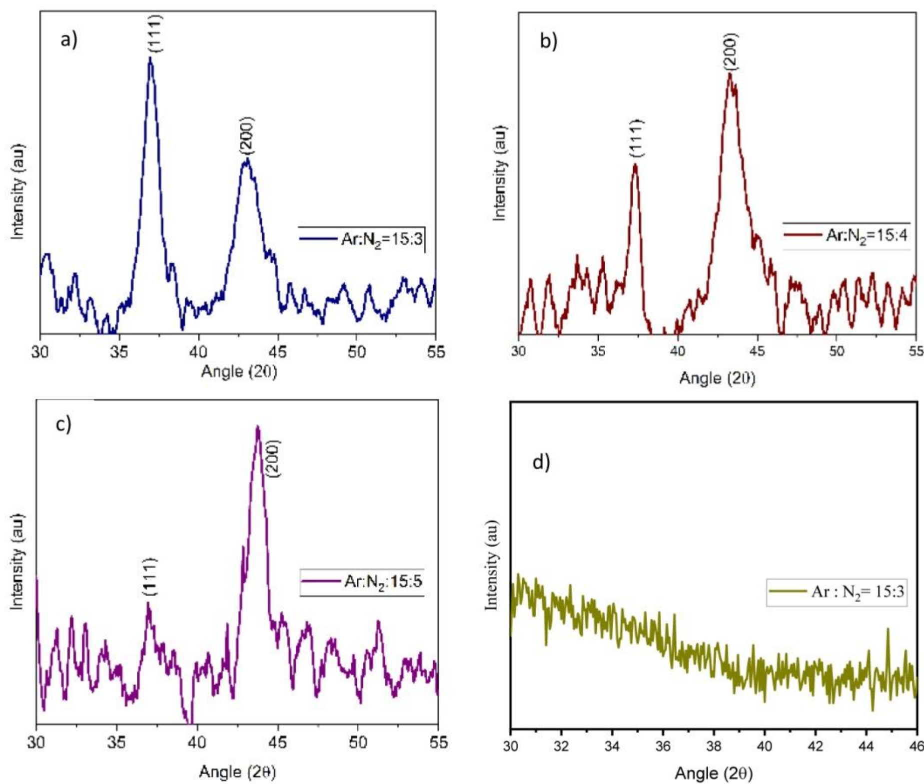

Fig 3.1. X-ray diffraction patterns of the as-deposited titanium nitride films a) TIN1, b) TIN2, c) TIN3 and d) TiN4

Fig. 3.1 (a-c) shows the XRD pattern of the titanium nitride film deposited at various Ar:N_2 ratios, along with the pattern of the films coated with low sputtering power (Fig. 3.1(d)). As seen, the patterns coated with higher sputtering power are having polycrystalline nature. Holmberg et al investigated the structure transition mechanism in titanium nitride thin films with the stoichiometry of the films [5]. When the value of N/Ti ratio or x <0.2, the nitrogen atom occupies interstitial octahedral positions of the hexagonal close packed structure of α-titanium metal film and form a distorted phase. For higher values of x, i.e., up to x = 0.52, the α and ε-tetragonal phases co-exist. Face centred cubic (FCC) phase is present when the value of x exceeds 0.6. [6].

It is reported that the thin film crystal texture growth is a competition between surface diffusion and ion bombardment of the particles [7]. The surface diffusion domination tends to end up with the lowest surface energy planes while the growth preferred by ion bombardment leads to form structure with the lowest strain energy planes. The (111) preferred orientation obtained in the film coated with an Ar/N_2 ratio of 15:3 (Fig. 3.1a) may be attributed due to the lowest strain energy for TIN1. As seen in Fig 3.11b, when the N_2 flow rate is increased, the strongest x-ray diffraction peak changed from (111) to (200) orientation. In this case, as the argon partial pressure decreases, the ion bombardment from the metal target decreases, and the preferred orientation shift from (111) to (200). The similar trend is visible in Fig.3.1c for TIN3 also, where the film is coated with Ar/N_2 ratio of 15:4. The intensity of the plane (111) is reduced more as compared to the other two films. The films coated with higher nitrogen concentrations of >6 sccm of nitrogen showed an amorphous nature, in the xrd analysis. As seen in 3.1(d), the film coated with low RF power (TIN4) appears to be amorphous in nature, may be due to the low thickness of the

films. Pennila et al reported similar amorphous titanium nitride films that were formed by DC sputtering with high chamber pressures, at room temperature [8]. Jeyachandran et.al reported similar nature for titanium nitride thin films with increase in nitrogen concentration [9-10]. The x-ray diffraction analysis confirms the formation of the crystalline structure of titanium nitride films coated with specified conditions.

The average crystallite size is calculated using the Scherrer formula [11]

$$D = \frac{0.9\lambda}{\beta \cos\theta} \quad \text{.................................(3.1)}$$

where λ, β, are the x-ray wavelength and the full width at half maximum (FWHM) at the corresponding θ position of the peak. The results are summarised in Table 3.2.

Table 3.2. Estimated Average Crystallite Size

Sample name	Peak position 2θ (°)	FWHM (°)	Average Crystallite size(nm)
TIN1	36.57	1.22	**7**
TIN2	42.47	1.66	**5**
TIN3	42.7	1.08	**8**

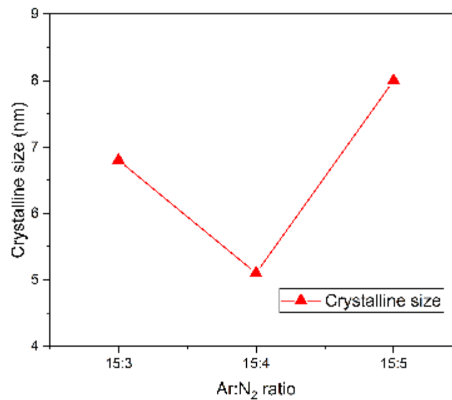

Fig. 3.2 Variation of average crystallite size with Ar : N_2 ratio

Fig. 3.2 depicts the variation of the average crystallite size of the films coated with various Ar:N_2 ratios. For the first sample, TIN1, the average crystallite size is determined from the (111) peak, since this film is grown predominantly in this crystallographic orientation. The other two films, TIN2 and TIN3. were grown predominantly in the preferred plane of (200), and hence the grain size has been calculated with respect to the (200) peak. The crystallite size initially decreases with increase in nitrogen concentration and then increases. Larger crystallite size is observed for the film deposited with Ar:N_2 ratio of 15:5, that is TiN3 [12].

3.2.2 X-ray Photoelectron Spectroscopic analysis

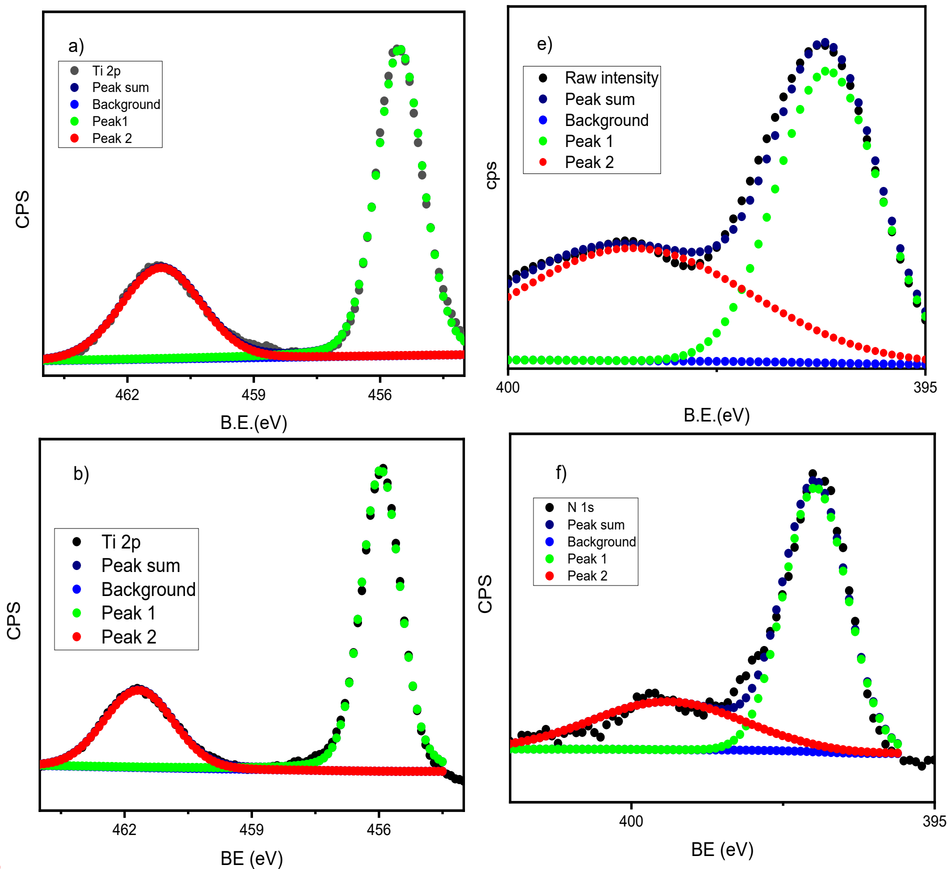

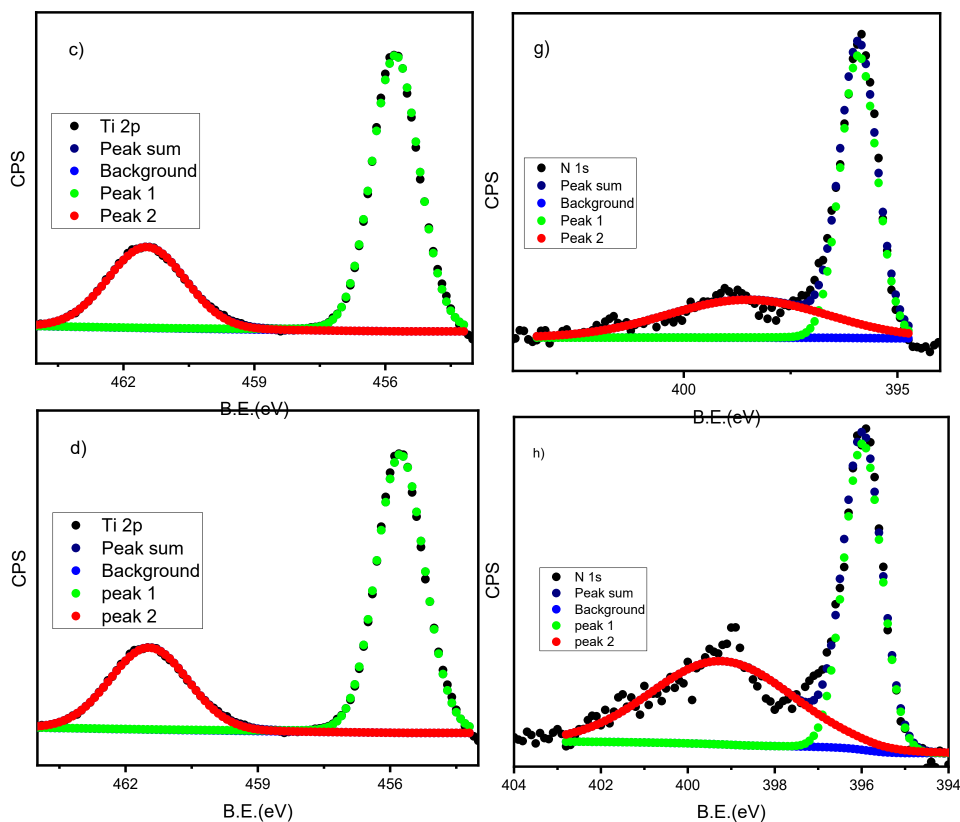

Fig. 3.3 Variations in Ti 2p (a, b, c) and N1s peak (e, f, g) for the films TIN1, TIN2, TIN3 deposited with different nitrogen concentrations (d,h), and TIN4, with low power (140W)

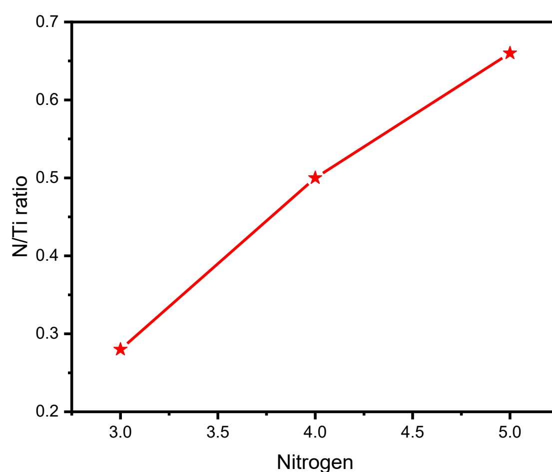

Fig. 3.4 Variation of N/Ti ratio in the coated films with Ar:N_2 ratio

XPS curves obtained from the films were referenced to the C 1s line of the adventitious carbon set at 284.6 eV. The XPS data obtained for titanium 2p core level and nitrogen 1s core level for the titanium nitride films with nitrogen variation is also shown in the Fig. 3.4. The peaks of XPS curve were deconvoluted using XPSPEAK41 software with Gaussian–Lorentzian (GL) function and Shirley (non-linear) background correction is used for nitrogen core level. The peaks are fitted using XPSPEAK4.1 software in order to calculate the stoichiometry in the coated films.

The background subtraction of titanium core level is of major concern for the stoichiometric calculation in titanium nitride compounds. The Tougaard background subtraction is adequate for Ti $2p_{3/2}$ Ti $2p_{1/2}$, since it fulfils the quantum mechanical requirements and yields an area ratio of 0.515 of the same peaks [13-14]. This subtraction considers contribution of an induced electric-field, generated with interaction of moving electron in solid and that of emitted electron. for the background intensity, which is present in metals like titanium nitride [15-16].

Fig. 3.3(a-f) show the variation of core level Ti 2p and N 1s peak in titanium nitride films with respect to the nitrogen flow during deposition. The surface composition analysis of the films was estimated from integrated area ratio after proper normalisation with sensitivity factors (ASF) using following equation [17].

$$\text{Aomic \% of } A = \frac{\frac{A}{a}}{\frac{A}{a}+\frac{B}{b}} \dots\dots\dots\dots\dots\dots..(3.2)$$

where A and B represents area under elements, a and b represent atomic sensitivity factors for respective elements. The results obtained are plotted in Fig. 3.4.

Titanium concentration shows an increased value when fabricated titanium nitride films with nitrogen flow rate of 3 sccm. However, the nitrogen content in the film is higher for all other flow rates, as seen in the Fig. 3.4. The N/Ti ratio is the lowest for TIN1, which is having more metallic nature. The gradual increase in nitrogen flow rate from 3 to 4 sccm contributed a N/Ti ratio change from 0.28 to 0.5, which confirms the metal rich nature of TIN1 and in this case the film was grown with preferred orientation in (111) direction. As flow increases to 5 sccm, the N/Ti ratio becomes 0.66, the intensity of (111) peak is reduced, and the changed preferred orientation to (200) direction.

Fig. 3.3 (d,h) corresponds to high resolution spectra for titanium and nitrogen core levels for the sample TIN4, coated with low RF power. The stoichiometric calculation predicts higher N/Ti ratio, that is, increased nitrogen content in the film. The reduction in RF power may decrease ion bombardment, which in turn contribute to the reduced titanium content.

The peaks at 396.1 eV and 398.1 eV, are corresponding to titanium nitride and oxynitride phase formations in N1s spectra of the film TIN1 [9]. The oxynitride phase formation may either due to residual oxygen present in the chamber at the time of deposition or due to the surface oxidation of samples [18]. Li et al reported the oxidation behaviour of the titanium nitride thin film samples when exposed to air in room temperature [19].

3.2.3 Raman Spectroscopic Analysis

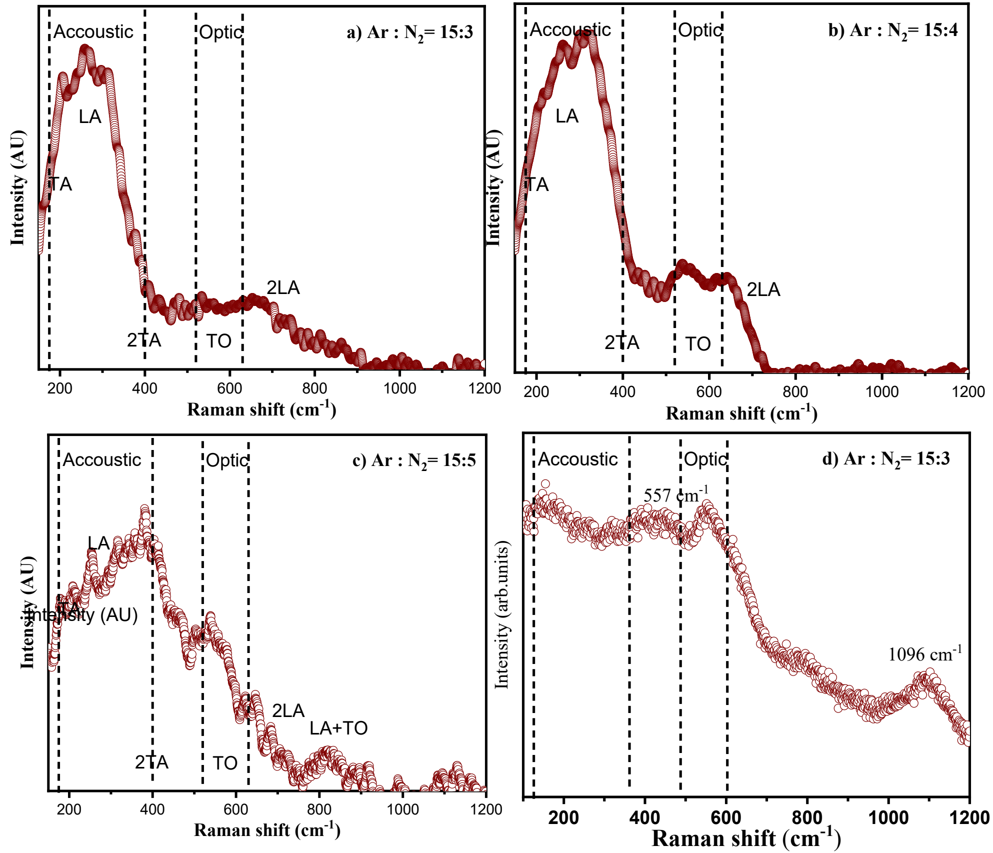

Fig 3.5. Raman spectra for the films a) TIN1 b) TIN2 c) TIN3 and d) TIN4

Raman measurements were performed using a 514 nm laser source, and the spectra were recorded with 10% laser power. 6 Lorentzian curves were created by deconvoluting the Raman spectra, and analysed the peak positions. Fig 3.5 depicts the variations in Raman spectra of titanium nitride films coated by RF sputtering with different nitrogen partial pressures. Due to the O_h symmetry of the molecule, cubic titanium nitride is Raman inactive [20]. However, according to Stoehr et al, even stoichiometric titanium nitride has defects that result in the first and second order Raman peaks [21]. The whole first-order Raman spectra of titanium nitride consists

of two regions corresponding to the acoustic (180–360 cm^{-1}) and optic (500–600 cm^{-1}) branches, respectively. The most characteristic feature of the Raman spectra is a wide band in the region around 550 cm^{-1} due to optical phonon. The complete Raman spectrum comprises of both first and second order modes, as in Table 3.3 [22].

Table 3.3. List of Raman modes in titanium nitride

Raman Modes	**Peak position (cm^{-1})**
First order Transverse acoustic mode (TA)	200
First order longitudinal acoustic mode (LA)	300
Second order Transverse acoustic mode (2TA)	400
TA + LA	500
First order transverse optical mode (TO)	550
Second order longitudinal acoustic mode (2LA)	600
LA + TO	800
Second order transverse optical mode (2TO)	1100

In Fig. 3.5 (a,b), the acoustic modes are prominent in comparison with the optic modes. The Raman scattering in the acoustic range is characterized by vibrations of the relatively heavy titanium ions, and the scattering at the optical range is due to lighter nitride ions. This indicates that the film prepared with lower nitrogen content is titanium rich or nitrogen deficient. The first-order transverse acoustic peak TA at 200 cm^{-1} and longitudinal acoustic peak LA at 300 cm^{-1} arise because of nitrogen vacancy, which together comprises the broad band of acoustic mode. Chowdhury et al reported the variation of acoustic mode intensity and peak shifting with respect to nitrogen deficiency [23].

From the observed spectra, it is clear that the first two films are metal rich in nature due to the presence of intensified acoustic bands. The acoustic band comprises of three peaks of transverse acoustic, longitudinal acoustic and second order transverse acoustic modes. As the N/Ti ratio increases in the films from 28% (TIN1) to 66% (TIN3), the TA, LA and 2TA modes showing a blue shift from 204 to 210 cm^{-1}, 286 to 315 cm^{-1}, and 355 to 393 cm^{-1} respectively. The same trend is observed when moving from 28% (TIN1) to 50% (TIN2). Intensity of second order longitudinal acoustic peak (2LA) increased in the TIN3 and LA +TO mode appears at 800 cm^{-1}. The 2TO mode is visible in TIN3 since the nitrogen content shows an increasing trend [21].

The ratio of the acoustical to the optical scattering intensities is a measure of the Ti : N ratio or stoichiometry [22]. The ratio of intensities of acoustic and optical mode is considerably reduced in Fig 3.4 (c), indicating an increase in N/Ti ratio of the films, which agrees with the results from the XPS analysis of the same, where the N/Ti ratio was found to increase from 28% to 66%. The film coated with 66% nitrogen (TIN3) possesses a broader peak at 550cm^{-1}, characteristic frequency band for titanium nitride represents the transverse optic mode (TO). They found to have a N/Ti ratio around 66% in the XPS analysis of the films. The analysis of Raman spectra confirm that TIN1 and TIN2 titanium nitride films are vacancy induced or highly nitrogen deficient.

In Fig 3.5 d, it can be noticed that, the Raman spectra of the film coated with Ar:N2 ratio of 15:3 with RF power of 140W, exhibits two peaks centred approximately at 550 cm^{-1} and 1100 cm^{-1}. Interestingly, the wavenumber of the second mode is two times of the first mode. Probably, these types of higher order modes occur for longitudinal optical (LO)

phonons coupled with electron transitions [24]. In general, the first and second order LO phonon modes as well as their higher order modes in Raman spectra were observed due to the strong Fröhlich interactions [25]. The Fröhlich interactions is generated due to the long-range coupling of free electrons with LO phonons [24]. In case of TIN4, the N/Ti ratio is observed to be 42%, which corresponds to wide band gap nature of titanium nitride film [26] compared to other samples. That is, the bandgap of the material becomes comparable to excitation energy of the Raman signal (source energy is 514nm, approximately 2.5eV), the resonance behaviour is visible as in Fig. 3.5.

3.3 SURFACE AND MICROSTRUCTURE ANALYSIS

3.3.1 Morphology analysis : FESEM

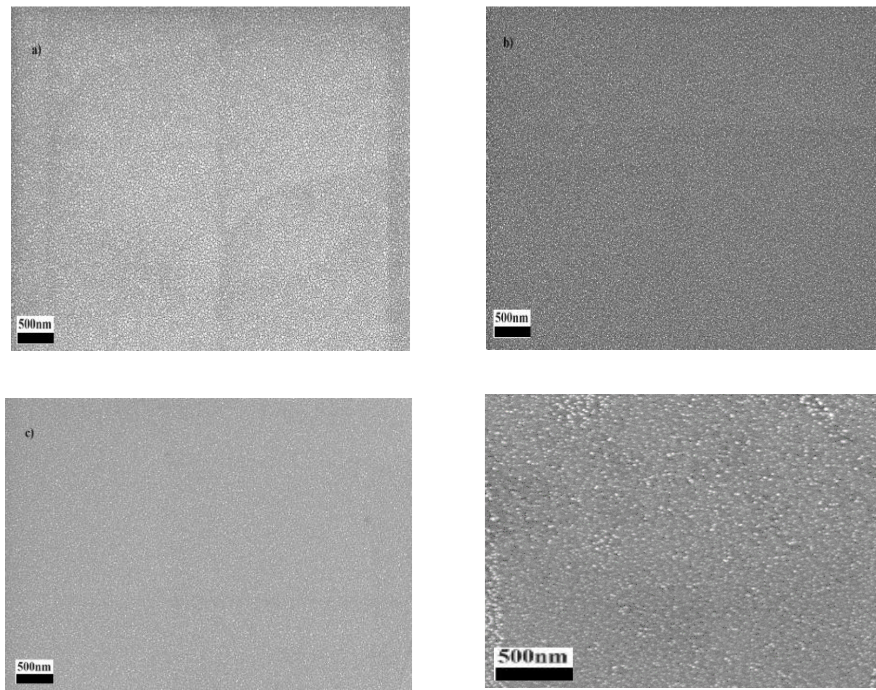

Fig. 3.6 Variation of surface morphology of TiN films with N/Ti ratio,
a) TIN1 b) TIN2 c) TIN3 and d) TIN4

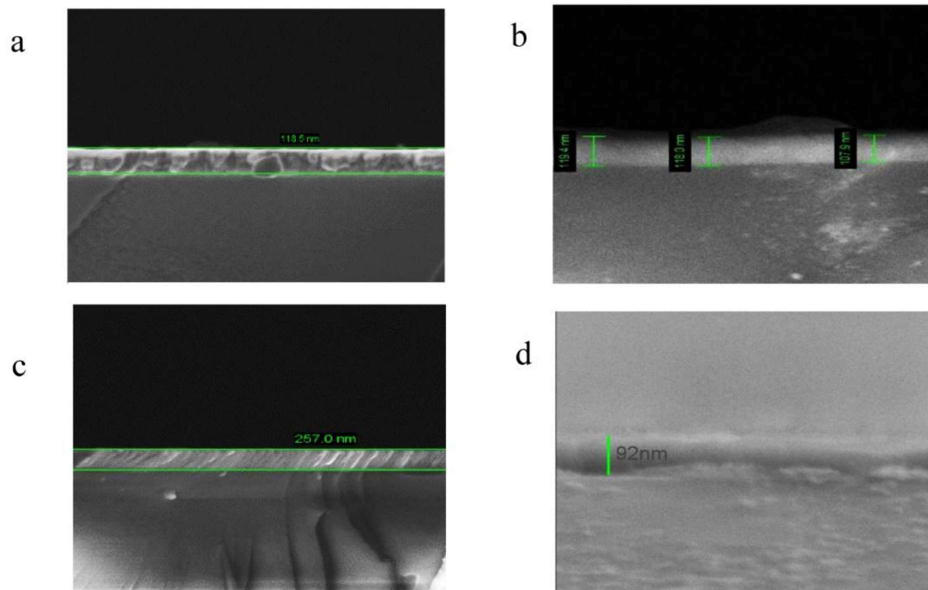

Fig.3.7 Cross-sectional FESEM images of TiN films, a) TIN1 b) TIN2 c) TIN3 and d) TIN4

Fig. 3.6 (a-c) show the field-emission scanning electron micrographs of the TiNx coatings with variable nitrogen partial pressures. As seen in the images, the deposited films are having uniform and crack-free surfaces. The images were taken with a scale of 500nm. The cross-sectional image shows a columnar growth with an oblique angle incident is in the film TIN3, which is having higher nitrogen content. The prediction of grain size variation is not possible since the obtained variation is really small. The cross-section images of the samples are as shown in Fig 3.7. As seen, the thickness of the films varies with respect to the N/Ti ratio. As the N/Ti ratio varies from 0.28 to 0.5 the thickness changes from approximately 120nm to 180nm. Further increase in N/Ti ratio to 0.66 changes the thickness to 250nm.

3.3.2 Atomic force microscopy Analysis

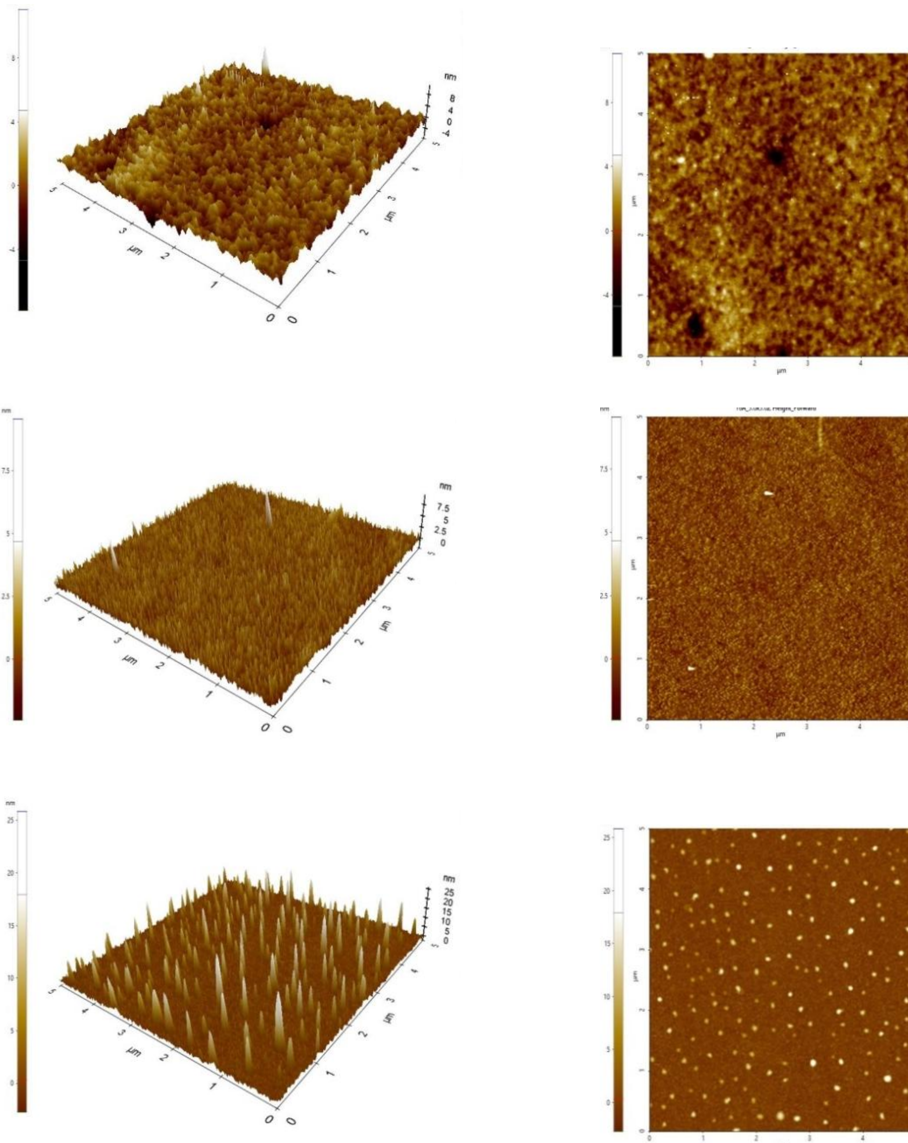

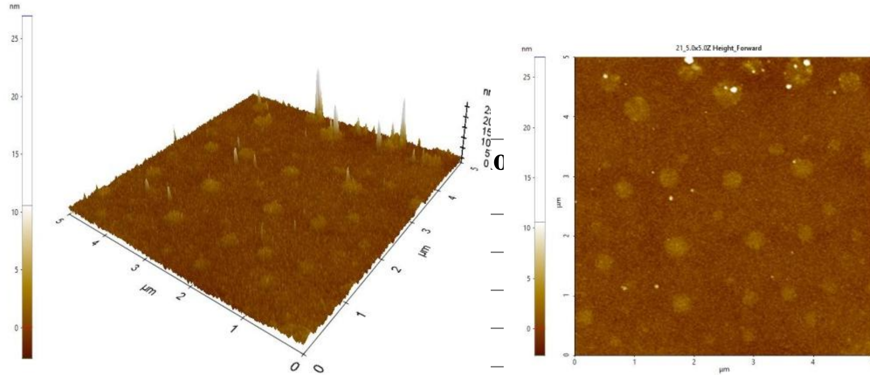

Fig 3.8: 2D and 3D images of titanium nitride films, a) TIN1 b) TIN2 c)TIN3 and d) TIN4

Table 3.4. Variation of RMS roughness with the N/Ti ratio		
Sample name	N/Ti ratio (%)	R in nm (roughness)
TIN1	28	0.81
TIN4	42	0.60
TIN2	50	0.531
TIN3	66	1.031

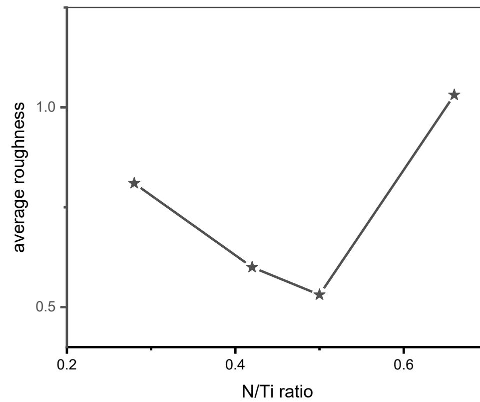

Fig 3.9. Variation of roughness with the N/Ti ratio

Fig 3.8 shows the average RMS surface roughness of the films coated with the different deposition conditions. The roughness values were analysed according to the N/Ti ratio. The values are tabulated in the Table 3.4 and the variation is plotted in Fig. 3.9. The surface roughness of the sample coated with low sputtering power is also included here. The surface topographies of the films deposited at room temperature obtained by scanning over 5μm x 5μm area are shown in Fig.3.8. The surface morphology of the titanium nitride films coated was mostly smooth with bright protrusions on the surface. The number of protrusions is less in the films deposited with lower nitrogen concentration. The height of these peaks reaches 15nm in TIN3 film. [27]. The film TIN3 having more protrusions and higher roughness. The FESEM cross-section image confirms columnar growth of the same. The roughness begins to increase with increasing thickness of the films [28]. The roughness decreases as the sample is stoichiometric.

3.4 ELECTRICAL PROPERTIES IN TIN FILMS

The electrical resistivity of a thin film depends on phase, composition, impurities, grain structure etc. Titanium nitride is well known conducting material whose conduction property mechanism is dependent on the stoichiometry of the films. The electrical properties of TiNx are tunable with respect the structure and composition of the samples. According to Igaski et.al, as nitrogen content increases in the titanium metal, the structure changes from hexagonal close packed to the face centred cubic structure [6]. When the of N/Ti ratio, x=0, pure metallic nature of titanium exist. A small increase in the nitrogen in the titanium film causes distortion in the hcp phase, which means disturbance in the periodicity of the lattice. When $0 < x < 0.5$, the total resistivity is a contribution of (i) the resistivity change caused by nitrogen inclusion (ρ_1), (ii) contribution from the scattering by grain boundaries (ρ_2), and (iii) contribution from the transport phenomena in terms of electronic band structure of titanium sublattice (ρ_3). Another small contribution is expected from amorphous phase of the films, which can be neglected for crystalline materials [6]. When the $x > 0.6$, the structure becomes FCC and vacancies in the nitrogen sublattice will be filled with nitrogen, which in turn creates a decrease in resistivity. The increased nitrogen content decreases the grain boundary and contributes to the conductivity. In addition, there is a shallow donor level in the bandgap of titanium nitride [29]. Hence, both titanium rich and stoichiometric films show conducting behaviour [30].

Table 3.5 depicts the Hall measurement results carried out in van der Pauw technique of the films, varying in the stoichiometry of the sample. The variations of carrier concentration with the N/Ti exhibited a linear trend. Titanium metal is highly conducting with carrier concentration in 10^{23}/cc range. With the introduction, Ti transforms from hexagonal close packed

phase to distorted α-TiN_X where $x < 0.2$. This randomness in the crystal structure contributes to the increased resistivity [31] The nitrogen atom occupies the interstitial sites randomly causes disorder in the structure with respect to x in TiN_x [32].

The transition of N/Ti ratio from 0.28 (TIN1) to 0.66 (TIN4) causes an increase in the roughness revealed by the AFM analysis, and hence the resistivity may increase with the increasing surface roughness [33]. With the N/Ti ratio of the films vary from 28% (TIN1) to 66% (TIN4), and the carrier concentration decrease, as given in Table 3.5. The carrier concentration shows a drastic decrease with 66% nitrogen content. When the N/Ti ratio is 0.28, the films exhibited higher carrier concentration, of the order of 10^{22}/cc, which decreases with further introduction of nitrogen. Both TIN2 and TIN4 have approximately similar composition and in turn resemblance in electrical properties. The oxynitride phase in the TIN2 reduced the carrier concentration in the stoichiometric sample. The mobility shows a lower value for TIN1 and TIN3, and this may be attributed to the increased roughness of the films. The carrier concentration of 10^{22} order is suitable to exhibit plasmonic properties in visible region.

Table 3.5. Summary of Hall measurement results of TiNx films with varying N/Ti ratio

Sample code	**Carrier concentration (cm^{-3})**	**Mobility ($\times 10^{-2}$) (cm^2/Vs)**
TIN1	1.08×10^{22}	1.16
TIN2	1.73×10^{21}	3.24
TIN3	8.07×10^{18}	1.84
TIN4	3.23×10^{21}	2.26

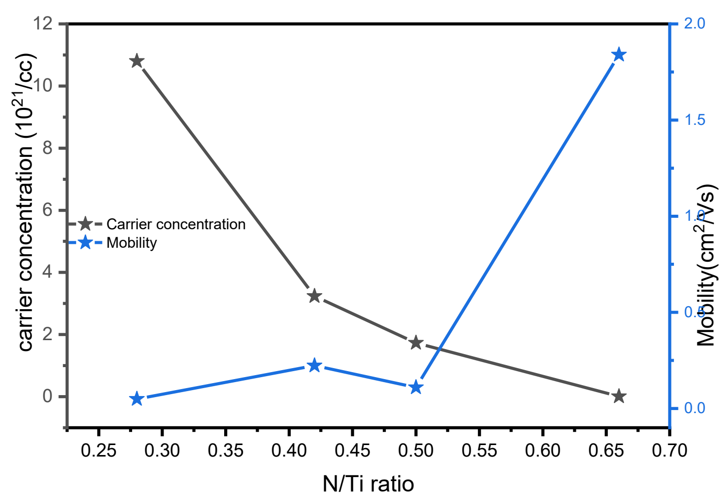

Fig. 3.10. Variation of carrier concentration and mobility in RF sputtered titanium nitride films with respect to nitrogen concentration.

3.5 OPTICAL PROPERTIES

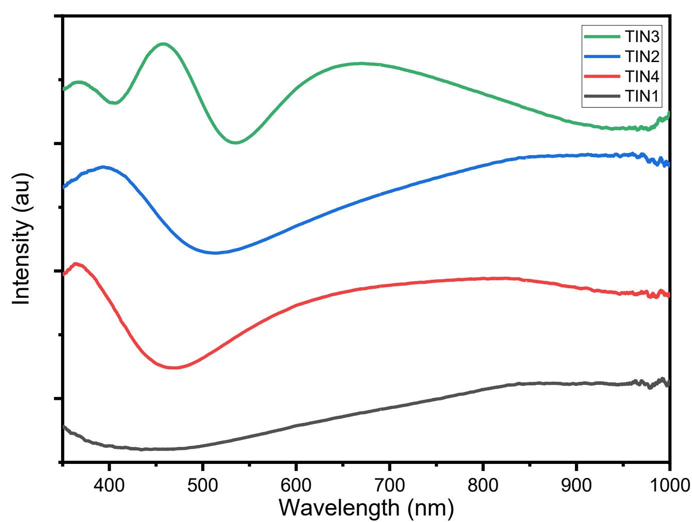

Fig 3.11. Reflectance spectra of the films with various N/Ti ratios

The optical reflectance spectra of the films fabricated with various N/Ti ratios is shown in Fig. 3.11. The reflectance patterns exhibit a resemblance to the appearance of gold [34]. It is evident from the figure that the plasma edge red shifts with increase in the nitrogen content in the sample. The NIR reflecting character arise from the metallic nature of the initial two samples in this wavelength region. This was evident in the results of the electrical analysis of these films.

Drude-Lorentz oscillator model was used for the fitting of the spectra. The Drude term corresponds to the free carriers present in the film and the Lorentz term indicates the bound electrons in a semiconductor nature [35-36]. The complex dielectric function extracted from fitted curve consists of two parts,

$$\varepsilon(\omega) = \varepsilon_1(\omega) + i\,\varepsilon_2(\omega) \quad \ldots\ldots\ldots\ldots\ldots\ldots(3.3)$$

where ε_1 and ε_2 are real and imaginary part of complex dielectric constant. For plasmonic applications, the real part of the dielectric constant should be negative and the imaginary part, corresponds to dielectric loss, should be small for optimum properties. In metals, free electron exists without bound electrons, and the energy position where $\varepsilon_1(\omega)=0$ defines the unscreened plasma energy (ω_{pu}). With bound electron or interband transition, it contributes to the red shift in the same point, which is called screened plasma energy ω_{ps} [37-38].

$$\omega_p = \sqrt{\frac{Ne^2}{\varepsilon_0 m^*}} \ldots\ldots\ldots\ldots\ldots\ldots\ldots\ldots\ldots\ldots.(3.4)$$

where N is the charge carrier density, e is the charge of electron, ε_0 is the permittivity of free space, and m^* is the effective mass of electron. Each

reflectance curve of the titanium nitride fitted with one Drude term and two Lorentz oscillators, as suggested by Patsalas et al [38]. The 2-Lorentz oscillator model were constrained to the energy range 1.5 - 5 eV due to their poor fit to the experimental data at energies below 1.5 eV. Here, we opted the D2L model, since the region of interest is 1.5 - 2.7 eV (visible range). The curve fitting has been done using a standard software (RefFit) [39]. The dielectric constant is expressed as,

$$\varepsilon = \varepsilon_{\infty} - \frac{\omega_p^2}{\omega^2 - i\Gamma_D\omega} + \sum_{j=1}^{2} \frac{f_j\omega_{oj}^2}{\omega_{0j}^2 - \omega^2 + i\gamma_j\omega} \ldots\ldots\ldots (3.5)$$

where ε_{∞} is high frequency dielectric constant, here a constant or greater than unity, Γ_D is the drude damping factor and ω_{0j} is the Lorentz oscillator with damping factor γ_j. $\Gamma = \frac{e}{\mu m^*}$ is the loss related Drude relaxation rate, or called momentum scattering rate, which is inversely related to the effective mass and mobility of carriers [40]. The Drude term dominates at lower energy in the region of intraband absorption by free electrons and accounts for the metallic behaviour and corresponding energy is the unscreened plasma energy [38].

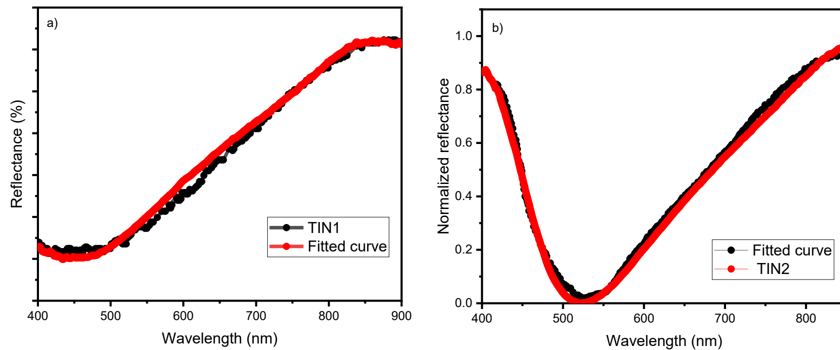

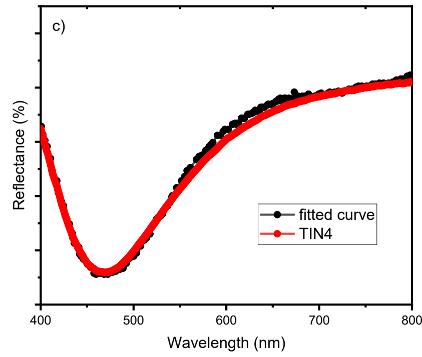

Fig. 3.12. Reflectance spectra with fitted curves a) for TIN1, TIN2 and TIN4, respectively

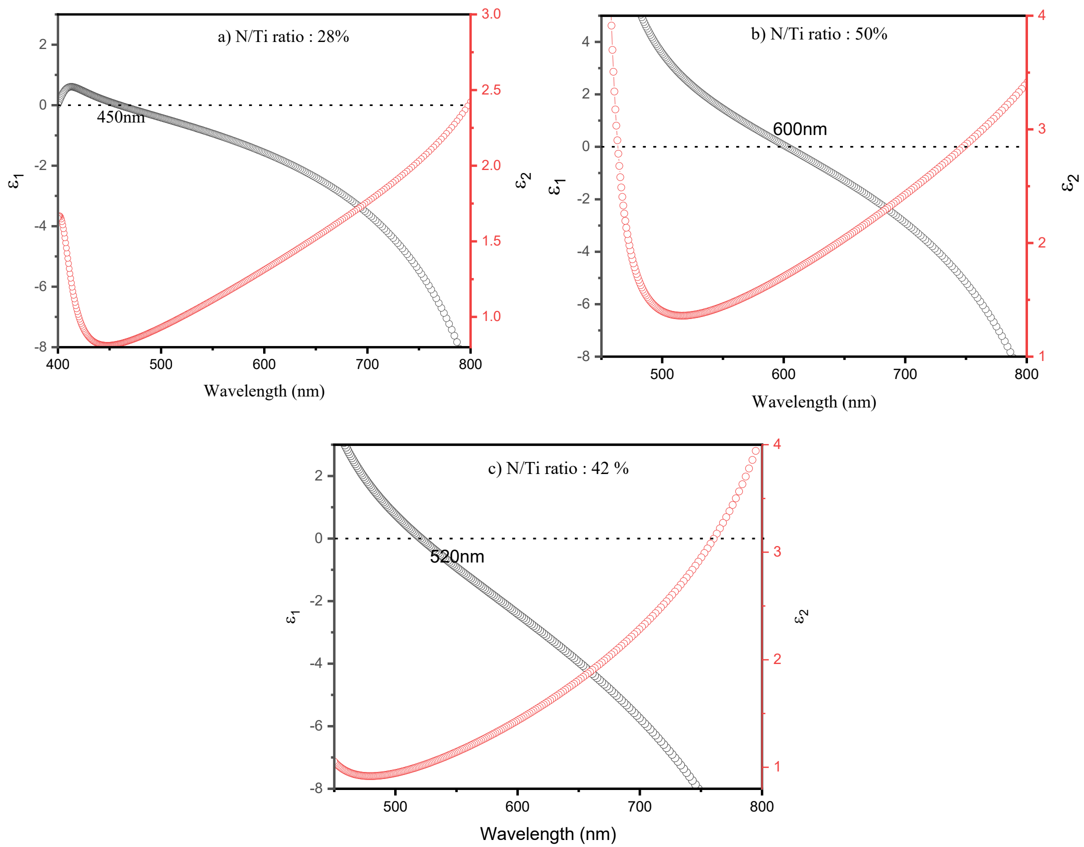

Fig 3.13 Extracted real and the imaginary parts of the dielectric function of (a) TIN1, (b) TIN2 and (c) TIN4

The reflectance patterns fitted with Drude-Lorentz approximation are shown in Fig.3.12 and the used parameters are tabulated in Table 3.6.

Table 3.6 Summary of fitting parameters used for extracting permittivity values from the reflectance spectra

Sample name	**ε_∞[39]**	**ω_p (eV)**	**ω_{0j} (eV)**	γ_j
TIN1	3	3.4405		1.997
		0.7419	3.100	0.1723
		2.3228	1.3735	0.0068
TIN2	3	4.463		0.0264
		2.5657	2.7941	0.1026
		1.1337	1.9188	0.6105
TIN4	2	4.1798		0.4489
		2.2062	1.5989	1.1082
		2.4823	2.9899	0.4999

The sample TIN3 has been excluded from the optical analysis, since it possesses lower carrier concentration. Tunable negative permittivity of titanium nitride powder in the radio frequency regime has been reported by Fan et al in 2017 [41]. Here, the focus was on the tunable negative permittivity nature of titanium nitride thin films with respect to carrier concentration in the UV-visible region. As seen in the curves in the Fig 3.13, the films exhibit negative real permittivity, which is essentially for the plasmonic behaviour in any material. The negative permittivity value is found to increase with increase in increase in carrier concentration. As seen, the negative real permittivity changes from 0 to -2 for the film TIN1 in the wavelength range 450 - 600nm. The variations in the crossover wavelength,

the wavelength at which the real part of permittivity changes to negative value, of the samples estimated are given in Table 3.7. The cross-over wavelength is found to shift from 450 nm to 520, and then to 600nm, when the N/Ti ratio is varied from 28 to 50%. This is in accordance with the carrier concentration, which agrees with earlier reports, where the composition or N/Ti ratio was 28%. Fan et al investigated the relation between carrier concentration and negative permittivity value and predicted that composition variation in $TiN/BaTiO_3$ is responsible for this dependence [42]. Similar variation in negative permittivity with respect to carrier concentration is reported for indium tin oxide ceramics in the MHz-KHz frequency region [43].

In addition, the dielectric loss associated with the wavelength range 500-700nm is very low ($\varepsilon_2 < 1.8$) for the film TIN2compared to all other samples. The increase in nitrogen content from 28% to 50% shifted the crossover wavelength from 450nm to 600nm, also resulted in reduced dielectric loss. While fabricating a multilayer film stack of metal and dielectric for TO devices, it is necessary for the magnitude of ε_1 to be relatively small and comparable to the value of ε_2 for the best performance. This is to achieve a balanced polarization response from both the dielectric and metal components [44].

Table 3.7 Summary of the results obtained from the reflectance spectra

Sample Code	**N/Ti ratio**	**Crossover wavelength (nm)**	**Real part (ε_1) of dielectric constant *(450-600nm)***	**Imaginary part (ε_2) of dielectric constant *(450-600nm)***
TIN1	28	450	0 to -2	0.8 to 1.3
TIN4	42	520	2 to -2.26	1.0 to 1.4
TiN2	50	600	4 to -0.04	1.3 to 1.7

3.6 EXCITATION OF SURFACE PLASMONS IN TiN FILMS

Prism geometry configuration is generally employed in angular interrogation mode to excite surface plasmons in plasmonic planar films. When TM polarised light is incident on a right-angled prism at an angle greater than the critical angle, it gets totally internally reflected from the surface of glass substrate coated with the plasmonic film placed on the base of the prism, and generates an evanescent field that propagates parallel to the interface and decays exponentially away from the interface. The evanescent field at the interface can achieve resonance condition when the two wave vectors, of the evanescent wave and surface plasmons, are same. The resonance condition for the excitation of the SPs at the film-dielectric (sensing medium) interface, can be written as:

$$\theta = \sin^{-1}\left[\frac{1}{n_p}\left(\frac{\varepsilon_m \varepsilon_d}{\varepsilon_m + \varepsilon_d}\right)^{\frac{1}{2}}\right] \qquad (3.6)$$

where n_p is the refractive index of prism (1.5) used, ε_m and ε_d are the permittivity values corresponding to the material of interest and the dielectric.

In this study, the surface plasmon resonance was generated by the Winspall program using a three-layer model in prism geometry, with the assumption that the thickness of the prism and dielectric medium were zero [45]. The reflectance of this model is given by

$$R_{123} = \frac{r_{12} + r_{23} e^{2ikz_2 d_2}}{1 + r_{p2} + r_{23} e^{2ikz_2 d_2}} \qquad (3.7)$$

where 1, 2, and 3 denote prism, film, and air, respectively. d_2 is the thickness of the film, and k_{z2} is the wave-vector in the film.

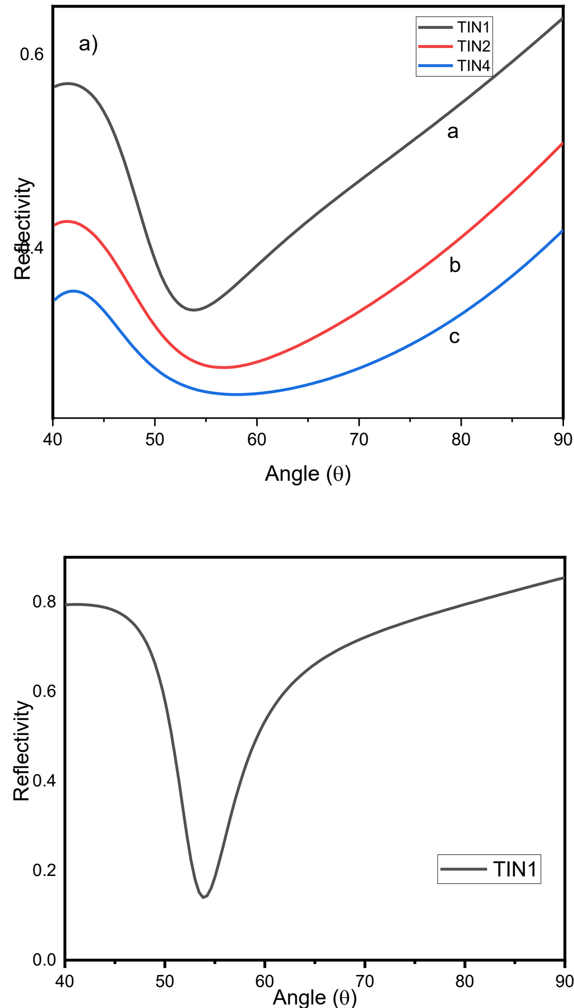

Fig 3.14 (Top) Simulated SPR curves for the samples a)TIN1 and b)TIN2 and c)TIN4, and (bottom) improved SPR curve with reduced loss in TIN1

Fig 3.14 shows the simulated SPR curves for the samples TIN1 TIN2 and TIN4. The permittivity values obtained from the reflectance patterns at the wavelength of 700nm were used for obtaining SPR curves. The SPR curves for the sample TIN1, TIN2 and TIN4 show a resonance dip position approximately at 53 °, 56.4° and 56.7° respectively. The Full Width at Half

Maximum (FWHM) of the SPR corresponding to the sample TIN1 is around 20°, while broad curves were obtained for the samples TIN2 and TIN4. The real and imaginary parts of the pseudo-dielectric permittivity can be directly employed to assess the plasmonic properties of the TiN thin films by means of a quality factor [44]

$$Q_{SPP} = \frac{\varepsilon_1^2}{\varepsilon_2} \quad \text{.............................. (3.8)}$$

The values obtained for Q_{spp} for the films TiN1 and TiN2 were found to vary from 7.8 to 3.34, respectively at a wavelength of 700 nm, while it is 2.81 for TIN4. This phenomenon is mainly associated with the real component of the permittivity, whereas the imaginary component of it plays a secondary role. The real permittivity exhibits better plasmonic properties when it has a greater negative value, as supported by the findings of Mascaretti et al [4]. The increasing ratio of N/Ti reduced the carrier concentration and the negative real part of permittivity in the films. As a result, the quality factor of the film TiN2 is increased. ε_2 shows decreasing nature with increase in nitrogen content. The variations in RF power and gas composition affect optical properties of the deposited titanium nitride. In these studies, the FWHM of these film samples exhibit higher values. Fig 3.14b shows the improved SPR curve when the dielectric loss is further reduced to 0.5. The impact of enhanced electrical mobility on the imaginary part of the permittivity of the sample was investigated by Khamh et al [46]. By enhancing mobility of the samples, there would be an improvement in the quality factor for surface plasmon polaritons in the films and also in the full width at half maximum of the surface plasmon resonance curves.

3.7 CONCLUSION

Titanium nitride thin films with high carrier concentration of the order of 10^{22}/cm and negative permittivity of 2 to 6 in the wavelength region from 600 to 800 nm were fabricated by RF sputtering, through the modification of the N/Ti ratio in the films. The structural analysis revealed changes in the preferred orientation and the XPS analysis showed a variation of the nitrogen content from 28% to 66% in the deposited films. The permittivity extracted from the reflectance spectra using Drude-Lorentz approximation confirmed negative real permittivity in order to exhibit the plasmonic properties in the visible wavelengths. These films also possess low loss of the order of 0.5 to 2 in the wavelength region from 500nm to 700nm. The cross-over wavelength showed a redshift with increase in nitrogen concentration in the films. The SPR curve simulated for the film with higher carrier concentration showed better plasmonic property. It has been shown that the FWHM of simulated curve improves with decreasing dielectric loss.

3.8 REFERENCES

1. Gu, P., Zhu, X., Li, J., Wu, H., & Yang, D. (2018). Influence of substrate and Ar/N 2 gas flow ratio on structural, optical and electrical properties of TiN thin films synthetized by DC magnetron sputtering. *Journal of Materials Science: Materials in Electronics*, *29*, 9893-9900. DOI: 9893-9900, 10.1007/s10854-018-9031-2.

2. Gadalla, M. N., Greenspon, A. S., Tamagnone, M., Capasso, F., & Hu, E. L. (2019). Excitation of strong localized surface plasmon resonances in highly metallic titanium nitride nano-antennas for stable performance at elevated temperatures. *ACS Applied Nano Materials*, *2*(6), 3444-3452.DOI: 10.1021/acsanm.9b00370

3. Catellani, A., D'Amico, P., & Calzolari, A. (2020). Tailoring the plasmonic properties of metals: The case of substoichiometric titanium nitride. *Physical Review Materials*, *4*(1), 015201.DOI: 10.1103/PhysRevMaterials.4.015201

4. Mascaretti, L., Barman, T., Bricchi, B. R., Münz, F., Bassi, A. L., Kment, Š., & Naldoni, A. (2021). Controlling the plasmonic properties of titanium nitride thin films by radiofrequency substrate biasing in magnetron sputtering. *Applied Surface Science*, *554*, 149543. DOI:10.1016/j.apsusc.2021.149543.

5. Holmberg, B. O., Yhland, M., & Dahlbom, R. (1962). Structural studies on the titanium-nitrogen system. *Acta Chem. Scand*, *16*(5), 1255-61. DOI : 10.3891/acta.chem.scand.16-1255

6. Igasaki, Y., Mitsuhashi, H., Azuma, K., & Muto, T. (1978). Structure and electrical properties of titanium nitride films. *Japanese Journal of Applied Physics*, *17*(1), 85.DOI:10.1143/JJAP.17.85

7. Ma, D., Deng, Q., Liu, H., & Leng, Y. (2021). Effect of ion energy on the microstructure and properties of titanium nitride thin films deposited by high power pulsed magnetron sputtering. *Coatings*, *11*(5), 579. DOI:10.3390/coatings11050579

8. Penilla, E., & Wang, J. (2008). Pressure and Temperature Effects on Stoichiometry and Microstructure of Nitrogen-Rich TiN Thin Films Synthesized via Reactive Magnetron DC-Sputtering. *Journal of Nanomaterials*, *2008*(1), 267161.

9. Jeyachandran, Y. L., Narayandass, S. K., Mangalaraj, D., Areva, S., & Mielczarski, J. A. (2007). Properties of titanium nitride films prepared by direct current magnetron sputtering. *Materials Science and Engineering: A*, *445*, 223-236. DOI:10.1016/j.msea.2006.09.021.

10. Meng, L. J., & Dos Santos, M. P. (1997). Characterization of titanium nitride films prepared by dc reactive magnetron sputtering at different nitrogen pressures. *Surface and Coatings Technology*, *90*(1-2), 64-70. DOI:10.1016/S0257-8972(96)03094-0

11. Patterson, A. L. (1939). The Scherrer formula for X-ray particle size determination. *Physical review*, *56*(10), 978., DOI: 10.1103/ Phys Rev.56.978.

12. Khojier, K., Savaloni, H., Shokrai, E., Dehghani, Z., & Dehnavi, N. Z. (2013). Influence of argon gas flow on mechanical and electrical properties of sputtered titanium nitride thin films. *Journal of Theoretical and Applied Physics*, *7*, 1-6. DOI:10.1186/2251-7235-7-37

13. Scofield, J. H. (1976). Hartree-Slater subshell photoionization cross-sections at 1254 and 1487 eV. *Journal of electron spectroscopy and related phenomena*, *8*(2), 129-137. DOI:10.1016/0368-2048(76)80015-1

14. Jaeger, D., & Patscheider, J. (2012). A complete and self-consistent evaluation of XPS spectra of TiN. *Journal of Electron Spectroscopy and Related Phenomena*, *185*(11), 523-534. DOI:10.1016/j.elspec.2012.10.011

15. Tougaard, S. (1997). Universality classes of inelastic electron scattering cross-sections. *Surface and Interface Analysis: An International Journal devoted to the development and application of techniques for the analysis of surfaces, interfaces and thin films*, *25*(3), 137-154.

16. Schmid, M., Steinrück, H. P., & Gottfried, J. M. (2014). A new asymmetric Pseudo-Voigt function for more efficient fitting of XPS lines. *Surface and Interface Analysis*, *46*(8), 505-511.DOI: 10.1002/sia.5847

17. Wagner, C. D. (1983). Sensitivity factors for XPS analysis of surface atoms. *Journal of electron spectroscopy and related phenomena*, *32*(2), 99-102. DOI:10.1016/0368-2048(83)85087-7

18. Trenczek-Zajac, M. Radecka, K. Zakrzewska, A. Brudnik, E. Kusior, S. Bourgeois, M.C. Marco de Lucas, L. Imhoff, (2009). Structural and electrical properties of magnetron sputtered Ti (ON) thin films: the case of TiN doped in situ with oxygen. *Journal of Power Sources*, *194*(1), 93-103.

19. Du, L., Edgar, J. H., Kenik, E. A., & Meyer, H. (2010). Sublimation growth of titanium nitride crystals. *Journal of Materials Science: Materials in Electronics*, *21*, 78-87. DOI:10.1007/s10854-009-9873-8.

20. Spengler, W., & Kaiser, R. (1976). First and second order Raman scattering in transition metal compounds. *Solid State Communications*, *18*(7), 881-884. DOI: 10.1016/0038-1098(76)90228-3.

21. Stoehr, M., Shin, C. S., Petrov, I., & Greene, J. E. (2011). Raman scattering from TiNx (0.67≤ x≤ 1.00) single crystals grown on MgO (001). *Journal of Applied Physics*, *110*(8). DOI:10.1063/1.3651381.

22. Logothetidis, S., Meletis, E. I., & Kourouklis, G. (1999). New approach in the monitoring and characterization of titanium nitride thin films. *Journal of materials research*, *14*(2), 436-441. DOI:10.1557/JMR.1999.0062

23. Chowdhury, R., Vispute, R. D., Jagannadham, K., & Narayan, J. (1996). Characteristics of titanium nitride films grown by pulsed laser deposition. *Journal of materials research*, *11*(6), 1458-1469, DOI:10.1557/JMR.1996.0182

24. Reshchikov, M. A. (2022). Point defects in GaN. In *Semiconductors and Semimetals* (Vol. 111, pp. 153-205). Elsevier. DOI:10.1016/ bs.semsem. 2022.08.002

25. Sivadasan, A. K., Patsha, A., & Dhara, S. (2015). Optically confined polarized resonance Raman studies in identifying crystalline orientation of sub-diffraction limited AlGaN nanostructure. *Applied Physics Letters*, *106*(17). DOI:10.1063/1.4919535

26. Solovan, M. N., Brus, V. V., Maistruk, E. V., & Maryanchuk, P. D. (2014). Electrical and optical properties of TiN thin films. *Inorganic materials*, *50*, 40-45.. DOI:10.1134/S0020168514010178

27. Maarouf, M., Haider, M. B., Drmosh, Q. A., & Mekki, M. B. (2021). X-ray photoelectron spectroscopy depth profiling of as-grown and annealed titanium nitride thin films. *Crystals*, *11*(3), 239. DOI:10.3390/cryst11030239

28. Liang, H., Xu, J., Zhou, D., Sun, X., Chu, S., & Bai, Y. (2016). Thickness dependent microstructural and electrical properties of TiN thin films prepared by DC reactive magnetron sputtering. *Ceramics International*, *42*(2), 2642-2647. DOI:10.1016/j.ceramint.2015.10.070

29. Kim, Jekyung & Bauers, Sage & Khan, Imran & Perkins, John & Park, Bo-In & Talley, Kevin & Kim, Daehan & Zakutayev, Andriy & Shin, Byungha (2020). Influence of hydrogen and oxygen on the structure and properties of sputtered magnesium zirconium oxynitride thin films. *Journal of Materials Chemistry A*, *8*(18), 9364-9372.DOI: 10.1039/D0TA00654H.

30. Eibler, R. (1998). Energetics of titanium nitrides of composition. *Journal of Physics: Condensed Matter*, *10*(45), 10223.DOI: 10.1088/0953-8984/10/ 45/010

31. Wriedt, H. A., & Murray, J. L. (1987). The N-Ti (nitrogen-titanium) system. *Bulletin of Alloy Phase Diagrams*, *8*, 378-388.DOI:10.1007/BF02869274A.

32. Mitsuhashi, H., Igasaki, Y., & Kaneko, M. (1978). Properties of titanium solid solutions prepared by reactive sputtering. *Journal of Crystal Growth*, *45*, 350-354. DOI:10.1016/0022-0248(78)90462-1.

33. Tang, W., Chao, Y., Weng, X., Deng, L., & Xu, K. (2012). Optical property and the relationship between resistivity and surface roughness of indium tin oxide thin films. *Physics Procedia*, *32*, 680-686. DOI:10.1016/j.phpro.2012.03.618.

34. Guo, W. P., Mishra, R., Cheng, C. W., Wu, B. H., Chen, L. J., Lin, M. T., & Gwo, S. (2019). Titanium nitride epitaxial films as a plasmonic material platform: alternative to gold. *ACS Photonics*, *6*(8), 1848-1854. DOI:10.1021/acsphotonics.9b00617.

35. Wooten, F. (1972). *Optical properties of solids*. Academic Press..

36. Ashcroft, N. W. (1976). N. David Mermin Solid State Physics..

37. Wang, Z., Chong, H., Yang, J., & Ye, H. (2019). Study on epsilon crossover wavelength tuning of heavily doped germanium-on-silicon in mid-infrared range. *Optics Express*, *27*(23), 33724-33736. DOI:10.1364/OE.27.033724

38. Patsalas, P., & Logothetidis, S. (2001). Optical, electronic, and transport properties of nanocrystalline titanium nitride thin films. *Journal of Applied Physics*, *90*(9), 4725-4734. DOI:10.1063/1.1403677.

39. Kuzmenko, A. B. (2005). Kramers–Kronig constrained variational analysis of optical spectra. *Review of scientific instruments*, *76*(8). DOI:10.1063/1.1979470.

40. Patsalas, P., Kalfagiannis, N., & Kassavetis, S. (2015). Optical properties and plasmonic performance of titanium nitride. *Materials*, *8*(6), 3128-3154. DOI:10.3390/ma8063128

41. Fan, G., Xie, P., Wang, Z., Qu, Y., Zhang, Z., Liu, Y., & Fan, R. (2017). Tailorable radio-frequency negative permittivity of titanium nitride sintered with different oxidation pretreatments. *Ceramics International*, *43*(18), 16980-16985.. DOI: 10.1016/j.ceramint.2017.09.105.

42. Fan, G., Zhang, X., Wang, Q., Su, R., Tang, Y., Hao, C., & Liu, Y. (2023). Dielectric evolution of permittivity transition from positive to negative induced by percolation in ceramic composites. *Ceramics International*, *49*(22), 35518-35523.DOI: 10.1016/j.ceramint.2023.08.230

43. Fan, G., Wang, Z., Sun, K., Liu, Y., & Fan, R. (2021). Doped ceramics of indium oxides for negative permittivity materials in MHz-kHz frequency regions. *Journal of Materials Science & Technology*, *61*, 125-131. DOI :10.1016/j.jmst.2020.06.013

44. West, P. R., Ishii, S., Naik, G. V., Emani, N. K., Shalaev, V. M., & Boltasseva, A. (2010). Searching for better plasmonic materials. *Laser & photonics reviews*, *4*(6), 795-808. DOI: 10.1002/lpor.200900055.

45. Zhang, R., Pu, S., & Li, X. (2019). Gold-film-thickness dependent SPR refractive index and temperature sensing with hetero-core optical fiber structure. *Sensors*, *19*(19), 4345. DOI:10.3390/s19194345.

46. Khamh, H., Sachet, E., Kelly, K., Maria, J. P., & Franzen, S. (2018). As good as gold and better: conducting metal oxide materials for mid-infrared plasmonic applications. *Journal of Materials Chemistry C*, *6*(31), 8326-8342. DOI: 10.1039/C7TC05760A.

CHAPTER 4

INVESTIGATION OF PLASMONIC PROPERTIES IN TiN_x THIN FILMS DERIVED FROM NITRIDATION OF TITANIUM METAL FILMS.

Introduction

In this chapter, a novel approach for the fabrication of titanium nitride thin films for plasmonic applications is described. The whole objective of this work was to enhance the opto-electrical properties suitable for plasmonic behaviour in TiN films in the visible region with low loss. Being non-stoichiometric in nature, the fabrication methods can influence the material properties of titanium nitride films. In the previous chapter, nitrogen gas served as source of nitrogen in the sputtering process for the development of TiN_x thin films from the Ti metal target.

In this work, the nascent nitrogen evolved from the disassociation of ammonia at high temperature was used as nitrogen source for nitridating Ti metal film. As already pointed out, in order to exhibit surface plasmon resonance properties in visible region, the thin film should possess important properties, such as, high carrier concentration of the order of 10^{22}/cc, low dielectric loss and negative permittivity in the wavelength region. These properties can be achieved by tuning the stoichiometry in titanium nitride films. The nitridation process discussed in this chapter provides a better platform for tuning titanium and nitrogen compositions in TiN, which consequently accomplished better plasmonic behaviour in the visible wavelength region. Titanium metal film coated on to glass substrates by RF sputtering served as titanium source. By varying both thickness of the films and the nitridation temperature, the stoichiometry in the nitridated thin films was tuned, in order to optimise the plasmonic properties. Further investigations were carried out to evaluate the plasmonic performance of the nitridated films. The efforts produced films with optimum electrical properties and required cross-over wavelength for the successful excitation of surface plasmons in the visible region using Kretchsmann type prism

geometry in wavelength interrogation mode. The schematic representation of the overall process is shown in Fig. 4.1. Titanium metal films fabricated by RF sputtering shown with metallic grey appearance (Fig 4.1a) was subjected to ammonia gas nitridation (Fig 4.1b). The nitridated titanium nitride films having golden colour is shown in Fig 4.1c. The prism geometry used for SPR excitation in wavelength interrogation mode is seen in Fig 4.1d.

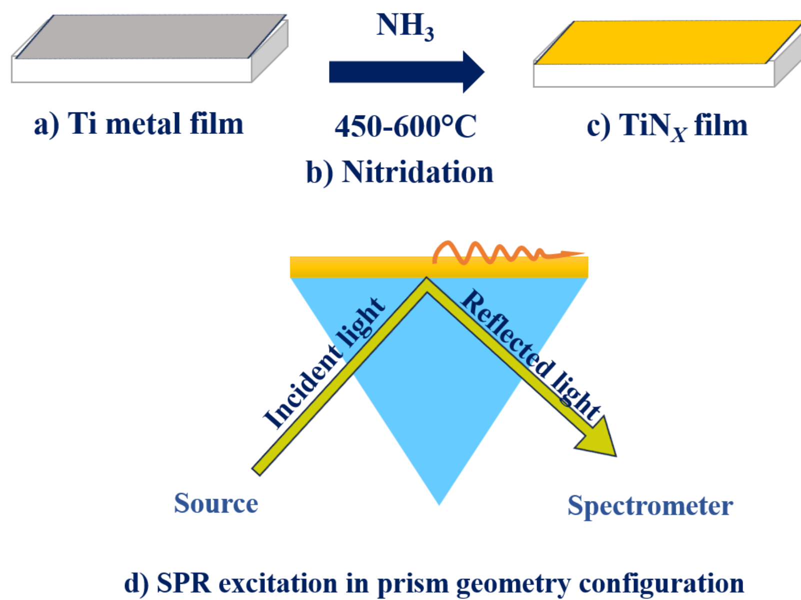

Fig.4.1 Schematic representation of the whole process a) RF sputtered titanium metal film b) process of nitridation, c) titanium nitride film after nitridation, and d) SPR excitation in Kretschmann configuration

4.1 DEVELOPMENT OF TiN FILMS

Fig. 4.2 Deposition conditions of titanium metal films

4.1.1 Film preparation

Titanium metal films were RF magnetron sputtered on to 3’’×1’’glass substrates using a titanium metal target (2 inch diameter (99.99%) in Ar (99.99%) atmosphere. Prior to coating, the glass substrates were cleaned ultrasonically in succession with soap water, distilled water, acetone and isopropyl alcohol, and finally dried in nitrogen flow. The RF power and substrate rotation for metal coating were optimized to 120W and 10rpm, respectively. The sputter chamber was initially pumped down to a base pressure of 5×10^{-6} mbar and argon gas (4N purity) was then introduced to maintain the working pressure at 6×10^{-3} mbar. The glass substrates were pre-sputtered for 5 minutes. The films were coated at various thicknesses in the range 50-150nm. The film thickness was estimated from FESEM cross-section measurements, and the details are explained in the section 4.3.1 of this chapter.

4.1.2 Nitridation conditions

Titanium metal films are prone to oxidation and hence in order to avoid oxidation, the coated metal samples were directly taken to nitridation furnace after sputtering. Titanium metal films were heat-treated in continuous flow of ammonia gas (99.5% purity) inside a tubular furnace for converting to titanium nitride. The furnace was initially purged with nitrogen (99.99%) for 15 minutes to remove the air inside the quartz tube. The furnace was then heated to 150°C in nitrogen flow, and thereafter switched to the ammonia gas flow and maintained for nitridation temperatures in the range from 450°C to 600°C in 50°C steps. The furnace was then allowed to cool to room temperature in nitrogen flow. In all the nitridations, the ammonia gas was flown for 45 min. at the selected nitridation temperatures. The film samples were directly transferred from the vacuum chamber to annealing furnace after coating in order to avoid surface oxidation of the samples.

In this study, the investigation was on the variations in the film properties of titanium metal coated with thickness of 100±5nm at various nitridation temperatures. These samples were named according to their nitridation temperatures, as TIN 145 (at 450°C), TIN 150 (at 500°C), TIN 155 (at 550°C) and TIN 160 (at 600°C). In addition, Ti films with thickness 50±5nm and 150±10nm were also fabricated and nitridated at 450°C (TIN 045) and 550°C (TIN 255) respectively, for plasmonic property analysis, based on the carrier concentration analysis.

4.2 STRUCTURAL ANALYSIS

4.2.*1 G1-XRD studies*

The x-ray diffraction patterns of the nitridated films are shown in Fig.2. The patters of titanium metal layers deposited initially are not included since they possessed amorphous crystal structure. The figures illustrate the alterations observed in the crystal structure when the temperature of nitridation is progressively elevated from 450°C to 600°C. The recorded patterns were matched to the cubic symmetry of titanium nitride with aid of the ICDD powder diffraction file 00-038-1420. The XRD pattern of these samples consists of three distinct peaks at angles of 36.5°, 42.6°, and corresponding to the crystallographic planes (111), and (200) of the TiN phase, respectively. In general, for titanium nitride films prepared by sputtering process, the evolution of crystal texture arises from the interplay between surface diffusion and ion bombardment, which is controlled by the deposition conditions. Qi et al reported preferred orientation along (200) plane with increase in nitrogen concentration for their sputtered films [1]. Srikrishna et al showed an increase in the nitrogen content in titanium metal as the nitridation temperature is increased [2]. Hence, the (200) preferred orientation in this study may be due to the increase in nitrogen concentration during the transition from titanium metal to titanium nitride.

As seen in Fig.4.3, an increase in the intensity of the (200) plane is observed in the films, when the nitridation temperature was raised from 450°C to 600°C. The increase in temperature may be a contributing factor for the generation of a greater amount of nascent nitrogen, resulting in the preferred crystallographic orientation towards the (200) plane. Chang et al. have documented that TiN films with preferred orientation of (200) exhibit superior plasmonic properties compared to the films oriented along (111)

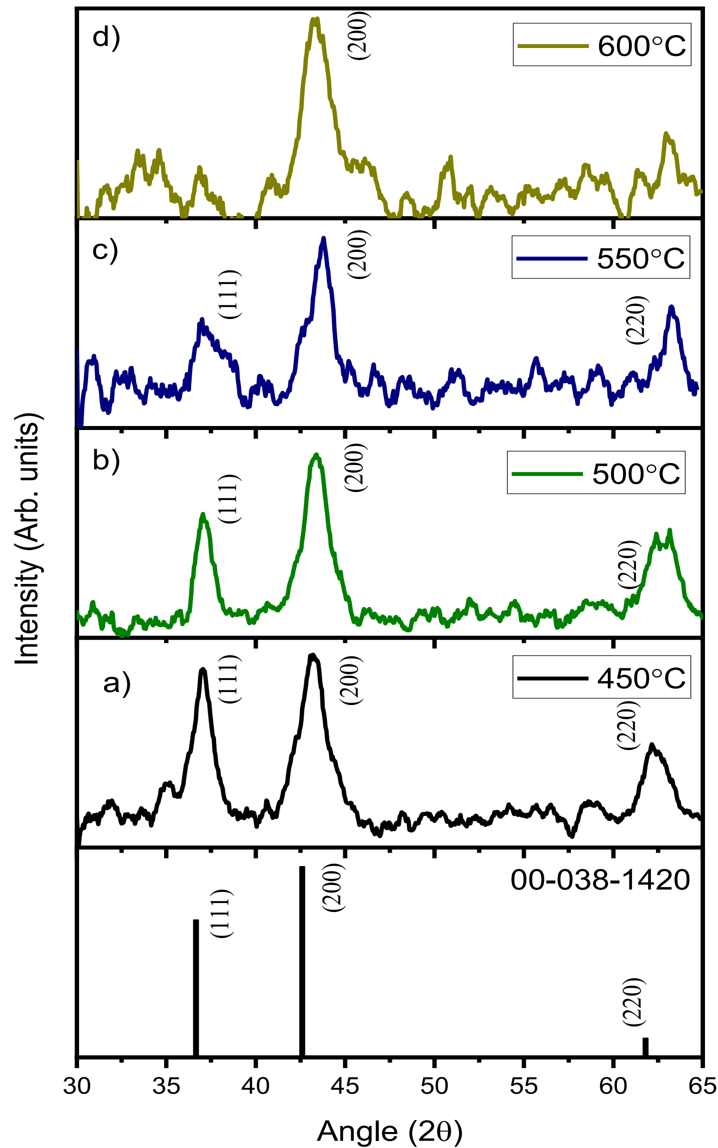

Fig. 4.3. GI-XRD pattern obtained for titanium metal films after nitridation a) TIN145, b) TIN150, c) TIN155 and d) TIN160

[3]. Yangsheng et al also reported a orientation change from (111) to (200) with respect to temperature [4]. As seen in the Fig.4.3, the full width at half maximum (FWHM) of the films seem to be broader compared to those in

the recent reports. It may be due the substrate dependency on the film growth. Guo et al reported FWHM of 0.22° for their MBE grown TiN thin films coated on sapphire substrates [5]. Amorphous nature of soda lime glass substrate may deteriorate the crystalline properties of thin films coated on it. The substrate dependency of the growth of TiN films were reported by Chang et al [3].

4.2.*2 XPS studies*

All of the samples were obtained with the charge neutralization gun activated, and if necessary, the XPS spectra were compared to the adventitious carbon's C1s line at 284.6 eV [6]. The obtained XPS data for Titanium 2p core level and Nitrogen 1s core level for the nitridated metal films with average thickness of 100nm at different temperatures are as shown in the Fig. 2 (a-f). Using the Gaussian-Lorentzian (GL) function in XPSPEAK4.1 software, the peaks of the XPS data were deconvoluted. Here a Tougaard back ground correction for Titanium core level and Shirley background correction for nitrogen core level is used as reported by Saha et al [7].

As seen in the Fig.4.4, the Ti $2p_{3/2}$ and the Ti $2p_{1/2}$ peaks are located at 458eV and 463eV, rather than at 455.6 and 461.2eV, respectively. Saha et al reported native oxide layer formation in the TiN sample, and this altered the BE of Ti 2p levels from 455.6eV to 458.2eV [7]. The observed binding energies of Ti 2p doublets on the TiN film were lower than the corresponding values for the crystalline TiO_2 layer (458.8-459.1 eV), but agree well with literature values for amorphous TiO_2 (458.2 eV) [8]. Ti 2p3/2 is claimed to be in the range 454.6–455.6 eV on nearly stoichiometric TiNx, (x =1), and the peak between 458.2 and 458.9 eV is clearly identified as Ti^{4+} in a TiO_2 environment [9]. Jeyachandran et al also observed the

presence of 3 phases; nitride (TiN), oxynitride (TiO_xN_y) and oxide (TiO_2) phases on the surface of the DC sputtered titanium nitride films and shifted Ti $2p_{3/2}$ peak due to these components [10]. In this case, the sputter cleaning prior to XPS analysis shifted the Ti $2p_{3/2}$ to 455.6eV. Jiang et al investigated the variation in the XPS peak shape of TiN films before and after etching of the films, and identified a shift in the binding energy of Ti 2p peaks and also a reduction in the FWHM of N 1s peak with increased intensity [11]. The shifting in this work was interpreted as due to the removal of surface oxidation. Hence, it is important to note the presence of oxygen impurities [12] to comprehensively understand the connection between the structural characteristics of the films and their corresponding plasmonic response. The XPS is a surface sensitive technique where there is chance of detection of surface oxidation of the titanium content when exposed to atmosphere.

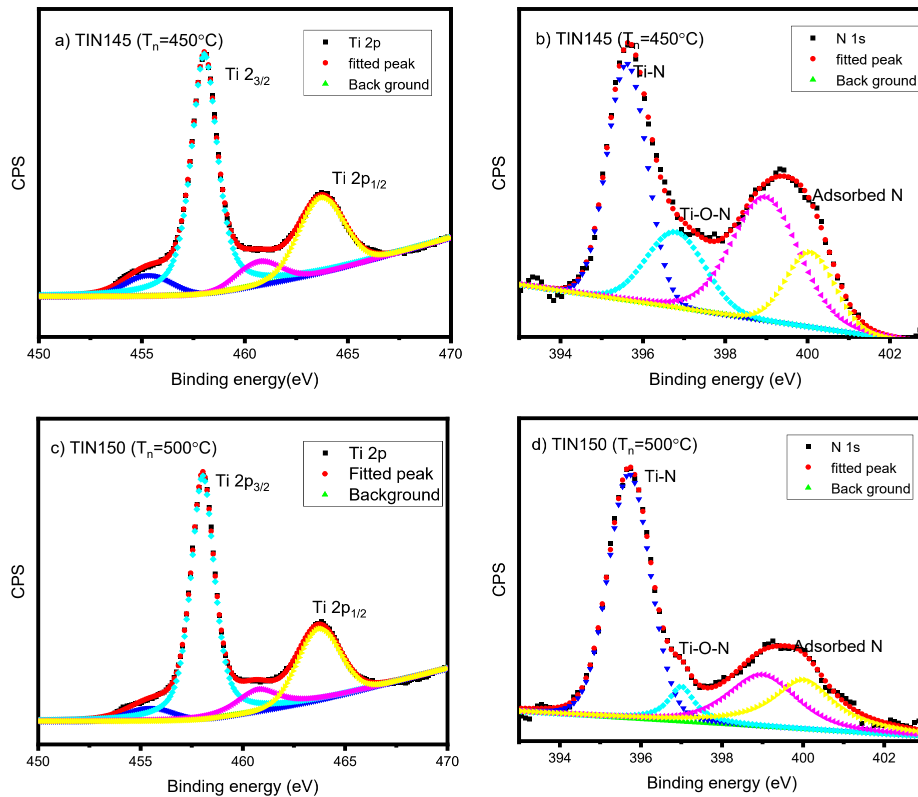

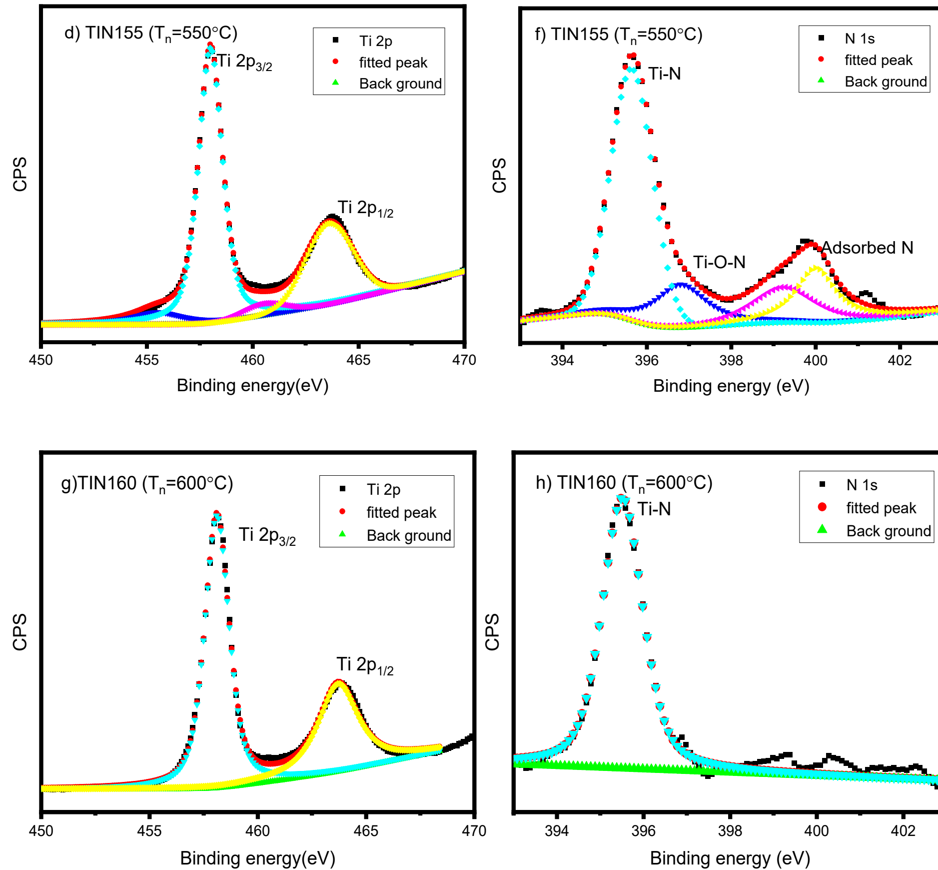

Fig. 4.4. Detailed scans of Ti2p (a, c, e, g) and N1s spectra (b, d, f, h) of samples with respect to the nitridation temperatures TIN145, TIN150, TIN155 and TIN160, respectively

The Nitrogen 1s core level spectra has been deconvoluted to 4 peaks, and given in Table 1. The XPS pattern indicates the major peak corresponding to titanium-nitrogen bonding along with minor contribution from oxynitride phase and other components. The core level peak of N 1s obtained for the TIN145 shows an increased intensity for oxynitride phase. The peak intensity corresponding to the oxynitride phase at 396.8eV is found to

decrease, as the nitridation temperature is increased from 450°C to 550°C. The gradual increment in the nitridation temperature causes a decrease in the oxynitride peak intensity may be due to the reduced atmosphere creation during nascent nitrogen production from ammonia [13]. The nitridation at a temperature of 600°C corresponds to only one peak at 395.6, where the envelope structure disappears in the N1s core level. This reveals the formation of phase pure titanium nitride at 600°C. The XPS analysis thus confirms the titanium nitride phase formation in all the samples. Saha et al reported the oxidation chemistry of TiN samples by keeping them in air for two weeks and observed a native oxide layer formation on the surface which agrees with the predictions [7]. Macak et al. showed the existence of a chemisorbed nitrogen peak in the N1s spectrum obtained after nitridation at 500°C using ammonia gas, confirming the potential for multicomponent nitrogen species in nitridated samples using ammonia [14]. Bertoti et al also investigated the nitride surface of titanium metal film using nitrogen gas and reported the similar nature of the N1s line shape function [9].

Table 4.1. Assigned bonds to binding energy values

	Binding energy (eV)	**Assigned bond**
1	395.6	Ti-N [7]
2	396.8	O-N (TiO_yN_x)[8]
3	399.1	N-H[4]
4	400.2	Adsorbed N_2 [14]

4.3 MICROSTRUCTURAL ANALYSIS

4.3.1 FE-SEM studies

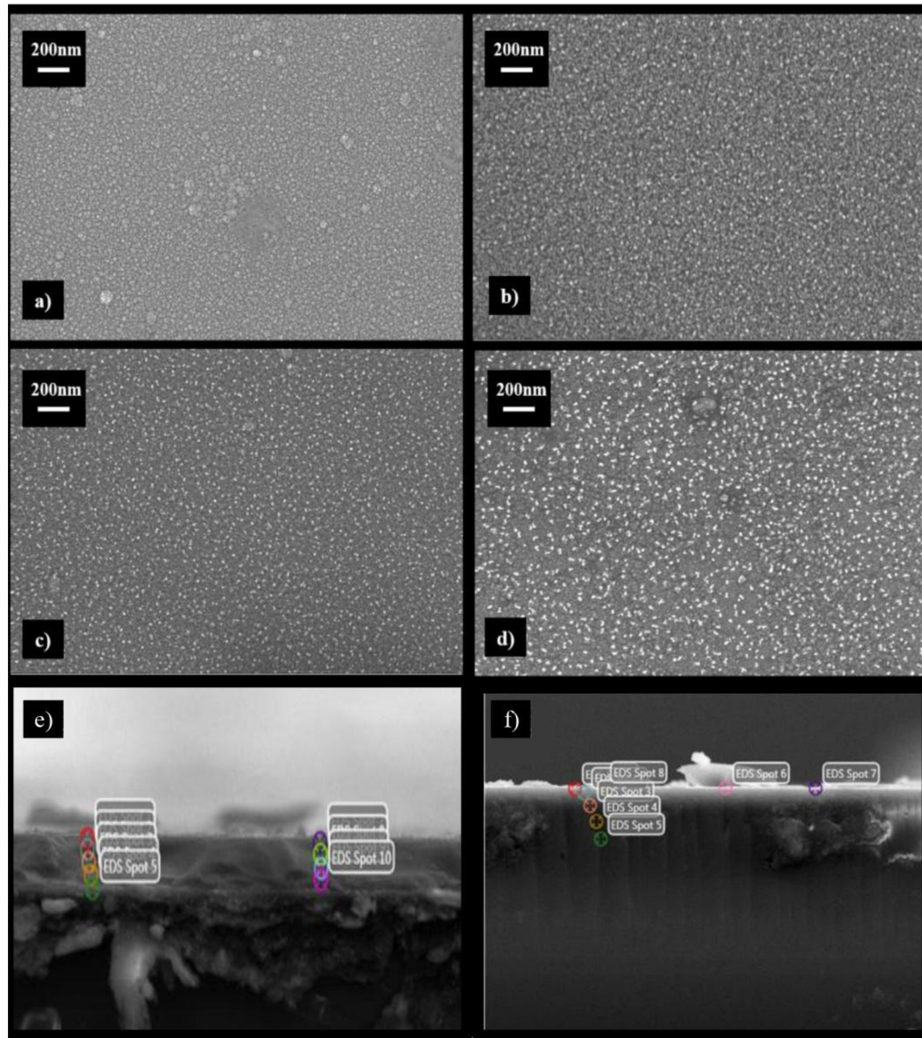

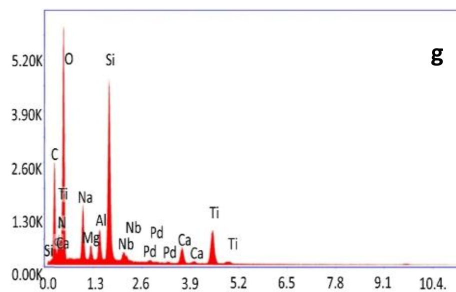

Fig. 4.5. FE-SEM images of the samples nitridated a) TIN145, b) TIN150, c) TIN155 and d) TIN160; e) composition analysis in depth profiling; f) composition analysis on the film surface; g) typical elemental distribution curve

Microstructural evolution of sputtered titanium nitride film depends on the deposition parameters such temperature of deposition, pressure of gases in the deposition chamber, and also the composition of the film. The microstructural features of the nitridated film samples at temperatures ranging from 450°C to 600°C were analysed. As seen in the Fig. 4.5 (a), the films nitridated are having uniform and crack-free surface. As the nitridation temperature is increased, the grain size decreases and that affects the surface roughness of the samples, as discussed in the Section 4.3.2. The EDX analysis were carried out in order to further investigate the compositions at different positions on the surface of the film and at different depth in the cross-section of the film. Depth profiling analysis was performed at positions 1,2,3 on the film surface as shown in Fig.4.5(e) and compositional analysis was performed at positions 1,6,7 on the film surface as shown in Fig.4.5(f). A typical elemental distribution curve obtained is shown in Fig. 4.5(g). The summary of the composition analysis is given in Table 4.2. For accurate composition determination, the elemental compositions with respect to titanium and nitrogen were estimated by incorporating atomic correction factor [15-16]. The results of the composition analysis indicate that there are no significant differences in the surface and depth compositions of the nitridated films.

Table 4.2. Results of the composition measurements

Composition analysis in the depth profiling [Fig. 4 (e)]			**Composition analysis on the film surface [Fig. 4 (f)]**		
Positions	Ti (At.%)	N(At.%)	Positions	Ti (At.%)	N(At.%)
1	45.89	54.11	1	45.89	54.11
2	43.72	56.28	6	42.56	57.44
3	39.55	60.45	7	46.76	53.24

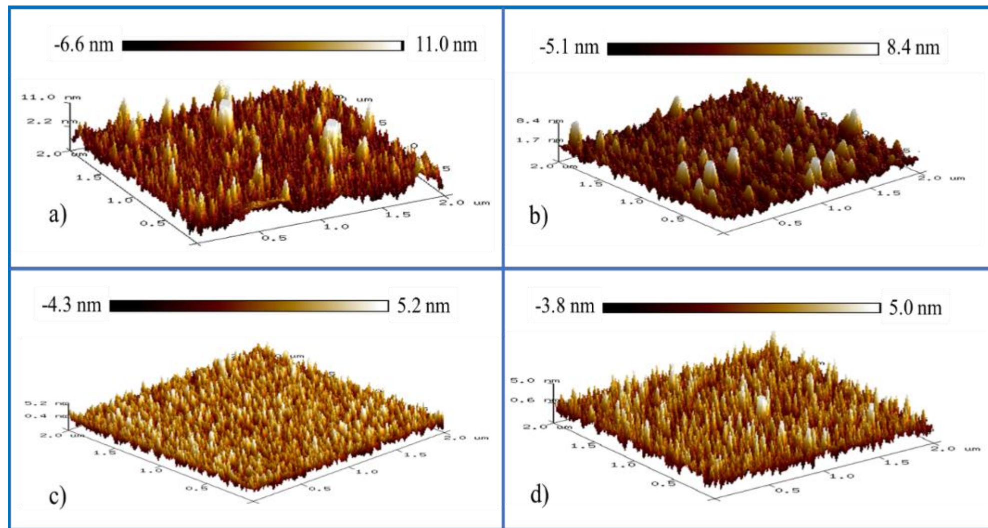

Fig.4.6 3D AFM images of TiN films nitridated at temperatures a) TIN145, b) TIN150, c) TIN155 and d) TIN160

4.3.2 Atomic force microscopic analysis

Fig.4.6 shows the 3D AFM images of TiN films nitridated at various temperatures, whereas Fig.4.7 shows the 2D images of the films. The scale bars in both Fig. 4.6 and Fig. 4.7 are identical. The images in Fig. 4.6 shows well-defined columnar structure of the titanium nitride film without pore nature, as the nitridation temperature is increased. There is a decreasing trend of average surface roughness observed with increase in nitridation temperature from 500°C to 600°C, as depicted in Fig. 4.8. There are reports describing similar nature for the surface roughness with Ar:N_2 ratio for sputtered TiN films [17], and projecting aggregation of small particles and reduction in grain boundary during deposition are the reasons for this [18]. As the nitridation temperature is increased, more nitrogen will be incorporated into the sample. Decreasing trend of roughness with increase in nitrogen in sputtered titanium nitride films has been reported by Qi et al.,

and interpreted it in terms of the smoother surface of the titanium nitride films with TiN (2 0 0) preferred orientation compared with that of the films with TiN (1 1 1) orientation [1]. PLD deposited titanium nitride films reported roughness value of >1nm, which exhibited better optical properties than one with increased roughness [4]. Kim et al investigated the roughness effect on the enhancement in light-matter interaction, by implementing a flat Ag film rather than rough surfaces of other metallic polycrystalline films [19]. The nitridated films of this study also exhibited a similar variations in the orientation and also in the average surface roughness with variation in nitrogen content, with increase in nitridation temperature. The protrusion height also exhibited a similar trend. The surface roughness values range from 1-2 nm having impact on the optical and electrical properties, as described in sections 4.3 and 4.4. The surface morphologies of the films shown in Fig. 4.7 agree well in appearance with that of FESEM feature.

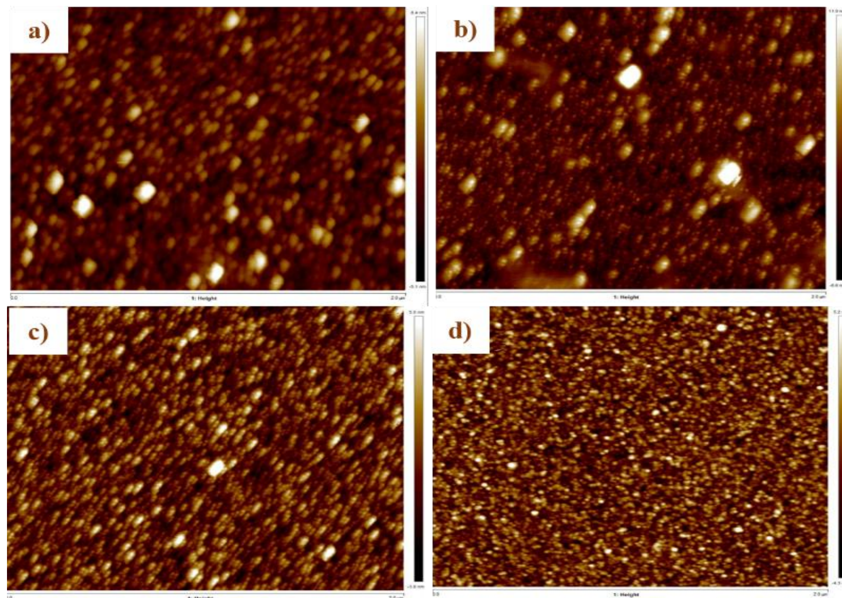

Fig. 4.7 2D AFM images of TiN films nitridated at temperatures a) TIN145, b) TIN150, c) TIN155 and d) TIN160

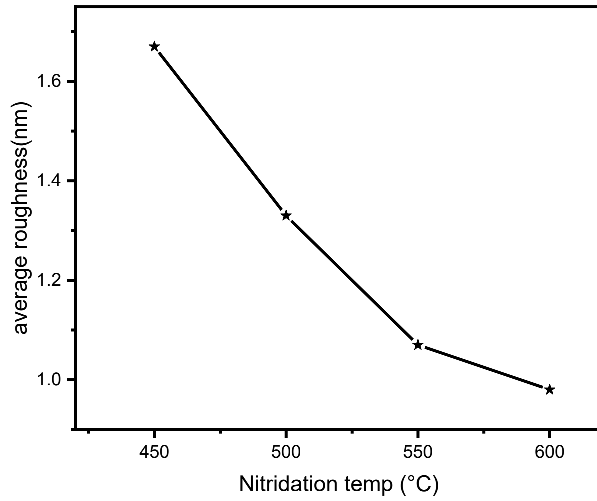

Fig. 4.8 Variation of average surface roughness with nitridation temperature

4.4 ELECTRICAL PROPERTY ANALYSIS

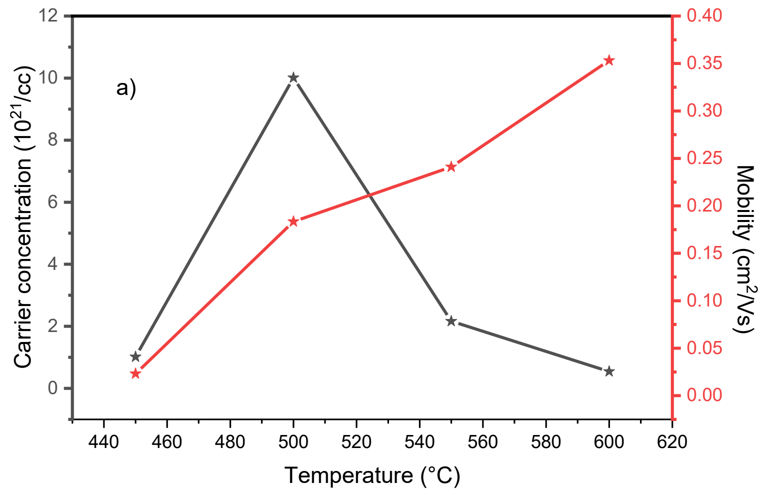

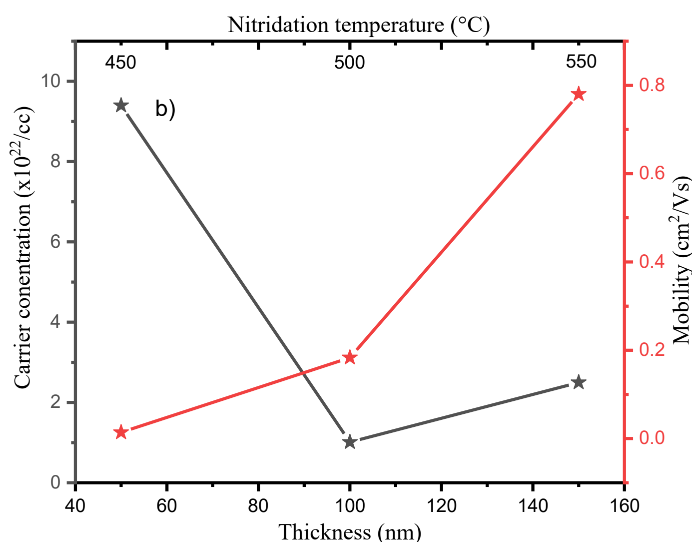

Fig.4.9 Electrical properties of nitridated titanium nitride films
(a) with different nitridation temperature (b) with variable thickness

Table 4.3. Electrical properties of titanium nitride films after nitridation

Sample name	Thickness	Carrier concentration (cm^{-3})	Mobility (cm^2/Vs)
TIN145	100±5nm	1.018×10^{21}	0.023
TIN150		**4.010×10^{22}**	0.183
TIN155		2.165×10^{21}	0.241
TIN160		5.436×10^{20}	0.353
TIN045	50±5nm	**9.399×10^{22}**	0.014
TIN255	150±10nm	**1.321×10^{22}**	0.780

Fig.4.9 shows the electrical properties of nitridated titanium nitride films with respect to the nitridation temperature as well as the thickness of the films. Table 4.3 presents the summary of analysis of carrier concentration and mobility of the films measured using Hall effect set up. The initial metal

films exhibited carrier concentration of the order of $10^{23}/cm^{-3}$ and resistivity of the order of 50-200 μΩcm. As the nitridation temperature was increased, the carrier concentration in the nitridated titanium film with a thickness of 100nm varied from 10^{20}/cc to 10^{22}/cc. The carrier concentration of films depends on the compositions of titanium and nitrogen. With the increase the nitridation temperature, the amount of nitrogen incorporated into the film increases [2] and this might have drastically changed the carrier concentration. Nitridation brings change from titanium metal to metal rich, then to stoichiometric, and finally to nitrogen rich titanium nitride. Titanium nitride exhibits maximum carrier concentration of $10^{22}/cm^{-3}$ in metal rich and stoichiometric conditions [20-21].

The initial metal film with a thickness of around 100nm nitridated at 450°C exhibited a carrier concentration of 10^{21}/cc, which steadily improved when the nitridation temperature was increased to 500°C. Fig. 4.9(a) shows the electrical properties of the samples with thickness around 100nm, and nitridated at various temperatures. The electrical characteristics of the films were improved at the nitridation temperature of 500°C, for the film, TIN150. There is a limited amount of literature available regarding the mobility characteristics of titanium nitride films. Andrievskii et al reported the mobility and hall coefficient of RF sputtered stoichiometric titanium nitride films, and suggested that the grain boundary scattering of the films as the main reason for the decrease in the mobility of carriers [22]. When comparing the observed mobility of the carriers in the films nitridated at various nitridated temperatures to this finding, it can be seen that the mobility value shows only a gradual increment from $0.065cm^2/Vs$ to $0.1834cm^2/Vs$, with nitridation temperature. Shin et al investigated the contribution of surface roughness on carrier mobility with respect to phonon and surface scattering [23]. They report an increase in the surface scattering

phenomenon due to increased surface roughness, and observed scattering phenomena as the main reason for the decrease in mobility. Her et al reported decrease in surface roughness with annealing temperature [24]. In this work, the surface roughness decreases with nitridation temperature, and hence the decrease in surface roughness might be the reason for the improved mobility in our case, due to the reduction in the surface scattering. Ponon et al also reported increase conductivity in titanium nitride films due the decrease in surface roughness [25]. Kasap also described the dependence of surface scattering on the conductivity of thin films [26].

Fig. 4.9(b) represents the carrier concentration and mobility of the three films varying in thickness, and possessing carrier concentrations of the order of 10^{22}/cc necessary to exhibit plasmonic behaviour in the visible region. As seen in the Fig. (4.9b), when the thin film thickness increased from 50 to 150 nm, the nitridation temperature required to obtain the high carrier concentration also changed. The study reveals particular stoichiometry for exhibiting a carrier concentration of the order of $10^{22}/cm^3$ and the same is obtained through nitridation at various temperature. In addition, the amount of nitrogen incorporated into the sample varies with respect to the nitridation kinetics such as temperature, time duration of nitridation etc. As seen in the Fig. 4.9 (b), the mobility values varied linearly with respect to the nitridation temperature.

4.5. OPTICAL PROPERTY ANALYSIS

For surface plasmon resonance in thin films, higher carrier concentration and low dielectric loss in the chosen wavelength region are necessary. In metals, the complex dielectric permittivity includes real (ε_1) and imaginary (ε_2) parts denoted as,

$$\varepsilon(\omega) = \varepsilon_1 (\omega) + i\, \varepsilon_2 (\omega) \qquad (4.1)$$

where ω is the angular frequency of the electromagnetic wave used. In a semiconductor, the interaction of the electromagnetic wave with the free electrons present in it is explained by the Drude-Lorents (D-L) model. Here, the Drude term corresponds to the free carriers and the Lorentz term corresponds to the bound electrons in the semiconducting film. According to this model, the complex electrical permittivity is defined as [27],

$$\varepsilon = \varepsilon_\infty - \frac{\omega_{pu}^2}{\omega^2 - i\Gamma_D \omega} + \sum_{j=1}^{2} \frac{f_j \omega_{oj}^2}{\omega_{0j}^2 - \omega^2 + i\gamma_j \omega} \qquad (4.2)$$

where ε_∞ is high frequency dielectric constant, >1, Γ_D is the drude damping factor and ω_{0j} is the frequency of jth Lorentz oscillator with damping factor γ_j. $\Gamma = \frac{e}{\mu m^*}$, is the loss related Drude relaxation rate, or called momentum scattering rate.

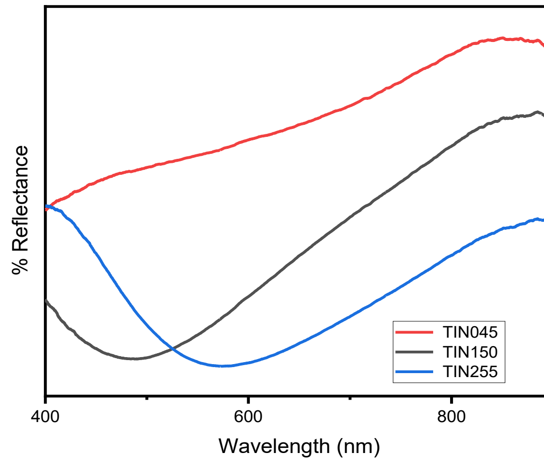

Fig. 4.10 Reflectance spectra of titanium nitride films having carrier concentration of $10^{22}/cm^3$

Fig. 4.10 represents the reflectance spectra obtained for the films having carrier concentration of the order of $10^{22}/cm^3$. By optimising the carrier concentration necessary for the plasmonic behaviour at visible wavelength, the films were further subjected to permittivity analysis by treating their reflectance spectra using the Drude Lorentz approximation with the help of Refit software [28]. Fig. 4.11. shows the fitted reflectance curves along with the real and imaginary parts of the permittivity values extracted from fitted curves for the films TIN045, TIN150 and TIN255. This way extracted the corresponding real and imaginary permittivity values of the films. The parameters used for the fitting are tabulated in Table 4.4. The frequency at which the real part of permittivity becomes zero is called as screened plasma frequency [29]. Patsalas et al reported a variation of screened plasma energy from 1.8 to 3 eV (410 to 700 nm in wavelength) extracted using ellipsometry [30]. Fig. 4.11 (a) represents the real and imaginary permittivity values of sample TIN045 having a carrier concentration $10^{22}/cm^3$. It is evident from the figure that the ε_1 is negative in the whole visible region, accomplishes the primary criterion for plasmonic excitation in the film. As the thickness is increased to 100 nm (TIN150), the screened plasma wavelength shifts to 559nm. With increase in thickness to 150nm (TIN255), it again shifts to 705nm. The variation may be due to the difference in the carrier density in the films. The optical property analysis thus confirmed the required negative permittivity of the nitridated films for the plasmonic behaviour in the visible region.

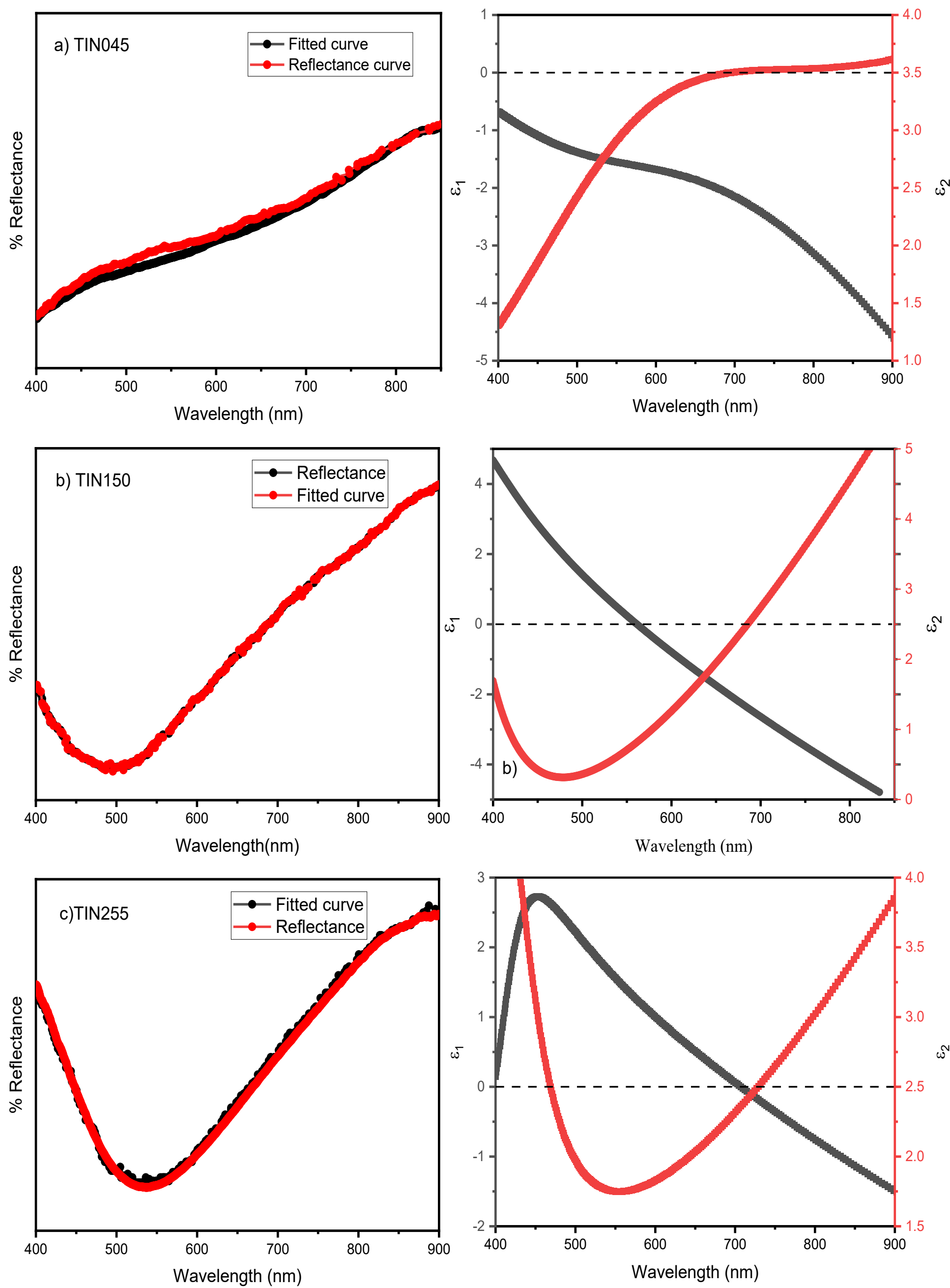

Fig. 4.11. Fitted reflectance curves (left) and the real and imaginary parts of the permittivity values extracted from fitted curves for the films a) TIN045, b) TIN150 and c) TIN255 (right)

Table 4.4. Parameters used for fitting the reflectance spectra for the samples a) TIN045 b) TIN150 and c) TIN255

Sample name	ε_∞	ω_p (eV)	ω_{0j} (eV)	$\gamma_j(eV)$
TIN045	2.31	3.514	2.22	2.07
		4.67	0	0.61
TIN150	2	4.78	3.45	0.864
		5.13	0	0.982
TIN255	2.12	2.89	3.05	0.67
		3.81	0	1.08

The dielectric properties measurements revealed a reduced metallic characteristic in the titanium nitride films, with increase in the nitridation temperature. This may be a contributing factor to the low dielectric loss of titanium metal derived TiN films. The reduction in dielectric loss in titanium nitride films is reported by Christine et al with increase in the nitrogen concentration [31]. Plasmonic applications in chosen wavelength region tend to choose films that exhibit high quality factor in the wavelength of interest, where ratio of the $-\varepsilon_1^2/\varepsilon_2$ matters [32]. Thus, the reduction in the dielectric loss (ε_2) improves the quality factor. The quality factor corresponding to each case is calculated and summarized in Table 4.5. Mascaretti et al theoretically reported the quality factor by extracting permittivity values from ellipsometry data and are <5 in visible region, which agrees well with the obtained values [33]. We have calculated the quality factor of the films near to their screened plasma wavelength in each sample. The dielectric loss results from the contribution of band transitions and scattering due to grain boundary and lattice defect scattering [32].

Table 4.5 Quality factor estimated for the samples a) TIN045 b) TIN150 and c) TIN255

Sample name	ε_1	ε_2	Quality factor ($-\varepsilon_1^2/\varepsilon_2$)
TIN045	-1.68	3.23	0.874 (λ=600 nm)
TIN150	-1.79	1.95	1.645 (λ=650 nm)
TIN255	-0.37	2.66	0.051 (λ=750 nm)

4.6 PLASMONIC PROPERTY ANALYSIS

Kretschman based prism geometry configuration with right-angled prism was employed in the wavelength interrogation mode for exciting surface plasmons in the titanium nitride films of this study. The experiments were conducted at various angles for incident light on the right-angled prism. The film coated on glass substrates was placed on the base of the right-angled prism using ethylene glycol as index matching fluid. When transverse magnetic polarised light is incident at an incident angle greater than the critical angle of the prism, the light is reflected completely back to the prism and creates an evanescent wave that propagates parallel to the substrate on which the film is coated and the air interface. Resonance takes place when the incident light and that of surface plasmon wave vector matches. The resonance criteria for the surface plasmon polariton excitation at the film-dielectric interface, can be written as:

$$\theta = \sin^{-1}\left[\frac{1}{n_p}\left(\frac{\varepsilon_m \varepsilon_d}{\varepsilon_m + \varepsilon_d}\right)^{\frac{1}{2}}\right] \qquad (4.3)$$

where θ is angle of incidence n_p is the refractive index of the BK7 prism used, ε_m and ε_d are the permittivity values corresponding to the plasmonic material and dielectric, respectively [33].

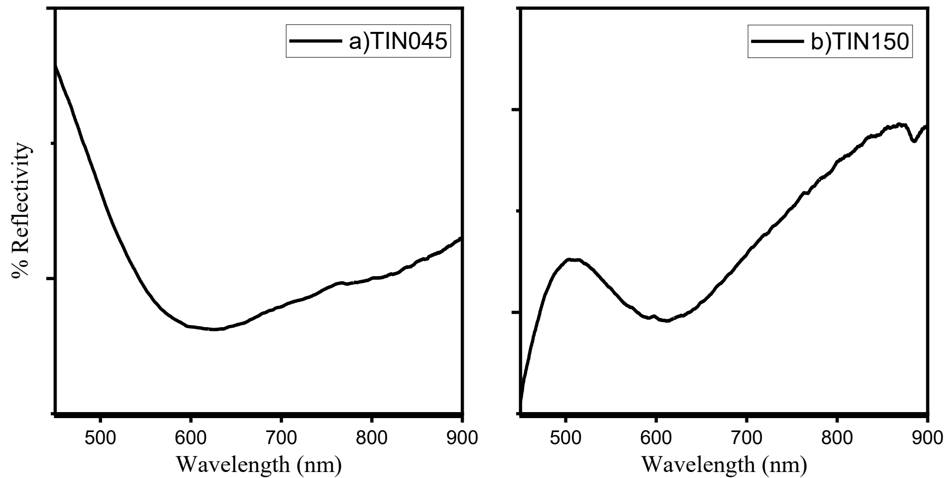

Fig. 4.12. Surface plasmon resonance excitation in titanium nitride films with different thickness (a) TIN045 and (b) TiN150

For SPR excitation, selected the samples TIN045 (nitridated at 450°C having thickness around 50nm) and TIN150 (nitridated at 500°C having thickness around 100nm), both have carrier densities of the order of 10^{22}/cc. The sample TIN255 has not been considered due to low quality factor. Fig. 4.12 (a) illustrates the SPR curves excited on the films with different thickness values and having carrier concentrations of the order of 10^{22}/cc at an angle of incidence of 45°. For the sample TIN045, the resonance dip position is observed at around 608nm and for TIN150 it is at around 623nm. The curve corresponding to TIN045 is much broader compared to that of TIN150 Fig. 4.12 (b). The quality factor estimated was high for this sample. Kim et al analysed the variation in the plasmonic excitation with respect to

the nanostructure dimension and observed enhanced plasmonic confinement and reduced scattering for an optimum dimension [34].

$$\omega_p = \sqrt{\frac{nq^2}{\varepsilon_0 m_e}} \qquad (4.4)$$

From above equation (4.4) , it can be seen that the plasma frequency depends on the variations in the carrier density and effective mass. In this study, all samples under SPR investigation are having the required carrier concentration. The carrier concentration is of the order of $10^{22}/cm^3$ and hence the difference in effective mass is important. Effective mass depends on properties such as band structure, defects and strain in the lattice structure of material, crystal structure of material, etc. The effective mass (m*) is given by

$$m^* = \frac{e<\tau>}{\mu} \qquad (4.5)$$

τ is the relaxation time and μ is mobility . Patsalas et al estimated the variation in the effective mass of titanium nitride film with respect to nitrogen content [35]. They investigated its dependence on deposition conditions such as substrate temperature and biasing, and reported a variation from $1.5m_0$ to $2.8m_0$]. In the present study, the excitation of surface plasmon in prism geometry in the films having carrier densities of $10^{22}/cc$ possessed surface plasmon dip at around 600nm in visible region. The optical property analysis revealed an increasing trend of screened plasma wavelength with the nitridation temperature. The exact role of the effective mass needs to be considered to explain this trend [36].

The dielectric loss (ε_2) in titanium nitride film depends on the damping constant

(γ), mobility and effective mass, as follows.

$$\varepsilon_2 = \frac{\omega_p^2 \gamma}{\omega^3 + \omega\gamma^2} \quad (4.6), \quad \text{where} \quad \gamma = \frac{q}{\mu m^*} \quad (4.7)$$

The equation 4.7 show the inverse relationship of the mobility and the effective mass to the damping constant. Thus, the increased mobility reduces dielectric loss, which enhances the coupling between surface plasmon polariton and the incident light [29].

The mobility values corresponding to TIN150 is greater than TIN045, and this may the reason for the narrow full width half maximum (FWHM) of the SPR curve in the film TIN150. It is evident from the Fig. 4.12 that the FWHM of the excited SPR curves are not proportional to the carrier mobility of the samples. Hence the study reveals that both the thickness of the films and the nitridation temperature increased the carrier mobility of the films. Khamh et al showed similar trend in ITO coated sample, where the increased mobility yielded sharp FWHM for the SPR curves [37]. In the present study, the increased carrier mobility and the high carrier concentration of the titanium nitride films having optimum film thickness processed through nitridation process exhibited surface plasmonic excitation in prism-bas ed configuration. For the first time, this work demonstrated SPR excitation in nitridation-processed titanium nitride films. Also, the range of wavelength of SPR excitation is in the visible region compared to the results of Mena et al [38].

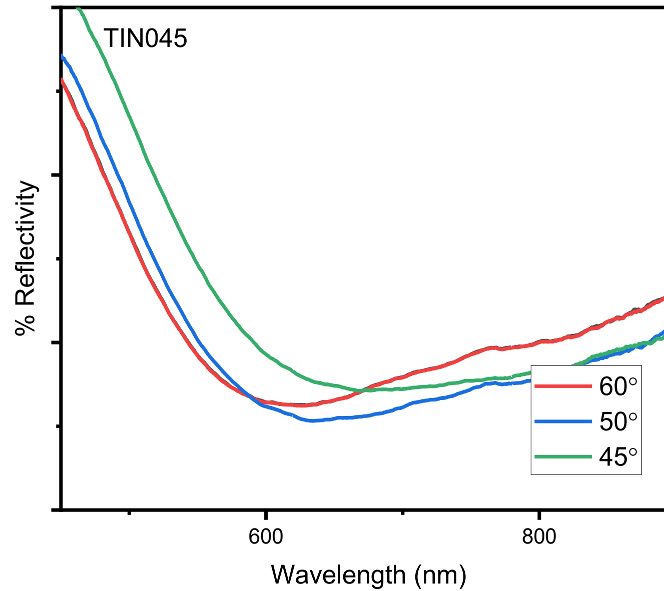

Fig. 4.13 Surface plasmon resonance excitation in titanium nitride films with variable angle of incidence for the film TIN045

In order to confirm the angular variation of the surface plasmon resonance excitation, the angle of incidence of the incident light has been varied. Typical result is shown in in Fig.4.13 for the sample TIN045. with air as dielectric medium. Favourable momentum matching between the surface plasmon and the incident wavelength at specific angle of incidence leads to the formation of a coupling, and thereby observes a minimum at a specific wavelength in the reflected light intensity. The permittivity analysis indicated a decrease in the real permittivity as the wavelength increases (from -1 to -4 in the wavelength range 500nm to 800nm). In equation (4.3), substituting for n_p (1.5) and ε_d (for air, 1), one can see a decrease in the permittivity with decrease in the resonance angle. A shift of the incidence angle from 45° to 60° contributes a blue shift in surface plasmon resonance wavelength.

Sugavaneshwar et al claimed the realization of the TiN flms with the best plasmonic character by pulsed laser deposition (PLD) by analysing their carrier concentration and permittivity values [39]. Despite the demonstrated high plasmonic character, the PLD coated TiN films were in fact much thicker (180nm) than those reported till date. This study indicates that proper optimisation of thickness is necessary for SPR excitation in visible region. In the present work, the increased high carrier concentration along with increased carrier mobility of the titanium nitride films having optimum film thickness processed through nitridation process exhibited surface plasmonic excitation in visible region using prism-based configuration.

4.7 CONCLUSION

Titanium nitride films with thickness in the range 50-150nm fabricated via nitridation of titanium metal films at temperatures 450°C, 500°C, 550°C, and 600°C showed significant enhancement in the electrical and optical properties. The structural investigations carried out with XRD and XPS confirmed the titanium nitride phase formation. Reduced roughness of the films improved further the electrical and thereby the optical properties. The dielectric permittivity values were extracted from reflectance spectra using Drude Lorentz oscillator model, and correlated with electrical properties obtained from Hall measurement. The enhanced electrical properties with optimised film thickness contributed to the plasmonic excitation in the films, and the same is confirmed by the prism-based geometry. Here, the dependence of electrical mobility on the dielectric loss in the films, and also on the FWHM of the surface plasmon resonance curve has been observed. The increased nitridation temperature enhanced the electrical mobility of thin films.

4.8 REFERENCES

1. Qi, R., Pan, L., Feng, Y., Wu, J., Li, W., & Wang, Z. (2020). Evolution of chemical, structural, and mechanical properties of titanium nitride thin films deposited under different nitrogen partial pressure. *Results in Physics*, *19*, 103416. 10.1016/j.rinp.2020.103416.

2. Srikrishna, K., Jairath, R., & Huglin, G. (1991). Rapid thermal annealing of titanium in an ammonia ambient: Kinetics and film properties. *MRS Online Proceedings Library*, *224*(1), 123-128. DOI: 10.1557/PROC-224-123.

3. Chang, C. C., Nogan, J., Yang, Z. P., Kort-Kamp, W. J., Ross, W., Luk, T. S., ... & Chen, H. T. (2019). Highly plasmonic titanium nitride by room-temperature sputtering. *Scientific reports*, *9*(1), 15287. DOI: 10.1038/s41598-019-51236-3

4. Gong, Y., Tu, R., & Goto, T. (2009). Microstructure and preferred orientation of titanium nitride films prepared by laser CVD. *Materials transactions*, *50*(8), 2028-2034. DOI: 10.2320/matertrans.M2009101.

5. Guo, Wan-Ping & Mishra, Ragini & Cheng, Chang-Wei & Wu, Bao-Hsien & Chen, Lih-Juann & Lin, Minn-Tsong. (2019). Titanium Nitride Epitaxial Films as a Plasmonic Material Platform: Alternative to Gold. ACS Photonics. 6. DOI: 10.1021/acsphotonics.9b00617

6. Fang, De & He, Feng & Xie, Junlin & Xue, Lihui. (2020), Calibration of Binding Energy Positions with C1s for XPS Results. J. Wuhan Univ. Technol. Mater. Sci. Ed. 35, 711-718 DOI: 10.1007/s11595-020-2312-7.

7. Naresh C. Saha and Harland G. Tompkins, (1992), Titanium nitride oxidation chemistry: An x-ray photoelectron spectroscopy study, J. Appl. Phys. 72, 3072–3079 DOI: 10.1063/1.351465.

8. Perkin-Elmer ESCA Manual, (1991), Version 3.0 (Perkin-Elmer, Eden Prairie, MN.

9. Bertóti, M. Mohai, J.L. Sullivan, S.O. Saied, (1995), Surface characterisation of plasma-nitrided titanium: an XPS study, Appl Surf Sci., 84, 357-371, DOI:10.1016/0169-4332(94)00545-1.

10. Y.L. Jeyachandran, K. Narayandass, D. Mangalaraj, Sami Areva, J.A. Mielczarski, (2007), Properties of titanium nitride films prepared by direct current magnetron sputtering, Mat Sci and Eng: A, 445–446, 223-236 DOI: 10.1016/j.msea.2006.09.021.

11. Jiang N, Zhang H J, Bao S N, Shen Y G, Zhou Z F. (2004), XPS study for reactively sputtered titanium nitride thin films deposited under different

substrate bias Physica B: condensed mat. 352,128-136, DOI: 10.1016/j.physb.2004.07.001.

12. Zgrabik, C. M. & Hu, E. L. (2015),Optimization of sputtered titanium nitride as a tunable metal for plasmonic applications, Opt. Mater. Express 5, 2786 DOI: 10.1364/OME.5.002786

13. Liu, Y., Zhang, Y., You, Z., Lv, X. (2020), Preparation of Transition Metal Nitrides via Reduction–Nitridation with Ammonia. 11th International Symposium on High-Temperature Metallurgical Processing. The Minerals, Metals & Materials Series. Springer, Cham. DOI: 10.1007/978-3-030-36540-0_54.

14. Macak, Jan & Ghicov, Andrei & Hahn, Robert & Tsuchiya, Hiroaki & Schmuki, Patrik. (2006). Photoelectrochemical properties of N-doped self-organized titania nanotube layers with different thickness. J. Mater. Res. 21, 2824 - 2828. 10.1557/jmr.2006.0344.

15. K. Muraleedharan and D. Banerjee, (1989) Alloy partitioning in Ti-24Al-11Nb by analytical electron microscopy, Metall. Trans. A, vol. 20, no. 6, pp. 1139-1142,.

16. D. B. Williams, (1986), Practical analytical electron microscopy in materials science in Analytical Proceedings, vol. 23, p. 41.

17. Shidong Zhang, Fuyao Yan, Yang Yang, Mufu Yan, Yanxiang Zhang, Jinhao Guo, Hongtao Li, (2019), Effects of sputtering gas on microstructure and tribological properties of titanium nitride films, App. Surf. Sci., 488, 61-69 DOI: 10.1016/j.apsusc.2019.05.148

18. B. Pécz, N. Frangis, S. Logothetidis, I. Alexandrou, P.B. Barna, J. Stoemenos, (1995), Electron microscopy characterization of TiN films on Si, grown by d.c. reactive magnetron sputtering, Thin Solid Films, 268, 57-63 DOI:10.1016/0040-6090(95)06692-6.

19. Jung Ho Kim, Jubok Lee, Sehwan Park, Changwon Seo, Seok Joon Yun, Gang Hee Han, Jeongyong Kim, Young Hee Lee, Hyun Seok Lee, (2022) ,Locally enhanced light–matter interaction of MoS2 monolayers at density-controllable nanogrooves of template-stripped Ag films, Curr. Appl. Phys., 33,59-65 DOI: 10.1016/j.cap.2021.11.002.

20. Qiu, Guangyu & Ng, Siu Pang & Wu, Lawrence. (2018). Label-free Surface Plasmon Resonance Biosensing with Titanium Nitride Thin film. Biosensors and Bioelectronics. 106, 129-135. DOI: 10.1016/j.bios.2018.02.006.

21. Zih-Ying Yang, Yi-Hsun Chen, Bo-Huei Liao, and Kuo-Ping Chen, (2016) "Room temperature fabrication of titanium nitride thin films as plasmonic

materials by high-power impulse magnetron sputtering," Opt. Mater. Express 6, 540-551, DOI: 10.1364/OME.6.000540

22. Andrievskii, R. & Dashevsky, Zinovi & Kalinnikov, G, (2004), Conductivity and the Hall coefficient of nanostructured titanium nitride films. Tech. Phys. Lett. 30, 930-932 DOI: 10.1134/1.1829346.

23. Shin H, Han IK, Ko JH, Jang M. (2018), Hole Mobility Characteristics with Surface Roughness on Silicon-on-Insulator Substrate. J Nanosci. Nanotechnol.,18, 6017-6020 DOI: 10.1166/jnn.2018.15582.

24. Her, S.C., Wu, C.L. (2014) Annealing Effect on the Microstructure and Mechanical Properties of a Thin Titanium Nitride Film. Strength Mater. 46, 208–213 DOI: 10.1007/s11223-014-9537-7.

25. Nikhil K. Ponon, Daniel J.R. Appleby, Erhan Arac, P.J. King, Srinivas Ganti, Kelvin S.K. Kwa, Anthony O'Neill, (2015), Effect of deposition conditions and post deposition anneal on reactively sputtered titanium nitride thin films. Thin Solid Films, 578, 31–37 DOI: 10.1016/j.tsf.2015.02.009

26. S. O. Kasap, (2006), Principles of Electronic Materials and Devices, McGraw-Hill Edition, New York, 401–404,

27. F. Wooten, (1972), Optical Properties of Solids, Academic press, New York 10003. United Kingdom Edition,

28. Kuzmenko, Alexey. (2005), Kramers-Kronig constrained variational analysis of optical spectra. Rev. Sci. Instrum. 76, 083108 DOI: 10.1063/1.1979470

29. Logothetidis, S.; Alexandrou, I.; Papadopoulos, A. (1995), In-situ spectroscopic ellipsometry to monitor the process of TiN thin films deposited by reactive sputtering. J. Appl. Phys., 77, 1043–1047 DOI:10.1063/1.358963

30. Patsalas P, Kalfagiannis N, Kassavetis S. (2015), Optical Properties and Plasmonic Performance of Titanium Nitride. Materials, 8, 3128-3154 DOI: 10.3390/ma8063128.

31. Christine M. Zgrabik and Evelyn L. Hu, (2015),Optimization of sputtered titanium nitride as a tunable metal for plasmonic applications, Opt. Mater. Express 5, 2786-2797 DOI:10.1364/OME.5.002786

32. West P R, Ishii S, Naik G V, Emani N K, Shalaev V M and Boltasseva A, (2010), Searching for better plasmonic materials, Laser Photon. *Rev.* 4, 795–808
DOI:10.1002/lpor.200900055.

33. Luca Mascaretti, Tapan Barman, Beatrice Roberta Bricchi, Filip Münz, Andrea Li Bassi, Štěpán Kment, Alberto Naldoni, (2021), Controlling the plasmonic properties of titanium nitride thin films by radiofrequency substrate biasing in magnetron sputtering, Appl. Surf. Sci., 554,149543 DOI:10.1016/j.apsusc.2021.149543

34. Jung Ho Kim, Hyun Seok Lee, Gwang Hwi An, Jubok Lee, Hye Min Oh, Jihoon Choi,Young Hee Lee, (2020) Dielectric Nanowire Hybrids for Plasmon-Enhanced Light–Matter Interaction in 2D Semiconductors, ACS Nano, 14, 9, 11985–11994.

35. P. Patsalas, C. Charitidis, S. Logothetidis, C. A. Dimitriadis, O. Valassiades; (1999), Combined electrical and mechanical properties of titanium nitride thin films as metallization materials. J. Appl. Phys. 86, 5296–5298 DOI:10.1063/1.371514.

36. Tsong-Ru Tsai, Shi-Jie Chen, Chih-Fu Chang, Sheng-Hsien Hsu, Tai-Yuan Lin, and Cheng-Chung Chi, (2006), Terahertz response of GaN thin films, Opt. Express 14, 4898-4907 DOI:10.1364/OE.14.004898

37. Khamh, Hniang & Sachet, Edward & Kelley, Kyle & Maria, Jon-Paul & Franzen, Stefan. (2018), As Good as Gold and Better: Conducting metal oxide materials for mid-infrared plasmonic applications. J. Mater. Chem. C. 6, 8326-8342 DOI:10.1039/C7TC05760A

38. Mena N. Gadalla, Andrew S. Greenspon, Michele Tamagnone, Federico Capasso and Evelyn L. Hu, (2019) Excitation of Strong Localized Surface Plasmon Resonances in Highly Metallic Titanium Nitride Nano-Antennas for Stable Performance at Elevated Temperatures, ACS Appl. Nano Mater. , 6, 3444–3452, (2019), DOI: 10.1021/acsanm.9b00370

39. Ramu Pasupathi Sugavaneshwar, Satoshi Ishii, Thang Duy Dao, Akihiko Ohi, Toshihide Nabatame and Tadaaki Nagao, (2018), Fabrication of highly metallic TiN films by pulsed laser deposition method for plasmonic applications. ACS Photonics 5, 814–819 DOI:10.1021/ acsphotonics. 7b00942.

CHAPTER 5

INVESTIGATION OF SURFACE PLASMON RESONANCE PROPERTIES IN TiN_x THIN FILMS FABRICATED FROM SPIN COATED TiO_2 THIN FILMS

Introduction

In this chapter, the focus is on the nanoscale fabrication of titanium nitride thin films with a simple and cost-effective route. The studies described in the previous chapters included the plasmonic properties of RF-sputtered titanium nitride films with respect to stoichiometry, and the conversion of Ti metal film to TiN_x films through nitridation process. In the work described in chis chapter, the methodology consists of preparing titanium dioxide films via spin coating, followed by nitridation reaction using ammonia gas. The difficulty remained in obtaining porous-free TiN films through nitridation route, and the approach adopted here resulted in films with excellent material properties for plasmonic applications in visible region. The films exhibited high carrier concentration of 10^{22}/cc with significant reduction in resistivity of more than three order of magnitude, indicating the conversion to the nitride phase. The correlated opto-electrical properties confirmed all the necessary conditions for the surface plasmon polariton.

The spin-coated titanium dioxide thin films were subjected to a nitridation reaction at a temperature of 950°C and converted to titanium nitride films. The required negative permittivity and low-loss nature of the film suitable for plasmonic behaviour were confirmed by extracting the dielectric function with the help of Drude-Lorentz model. Thus, in this Chapter, for the first time, the development of plasmonic titanium nitride thin films through a novel chemical rote, having optimal material properties for plasmonic application in visible region is discussed. Finally, surface plasmon resonance in the nitridated films has been successfully excited using a Kretchsmann type prism geometry configuration with air as dielectric medium in wavelength interrogation mode.

5.1 DEVELOPMENT OF TIN THIN FILMS

Titanium dioxide is a well-studied material for applications in dielectrics, dye sensitized solar cells, antireflection films, etc. The existence of 3 structures (polymorphs) of TiO_2 in a) anatase b) rutile and c) brookite, with respect to annealing temperature has been reported by Helen [1]. As the annealing temperature is increased, the structural change occurs from amorphous to anatase, rutile and brookite, respectively [2]. The crystal structures of anatase and rutile phase are tetragonal, while that of the brookite phase is orthorhombic, as shown in Fig 5.1. The structural change is a consequence of corner or edge sharing octahedra network in the anatase phase [3-4]. Each structure has their own advantage in applications; for example, anatase phase enhances photocatalytic activity.

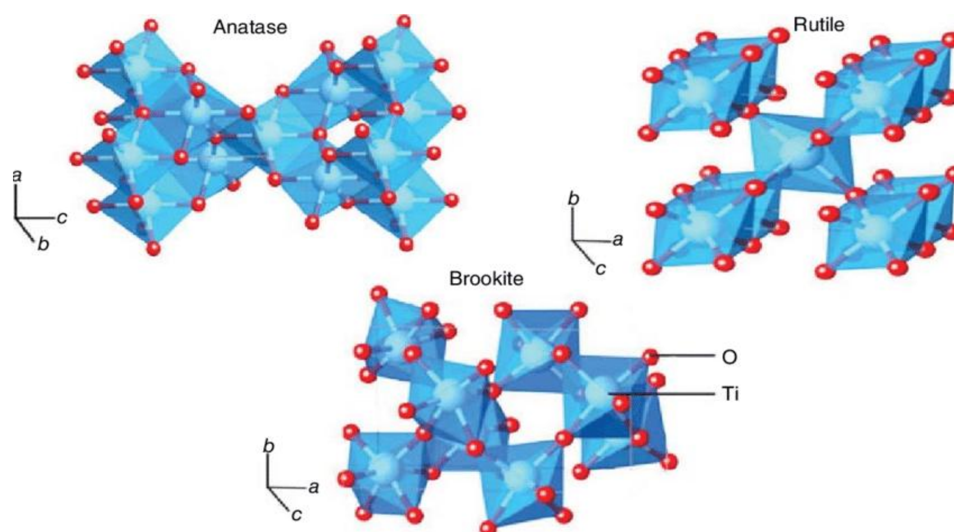

Fig 5.1. Different structures of TiO_2 a) Anatase b) Rutile c) Brookite [3]

5.1.1 Mechanism of conversion to titanium nitride

The nitridation of TiO_2 to form TiN requires a reducing agent in order to substitute oxygen with nitrogen. Among the various possibilities, one of the most described processes is the nitridation of TiO_2 with NH_3 [5]. In this case, the ammonia gas acts both as a reducing agent and a nitrogen source. This nitridation technique was first developed in 1987 by Kamiya et al. [6] to nitride TiO_2 fibers prepared from a TiO_2 sol-gel. It has then been adapted to nitride sol-gel derived TiO_2 films in 1990 [7]. The first step of the nitridation of TiO_2 with NH_3 is the dissociation of the ammonia and generates nascent nitrogen as per the equation 5.1[8,9]. The reaction of dissociation is described by Cooper et al. [10].

$$2NH_3\ (g) \rightarrow N_2\ (g) + 3H_2\ (g) \qquad (5.1)$$

Kamiya et al. reported reduction of TiO_2 and addition of nitrogen in the reaction mechanism [6],

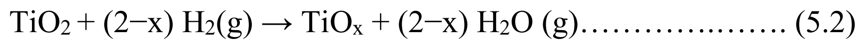

$$TiO_2 + (2-x)\ H_2(g) \rightarrow TiO_x + (2-x)\ H_2O\ (g) \qquad (5.2)$$

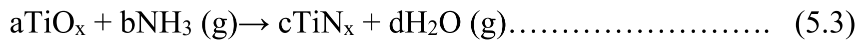

$$aTiO_x + bNH_3\ (g) \rightarrow cTiN_x + dH_2O\ (g) \qquad (5.3)$$

where TiOx may be TiO, Ti_2O_3, or other reduced titanium oxides [11]. Liu et al. investigated the conversion mechanism of titania powder to titanium nitride with respect to the nitridation temperature [12]. They report that the above reaction path is followed for the nitridations carried out at temperature < 1000°C, reach the intermediate stage of rutile TiO_2 and then convert to titanium nitride. This mechanism also depends upon the duration of annealing, ammonia flow rate, and precursor solution used [13-15]. During the nitridation, titanium oxynitride formation is reported to begin at temperatures between 600 and 700°C [16,17]. Romero-Gómez et al. [18] tried to spot the limit temperature for the main crystalline phase of TiN.

According to them, NH_3 treatment at 650 °C leads to a retention of the anatase phase doped with nitrogen atoms while at 660°C the first TiN crystalline structure is formed. These reaction temperatures are impacted by other parameters such as pressure, heating rate and presence of catalyzer, if any [19].

5.1.2 Spin coating of titanium dioxide thin film

The precursor solution for spin-coating titanium dioxide film was prepared by the partial hydrolysis of the titanium isopropoxide (Sigma Aldrich). For this, 2 ml of titanium isopropoxide was added to a mixture of 2 ml of diethanolamine and 20 ml of ethanol, followed by stirring for 1 hr at 40 °C. The clear and transparent solution obtained was aged for 24 hr. The quartz substrates (with dimension 2.5cm × 2.5cm) were ultrasonically cleaned using soap water, distilled water, acetone and isopropanol successively for 15 min each. In this study, quartz substrates were used instead of glass substrates for the coating in order to withstand higher nitridation temperatures. The cleaned substrates were finally dried in flow of nitrogen gas. Films were coated onto the clean substrates by spin coating. 75 μl solution was used for each coating, using a Chemat KW-4A spin coater, at 3000 rpm for 20 s. The as-deposited films were dried at 200 °C for 10 min. The cycle is repeated for achieving a final thickness of around 100nm. The films were finally annealed in air for 1 hr at a temperature of 550 °C. The detailed description on spin coating process is given in chapter 2.

5.1.3 Nitridation of the spin-coated TiO_2 film

The annealed titanium dioxide films were placed in a tubular furnace with its two ends closed with stainless steel flanges having provision for tube connections for the nitridation process. The furnace was initially purged

with nitrogen gas (99.99%) for 10 min to remove all gases inside the furnace, and then heated to a temperature of 100°C. Nitrogen gas flow was switched to ammonia gas (99.99%, Bhoruka, India) at this temperature. The furnace was heated up to the nitridation temperatures 800 °C, 950 °C, 1000°C and 1100 °C at a ramp rate of 5 °C/min and maintained there for 45 min, and after that, allowed to cool in a nitrogen atmosphere. The schematic diagram of nitridation setup is shown in the Fig. 2.6, in the Chapter 2.

The spin-coated titanium dioxide films are highly transparent, as seen in Fig 5.2 (a). After nitridating at 800°C, the samples became darker in appearance (Fig. 5.2(b)). As the nitridation temperature is increased to 950 °C, the sample exhibited gold like appearance, as shown in Fig 5.2 (c). The films nitridated at temperatures >1000 °C resulted in the formation of porosity [7]. Films with porosity will deteriorate the plasmonic performance. Hence, further optimisation studies were carried out with films nitridated at temperatures <1000°C.

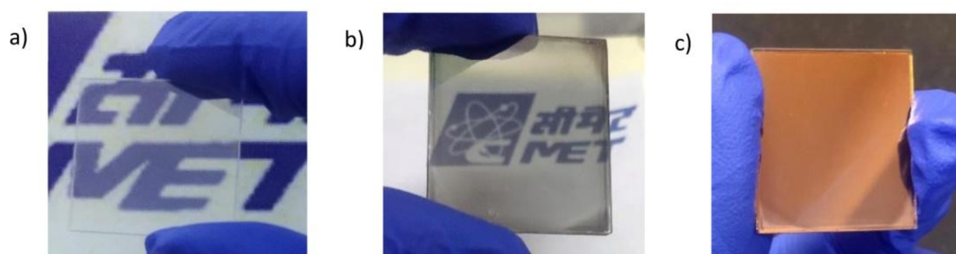

Fig 5.2. a) as-deposited TiO_2 b) after nitridation at 800 °C
c) after nitridation at 950 °C

Table 5.1 Analysis of GI-XRD peak values

[illegible]	[illegible]	
Nitridation 950°C	4.22	22 ± 0.33

5.2 INVESTIGATION OF THE STRUCTURAL PROPERTIES OF THE FILMS

5.2.1 Grazing incident X-Ray Diffraction studies

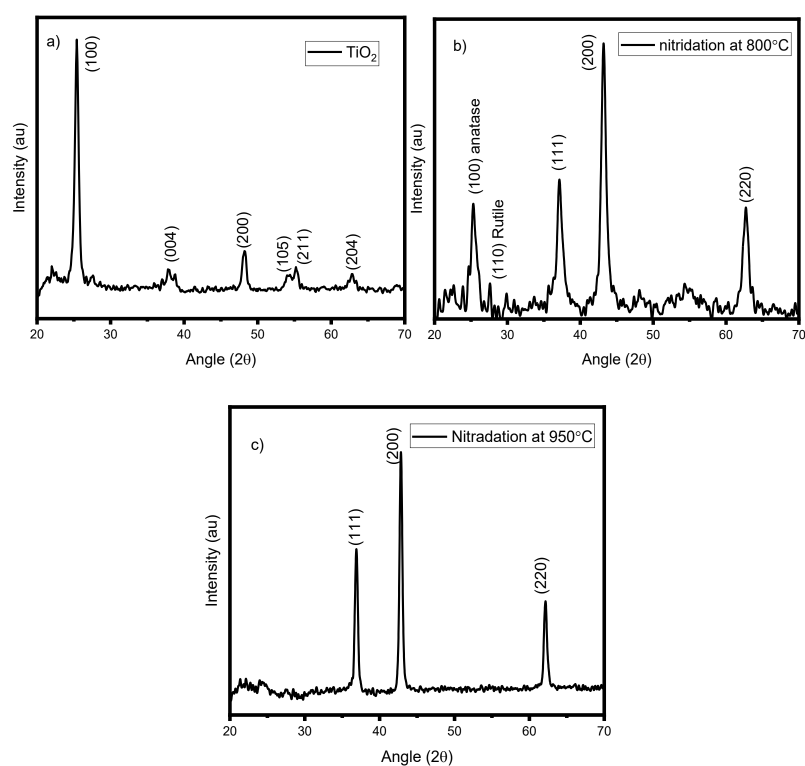

Fig 5.3. The GI-XRD patterns obtained for a) as-deposited TiO_2 b) after nitridation at 800 °C c) after nitridation at 950 °C

Fig. 5.3 a,b,c illustrate the glancing incidence angle x-ray diffraction (GI-XRD) pattern obtained for the as-deposited and nitridated thin film samples. The lattice parameter and the average crystallite size of the TiN phase of the samples were calculated, and the values are summarised in Table 5.1. The xrd pattern of the film annealed in air at 550 °C sample (Fig. 5.3a) is matched with the ICDD pattern number 00-021-1272 of TiO_2 confirms the anatase crystal structure. The peaks at 25.41° and 48.24° for this film corresponds to the (100) and (200) planes of the anatase phase, respectively.

The crystalline size of the nitridated films were calculated using Scherrer formula [20]

$$D = \frac{0.9\lambda}{\beta \cos\theta} \qquad (5.4)$$

where λ, β, are the x-ray wavelength and the full width at half maximum (FWHM) at the corresponding θ position of the peak.

The anatase form of the titanium dioxide phase changes after nitridation at 800 °C, which consists of a combination of 3 phases, such as anatase and rutile phases of TiO_2 and titanium nitride. The peaks at 25.41° and 27.46° correspond to the anatase (100) and rutile (110) planes of TiO_2 in the film, respectively. The peaks 37.17°, 43.19° and 62.69° correspond to (111), (200) and (220) planes of the titanium nitride phase, respectively. Fig 5.3(b) shows the titanium nitride phase along with the peaks of titanium dioxide, which confirms the partial conversion of the TiO_2 phase. Kamiya et al. also reported the conversion of anatase titanium dioxide to a rutile phase at a nitridation temperature of 700 °C [6]. As the nitridation temperature is increased to 950 °C, the oxide phase disappears and forms the phase pure titanium nitride. Fig 5.3(c) shows the phase pure titanium nitride formation by comparing with the ICDD pattern, 00-038-1420. The pattern consists of

3 peaks at 36.8°, 48.8° and 62.1°, which corresponds to the (111), (200) and (220) orientations of the titanium nitride. Table 5.1 shows the estimated lattice parameter and the average crystallite size of the nitridated films. Wei et al. reported a reduction in the lattice parameter with an increase in temperature as a result of a reduction in the oxygen content [21]. As discussed in the SEM analysis in the section 5.3.1, the reduction in the grain boundary with an increase in nitridation temperature may be the reason behind the increased crystallite size.

5.2.2 X-ray photoelectron spectroscopy

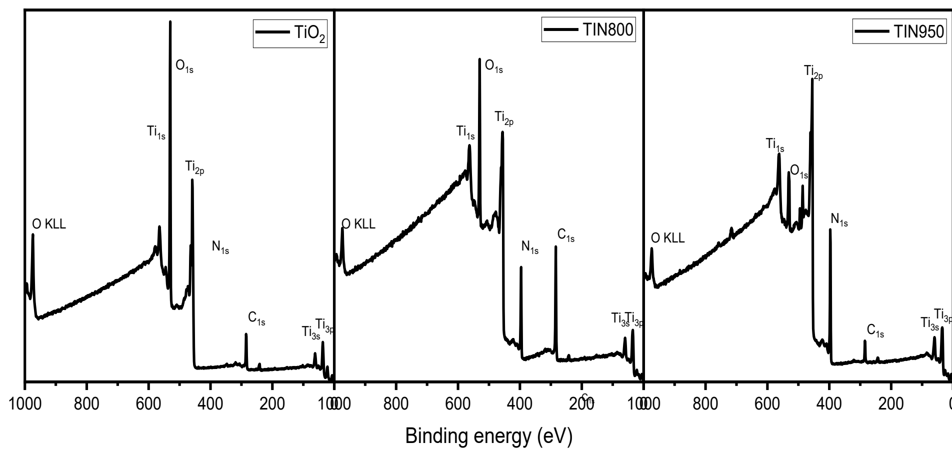

Fig 5.4. Survey scan XPS spectra of the films a) titanium dioxide b) titanium dioxide after nitridation at 800ºC c) titanium dioxide after nitridation at 950ºC

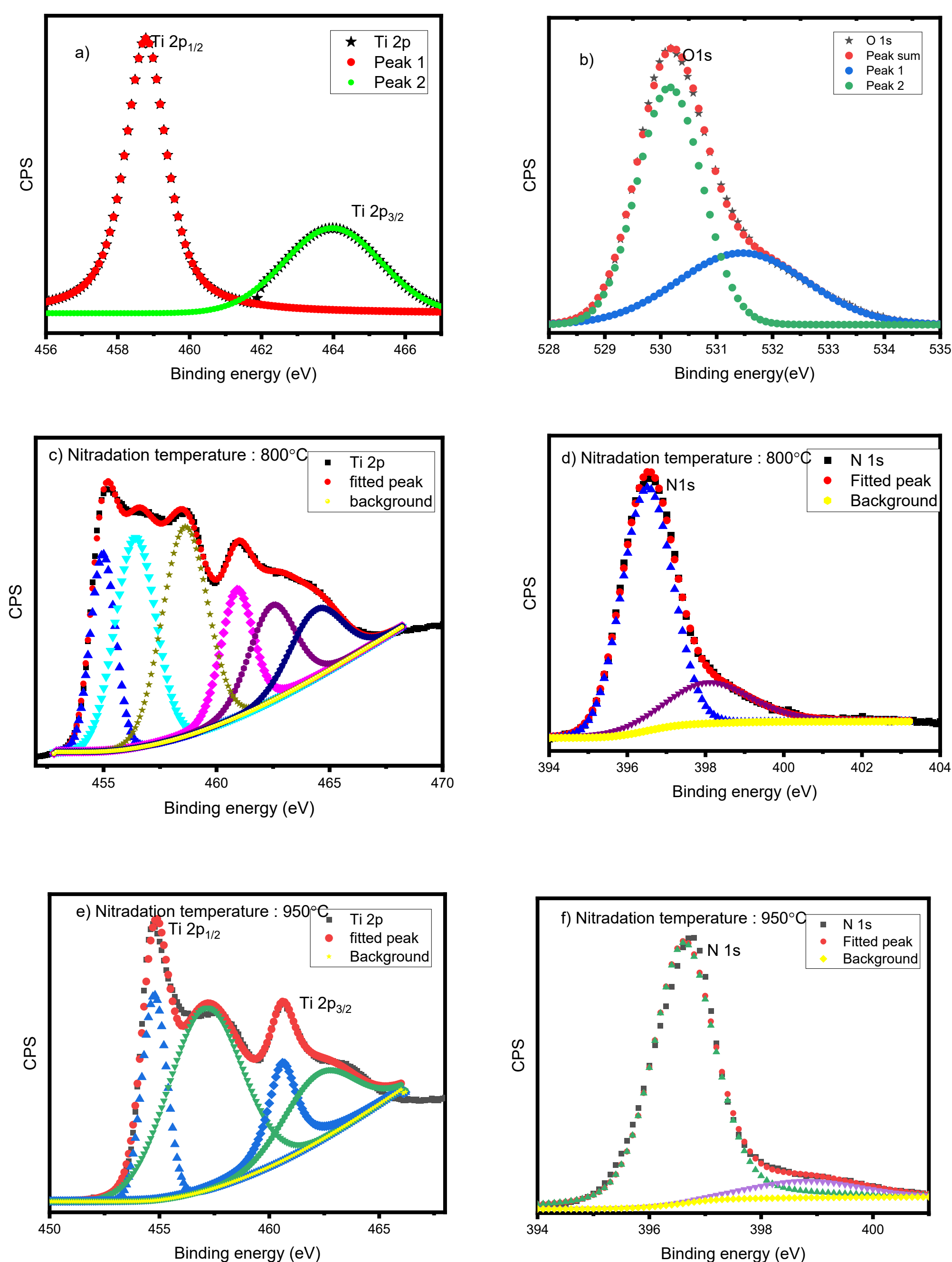

Fig 5.5. High resolution scan spectra of (a, b) Ti 2p and O 1s of air annealed TiO_2 film, (b,c) Ti 2p and N 1s of 800°C nitridated film, and (e, f) Ti 2p and N 1s of 950°C nitridated film, respectively.

Fig.5.4 (a-c) illustrate the survey scan spectra of titanium dioxide film and the films nitridated at temperature 800°C and 950°C. Fig. 5.5 shows the high-resolution x-ray photoelectron spectroscopy scan spectra of the samples. The binding energy calibration of obtained XPS core level peaks was done with C1s peak position of 284.6 eV. The Tougaard background correction has been done for Ti core level spectra [22]. The peaks were deconvoluted using XPSPEAK4.1 software. A combination of Gaussian Lorentzian functions was used to fit each peak. The high-resolution scan of Ti 2p and O 1s core levels in the titanium dioxide film is shown in Fig. 5.5 (a,b), respectively. The Ti $2p_{3/2}$ and Ti $2p_{1/2}$ exist at 458.8 and 464 eV, respectively. The peak positions of the Ti 2p doublet and their separation of 5.8 eV agree well with the binding energy reported for TiO_2 [22]. The core level O1s consists of one major peak at 530.8eV, which corresponds to lattice oxygen (O^{2-}) [23]. The peaks of pure TiO_2 are located at 532 eV and belong to either the surface hydroxyl groups (OH^-) or due to surface contamination [24].

Fig. 5.5 (c, d) represents the high resolution XPS scan of titanium dioxide film after the nitridation at 800 °C. The XRD pattern confirmed the existence of titanium dioxide and titanium nitride formation in the sample after nitridation at 800 °C. The nitrogen 1s core level in Fig. 2d represents both Ti-N phase at 396.6 eV and the oxynitride phase at 398.3 eV [25]. Hence, the Ti core level spectra were deconvoluted with respect to the valency state of titanium dioxide, titanium oxynitride and titanium nitride, where the corresponding binding energy states are reported by Jeyachandran et al., as shown in Table 5.2 [26]. The peak deconvolution confirmed mixed phase formation at the nitridation temperature of 800 °C. Liu et al. reported the identification of such mixed phases after the nitridation of titanium dioxide powder. [12].

Table 5.2. Peak assignments for TiO_2, TiN, TiON

Peak	*Ti $2p_{3/2}$ (eV)*	*Ti $2p_{1/2}$ (eV)*
TiN	460.8	455.4 [14]
TiN shake-up	462.6	457.2 [10]
TiO_xN_y	462.4	457.4 [14]
TiO_2	463.8	458.8 [14]

Fig. 5.5 (e, f) illustrates the core level peaks of titanium and nitrogen in the film nitridated at 950 °C. The complex Ti 2p core spectra of TiN_x consist of two main peaks and two shake-up peaks, as shown in Table 2. The peak shape obtained largely agrees with that reported by Jaegar [22]. The discrete intrinsic electron-electron interaction in the sample may be the reason for the emergence of shake up photoelectron peaks [27]. There were many interpretations of the origin of the shake up nature of the films [28-29]. The generated photoelectron during the emission process of XPS analysis interacts with and excites the valance electrons in the material and loses an amount of energy in the process. The whole response to this process constitutes a main and shake-up photoelectron peak. Porte et al. reported that as the nitrogen content was increased, the shake-up photoelectron peak disappeared below a critical limit of $x < 0.8$ in TiN_x [30]. The core level spectra of the titanium nitride formed after the nitridation at 950 °C were deconvoluted to 4 peaks, as shown in Fig. 5.5 e, which confirms the near stoichiometric nature of the film. The presence of titanium dioxide phase in the film nitridated at a temperature 950 °C was ruled out in the X-ray diffraction and XPS analyses.

The nitrogen core level spectra consist of a high intensity peak at 396.1 eV corresponding to the titanium nitride phase [26]. Bertóti et al. claim that the

shake-up lines in TiN can be separated from any TiO_xN_y contributions; however, according to them, it is difficult to separate in the case of very low oxygen concentrations [31].

5.2.3 Analysis of Raman spectra

The GI-XRD pattern confirmed the anatase phase of titanium dioxide in the samples. The factor group analysis indicates the 15 optical modes for the anatase phase in which the A_{1g}, B_{1g} and Eg modes are Raman active in 100-900 cm^{-1} region. The prominent characteristic peaks of titanium dioxide film at 144 and 194 cm^{-1}, along with other minor peaks, are listed in Table 5.3 [32-33]. Fig. 5.6a shows the Raman spectrum of the 550 °C air annealed film, which exhibits prominent Raman modes corresponding to the anatase phase with minor peaks at 398, 515 and 640 cm^{-1}. When the TiO_2 films are subjected to nitridation at 800 °C a combined process of reduction-nitridation takes place. Fig. 5.6b exhibits a Raman spectrum of the intermediate phase between oxide and nitride as a combined phase of TiO_2 and TiN. The combined phase of titanium dioxide and titanium nitride consists of Raman modes at 150, 200, 521, 631, 1083 cm^{-1}. The peak position corresponding to transverse acoustic (TA) mode at 200 cm^{-1} of titanium nitride is slowly emerging. The intensity of TiO_2 mode E_g at 144 cm^{-1} reduces and shifts to 150 cm^{-1}. As the temperature is increased, the peak again shifts to 200 $cm^{-1,}$ corresponding to the TA mode of titanium nitride. Due to Oh symmetry, first-order Raman scattering is forbidden in NaCl structured molecules [34]. However, because of the presence of a high percentage of defects owing to the deficiency of one component, a defect-induced first-order Raman scattering is readily observed [35]. In Fig. 5.6 c the TA peak at 200 cm^{-1} arises because of vacancy type defects due to nitrogen deficiency so that the Ti atom vibrations contribute to a larger

intensity of these peaks. The peaks at 312, 440, 535, 836, 1078 cm^{-1} correspond to longitudinal acoustic (LA), second-order TA (2TA), first-order transverse optical mode (TO), combination mode of LA+TA and second-order TO mode (2TO), respectively [36-37]. The modes are also tabulated in Table 5.3 with possible origins.

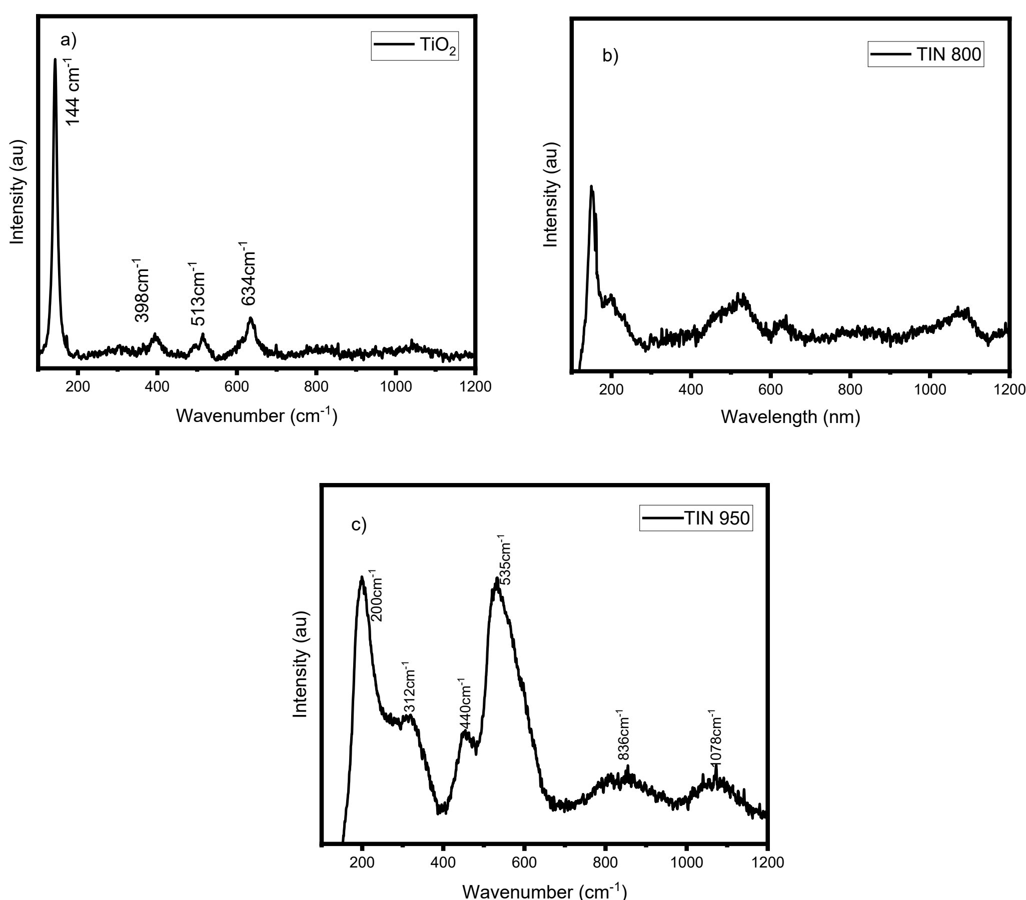

Fig. 5.6. Raman spectra of the films a) titanium dioxide b) after nitridation at 800°C c) after nitridation at 950 °C

Table 5.3. Raman modes of titanium dioxide and titanium nitride

Titanium dioxide		**Titanium Nitride**	
Peak position (cm^{-1})	Mode	Peak position (cm^{-1})	Modes and their Origin
144	Eg	200	First order Transverse acoustic mode (TA)
194	Eg	300	First order longitudinal acoustic mode (LA)
398	B_{1g}	400	Second order Transverse acoustic mode (2TA)
515	A_{1g} and B_{1g}	500	TA + LA
640	E_{1g}	520 to 580	First order transverse optical mode (TO)
		600	Second order longitudinal acoustic mode (2LA)
		800	LA + TO
		1100	Second order transverse optical mode (2TO)

5.3 MORPHOLOGY ANALYSIS

5.3.1 surface morphology

Fig. 5.7. represents the variation in the surface morphologies of the titanium dioxide film and the titanium nitride films after nitridation treatments at 800 °C and 950 °C. The as-deposited films have smooth crack-free surfaces. As the initial TiO_2 film is treated with ammonia at a temperature 800 °C, the formation of needle-type crystal structure occurs. The size of the needle-type crystal structure increased when the nitridation temperature was further increased. This may cause an increase in average surface roughness in the films. Jeyachandran et al. also observed such needle-like formation in DC sputtered titanium nitride films [26]. The cross-section image of the films nitridated at temperatures 800 °C and 950 °C are shown in Fig 5.8. The thickness of the films were estimated to be around 100nm for both films from these images.

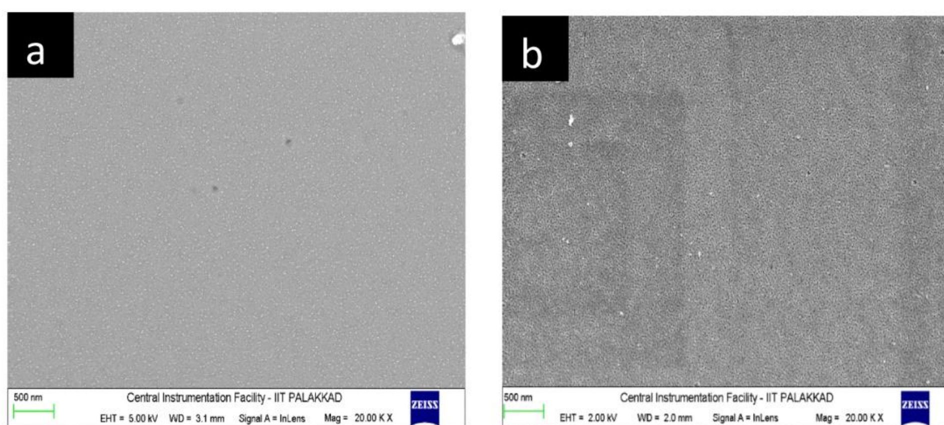

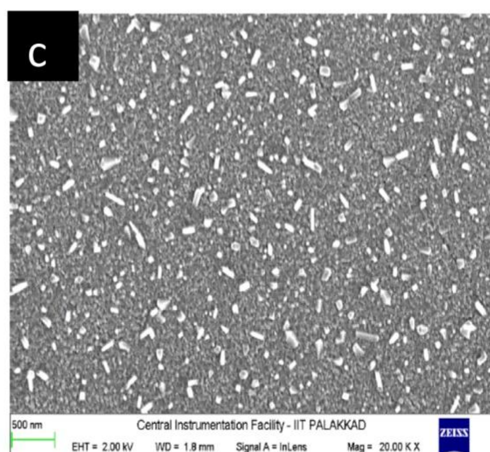

Fig. 5.7. Surface morphology of a) TiO_2 film, and the films nitridated at temperatures b) 800 °C and c) 950 °C

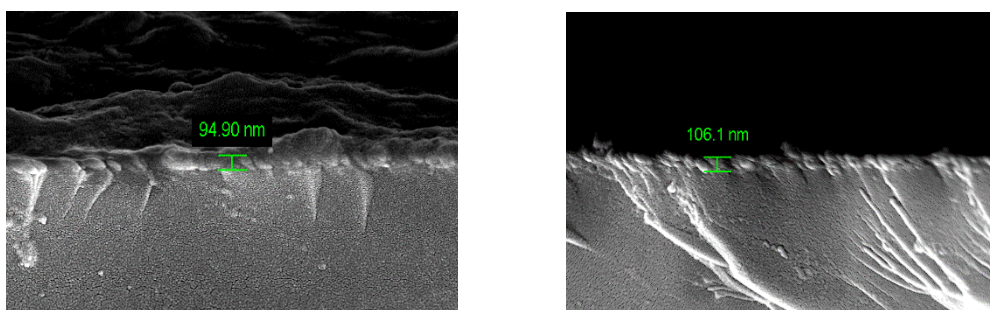

Fig. 5.8. Cros-section images of the films nitridated at temperatures a) 800 °C and b) 950 °C

5.3.2. Atomic force microscopic analysis

Fig 5.9 illustrates the 2D and 3D variations in the surface roughness of the as-deposited TiO_2 film and the films after nitridation at 800 °C and 950 °C. The scan area was fixed at 5 μm × 5 μm for all samples. As the nitridation temperature is increased, the average surface roughness of the sample is

increased from 0.613 nm to 0.907 nm, as seen in Table 5.4. Roughness in titanium dioxide film are reported to vary from 0.2nm to higher values with increased film thickness [38-39]. Further, increase in nitridation temperature caused an increase in the roughness, where there may be a contribution due to the increased crystallite size [40]. As estimated by the Scherrer equation, the 550 °C air annealed titanium dioxide film had a small crystallite size, which possessed reduced average surface roughness. The needle-like formation may also have an impact on the increased roughness in the 900 °C nitridated film. Moreover, the protrusion height also increased with the nitridation temperature. The increased roughness for the sample TIN950 is evident from the 2D AFM images. The 2D AFM and FESEM images of spin coated TiO_2 indicates similar resemblance.

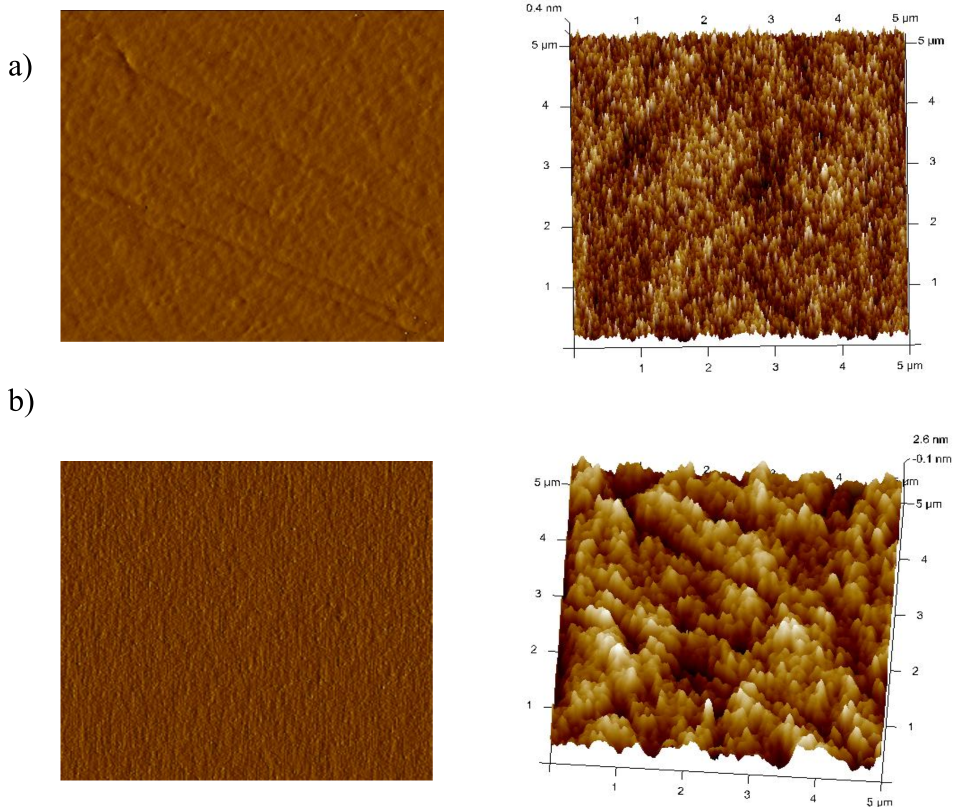

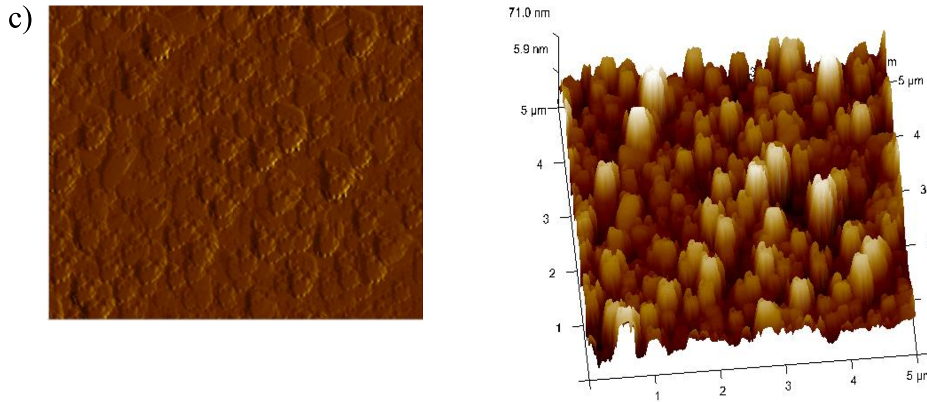

Fig. 5.9. 2D and 3D AFM images of a) TiO_2 film and the films nitridated at temperatures b) 800 °C and c) 950 °C

Table 5.4. Average surface roughness in TiO_2 and nitridated films

Sample name	Average roughness (nm)
TiO_2	0.613
TiN800	0.907
TiN950	9

5.4 INVESTIGATION OF THE ELECTRICAL PROPERTIES OF THE FILMS

Hall measurements were carried out in van der Pauw configuration with a constant magnetic field of 1.05 T to study the electrical properties of the films. Carrier concentration, mobility and resistivity estimated were given in Table 5.5. The negative sign of the Hall coefficient and carrier concentration verified the n-type nature of the films. Titanium dioxide films were reported

to have high electrical resistivity of the order of 10^6 Ω·cm [41] owing to the variations with respect to thickness and to the O/Ti ratio in the films [42]. When the TiO_2 films were subjected to nitridation at temperatures of 800 °C and 900 °C, the crystal structure of the TiO_2 changes, as described earlier in the section 5.1 In the case of TIN80, which consists of the mixed phases of TiO_2 and TiN, it corresponds to a carrier concentration of 10^{18}/cc, as shown in Table 5.5. However, in the film TIN950, consisting of stoichiometric TiN phase, the reduction nitridation process improved the electrical properties. The carrier concentration changed from 10^{18}/cc to 10^{22}/cc in the film nitridated at temperature of 950°C. As seen in the Table 5.5, the gradual increment in the nitridation temperature decreased the carrier mobility of the films, which may be due to the increased average surface roughness with nitridation temperature, as discussed in section 5.3 with the atomic force microscopic results [43]. TIN95 reports to have lower resistivity compared to other films. Here, the whole conversion of titanium dioxide resulted in the formation of low resistivity titanium nitride film with resistivity 10^{-4} Ω cm. which agrees with the earlier reports [44].

Table 5.5. Electrical properties of titanium nitride films with different nitridation temperature

Sample name	Carrier concentration (/cm^3)	Mobility (cm^2/Vs)	Resistivity (Ω·cm)
TIN800	4.228×10^{18}	1.79×10^{-1}	8.248×10^{0}
TIN950	6.098×10^{22}	2.50×10^{-2}	4.094×10^{-3}

The metallic nature of titanium nitride films in visible region is established from the low energy xps spectrum, as shown in Fig.5.10. XPS analysis at low binding energies can reveal the electron density within the valence band at the film surface [45]. In the case of the initial titanium dioxide film, the valence band was observed very far from the Fermi level (E_F). The valance band maximum is found to be 2.0eV. As the nitridation temperature is increased, the valance band maximum exhibits red shift, and approaches to the Fermi level, at the nitridation of 800 ºC, indicating an increase in the electric conduction [46], which can be seen in Fig. 5.10. At the nitridation temperature 950 ºC, the valance peak positioned on the Fermi level, which corresponds to the nature of a good electric conductor. Thus, the low energy XPS spectrum agrees well with the higher carrier density in titanium nitride films obtained from the Hall measurement analysis.

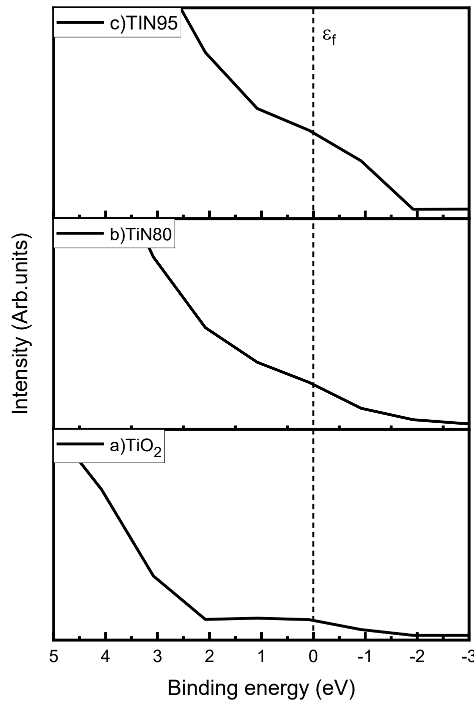

Fig. 5.10. Low energy XPS spectrum of a) titanium dioxide, b) after nitridation at 800ºC, c) after nitridation at 950ºC

5.5 OPTICAL PROPERTIES OF THE FILMS

5.5.1 Estimation of energy band gap

Wide band gap semiconductors include stoichiometric titanium nitride and titanium dioxide. Tauc's relation was used to estimate the energy band gap for the direct band gap materials [47], which is given by

$$\alpha h\upsilon = A(h\upsilon - E_g)^{\,n} \quad \text{........................(5.5)}$$

where, A is a constant, h is the planks constant, ν is frequency of light, Eg is the energy band gap and n characterize the transition process. The energy bandgap energy was estimated as shown in Fig. 5.11, by extrapolating the linear portion of the $(\alpha h\upsilon)^2$ versus energy plot to the x axis. The materials TiN and TiO_2, being direct band gap materials, the value of n is taken as 2 [48]. As seen, the band gap energy change with nitridation temperature. For the film TiO_2, which is having anatase phase, the bandgap was calculated to be 3.69eV, which agrees with earlier reports [40,49]. The combined titanium dioxide-nitride composition has a bandgap of 2.54 eV at nitridation temperature of 800°C. Xie et al described the variation of bandgap of titanium nitride film with addition of oxygen via air annealing [50]. In the present work, with increase in the nitridation temperature, the bandgap showed an increase to 2.8eV corresponding to nearly stoichiometric titanium nitride [51]. The bandgap of titanium nitride is highly composition and thickness dependent, and it varies from 2.11 to 3.4eV [52].

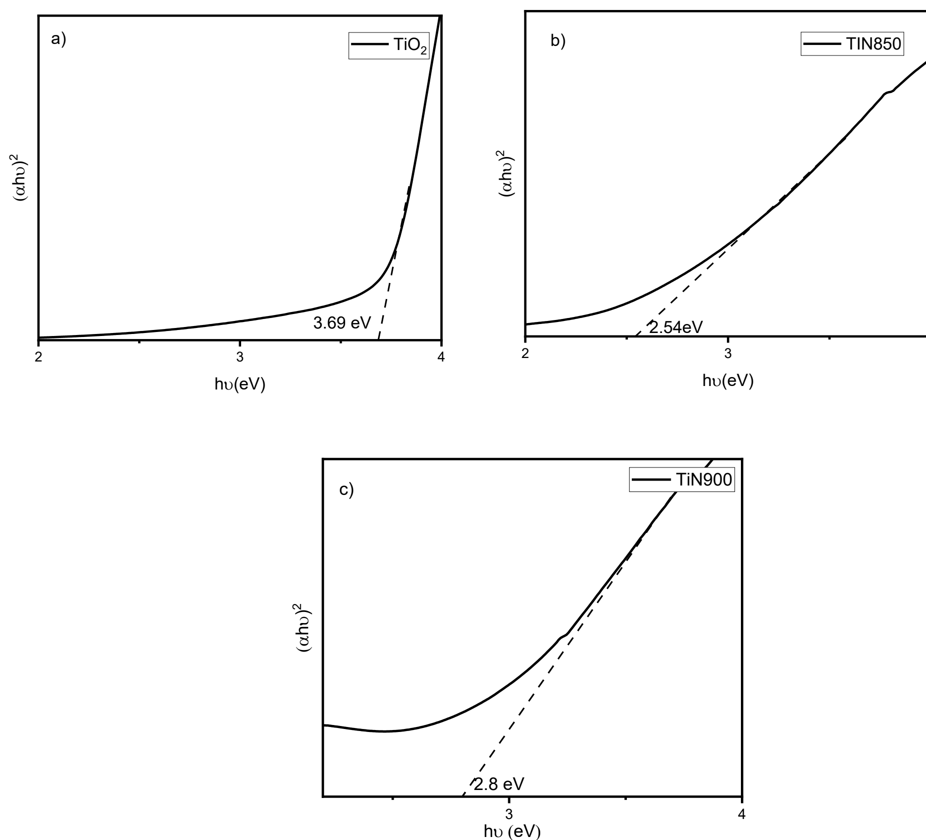

Fig. 5.11. Energy bandgap estimated for the films a) titanium dioxide b) nitridated at 800°C, and c) nitridated at 950°C

5.5.2 Plasmonic properties

TiO_2 and TiN_x are two distinct materials according to their optical properties. Titanium dioxide is transparent and exhibits a reflectance of less than 30% in the visible wavelength region. Arnaud et al. investigated the conversion of titanium dioxide film to titanium nitride through a rapid thermal nitridation treatment using a halogen infrared lamp-heated furnace

and reported percentage reflectance variation from 20% to 80% in the visible region [53]. In this work, the TiO_2 films are having absorption band around 400 nm due to the yellowish appearance of the sample, which appears as a dip in the reflectance pattern of TiO_2 films. After the nitridation at 800 °C, the reflectance of the film is reduced, and with further increase in the nitridation temperature, complete conversion of titanium dioxide to metallic titanium nitride occurs with a high electron carrier concentration 10^{22}/cc. Moreover, the films exhibit higher NIR reflectance, which confirms the suitability of the films for use as NIR reflecting mirrors, as shown in Fig. 5.12(a).

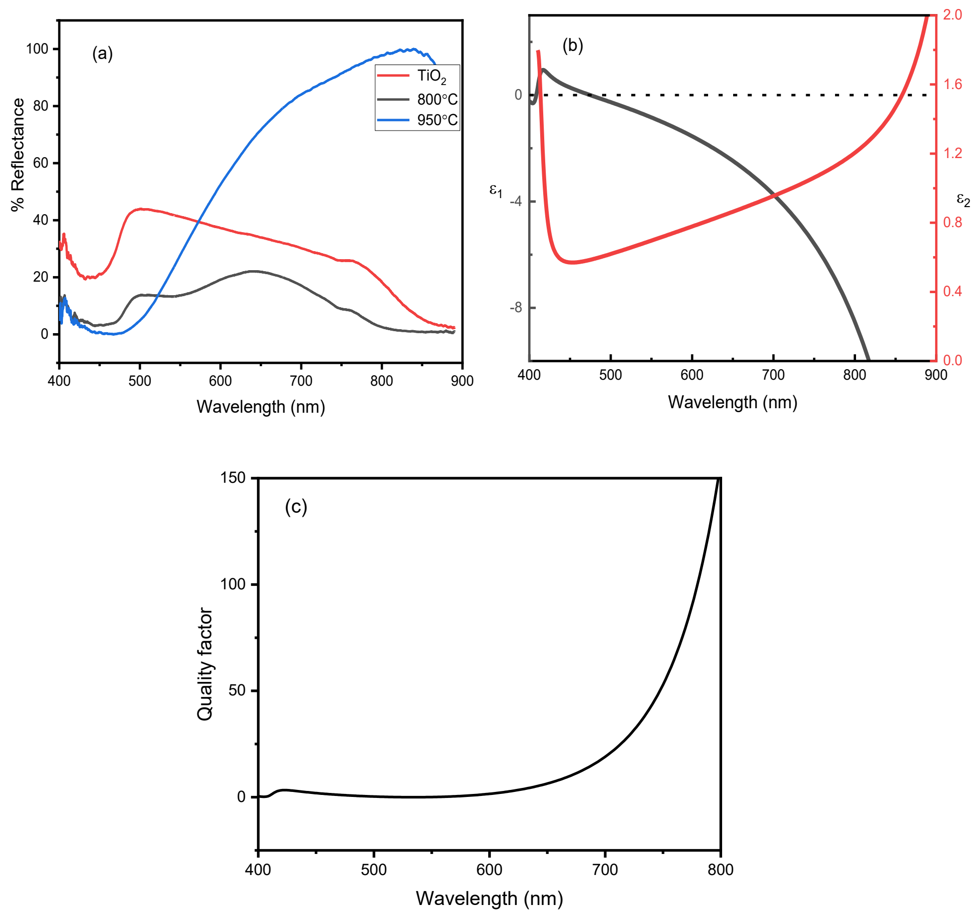

Fig 5.12 (a) Reflectance spectra of TIO_2, TIN80, TIN95, (b) extracted dielectric permittivity values for TIN95, (c) quality factor of TIN950

According to the electrical and optical results, the sample TIN950 can be further studied for the excitation of the surface plasmons. The essential parameter for surface plasmon resonance excitation is the high negative permittivity of the plasmonic material. Low loss is an important factor needed for any efficient plasmonic material.

The dielectric permittivity function is given by

$$\varepsilon(\lambda) = \varepsilon_1(\lambda) + \varepsilon_2(\lambda) \ldots\ldots\ldots\ldots (5.6)$$

where the real part of permittivity (ε_1) denotes the strength of polarization and the imaginary part of permittivity(ε_2) describes the dielectric loss of the plasmonic material. Since titanium nitride contains both free and bound electrons, Drude-Lorentz approximation was used to extract the dielectric function from the reflection spectra with the aid of a standard package, ReFfit [54]. The dielectric permittivity in terms of Drude-Lorentz approximation is given by

$$\varepsilon = \varepsilon_\infty - \frac{\omega_{pu}^2}{\omega^2 - i\Gamma_D\omega} + \sum_{j=1}^{2} \frac{f_j\omega_{oj}^2}{\omega_{0j}^2 - \omega^2 + i\gamma_j\omega} \ldots\ldots\ldots (5.7)$$

where ε_∞ is high frequency dielectric constant, greater than unity, Γ_D is the drude damping factor and ω_{0j} is the Lorentz oscillator with damping factor γ_j. $\Gamma_D = \frac{e}{\mu m^*}$ is the loss-related Drude relaxation rate, or called momentum scattering rate [55-56].

The extracted permittivity values for the TiN_X film obtained after nitridation at 950 °C having high carrier concentration are shown in Fig 5.12(b). With the increase in wavelength, the ε_1 exhibits a decreasing trend with positive to negative values, and the negative permittivity region starts from 463 nm. As seen, the dielectric loss is <1.5 in the whole 400-900 nm wavelength region,

that is, throughout the visible region, which confirms the low loss behaviour of the film. As seen the dielectric loss (ε_2) increases after the crossover wavelength. The negative permittivity indicates the suitability of the films for SPR excitation in the visible region. These properties indicates the usage of TiO_2 derived TiN_x as efficient plasmonic material for SPP excitation.

5.6 EXCITATION OF SURFACE PLASMON RESONANCE

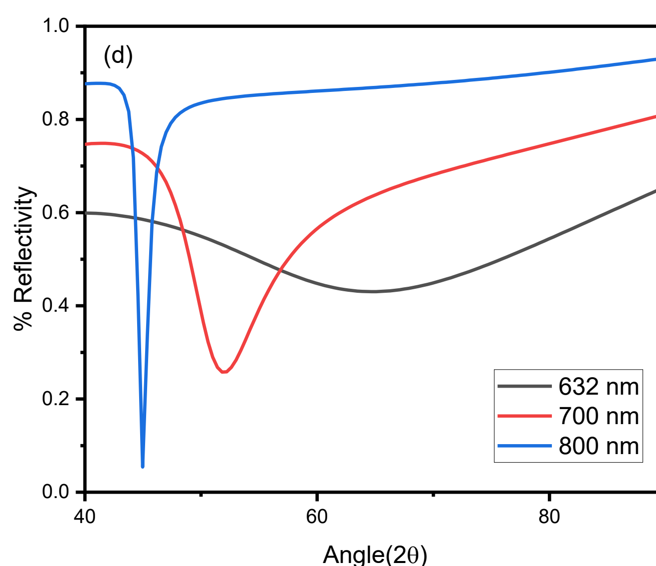

Fig 5.13 SPR theoretical curve obtained in angular interrogation mode

In order to further explore the plasmonic behaviour on the TiO_2 derived nitride films, a simulation study has been carried out using a 3-layer geometry consisting of a BK7 prism, metallic film, and air as dielectric medium [57]. For the excitation surface plasmons in thin metallic film, one would require a momentum matching mechanism, which is normally

provided by a prism geometry. Rajak et al theoretically predicted the spectral curve intensity using Fresnel's reflection formula [58]. The multilayer model depends on the dielectric permittivity of the layers and thickness of the film[59]. The equation for 3-layer reflectance is given as,

$$r_{123} = \frac{r_{12}+r_{23}e^{2ikz_2d_2}}{1+r_{p2}+r_{23}e^{2ikz_2d_2}} \quad \text{.......................(5.8)}$$

where 1,2,3 represents each layer, k_{z2} represents wavevector of the film and d_2 is the thickness of the film. Using the above formula, the polarised reflections from film-air interface after total internal reflection were modelled using Winspall software [60], in angular interrogation mode with monochromatic sources of wavelength 632nm, 700nm and 800nm. The permittivity values extracted from the DL model were used for the study. The simulation study revealed the excitation of surface plasmon resonance with a broad curve with resonance angle of ~65°, as shown in Fig 5.13. Quality factor for the Surface Plasmon Polariton (SPP) propagation is given by [61]

$$Q = < -\varepsilon_1^2 > / < \varepsilon_2 > \quad \text{........................(5.9)}$$

The quality factor for the sample at 632.8nm wavelength is found to be more than 5. With further increase in the wavelength of incident light from 632 to 800nm, the resonance dip shifted to lower resonance angles from 65° to 45°. It is evident from the Fig 5.12 (c) that the increment in wavelength contributes to the increased quality factor. Thereby increases the plasmonic properties of the films in higher wavelength. SPR excitation shows a narrow bandwidth response at higher wavelength region. The reported quality factor for titanium nitride film coated on sapphire substrate is less than 100 in the visible region of wavelength [62]. Resulting SPR dip are broader compared to the narrow resonance dip obtained here at an angle

of 45º angle. The narrow resonance curve directs the use of these for sensing applications. In SPR sensing, the narrowness of the resonance curve (or full width at half maximum, FWHM) is critically important, because it directly governs the sensitivity, resolution, and detection accuracy of the sensor [63]. A narrow resonance curve corresponds to reduced optical losses [64] and longer plasmon propagation lengths [65] which lead to sharper resonance curves. This sharpness allows even small changes in the refractive index at the sensing interface to generate a measurable spectral change, thereby increasing the detection limit of the sensor. The quality factor obtained for the films possess higher values compared to that of gold, which indicates an enhanced plasmonic performance of TiO_2 derived TiN_x films [66,67].

5.7 CONCLUSION

Stoichiometric titanium nitride film exhibiting plasmonic behaviour with higher quality factor 5 to 50 in the visible region has been fabricated successfully via nitridation of spin-coated titanium dioxide film, for the first time. The nitride films possessed high carrier concentration of the order of 10^{22}/cc, needed for the excitation of SPP in visible region. GI-XRD, XPS and Raman spectroscopic studies provided detailed structural confirmation. The optical and electrical results were correlated, and the low loss nature with $\varepsilon_2 < 1.5$ for the film nitridated at 950 °C was verified with the Drude-Lorentz approximation. A 3-layer geometry based on Fresnel equation has been used to investigate the plasmonic behaviour in the developed films. The study revealed an excitation wavelength of 800 nm for a narrow resonance dip at an incidence angle of 45º, suitable for further sensing applications.

5.8 REFERENCES

1. Helen Y. Playford, (2020),Variations in the local structure of nano-sized anatase TiO2, J. Solid State Chem., 288, 121414, DOI:10.1016/j.jssc.2020.121414.

2. Dongsun Yoo, Ilgon Kim, Sangsoo Kim, Chang Hie Hahn, Changyu Lee, Seongjin Cho, (2007), Effects of annealing temperature and method on structural and optical properties of TiO2 films prepared by RF magnetron sputtering at room temperature, Appl. Surf. Sci., 253, 3888-3892 DOI: 10.1016/j.apsusc.2006.08.019.

3. Haggerty, James & Schelhas, Laura & Kitchaev, Daniil & Mangum, John & Garten, Lauren & Sun, Wenhao & Stone, Kevin & Perkins, John & Toney, Michael & Ceder, Gerbrand & Ginley, David & Gorman, B. & Tate, Janet. (2017), High-fraction brookite films from amorphous precursors. Sci. Rep. 7, 15232 DOI:10.1038/s41598-017-15364-y.

4. A.F. Wells, (1975) Structural inorganic chemistry, 4th ed., Oxford University Press, London,. Doi: 10.1038/157386a0.

5. Valour, Arnaud & Usuga Higuita, Maria & Guillonneau, Gaylord & Crespo-Monteiro, Nicolas & Jamon, Damien & Hochedel, Marion & Michalon, Jean-Yves & Reynaud, S. & Vocanson, Francis & Jiménez, Carmen & Langlet, Michel & Donnet, Christophe & Jourlin, Yves. (2021), Optical, electrical and mechanical properties of TiN thin film obtained from a TiO2 sol-gel coating and rapid thermal nitridation, Surf. Coat. Technol., 413, 127089. 10.1016/j.surfcoat.2021.127089.

6. Kamiya, K., Yoko, T. & Bessho, M. (1987), Nitridation of TiO2 fibres prepared by the sol-gel method, J. Mater. Sci. 22, 937–941, DOI:10.1007/BF01103533.

7. Kamiya, K., Nishijima, T. and Tanaka, K. (1990), Nitridation of the Sol–Gel-Derived Titanium Oxide Films by Heating in Ammonia Gas. J. Am. Ceram. Soc., 73, 2750-2752. DOI : 10.1111/j.1151-2916.1990.tb06758.x

8. Moon, G.D., Joo, J.B., Dahl, M., Jung, H. and Yin, Y. (2014), Nitridation and Layered Assembly of Hollow TiO2 Shells for Electrochemical Energy Storage. Adv. Funct. Mater., 24, 848-856. DOI: 10.1002/adfm.201301718

9. Mojtaba Samiee, Jian Luo, (2014), A facile nitridation method to improve the rate capability of TiO2 for lithium-ion batteries, J. Power Sources, 245, 594-598, DOI: 10.1016/j.jpowsour.2013.06.113

10. Cooper, D. A., & Ljungstroem, E. B. (1988), Decomposition of ammonia over quartz sand at 840-960.degree.C. Energy & Fuels, 2(5), 716–719.DOI:10.1021/ef00011a019

11. Duta L, Stan GE, Popa AC, Husanu MA, Moga S, Socol M, Zgura I, Miculescu F, Urzica I, Popescu AC, (2016), Thickness Influence on In Vitro Biocompatibility of Titanium Nitride Thin Films Synthesized by Pulsed Laser Deposition, Materials, 9, 38 DOI : 10.3390/ma9010038

12. Liu Y, Wang Y, Zhang Y, You Z, Lv X. (2020), Mechanism on reduction and nitridation of micrometer-sized titania with ammonia gas, J. Am. Ceram. Soc., 103, 3905–3916, DOI: 10.1111/jace.17067

13. Sato, T., Yasuda, S., Usuki, K., Yoshioka, T., & Okuwaki, A. (1996), Synthesis of titanium nitride by a spark-discharge method in liquid ammonia. J. Mater. Sci. 31, 2495–2499 . DOI: 10.1007/BF01152967

14. Kawano, S., Takahashi, J. and Shimada, S. (2003), Spark Plasma Sintering of Nano-Sized TiN Prepared from TiO2 by Controlled Hydrolysis of TiCl4 and Ti(O-i-C3H7)4 Solution. J. Am. Ceram. Soc., 86, 1609-1611. DOI: 10.1111/j.1151-2916.2003.tb03524.x

15. Martínez-Ferrero, E., Sakatani, Y., Boissière, C., Grosso, D., Fuertes, A., Fraxedas, J. and Sanchez, C. (2007) Nanostructured Titanium Oxynitride Porous Thin Films as Efficient Visible-Active Photocatalysts, Adv. Funct. Mater., 17, 3348-3354. DOI :10.1002/adfm.200700396

16. Gartner, Mariuca & Osiceanu, P. & Anastasescu, Mihai & Stoica, Toma & Trapalis, Christos & Giannakopoulou, Tatiana & Todorova, Nadia & Lagoyannis, Anastasios. (2008). Investigation on the nitrogen doping of multilayered, porous TiO2 thin films. Thin Solid Films. 516. 8184-8189.DOI: 10.1016/j.tsf.2008.04.027.

17. Keddie, J.L., Li, J., Mayer, J.W. and Giannelis, E.P. (1991), Effect of Nitridation Rate on the Composition and Conductivity of Titanium Nitride Films Prepared from Sol–Gel Titania. J. Am. Ceram. Soc., 74, 2937-2940. DOI:10.1111/j.1151-2916.1991.tb06869.x

18. Romero-Gomez, P. & Rico, V. & Espinós, Juan & Gonzalez-Elipe, Agustin & Palgrave, Robert & Egdell, Russell. (2011), Nitridation of nanocrystalline TiO2 thin films by treatment with ammonia. Thin Solid Films. 519, 3587-3595. DOI: 10.1016/j.tsf.2011.01.267.

19. Tohru Hara, Kouichi Tani, Ken Inoue, Shigeaki Nakamura, Takeshi Murai (1990), Formation of titanium nitride layers by the nitridation of titanium in high-pressure ammonium ambient. Appl. Phys. Lett. 15, 57, 1660–1662. DOI:10.1063/1.104078

20. Ryland, A. L. (1958). X-ray diffraction. Journal of Chemical Education 35, 80.

21. Wei, H., Wu, M., Dong, Z., Chen, Y., Bu, J., Lin, J., Yu, Y., Wei, Y., Cui, Y , Wang, R, (2017), Composition, microstructure and SERS properties of titanium nitride thin film prepared via nitridation of sol–gel derived titania thin films, J. Raman Spectrosc., 48, 578–585, DOI: 10.1002/jrs.5080

22. Dominik Jaeger, Jörg Patscheider, (2012), A complete and self-consistent evaluation of XPS spectra of TiN, J. Electron Spectros. Relat. Phenomena., 185, 523-534 DOI: 10.1016/j.elspec.2012.10.011

23. Hu W, Liu Y, Withers RL, Frankcombe TJ, Norén L, Snashall A, Kitchin M, Smith P, Gong B, Chen H, Schiemer J, Brink F, Wong-Leung J., (2013), Electron-pinned defect-dipoles for high-performance colossal permittivity materials, Nat. Mater., 9, 821-6 DOI: 10.1038/nmat369X.

24. Xiao Fan, Jun Fan, Xiaoyun Hu, Enzhou Liu, Limin Kang, Chunni Tang, Yongning Ma, Huitong Wu, Yinye Li, (2014), Preparation and characterization of Ag deposited and Fe doped TiO2 nanotube arrays for photocatalytic hydrogen production by water splitting, Ceram. Inter., 40, 15907-15917 DOI:10.1016/j.ceramint.2014.07.119Y.

25. Yu Zhang, Tao Wang, Ming Zhou, Yong Wang, Zhengmei Zhang, (2017), Hydrothermal preparation of Ag-TiO2 nanostructures with exposed {001}/{101} facets for enhancing visible light photocatalytic activity, Ceram. Int, 43, 3118-3126 DOI: 10.1016/j.ceramint.2016.11.127.

26. Y.L. Jeyachandran, Sa.K. Narayandass, D. Mangalaraj, Sami Areva, J.A. Mielczarski, (2007), Properties of titanium nitride films prepared by direct current magnetron sputtering , Mat. Sci. and Eng. A, 445-446, 223-236 DOI:10.1016/j.msea.2006.09.021

27. S. Hüfner, (2003), Photoelectron Spectroscopy, Springer-Verlag, Berlin, Heidelberg, New York, , p. 682.

28. K.S. Kim, R.E. Davis, (1973), Electron spectroscopy of the nickel-oxygen system, J. Electron Spectrosc. Relat. Phenom, 1, 251-258, DOI: 10.1016/0368-2048(72)85014-X

29. Sven Larsson, (1976), Satellites in ESCA inner-shell spectra of 3d0 transition metal complexes, J. Electron Spectrosc. Relat. Phenom, 8, 171-178 DOI: 10.1016/0368-2048(76)81003-1

30. Porte, Louis and Roux, Laurent and Hanus, Jean, (1983), Vacancy effects in the x-ray photoelectron spectra of TiNX, Phys. Rev. B, 28, 3214-3224.DOI :10.1103/PhysRevB.28.3214

31. Bertóti, M. Mohai, J.L. Sullivan, S.O. Saied, (1995), Surface characterization of plasma-nitrided titanium: an XPS study, Appl. Surf. Sci., 84, 357-371, DOI:10.1016/0169-4332(94)00545-1.

32. Lewkowicz A., Synak A., Grobelna B., Bojarski P., Bogdanowicz R., Karczewski J., Szczodrowski, K., & Behrendt M. (2014), Thickness and structure change of titanium (IV) oxide thin films synthesized by the sol–gel spin coating method. Optical Materials, 36, 1739–1744. DOI:10.1016/j.optmat.2014.02.033

33. U. Balachandran, N.G. Eror (1982) Raman spectra of titanium dioxide, J. Solid State Chem., 42, 276-282, DOI:10.1016/0022-4596(82)90006-8.

34. Kaiser, R., Spencler, W. and Möller, W, (1973), Impurity Induced Raman Spectra of Annealed and Quenched NaCl: Ca Crystals. phys. stat. sol. (b) 55, 659-666, DOI:10.1002/pssb.2220550222

35. Logothetidis, S., Meletis, E.I. & Kourouklis, G. (1999), New approach in the monitoring and characterization of titanium nitride thin films, J. Mater. Res. 14, 436–441 DOI: 10.1557/JMR.1999.0062

36. Chowdhury, R., Vispute, R.D., Jagannadham, K. (1996), Characteristics of titanium nitride films grown by pulsed laser deposition, J. Mater. Res., 11, 1458–1469 DOI: 10.1557/JMR.1996.0182

37. M. Stoehr, C.-S. Shin, I. Petrov, and J. E. Greene (2011), Raman scattering from TiNx ($0.67 \leq x \leq 1.00$) single crystals grown on MgO (001), J. Appl. Phys. 110, 083503 doi: 10.1063/1.3651381

38. Puurunen RL, Sajavaara T, Santala E, Miikkulainen V, Saukkonen T, Laitinen M, Leskelä M. (2011), Controlling the crystallinity and roughness of atomic layer deposited titanium dioxide films. J Nanosci Nanotechnol. 11, 8101-7 DOI: 10.1166/jnn.2011.5060.

39. Tahernia, Atefeh & Raoufi, Davood, (2018), Thickness dependence of structural, optical and morphological properties of sol-gel derived TiO2 thin film. Materials Research Express. 6, 016417 DOI: 10.1088/2053-1591/aae4d0.

40. Qi, R., Pan, L., Feng, Y., Wu, J., Li, W., Wang, Z., (2020), Evolution of chemical, structural, and mechanical properties of titanium nitride thin films deposited under different nitrogen partial pressure, Results in Physics, 19, 103416 DOI:10.1016/j.rinp.2020.103416

41. A.A. Akl, H. Kamal, K. Abdel-Hady, (2006), Fabrication and characterization of sputtered titanium dioxide films, App Surf Sci, 252, 8651-8656 DOI:10.1016/j.apsusc.2005.12.001.

42. Yunjie Fan, Chao Zhang, Xiang Liu, Yue Lin, Guanyin Gao, Chao Ma, Yuewei Yin, Xiaoguang Li, (2019),Structure and transport properties of titanium oxide (Ti2O, TiO1+δ, and Ti3O5) thin films, J. Alloy Comp, 786, 607-613 DOI: 10.1016/j.jallcom.2019.01.381.

43. M. Geiger, R. Acharya, E. Reutter, T. Ferschke, U. Zschieschang, Jürgen Weis, J. Pflaum, H. Klauk, R. T. Weitz, (2020), Effect of the Degree of the Gate-Dielectric Surface Roughness on the Performance of Bottom-Gate Organic Thin-Film Transistors, Adv. Mater. Interfaces, 7, 1902145. DOI: 10.1002/admi.201902145

44. K. Lal, A.K. Meikap, S.K. Chattopadhyay, S.K. Chatterjee, M. Ghosh, K. Baba, R. Hatada, (2001), Electrical resistivity of titanium nitride thin films prepared by ion beam-assisted deposition, Physica B: Condensed Matter, 307, 150-157

45. O. Akhavan, 2010, The effect of heat treatment on formation of graphene thin films from graphene oxide nanosheets, carbon 48, 509-519, DOI:10.1016/j.carbon.2009.09.069

46. Akhavan O, Azimirad R, Moshfegh AZ. (2008), Self-encapsulation of single-texture CoSi2 nanolayer by TaSi2. Thin Solid Films, 516, 6008-12, DOI:10.1016/j.tsf.2007.10.100

47. J. Tauc, (1972) Optical Properties of Solids ,North-Holland Pub, Amsterdam,

48. A.A. Akl, H. Kamal, K. Abdel-Hady, (2006), Fabrication and characterization of sputtered titanium dioxide films, App. Surf. Sci, 252, 8651-8656 DOI:10.1016/j.apsusc.2005.12.001.

49. Aneta Lewkowicz, Anna Synak, Beata Grobelna, Piotr Bojarski, Robert Bogdanowicz, Jakub Karczewski, Karol Szczodrowski, Mirosław Behrendt, (2014), Thickness and structure change of titanium (IV) oxide thin films synthesized by the sol–gel spin coating method, Optical Materials, 36, 1739-1744.

50. Zheng Xie, Xiangxuan Liu, Peng Zhan, Weipeng Wang, and Zhengjun Zhang, (2013), Tuning the optical bandgap of TiO2-TiN composite films as photocatalyst in the visible light, AIP Advances 3, 062129, doi: 10.1063/1.4812702

51. Kavitha, R. Kannan, P. Sreedhara Reddy, S. Rajashabala, (2016), J. Mater. Sci. 27, 10427–10434 DOI:10.1007/s10854-016-5130-0

52. M. Abd El-Rahman, S. H. Mohamed, Mohd Taukeer Khan & M. A. Awad. (2021), Plasmonic performance, electrical and optical properties of titanium nitride nanostructured thin films for optoelectronic applications. J. Mater.

Sci.: Mater. Electron.,. 32, 28204–28213,. DOI:10.1007/s10854-021-07197-3.

53. Arnaud Valour, Maria Alejandra Usuga Higuita, Gaylord Guillonneau, Nicolas Crespo-Monteiro, Damien Jamon, Marion Hochedel, Jean-Yves Michalon, Stéphanie Reynaud, Francis Vocanson, Carmen Jiménez, Michel Langlet, Christophe Donnet, Yves Jourlin, (2021) Optical, electrical and mechanical properties of TiN thin film obtained from a TiO2 sol-gel coating and rapid thermal nitridation, Surf. Coat. Tech. 413, 127089, DOI:10.1016/j.surfcoat.2021.127089

54. Kuzmenko, Alexey. Kuzmenko, A. (2005), Kramers-Kronig constrained variational analysis of optical spectra. Rev. Sci. Instrum. 76, 083108, DOI:10.1063/1.1979470.

55. Judek, J., Wróbel, P, Michałowski, P.P., Ożga, M., Witkowski, B.; Seweryn, A.; Struzik, M.; Jastrzębski, C.; Zberecki, K. (2021), Titanium Nitride as a Plasmonic Material from Near-Ultr,aviolet to Very-Long Wavelength Infrared Range. Materials , 14, 7095. DOI: 10.3390/ma14227095

56. Zhewei Wang, Haining Chong, Jianhan Yang, and Hui Ye, (2019), Study on epsilon crossover wavelength tuning of heavily doped germanium-on-silicon in mid-infrared range, Opt. Express 27, 33724-33736,. DOI: 10.1364/OE.27.033724

57. Knoll W. (1998), Interfaces and thin films as seen by bound electromagnetic waves, Annual Review of Physical Chemistry, 49, 569-638, DOI: 10.1146/annurev.physchem.49.1.569

58. Sukla Rajak, Jayeta Banerjee, Mina Ray (2019), Parametric influence of film thickness and incident angle on resonance spectra of pre- and post-annealed Ga doped ZnO, J. Appl. Phys. 125, 243105. DOI : 10.1063/1.5096828.

59. David S. Kliger, James W. Lewis, Cora Einterz Randall, (1990), Polarized Light in Condensed Phases, in Polarized Light in Optics and Spectroscopy, Academic Press, , 237-274, DOI:10.1016/B978-0-08-057104-1.50011-9.

60. Thorsten Liebermann, Wolfgang Knoll, (2000), Surface-plasmon field-enhanced fluorescence spectroscopy, Colloids and Surfaces A: Physicochemical and Engineering Aspects,171, 115-130. DOI:10.1016/S0927-7757(99)00550-6.

61. P.R. West, S. Ishii, G.V. Naik, N.K. Emani, V.M. Shalaev, A. Boltasseva, (2010), Searching for better plasmonic materials, Laser Photon. Rev. 4, 795-808, DOI:10.1002/lpor.200900055.

62. N. C. Chen, W. C. Lien, C. R. Liu, Y. L. Huang, Y. R. Lin, C. Chou, S. Y. Chang, C. W. Ho; (2011) Excitation of surface plasma wave at TiN/air

interface in the Kretschmann geometry. J. Appl. Phys. 109, 043104, DOI:10.1063/1.3549732

63. T. B. A., Mostufa, S., Rana, M. M., Hossain, M. B., & Islam, M. R. (2023). A performance comparison of heterostructure surface plasmon resonance biosensor for the diagnosis of novel coronavirus SARS-CoV-2. Optical and Quantum Electronics, 55(5). DOI:10.1007/s11082-023-04700-4

64. Chiu, N., Tu, Y., & Huang, T. (2013). Enhanced Sensitivity of Anti-Symmetrically Structured Surface Plasmon Resonance Sensors with Zinc Oxide Intermediate Layers. Sensors, 14(1), 170–187. DOI:10.3390/s140100170

65. Dastmalchi, B., Tassin, P., Koschny, T., & Soukoulis, C. M. (2015). A new perspective on plasmonics: confinement and propagation length of surface plasmons for different materials and geometries. Advanced OpticalMaterials, 4(1),177184. DOI:10.1002/adom.201500446

66. Mascaretti, Luca & Barman, Tapan & Bricchi, Beatrice & Münz, Filip & Bassi, Andrea & Kment, Stepan & Naldoni, Alberto. (2021), Controlling the plasmonic properties of titanium nitride thin films by radiofrequency substrate biasing in magnetron sputtering. App Surf Sci. 554, 149543, DOI: 10.1016/j.apsusc.2021.149543.

67. Po-Ting Shen, Yonatan Sivan, Cheng-Wei Lin, Hsiang-Lin Liu, Chih-Wei Chang, and Shi-Wei Chu, (2016), Temperature- and roughness-dependent permittivity of annealed/unannealed gold films, Opt. Express 24, 19254-19263. DOI: 10.1364/OE.24.019254.

CHAPTER 6

INVESTIGATION OF PLASMONIC PROPERTIES IN DC SPUTTERED ZIRCONIUM NITRIDE THIN FILMS

Introduction

Zirconium nitride is another promising material for plasmonic applications due to its unique electrical and optical properties. ZrN exhibits high carrier density, ability to support surface plasmon polaritons in the visible wavelength region and high resistance to oxidation compared to the traditional plasmonic materials like gold and silver [1-4]. Zirconium nitride exhibits a metallic-like optical response with high reflectivity across the visible and near-infrared spectrum [5]. Its ability to support surface plasmons and the possibility of tuning plasmonic behaviour by tailoring opto-electronic properties through compositional control make ZrN an excellent alternative to noble metals for applications like nanoantennas, metamaterials, and plasmonic waveguides [6]. The performance of ZrN-based plasmonic devices is strongly dependent on the microstructure and surface properties of the material, which can be tailored through careful control of the deposition process and post-processing treatments [7]. Reactive sputtering and pulsed laser deposition are two common techniques used to coat ZrN thin films [8-9]. Being composition dependent, the structure and properties of the films can be tuned by adjusting parameters like gas composition, pressure, and substrate temperature.

This chapter will provide a description on the reactive sputtering of ZrN thin films coated to cover glass slides, the optical and electrical properties of the material along with structural and morphological analysis. The film properties were tuned with respect to the variations in the gas composition and sputtering power. Grazing Incident-XRD and XPS characterisation techniques were used to elucidate the structural properties. Plasmonic behaviour of the films were investigated with opto-electrical property correlations, as done for titanium nitride, discussed in the previous chapters.

The negative permittivity and low loss nature were confirmed in the samples by analysing the optical reflectance spectra. The surface plasmon resonance excitations were experimentally conducted using prism based Kretchsmann configuration in wavelength interrogation.

6.1 Development of zirconium nitride films for plasmonic applications

Zirconium nitride films with variable stoichiometry were prepared by changing the deposition conditions in DC reactive sputtering. Thin films with ZrN_x compositions were prepared initially by evacuating the deposition chamber to a base pressure of 5×10^{-6} mbar using a turbo molecular pump followed by admitting argon (4N purity) gas for plasma creation and nitrogen (4N purity) gas as reactive source. The overall gas flow was controlled using mass flow controller. Zirconium nitride films were reactively dc sputtered using a Zr metal target with 4N purity having 2-inch diameter. The working pressure was maintained at 9×10^{-3}mbar throughout the deposition. After admitting argon and nitrogen gases to the chamber, the metal target was pre-sputtered for 5 minutes to remove impurities, if any, on the target. Depositions were carried out at room temperature onto pre-cleaned soda-lime glass substrates. The cleaning process of the glass slides was carried out by ultrasonicating in soap water, distilled water, acetone, and isopropanol one after the other for 15 minutes, followed by drying in a nitrogen stream. During the deposition, the substrate to target distance was kept constant at 55mm. The substrate holder is rotated with speed 10 rpm to ensure uniformity for the films. The depositions were carried out at two different sputtering power, 60W and 80W, as given in Table 6.1.

Table 6.1. Experimental conditions used for sputtering

N_2 Gas	60W	80W
0.5 SCCM	ZRN1	ZRN4
1.0 SCCM	ZRN2	ZRN5
1.5 SCCM	ZRN3	ZRN6

6.2 Structural properties sputtered Zirconium nitride films

6.2.1 X-ray diffraction Studies

Fig. 6.1 illustrates the GI-XRD patterns obtained for the zirconium nitride films with variable deposition power and different Ar/N_2 gas compositions. The X-ray diffraction analysis was carried out from 25 to 70 degrees with a grazing angle of 1 degree. The aforementioned patterns were matched with the ICDD file 00-035-0753 of cubic zirconium nitride with peaks corresponding to (111), (200), (220), and (311) crystal planes at 2-theta angles 33.89°, 39.33°, 56.83° and 67.85°, respectively. All the sputtered films predominantly oriented along the (111) crystal plane. The samples were deposited with 2 different sputtering power, in which high sputtering power led to more prominent (200) and (220) peaks, which may be due the increased deposition rate with high power.

The samples were deposited with variable nitrogen gas flow during deposition in order to vary the stoichiometry in the coated films. Increase in the nitrogen gas flow contributes to the increased nitrogen content in the films fabricated As the nitrogen flow was increased from 0.5sccm to 1.5sccm i.e. for ZRN1 to ZRN3, the full width at half maximum of the XRD peaks increased, as seen in Fig.6.1, may be due to the decrease in the crystalline Klumdong et al reported crystalline to amorphous phase transition for nitrogen variation from 0.5-1.5 sccm [10]. Zirconium nitride

structural phase is found to fluctuate highly for small gas composition variation. When the nitrogen flow rate was 1sccm, the ratio of intensities of (111)/(200) peak is found to be small compared to other cases, irrespective of the sputtering power [11], In zirconium nitride samples ZRN1 and ZRN3, as indicated by the slight shift in the (111) peak position [12-13].The samples coated at higher deposition power exhibited more crystalline nature.

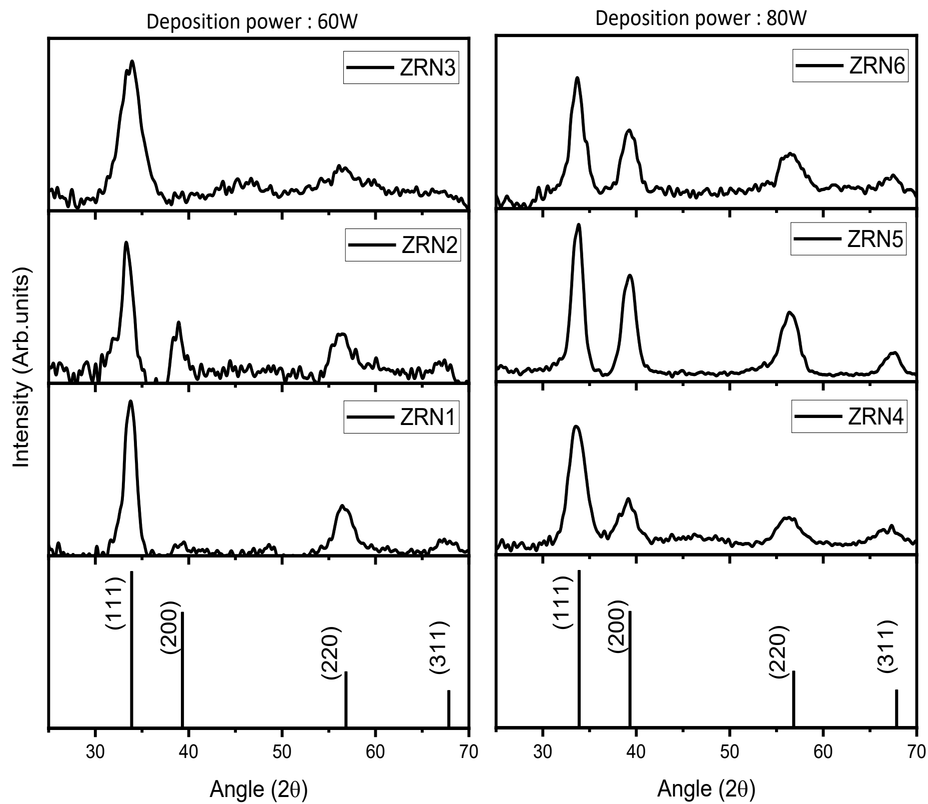

Fig. 6.1: GI-XRD patterns of the zirconium nitride films deposited with two sputtering power, 60W (left) and 80W (right), and with different Ar/N_2 gas compositions (ZRN1 to ZRN 6). The ICDD file 00-035-0753 of cubic zirconium nitride is shown at the bottom.

6.2.2 X-ray Photoelectron Spectroscopic analysis

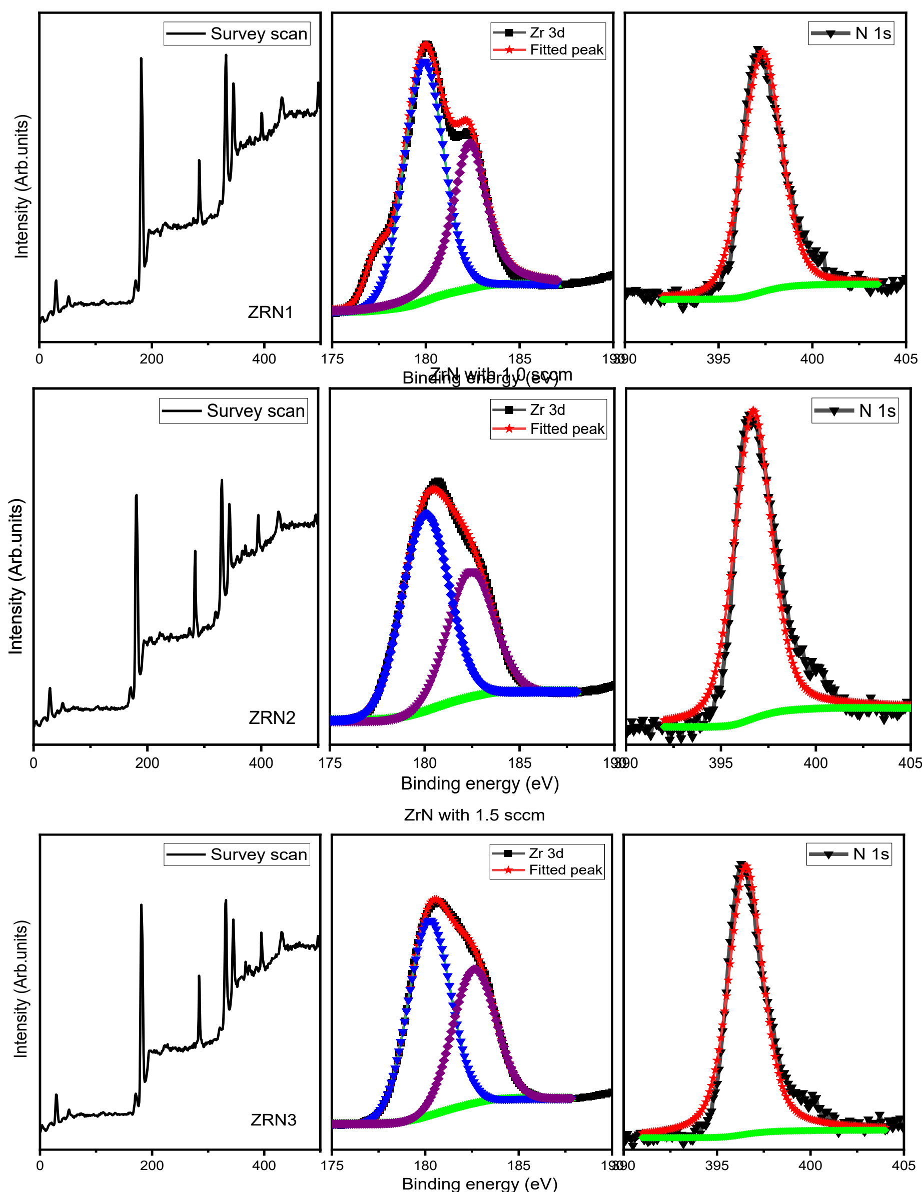

Fig. 6.2. Survey scan spectrum, high resolution scan spectra of Zirconium and nitrogen of DC sputtered zirconium nitride thin film samples (ZRN1, ZRN2 and ZRN3) deposited with different Ar/N_2 gas compositions at constant DC power of 60W

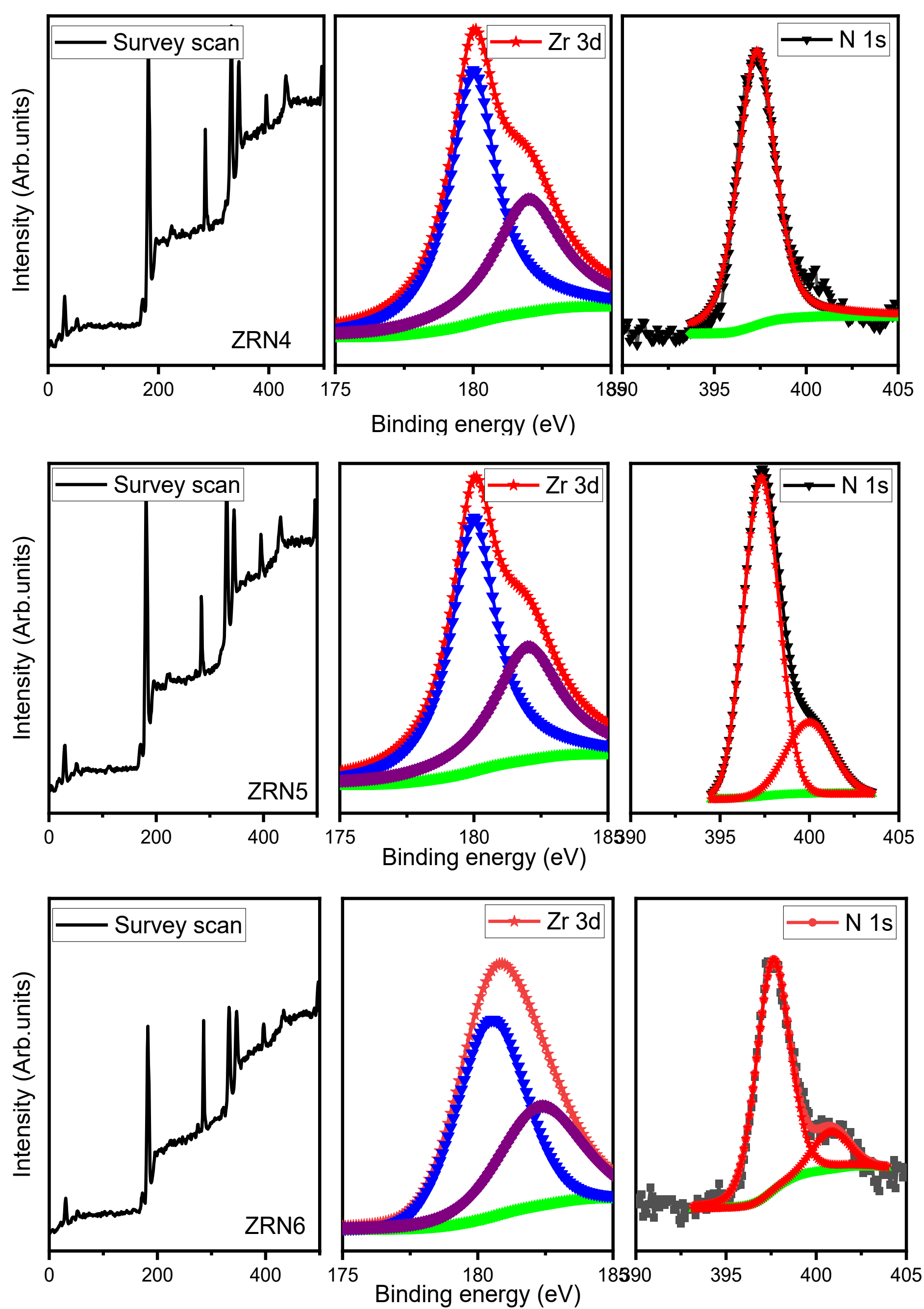

Fig. 6.3. Survey scan spectrum, high resolution scan spectra of Zirconium and nitrogen of DC sputtered zirconium nitride thin film samples (ZRN4, ZRN5 and ZRN6) deposited with different Ar/N_2 gas compositions at constant DC power of 80W

For further proving the stoichiometric nature for plasmonic applications, surface composition analysis was carried out further with X-ray photoelectron spectroscopic analysis. The films deposited with variable nitrogen flow at constant DC power of 60W and 80W were subjected for XPS measurements and the survey scan spectrum obtained along with the high-resolution spectra of Zr 3d and N1s are shown in Fig. 6.2 and Fig. 6.3, respectively. The peak positions were corrected with adventious carbon peak at 284.6eV [14-15]. The binding energy values corresponding to core level spectra of Zirconium and Nitrogen are given in Table 6.2. The elemental contributions were calculated from the ratio of the area under the high-resolution spectra, and the intensity ratios were corrected with sensitivity factors [16].

The elemental composition is found out using the given equation

$$\text{Aomic \% of } A = \frac{\frac{A}{a}}{\frac{A}{a} + \frac{B}{b}} \dots\dots\dots\dots\dots\dots..(6.1)$$

where A and B represents area under elements, a and b represent atomic sensitivity factors for respective elements. The values obtained are tabulated in Table 6.3 and the corresponding graph for 60W deposition power is plotted in Fig 6.3.

Table 6.2. Peak assignments for ZrN

Element	Peak energy (eV)	Peak assignment
Zirconium	180.1 [16]	Zr $3d_{5/2}$
	182.5 [16]	Zr $3d_{3/2}$
Nitrogen	397.2 [17]	N 1s

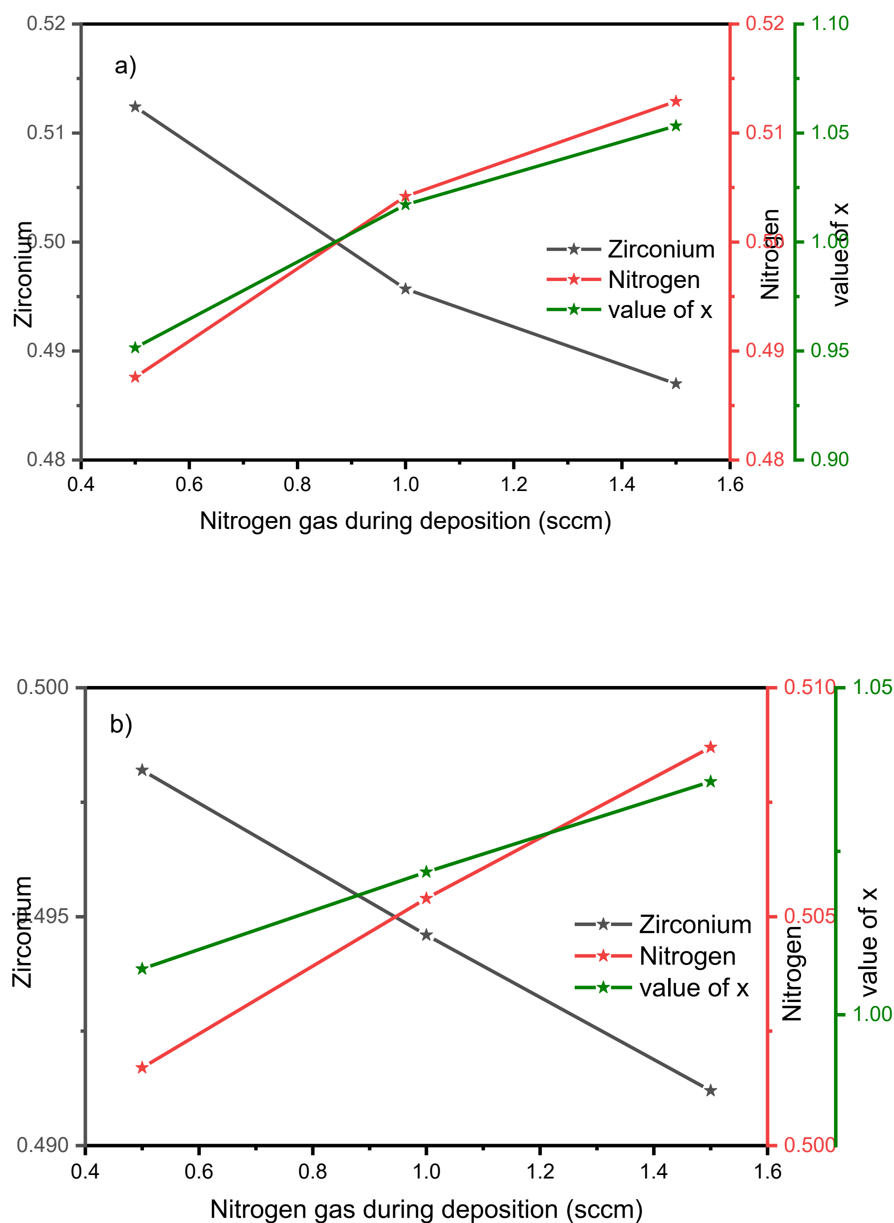

Fig. 6.4 Variation in elemental composition with respect to amount of nitrogen gas during deposition with power (a) 60W and (b) 80W

Table 6.3 Variation in elemental composition with respect to amount of nitrogen gas during deposition

Sample name	Zirconium	Nitrogen	N/Zr ratio (Value of x)
ZRN1	0.5124	0.4876	0.9515
ZRN2	0.4957	0.5042	1.0171
ZRN3	0.4870	0.5129	1.0533
ZRN4	0.4982	0.5017	1.0069
ZRN5	0.4946	0.5054	1.0218
ZRN6	0.4912	0.5087	1.0356

Elemental compositions in each sample was calculated and the percentage obtained is illustrated in Fig 6.4a and 6.4b. Zirconium contribution with varying nitrogen gas during deposition of 60W shows a gradual decrease from 0.51 to 0.48. Corresponding gradual increase in the nitrogen elemental concentration from 0.48 to 0.51 is found, which agrees with the earlier observations [18-19]. The calculated x value in ZrN_x from elemental composition confirms the stoichiometric nature of reactively sputtered zirconium nitride thin films. N/Zr ratio varies from 0.95 to 1.05 with the variation of nitrogen from 0.5sccm to 1.5sccm, during deposition for deposition power of 60W, while that of 80W of deposition power varies from 1.00 to 1.035. XPS analysis carried out for the films coated at 60W and 80W sputtering power confirm the stoichiometric nature of zirconium nitride films.

6.3 Morphological analysis

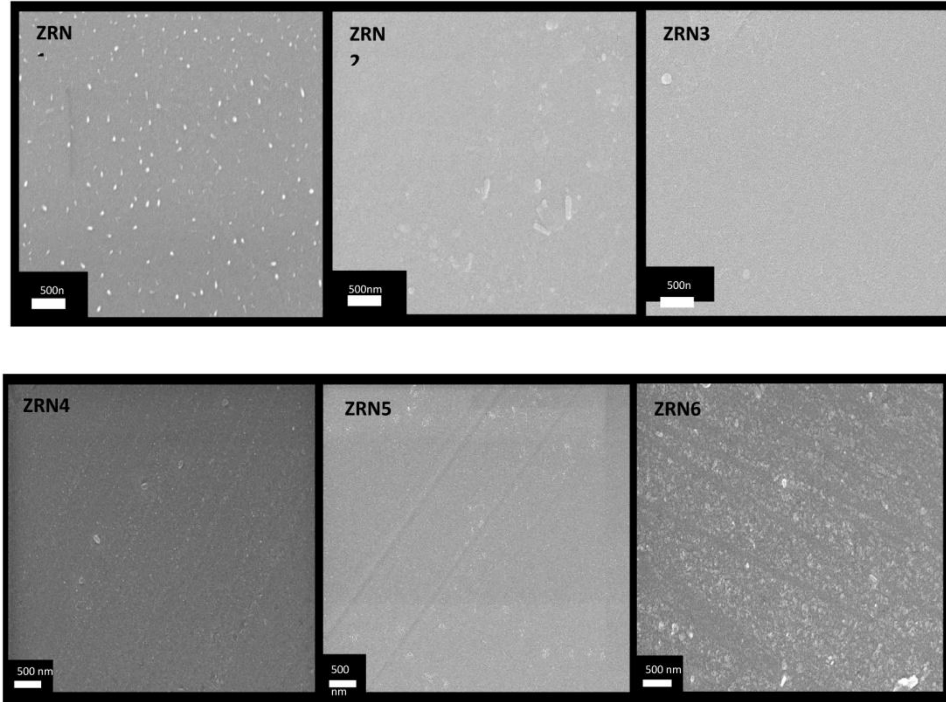

Fig. 6.5 Surface morphology of zirconium nitride thin films coated at sputtering power of 60 W (ZRN1, ZRN2 and ZRN3) and 80W (ZRN4, ZRN5 and ZRN6) with variable nitrogen gas concentration

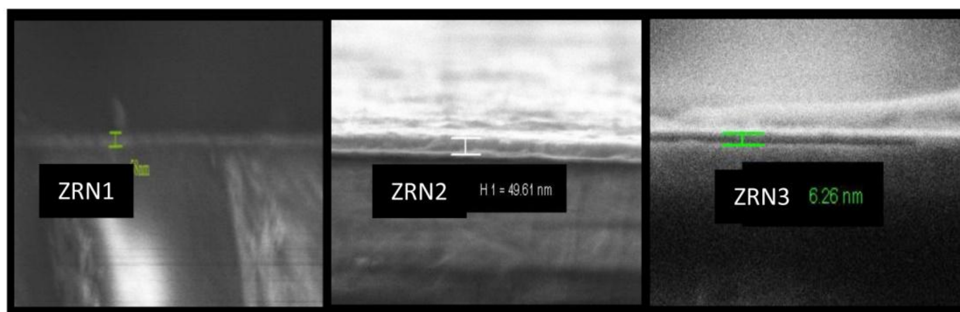

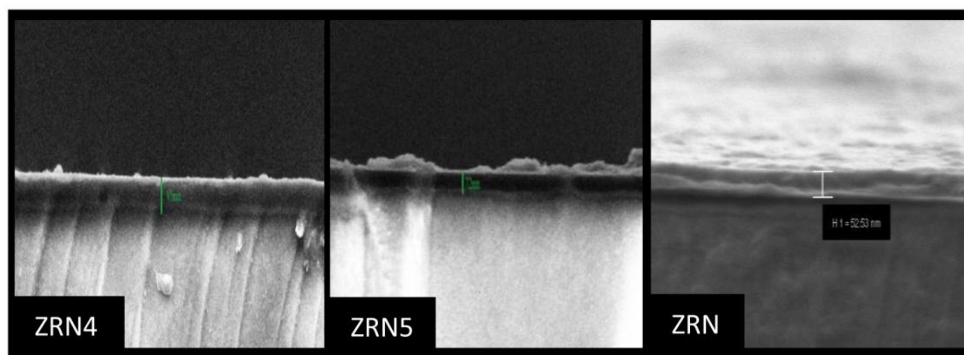

Fig. 6.6 Cross-section images of zirconium nitride thin films deposited at sputtering power of 60W (ZRN1, ZRN2, ZRN3) and 80W (ZRN4, ZRN5, ZRN6) with different nitrogen gas concentrations.

Fig. 6.5 represents the smooth uniform crack free surfaces obtained for DC sputtered zirconium nitride thin films with variable nitrogen gas compositions during the deposition process. Cross-section analysis provided thickness of the thin film samples, which shows a gradual decrement with increased nitrogen content. As the nitrogen gas during deposition increases from 0.5sccm to 1.5sccm, the XPS analysis confirmed the increase in nitrogen content in the sample from 0.48 to 0.51. The film thickness reduced from 57 nm to 27 nm, as seen in the cross-section SEM (Fig.6.6). These variations are plotted in the Fig 6.7. Therefore, by correlating XPS and FESEM cross-section analysis, it can be concluded that the deposition rate decreases as the nitrogen content in the films increases. Zhang et al reported a variation of film thickness from 1.5 µm to 0.8µm with increase in nitrogen concentration during the deposition [20]. Klumdong et al also reported similar nature of decrease in deposition rate in zirconium nitride films [21]. As seen, smooth surface morphology is obtained for the film ZRN3 compared to other samples deposited at 60W sputtering power. In the case

of the samples coated at 80W, both ZRN4 and ZRN5 are having smooth surface. The increase in the RF power contributes to increase in the kinetic energy of plasma density, and thereby causing increase in the plasma density [22], which may be reason for the increase in the thickness of the film with increase in the deposition power.

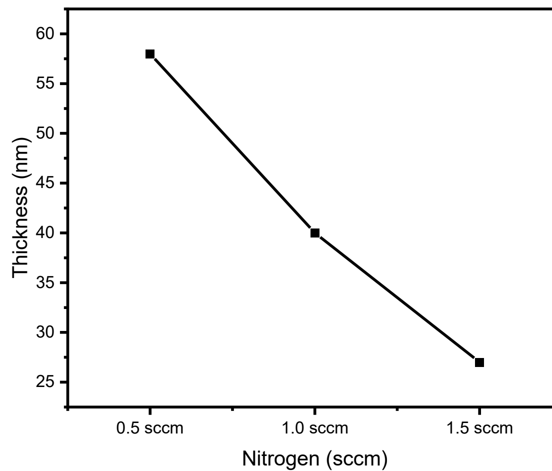

Fig. 6.7. Variations in the thickness of the films deposited with different nitrogen gas concentrations at constant power

6.4 Electrical properties

Carrier concentration of the order of 10^{22} /cm^3 is necessary for exhibiting plasmonic properties in the visible region of the electromagnetic spectrum. Hall measurements were carried out for investigating the electrical properties of the sputtered zirconium nitride thin films.

Table 6.4. Electrical properties of ZrN films

Sample name	Carrier concentration (cm^{-3})	Mobility (cm^2/Vs)
ZRN1	5.726×10^{21}	0.3803
ZRN2	4.039×10^{21}	0.5416
ZRN3	8.470×10^{19}	3.312
ZRN4	5.633×10^{22}	0.1899
ZRN5	2.885×10^{22}	0.2346
ZRN6	8.695×10^{20}	0.2976

Table 6.4 illustrates the carrier concentration and mobility estimated from Hall measurements in the coated ZrN_x thin films deposited at sputtering power of 60W and 80W. The resistivity of the film samples were found to be in the μΩ cm range. Carrier concentration shows a gradual decrease with increase in the N/Zr ratio, where the deposition was carried out with variable nitrogen gas concentration. As seen in the Table 6.4, the samples from ZrN1 to ZRN3 and ZrN4 to ZRN6, the carrier concentration decreases, while the mobility of electrons increases. Han et al. investigated the carrier density of ZrN films in relation to the decremental behaviour with nitrogen vacancy concentration [23]. He reported that a variation in nitrogen vacancy density from 25% to 5% resulted in an increase in valence band electron density [24], in which most of them gradually fill the covalent pdσ band and few fill the metallic σ band. The covalent pdσ band is below the Fermi level, which contributes little to the conduction electron, while the metallic σ band above the Fermi level can increase the conduction electron [23-25]. Although the carrier concentration decreases with gradual increase in the N/Zr ratio, the electron mobility increases in direct proportion with the variation in the N/Zr ratio. That is, the carrier mobility increased in the films from ZRN1 to ZRN3 and ZRN4 to ZRN6, where the deposition was carried out with increase in the nitrogen gas concentration, which in turn improved the surface smoothness in the samples, as described in the

previous section. There are reports on the high carrier concentration of zirconium nitride thin film suitable for plasmonic application [26]. However, the substrates used for coating were silica or sapphire substrates. In this work, the substrates used were standard microscopic cover glass slides, which provided electron density equivalent to films on the crystalline substrates.

6.5 Optical properties

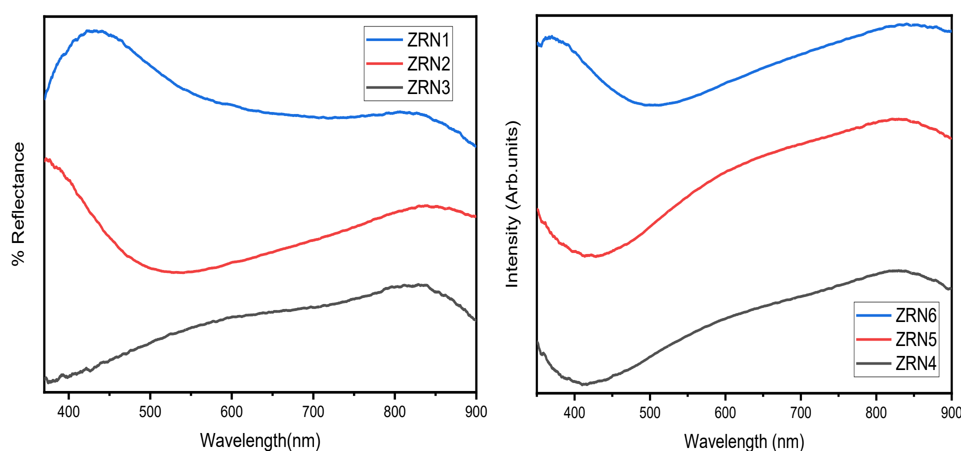

Fig. 6.8 Reflectance spectra of DC sputtered ZrN_x films.

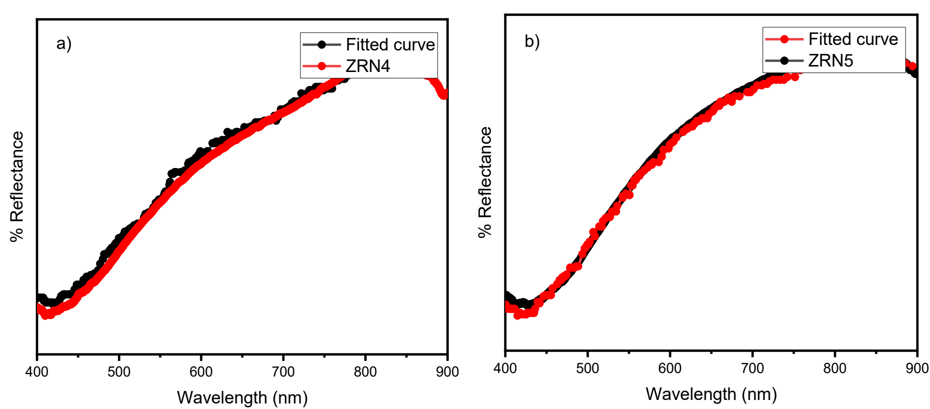

Fig. 6.9. Reflected spectra of the ZRN samples a) ZRN4 b) ZRN5 along with fitted patterns

Table 6.5. Fitting parameters used for Drude Lorentz fitting

Sample name	ε_∞	ω_p (eV)	ω_{0j} (eV)	γ_j (eV)
ZRN4	2	2.441	2.743	1.4202
		6.787	0	0.0304
ZRN5	2.01	1.851	2.456	0.7497
		2.549	3.064	0.7318
		7.353	0	0.0819

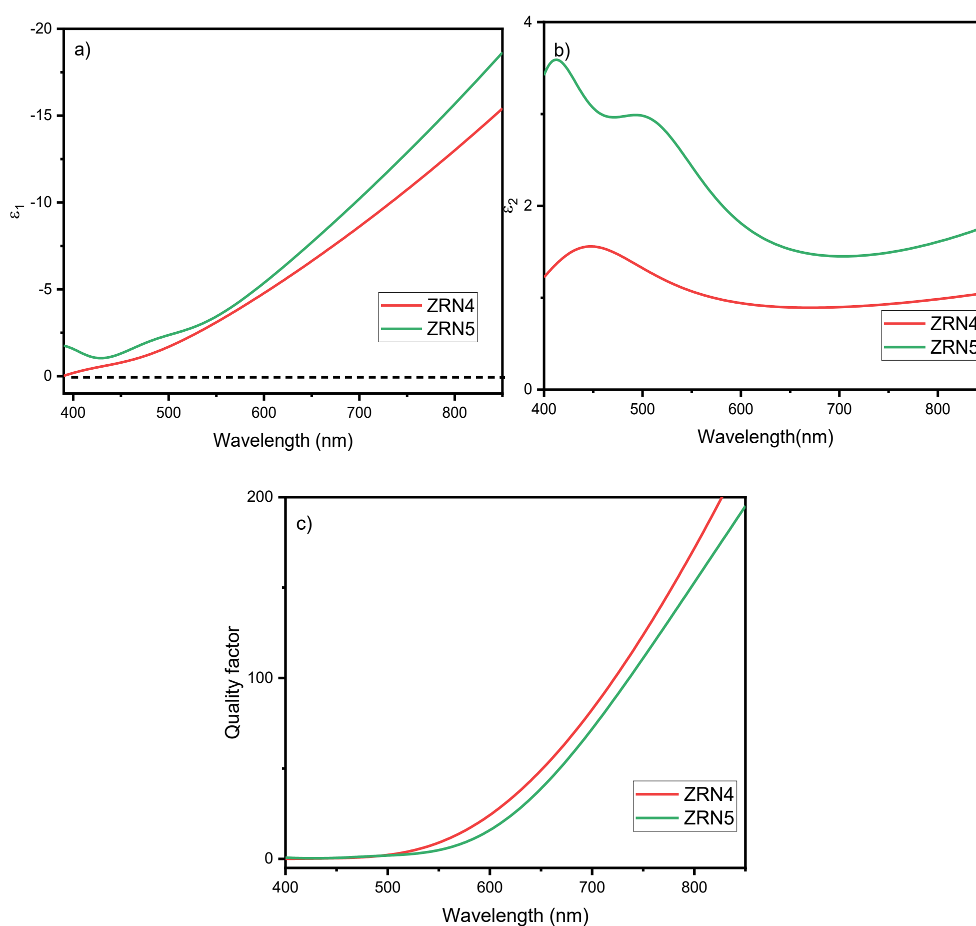

Fig. 6.10. Extracted real (a) and imaginary (b) parts of the complex permittivity, and the quality factor of DC sputtered ZrN_x films (c) of films having high carrier concentration

The complex dielectric permittivity is given by

$$\varepsilon(\omega) = \varepsilon_1(\omega) + i\,\varepsilon_2(\omega) \qquad (6.2)$$

The extraction of the real and imaginary parts of the complex permittivity, as per the equation 6.2 is essential to confirm the suitability for plasmonic applications. Reflectance spectra of DC sputtered zirconium nitride films were recorded in visible region, as shown in Fig.6.8. The reflectance R for normal incidence and a semi-infinite medium is provided by the Fresnel relation [27]

$$R = \left|\frac{1-\sqrt{\varepsilon_r}}{1+\sqrt{\varepsilon_r}}\right|^2 \qquad (6.3)$$

Zirconium nitride consist of both free electrons and bound electrons. Hence the optical parameters can be extracted by using Drude-Lorentz approximation, where the Drude term consider the contribution of free electrons, while the Lorentz term accounts for the bound electrons to the dielectric function. The dielectric function can be written as,

$$\varepsilon_r = \varepsilon_\infty - \frac{\omega_{pu}^2}{\omega^2 - i\Gamma_D\omega} + \sum_{j=1}^{2}\frac{f_j\omega_{oj}^2}{\omega_{0j}^2 - \omega^2 + i\gamma_j\omega} \qquad (6.4)$$

where ε_∞ is high frequency dielectric constant, >1, Γ_D is the drude damping factor and ω_{0j} is the frequency of jth Lorentz oscillator with damping factor γ_j. $\Gamma = \frac{e}{\mu m^*}$, is the loss related Drude relaxation rate, or called momentum scattering rate [28].

Fig. 6.8 shows the reflectance spectra of the zirconium nitride films coated with two sputtering powers. The films possessing high carrier concentration (ZRN4 and ZRN5) were subjected for permittivity analysis. The dielectric function from the reflection spectra were extracted with the help of a

standard package, ReFfit [29], as explained in the previous chapters. The fitting parameter used to fit the reflectance spectra are tabulated in Table 6.5. The resultant fitted reflected pattern and sample reflectance patterns are given in Fig. 6.9 The real and imaginary parts of the complex permittivity extracted are as shown in Fig 6.10 (a) and (b). As discussed in the previous chapters, in the realm of plasmonics, the cross-over wavelength or screened plasma energy is important, which is given by the wavelength at $\varepsilon_1=0$. This wavelength marks the distinction between the positive and negative values of real part of the permittivity. The crossover wavelengths, as seen in the Fig 6.10(a), shows remarkable variation with respect to carrier concentration. The results are summarised in Table 6.6. In case of the samples ZRN4 and ZRN5, there is not much variation in the carrier density although the nitrogen gas during deposition was varied. Hence, there is no evident variation in the crossover wavelength, and the same is obtained to be less than 390 nm.

Table 6.6. Estimated crossover wavelength of the ZrN film samples

Sample name	Crossover wavelength (nm)
ZRN4	390
ZRN5	389

Patsalas et al reported the imaginary part of the dielectric constant (ε_2) to be <6 in the entire region of 1- 6 eV (200-1300nm) [30], which agrees with our observation for sputtered zirconium nitride thin films. The range of the imaginary permittivity value is less than 2, in the visible region as seen in Fig 6.10(a), which increases as wavelength increases. The negative permittivity region are most suited for plasmonic applications.

The plasmonic performance of a thin film depends on the quality factor of surface plasmon polariton propagation [31], which is given by

$$Q = \langle -\varepsilon_1^2 \rangle / \langle \varepsilon_2 \rangle \ldots\ldots\ldots\ldots\ldots\ldots\ldots\ldots (6.5)$$

Figure 6.10(c) shows the estimated quality factor for the thin film samples, which confirms the high plasmonic performance of the ZRN4 and ZRN5 samples, with excellent opto-electrical property correlation suitable for plasmonic excitations. From the quality factor values in Fig 6.10(c), it can be seen that the values exhibit drastic increase as the wavelength increases.

Nieborek et al reported that the combined effect of improved crystallinity and smooth microstructure is necessary for enhanced plasmonic performance [32]. Those two factors largely dependent on the deposition parameters of sputtering. Increase in the kinetic energy of the plasma density in sputtering may result in increase in the metallicity of the deposited film. [32]. Both the increase in deposition power and the decrease in Ar working pressure result in an increase in the kinetic energy. [22]. The analysis provided here proved better crystallinity, better surface characteristic and enhanced opto-electrical property in the films ZRN4 and ZRN5.

6.6 INVESTIGATION OF PLASMONIC PROPERTIES

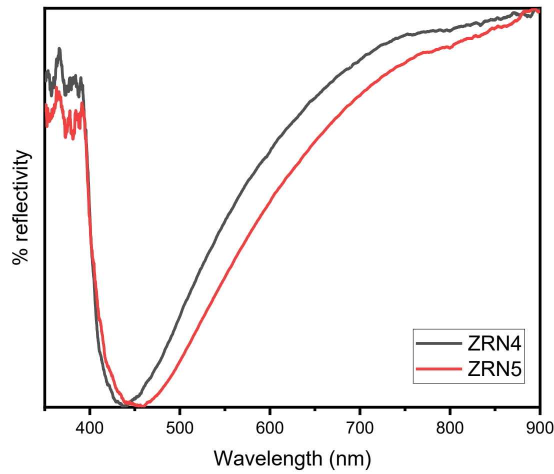

Fig. 6.11. Surface plasmon resonance excitation curve obtained in ZRN4 and ZRN5 in Kretchsmann configuration at an incidence angle of 45°.

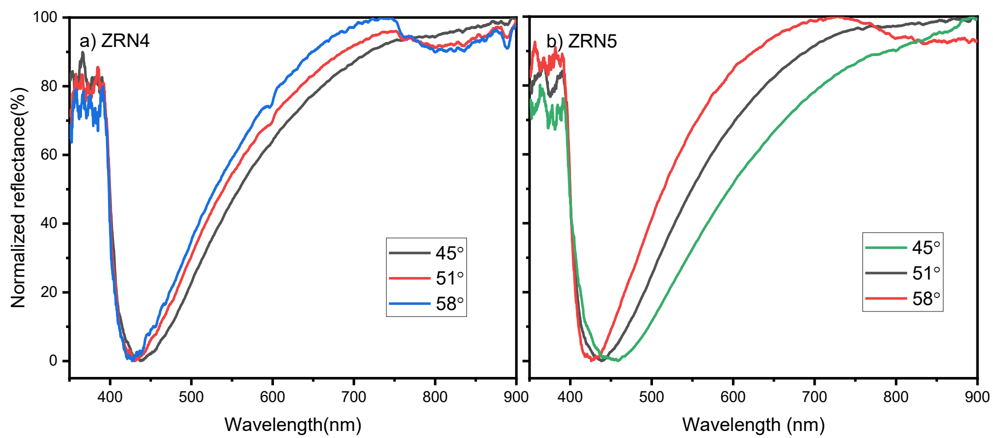

Fig. 6.12. Surface plasmon resonance curves obtained in the films (a) ZRN4 and (b) ZRN5 with different angles of incidence, 45°, 51° and 58°

superior electrical properties in terms of carrier concentration and mobility, and also possess higher quality factor when compared to the other samples.

A suitable momentum matching configuration is required in order to excite the surface plasmon polaritons in the sample as discussed in the Section 1.5 of this thesis. In the prism geometry configuration, p polarised visible light is allowed to fall on the zirconium nitride film coated on glass substrates, attached to the base of the BK7 prism with index matching fluid, at an angle greater than the critical angle. Evanescent field will be generated outside at the film-dielectric (air) interface. The reflected light intensity was analysed using spectrophotometer, which demonstrated the characteristic resonance dip corresponding to the SPR excitation in the visible region. The surface plasmon resonance excitation curves obtained with an incidence angle of 45° is shown in Fig 6.10, for the samples ZRN4 and ZRN5. As seen in the figure, a red shift in the SPR position from 441 to 456nm has been observed from the samples ZRN4 and ZRN5, deposited with variable nitrogen gas concentrations at specific sputtering power. The carrier density indicated a slight decrease from $5.63 \times 10^{22}/cm^3$ to $2.89 \times 10^{22}/cm^3$ for these samples. The decrease in carrier density marked red shift in the resonance wavelength position. The full width half maximum of SPR of the sample ZRN4 is found to be less in comparison with the sample ZRN5. For the film ZRN4, the observed FWHM is estimated to be 134nm, while it was 181nm for the film ZRN5.

When the incidence angle was increased, the coupling of SPP and incident light became more prominent and further narrower FWHM was observed. In case of the sample ZRN5, as the angle of incidence was changed from 45° to 58°, the corresponding surface plasmon resonance wavelength changed from 456nm to 424nm, as shown in Fig 6.12 (b). The blue shift observed in

the SPR wavelength was explained in the section 4.6 of this thesis. Similar blue shift was reported by Daniyal et al [33]; the author theoretically predicted that increasing the incidence angle would result in a reduction in the resonant wavelength. An optimum metal film thickness is always preferred for better SPP excitation [34]. Here, the quality factor estimated is significant. The quality factor is high for the sample ZRN4, which indicates better features for the SPR curve [35-36].

There are numerous reports on the theoretical predictions of plasmonic behaviour of zirconium nitride on the basis of the extraction of dielectric function using ellipsometry analysis. This is achieved by establishing negative permittivity and low loss characteristics in the films.. However, there is no experimental evidence reported so far of SPR excitation in zirconium nitride films [37-39]. In this work, the plasmonic behaviour of coated films has a theoretical background, and in addition, the plasmonic properties have been experimentally demonstrated. Zirconium nitride films fabricated with a high-quality factor and carrier densities of the order of $10^{22}/cm^3$ were provided successful experimental excitation in wavelength interrogation mode.

6.7 CONCLUSION

Stoichiometric zirconium nitride films possessing enhanced plasmonic properties due to high quality factor were fabricated by the DC sputtering with varying deposition power and gas composition during sputtering. The films coated on glass substrates exhibited a high carrier concentration of the order of 10^{22}/cc and low loss nature (<2), essential for plasmonic excitations in the visible region. The structural property analysis revealed (111) preferred orientation for the films. Smooth uniform morphology of the films were confirmed via FESEM analysis. The films having higher carrier concentration were subjected for SPP excitation in prism geometry configuration in wavelength interrogation, using visible light at an angle of incidence of 45°. For the first time, the experimental demonstration provided SPR excitation in zirconium nitride films prepared with variation in nitrogen concentration during deposition, from the wavelength 456nm to 424 nm in the films, when excited using Kretschmann configuration. The FWHM of the resonance curve was found to decrease with increasing angle of incidence.

6.8 References:

1. Jun Adachi, Ken Kurosaki, Masayoshi Uno, Shinsuke Yamanaka, (2005), Thermal and electrical properties of zirconium nitride, J. Alloys Compd., 399, 242-244, DOI:10.1016/j.jallcom.2005.03.005.

2. Shabani, A., Tsegay Korsa, M., Petersen, S., Khazaei Nezhad, M., Kumar Mishra, Y. and Adam, J. (2021), Zirconium Nitride: Optical Properties of an Emerging Intermetallic for Plasmonic Applications. Adv. Photonics Res., 2: 2100178. DOI: 10.1002/adpr.202100178

3. Shangtao Zhang, Jian Wang, Rong Wu, Lang Liu, Boting Pan, Chunhai Liu, Structural and corrosion resistance properties of sputtered zirconium nitride thin films as electrode material for supercapacitor, J. Alloys Compd., 900, 2022, 163506, DOI:10.1016/j.jallcom.2021.163506

4. Prasanna Das, Bidesh Biswas, Krishna Chand Maurya, Magnus Garbrecht, and Bivas Saha, (2022) ,Refractory Plasmonic Hafnium Nitride and Zirconium Nitride Thin Films as Alternatives to Silver for Solar Mirror Applications, ACS Appl. Mater. Interfaces 14, 46708-46715, DOI: 10.1021/acsami.2c09852

5. Yujing Ran, Zhaotan Jiang, Zhi Wang, (2022) All-nitride broadband metamaterial absorbers, Results in Physics, 38, 105657, DOI:10.1016/j.rinp.2022.105657.

6. Anwar Ul-Hamid, (2020), The effect of deposition conditions on the properties of Zr-carbide, Zr-nitride and Zr-carbonitride coatings – a review, Mater. Adv., 1, 988-1011,DOI: 10.1039/D0MA00232A

7. Ghemras, Ismail & Abdelli-Messaci, Samira & Alili, Baya & Gonzalez-Elipe, Agustin & Rico, V. & Izerrouken, M. & Hadj-Larbi, Fayçal. (2021). Characterizing the physicochemical and mechanical properties of ZrN thin films deposited on Zr substrates by pulsed laser technique. Eur Phys J-Appl Phys., 95. 10301. 10.1051/epjap/2021210064.

8. P.C. Johnson, H. Randhawa, (1987), Zirconium nitride films prepared by cathodic arc plasma deposition process, Surf. Coat. Technol., 33, 53-62, DOI: 10.1016/0257-8972(87)90176-9.

9. Q. Meng, M. Wen, C. Qu, C. Hu and W. Zheng, (2011), Preferred orientation, phase transition and hardness for sputtered zirconium nitride films grown at different substrate biases, Surf. Coat. Technol., 205, 2865–2870

10. P. Klumdoung, A. Buranawong, S. Chaiyakun, P. Limsuwan, (2012), Variation of color in Zirconium nitride thin films prepared at high Ar flow

rates with reactive dc magnetron sputtering, Procedia Engineering 32, 916 - 921,. DOI: 10.1016/j.proeng.2012.02.032

11. Benia, Hadj & Guemmaz, M. & Schmerber, G. & Mosser, A. (2004). Optical and electrical properties of sputtered ZrN compounds. Catalysis today. 89. 10.1016/j.cattod.2003.12.006

12. JP Dauchot, S Edart, M Wautelet, M Hecq,,(1995),Synthesis of zirconium nitride films monitored by in situ soft X-ray spectrometry, Vacuum, 46, Issues 8-10,927-930, DOI:10.1016/0042-207X(95)00074-7.

13. Chengyan Gu, Zhanpeng Sui, Yuxiong Li, Haoyu Chu, Sunan Ding, Yanfei Zhao, Chunping Jiang, (2018). The growth of the metallic ZrNx thin films on P-GaN substrate by pulsed laser deposition, Appl. Surf Sci., 433, 306-311, DOI:10.1016/j.apsusc.2017.09.262.

14. Turner, N.H. (1992), Estimates of peak areas and relative atomic amounts from wide-scan XPS spectra‡. Surf. Interface Anal., 18: 47-51. DOI:10.1002/sia.740180108

15. Fred A. Stevie, Carrie L. Donley (2020), Introduction to x-ray photoelectron spectroscopy. J. Vac. Sci. Technol.; 38 (6): 063204. DOI:10.1116/6.0000412

16. Rizzo, A. & Signore, Maria & Mirenghi, Luciana & Tapfer, Leander & Piscopiello, Emanuela & Salernitano, Elena & Giorgi, R.. (2012). Sputtering deposition and characterization of zirconium nitride and oxynitride films. Thin Solid Films. 520. 3532–3538. DOI: 10.1016/j.tsf.2012.01.005.

17. Ingrid Milošev, Hans-Henning Strehblow, Boris Navinšek, Peter Panjan, (1998), Zirconium Nitride by XPS. Surf. Sci. Spectra 5, 152–158. DOI: 10.1116/1.1247861

18. Chuan-Pu Liu, Heng-Ghieh Yang, (2004), Deposition temperature and thickness effects on the characteristics of dc-sputtered ZrNx films, Mater. Chem. Phys., 86, 2–3, 370-374, DOI:10.1016/j.matchemphys.2004.03.026.

19. Han, Kechang & Lin, Guo-Qiang & Dong, Chuang & Tai, Kai-Ping & Jiang, Xin. (2017). Influence of Nitrogen Vacancy Concentration on Mechanical and Electrical Properties of Rocksalt Zirconium Nitride Films, Acta Metall. Sin. 30. DOI: 10.1007/s40195-017-0636-x.

20. Zhang, Zhiguo & Tianwei, Liu & Jun, Xu & Xinlu, Deng & Dong, Chuang. (2006). N-rich Zr–N films deposited by unbalanced magnetron sputtering enhanced with a highly reactive MW-ECR plasma. Surf Coat Tech. 200, 4918-4922. DOI:10.1016/j.surfcoat.2005.04.060.

21. P. Klumdoung, P. Asanithi, S. Chaiyakun and P. Limsuwan. (2011), Variation of color in Zirconium nitride thin films prepared by reactive dc magnetron sputtering. Adv. Mater. Res. 214, 320-324, DOI: 10.1016/j.proeng.2012.02.032.

22. Zhou, C., Li, T., Wei, X., & Yan, B. (2020). Effect of the Sputtering Power on the Structure, Morphology and Magnetic Properties of Fe Films. Metals, 10, 896. https://doi.org/10.3390/met10070896

23. Ke-Chang Han, Guo-Qiang Lin, Chuang Dong, Kai-Ping Tai, Xin Jiang, (2017) Influence of Nitrogen Vacancy Concentration on Mechanical and Electrical Properties of Rocksalt Zirconium Nitride Films. Acta Metall. Sin. (Engl. Lett.) **30**, 1100–1108. DOI:10.1007/s40195-017-0636-x

24. Hayder A. Al-Atabi, Xiaotian Zhang, Shanmei He, Cheng chen, Yulin Chen, Eli Rotenberg, James H. Edgar, (2022), Lattice and electronic structure of ScN observed by angle-resolved photoemission spectroscopy measurements, Appl. Phys. Lett. 121, 182102. DOI:10.1063/5.0119628

25. Stampfl, C., Mannstadt, W., Asahi, R., & Freeman, A. J. (2001). Electronic structure and physical properties of early transition metal mononitrides: Density-functional theory LDA, GGA, and screened-exchange LDA FLAPW calculations, Phys. Rev. B, 63, 155106. https://doi.org/10.1103/PhysRevB.63.155106

26. A. Dutta, N. Kinsey, S. Saha, U. Guler, V. M. Shalaev, and A. Boltasseva, (2016),Plasmonic Interconnects Using Zirconium Nitride, in *Conference on Lasers and Electro-Optics*, OSA Technical Digest (Optica Publishing Group,), paper JW2A.86.

27. J. Casaux, (1981), *Physique du solide*, Masson, Paris, , p. 273.

28. F. Wooten, (1972), *Optical Properties of Solids*, Academic press, New York 10003. United Kingdom Edition,

29. Kuzmenko, Alexey. (2005), Kramers-Kronig constrained variational analysis of optical spectra. Rev. Sci. Instrum. 76, 083108 DOI: 10.1063/1.1979470

30. Patsalas, Panos. (2019) Zirconium nitride: A viable candidate for photonics and plasmonics?. Thin Solid Films, 688. 137438. 10.1016/j.tsf.2019.137438.

31. P.R. West, S. Ishii, G.V. Naik, N.K. Emani, V.M. Shalaev, A. Boltasseva, (2010),Searching for better plasmonic materials, Laser Photon. Rev. 4, 795-808, , DOI:10.1002/lpor.200900055.

32. Mateusz Nieborek, Cezariusz Jastrzębski, Tomasz Płociński, Piotr Wróbel, Aleksandra Seweryn, Jarosław Judek, (2024), Optimization of the plasmonic properties of titanium nitride films sputtered at room temperature

through microstructure and thickness control. Sci. Rep. 14, 5762. https://doi.org/10.1038/s41598-024-56406-6

33. Daniyal, W. M. E. M. M., Fen, Y. W., Abdullah, J., Sadrolhosseini, A. R., & Mahdi, M. A. (2021). Design and Optimization of Surface Plasmon Resonance Spectroscopy for Optical Constant Characterization and Potential Sensing Application: Theoretical and Experimental Approaches. Photonics, 8, 361. DOI:10.3390/photonics8090361

34. Eduardo Fontana, (2006), Thickness optimization of metal films for the development of surface-plasmon-based sensors for nonabsorbing media," Appl. Opt. 45, 7632-7642

35. Zhang, R., Pu, S., & Li, X. (2019). Gold-Film-Thickness Dependent SPR Refractive Index and Temperature Sensing with Hetero-Core Optical Fiber Structure. Sensors, 19, 4345. https://doi.org/10.3390/s19194345

36. B. Wang, P. Yu, W. Wang, X. Zhang, H. Kuo, H. Xu, Z. M. Wang, (2021), High-Q Plasmonic Resonances: Fundamentals and Applications. *Adv. Optical Mater.*, 9, 2001520. https://doi.org/10.1002/adom.202001520

37. P. Patsalas, N. Kalfagiannis, S. Kassavetis, G. Abadias, D.V. Bellas, C. Lekka, E. Lidorikis, (2018), Conductive nitrides: Growth principles, optical and electronic properties, and their perspectives in photonics and plasmonics, Materials Science and Engineering R 123, 1-55. DOI:10.1016/j.mser.2017.11.001,

38. G.V. Naik, V.M. Shalaev, A. Boltasseva, (2013), Alternative Plasmonic Materials: Beyond Gold and Silver, Adv. Mater. 25, 3264-3294. DOI:10.1002/adma.201205076.

39. A. Lalisse, G. Tessier, J. Plain, G. Baffou, (2016) ,Plasmonic efficiencies of nanoparticles made of metal nitrides (TiN, ZrN) compared with gold, Sci. Rep. 6, 38647. DOI:10.1038/srep38647

CHAPTER 7

SUMMARY OF THESIS

Investigation of transition metal nitride (TMN) thin films as an alternative plasmonic material for visible region was carried out in the thesis. Titanium nitride and zirconium nitride were chosen as materials under this study. Since they are non-stoichiometric compounds, the properties of the materials depend on the preparation methods, which largely influence their plasmonic properties. Thus, tunability in the material composition of transition metal nitrides can be achieved.

All thesis chapters begin with initial phase formation confirmation through XRD analysis, followed by composition analysis via XPS measurement. After that, vacancy determination was performed using Raman spectroscopy. In order to focus on the plasmonic properties of TMN thin films, it is necessary to correlate with the opto-electrical properties and morphological analysis of the films. The overall conclusion points are given below.

- PROCESS DEPENDENCY: In the investigation of plasmonic properties in titanium nitride films, the film fabrication was carried out in 3 different ways: 1) full vacuum-based approach, 2) partial vacuum-based, and 3) solution-based. Since process dependent, each films have their own merits and demerits. Though the process parameters have been tuned to get the required high carrier concentration in all fabrication routes, other improved properties such as crystallinity, mobility the values of real and imaginary permittivity etc. achieved in accordance with deposition process, also contributed to this. That is, surface plasmon resonance has been achieved in titanium nitride by properly engineering the material properties. Therefore, it is clear that the plasmonic properties are tunable with process dependence. More crystalline films were deposited once the

titanium dioxide film was used as precursor film for nitridation with ammonia. This helped reduce the loss in titanium nitride.

- COMPOSITION DEPENDENCY: Among the 3 different fabrication methods chosen for titanium nitride, the compositions of the films fabricated was tuned in each case. This further tuned the overall properties of the films, such as preferred orientation, electrical and optical properties, etc. The improved plasmonic performance observed in the samples is the combined effect of all these properties. This further predicts that the plasmonic properties can be tuned by tuning the composition in the sample.
- COST EFFECTIVE APPROACH: The overall thesis motive is to develop cost-effective and stable alternative plasmonic material to replace the conventionally used metals. The study revealed a cost-effective route, when solution-based technique was used for the fabrication of titanium nitride thin films from titanium dioxide film, as the samples developed exhibits lower imaginary part of permittivity with high quality factor.
- SURFACE PLASMON RESONANCE EXCITATION: When the deposition methods were varied, differences were evident in the electrical properties. Even though they are exhibiting high carrier concentration, the mobility and hence resistivity in the sample varied due to the differences in the crystalline properties. Titanium nitride films deposited by ammonia nitriding titanium metal provided low resistivity. Combined with the much wider tunability of the thickness of the metal films, the successful experimental excitation of SPP in titanium nitride films have been achieved.

- BETTER PLASMONIC MATERIAL: In addition to all of the above, this work also investigated the plasmonic properties of another potential material, zirconium nitride. As predicted in the literature, it has proven to be a better alternative material than the titanium nitride. Successful SPP experimental excitation in sputtered films with Kretzmann configuration showed a blue shift in the crossover wavelength and a very narrow FWHM in the resonance curve.

CHAPTER 8

RECOMMENDATIONS

On the basis of the studies carried out on the plasmonic properties of titanium nitride and zirconium nitride films, it was found that they agree well with the idea of serving as alternative plasmonic materials. The complete thesis can be divided into two portions, one dealing with process dependence on the plasmonic properties of titanium nitride thin films. The latter involves an introductory understanding of the plasmonic properties of zirconium nitride films deposited using vacuum coating method.

In order to exhibit plasmonic properties in visible region, a high carrier density of the order of $10^{22}/cm^3$ is needed, and the same is achieved in titanium nitride thin films in all fabrication routes. Though successfully excited surface plasmon resonance in the fabricated samples through thickness control, the excitation mechanism used in this study was the prism geometry configuration. There is a lot of room available for further exploration of plasmonic behaviour. The prism type geometry is based on the Kretschmann configuration, which is suitable for various sensing studies. The next prime area is to choose other excitation mechanisms, such as grating and fiber-optic configurations, for titanium nitride. Successful excitation in these configurations has the advantage of further miniaturization of the sensing devices. The titanium nitride fabricated via the TiO_2 conversion offers a cost-effective solution for coating titanium nitride films on drillers and other equipment.

This thesis includes only a preliminary chapter on a comprehensive analysis of structural, optical, and electrical properties of zirconium nitride films, which sheds more light on the plasmonic properties of zirconium nitride samples. The investigation revealed reduced dielctric loss in ZrN samples, proving that zirconium nitride is a relatively better alternative material than titanium nitride. Other processes, such as nitridation using ammonia for

fabricating ZrN from a zirconium metal sample, can also be adopted. In addition, there is possibility of conversion of zirconium oxide to zirconium nitride via nitridation of ammonia gas. Investigation can extend to other excitation configurations, such as grating and fibet-optic.

The future of plasmonics lies in the fabrication of TO devices and metamaterials, overcoming the limitations of noble metals. Alternative plasmonic materials such as titanium and zirconium nitrides are a good solution to obtain improved TO and metamaterial platforms. Apart from these, transition metal nitride films have potential in solar cells and NIR reflectors.

UNIVERSITY OF CALICUT

CERTIFICATE ON PLAGIARISM CHECK

1.	Name of the Research Scholar	Liya Tony	
2.	Title of thesis / dissertation	Study of surface plasmon resonance in transition metal nitride thin films	
3.	Name of the Supervisor	Dr. S.N. Potty	
4.	Department/Institution	Centre for Materials for Electronics Technology (C-MET) Athani 680581	
5.		Non Core	Core
		Introduction/ Theoretical overview/Review of literature/ Materials & Methods/ Methodology	**Analysis/Result/Discussion / Summary/Conclusion/ Recommendations**
	Similar content (%) identified	**6**	**4**
	Acceptable maximum limit (%)	10	10
6.	Software used	iThenticate	
7.	Date of verification	Wed Apr 09 2025 00:00:00 GMT+0530 (India Standard Time)	

**Report on plagiarism check, specifying included/excluded items with % of similarity to be attached.*

Checked by (with name, designation & signature)

Dr. Nasirudheen. T
Assistant Librarian
University of Calicut, Kerala.

C.H. MOHAMMED KOYA LIBRARY, UNIVERSITY OF CALICUT, P.O., UNIVERSITY OF CALICUT

Name and signature of the Researcher

Name and signature of the Supervisor.

The Doctoral Committee* has verified the report on plagiarism check with the contents of the thesis, as summarized above and appropriate measures have been taken to ensure originality of the Research accomplished herein.

Name & Signature of the HoD/HoI (Chairperson of the Doctoral Committee)

**In case of languages like Malayalam, Tamil etc..on which no software is available for plagiarism check, a manual check shall be made by the Doctoral Committee, for which an additional certificate has to be attached.*